UNIVERSITY OF SOUTHAMPTON

FACULTY OF ENGINEERING AND THE ENVIRONMENT

Institute of Sound and Vibration Research

Active Control of Viscoelastic Metamaterials

by

Matthew Reynolds

Thesis for the degree of Doctor of Philosophy

March 2015

UNIVERSITY OF SOUTHAMPTON

ABSTRACT

FACULTY OF ENGINEERING AND THE ENVIRONMENT

Institute of Sound and Vibration Research

Doctor of Philosophy

ACTIVE CONTROL OF VISCOELASTIC METAMATERIALS

by Matthew John Reynolds

Metamaterials have been the subject of significant interest over the past decade due to their ability to produce novel acoustic behaviour beyond that seen in naturally occurring media. As well as their potential in acoustic cloaks and lenses, of particular interest is the appearance of band gaps which lead to very high levels of attenuation across the material within narrow frequency ranges. Unlike traditional periodic materials which have been employed at high frequencies, the resonant elements within metamaterials allow band gaps to form within the long wavelength limit; at low frequencies where it is most difficult to design satisfactory passive isolation solutions. Hence metamaterials may provide a useful path to high performance, low frequency isolation. Passively these band gaps occur over a narrow bandwidth, however the inclusion of active elements provide a method for enhancing this behaviour and producing attenuation over a broad band. Two active metamaterials are investigated in this thesis, first a novel viscoelastic metamaterial is developed that achieves double negativity and could be employed as a high performance vibration isolator at low frequencies. A prototype is produced, the band gap confirmed in the laboratory, and active control is applied to create a wideband region of attenuation. Next an acoustic metamaterial consisting of an array of Helmholtz resonators is presented and it is shown that such a metamaterial has a resonant band gap and dispersive density and bulk modulus. The acoustic metamaterial is produced using 3D printing techniques and the predicted behaviour confirmed in the laboratory. Finally an active Helmholtz resonator is introduced as a pathway to creating an active acoustic metamaterial and the potential for band gap and material parameter manipulation is investigated before a prototype resonator is produced and feedback controllers applied, enhancing the band gap attenuation.

Contents

List of Figures

List of Tables

Declaration Of Authorship

I, MATTHEW REYNOLDS, declare that this thesis entitled ’Active Control of Viscoelastic Metamaterials’ and the work presented in it are my own and has been generated by me as the result of my own original research. I confirm that:

- This work was done wholly or mainly while in candidature for a research degree at this University;
- Where any part of this thesis has previously been submitted for a degree or any other qualification at this University or any other institution, this has been clearly stated;
- Where I have consulted the published work of others, this is always clearly attributed;
- Where I have quoted from the work of others, the source is always given. With the exception of such quotations, this thesis is entirely my own work;
- I have acknowledged all main sources of help
- Where the thesis is based on work done by myself jointly with others, I have made clear exactly what was done by others and what I have contributed myself;
- Parts of this work have been published as:

  Journal Papers

  - M. Reynolds and S.Daley. An active viscoelastic metamaterial for isolation applications. *Smart Materials and Structures*, 23, 2014
  - M. Reynolds and S.Daley. Enhancing the band gap of an active metamaterial. *Journal of Vibration and Control*, (Submitted)

  Conference Papers

  - M. Reynolds, S.Daley, Y. Gao, V. Humphrey and S. A. Pope. *Controller architectures for optimum performance in practical active acoustic metamaterials*. Proceedings of Acoustic 2012: 11th Congres Français d’Acoustique and 2012 IOA annual meeting. Nantes, France, 2012.

- S. A. Pope, H. Laalej, S. Daley, M. Reynolds. *Active elastic metamaterials with applications in vibration and acoustics*. Proceedings of Internoise 2012. New York, USA, 2012.
- M. Reynolds, Y.Gao, S. Daley. *Experimental validation of the band-gap and dispersive bulk modulus behaviour of locally resonant acoustic metamaterials*. Proceedings of the 21st International Congress on Acoustics. Montreal, Canada, 2013. ***Winner of the Best Student Paper Award, Structural Acoustics and Vibration Category***
- M. Reynolds, Y.Gao, S. Daley. *An active viscoelastic metamaterial with enhanced band gap properties*. Proceedings of the 20th International Congress on Sound & Vibration. Bangkok, Thailand, 2013, ***Winner of the Sir James Lighthill Award for Best Student Paper***
- M. Reynolds, S. Daley. *Performance and stability constraints of an active acoustic metamaterial*. Proceedings of the 21st International Congress on Sound & Vibration. Beijing, China, 2014

Patents

- The active metamaterial design presented in Chapter 3 is the subject of a patent (pending), application number GB1304500.0, submitted and owned by BAE Systems. The author is listed as a named inventor

Signed: . . . .   Date: . . . .

Acknowledgements

Professor Steve Daley has contributed hugely to the work contained in this thesis. As well as administering the project he has helped guide the research, shared the wisdom of his experience and provided invaluable knowledge. His enthusiasm and encouragement ensured that I not only made it to the end but enjoyed my work over the last 3 years. I thank him unreservedly.

No project this large can be completed without the help of many people along the way and I would like to offer my sincere thanks (in no particular order) to

- Gao Yan, whose work on metamaterials in parallel with mine provided insight and useful discussion.
- The Engineering and Physical Sciences Research Council (EPSRC) and BAE Systems, the generous funding of whom made this research possible. Specifically Dave Hankey and Phil Atkinson at BAE Systems for providing an impetus for the project through their enthusiasm and vision for the subject matter.
- The EPSRC National Centre for Innovative Manufacturing in Additive Manufacturing, Nottingham University, in particular Dr Chris Tuck and Prof. Richard Hague for their assistance and patience in producing the metamaterial prototypes, and the Defence Science and Technology Laboratory (DSTL) MAST program for providing funding to make this collaboration happen.
- The technicians in the ISVR for their valuable advice and hard work to provide equipment and rigs; notably Phil Oxborrow and Antony Wood.
- Kevin Smith and Peter Sellen of the Faculty's Engineering Design and Manufacturing Centre for their help producing the steel metamaterial prototype to such a high standard
- My friends and colleagues in the Signal Processing and Control Group, with a particular mention for Jordan Cheer for the many helpful discussions shared over a cup of tea or a pint, and Alice Halpin for the tea and biscuits

I would particularly like to thank my parents, John and Sandra, for their unending love, encouragement and support (both moral and financial!) over the years and without whom I would never have made it this far. And finally, I reserve special gratitude for my partner Aimi Hill for putting up with the stress, complaining and long days in the office; thank you for being there and for making my second stay in Southampton so enjoyable.

List of Abbreviations

ALM	Additive layer manufacturing
ATLM	Acoustic transmission line method
CNO	Constrained non-linear optimisation
DNG	Double negative
DOF	Degrees of freedom
EM	Electromagnetic
FCC	Face centred cubic
FDTD	Finite difference time domain
FEM	Finite element method
FIR	Finite impulse response
FWHM	Full-width half-maximum
FxLMS	Filtered-x Least Mean Squares
HCP	Hexagonal closed packed
ISVR	Institute of Sound and Vibration Research
LISA	Local interaction simulation approach
LS	Laser sintering
MEMS	Micro electromechanical systems
MIMO	Multi-input, multi-output
MST	Multiple scattering theory
NFFT	Length of the vector used in a discrete Fourier transform

PWE	Plane wave expansion
SHS	Split hollow sphere
SISO	Single-input, single-output
SNG	Single negative
SPL	Sound pressure level
SRR	Split ring resonator
TM	Transfer matrix
VAMD	Volume averaged mass density
VM	Variational method

List of Symbols

B	Bulk modulus of elasticity, Pa
B_0	Ambient bulk modulus of air, Pa
B_e	Effective bulk modulus of the metamaterial, Pa
B_u	Multiplicative uncertainty of a nominal plant response within the robust stabilty constraints
C_e	Effective dynamic damping of the metamaterial
C_h	The compliance of the Helmholtz resonator cavity, m/N
K_e	Effective dynamic stiffness of the metamaterial
L'_{neck}	Helmholtz resonator effective neck length, m
L_h	Inertance of the Helmholtz resonator neck, kg/m^4
L_{neck}	Helmholtz resonator physical neck length, m
M_e	Effective dynamic mass of the metamaterial
P_R	Reflected acoustic pressure, Pa
P_T	Transmitted acoustic pressure, Pa
R_h	Resistance representing the viscoelastic losses within the Helmholtz resonator
R_r	Radiation resistance of a Helmholtz resonator, Ns/m
R_v	Thermoviscous resistance within a Helmholtz resonator, Ns/m
S_d	Cross sectional area of a duct, m^2
S_n	Helmholtz resonator neck area, m^2
T	Transmission Coefficient/Transfer function
V_H	Helmholtz resonator cavity volume, m^3
Z_h	Acoustic impedance of a Helmholtz resonator, rayls/m^2
Z_n	Acoustic impedance of a discrete layer of the transfer matrix model, rayls/m^2

Γ	Cost function minimised by the CNO optimisation routine
$\boldsymbol{G}$	Matrix of the dynamics of the control plant
$\boldsymbol{H}$	Matrix of controller dynamics
$\boldsymbol{P}$	Vector of the primary plant dynamics in a multichannel system
$\boldsymbol{Q}$	Weighting matrix used to tune the transmissibility element of the cost function of the MIMO CNO optimisation routine
$\boldsymbol{R}$	Regularisation matrix used to tune the cost function of the MIMO CNO optimisation routine
$\boldsymbol{c}(\boldsymbol{w})$	Non linear constraint function used within the CNO optimisation routine
$\boldsymbol{e}$	Vector of error signals
$\boldsymbol{u}$	Vector of control signals
$\boldsymbol{w}$	Vector of coefficients of the control filter
ϵ	Electromagnetic permittivity, F/m
$\mathbf{C}$	Damping matrix of the viscoelastic metamaterial
$\mathbf{F_c}$	Matrix of the active damping coefficients used in the local control and distributed control viscoelastic metamaterial
$\mathbf{F_k}$	Matrix of the active stiffness coefficients used in the local control and distributed control viscoelastic metamaterial
$\mathbf{K}$	Stiffness matrix of the viscoelastic metamaterial
$\mathbf{M}$	Mass matrix of the viscoelastic metamaterial
$\mathbf{T}$	Transfer matrix used in a 2-port network model
$\mathbf{f}$	Vector of disturbance forces incident on the viscoelastic metamaterial
$\mathbf{q}$	Vector of displacements of the mass elements of the viscoelastic metamaterial
μ	Electromagnetic permeabilty, H/m
ω	Angular frequency, rad/s

ω_0	Natural frequency, rad/s
ω_n	Natural frequency of the nth resonator, rads/s
$\omega_{0,r}$	Onset frequency of the band gap of the coupled viscoelastic metamaterial, rads/s
ω_{UL}	Upper frequency limit of the coupled viscoelastic metamaterial, rads/s
ω_{end}	Upper frequency limit of the band gap of the coupled viscoelastic metamaterial, rads/s
ω_{mid}	Frequency of peak attenuation of the band gap of the coupled viscoelastic metamaterial, rads/s
ρ	Material density, kg/m^3
ρ_0	Ambient density of air, kg/m^3
ρ_e	Effective density of the metamaterial, kg/m^3
c_0	Ambient sound speed in air, m/s
c_c	Damping constant for the active feedback force acting on the resonator elements, Ns/m
c_r	Damping element between the transmission medium and the resonator elements of the viscoelastic metamaterial, Ns/m
c_t	Damping element within the transmission medium of the viscoelastic metamaterial, Ns/m
c_h	Viscoelastic damping in the mechanical model of the Helmholtz resonator, Ns/m
c_{met}	Sound speed within the metamaterial, m/s
d_n	Lattice constant of a periodic material, m
f_n	A disturbance force applied to the nth transmission mass, N
f_c	The active control force applied to the resonator mass of the viscoelastic metamaterial, N
k	Wavenumber, m^{-1}
k_c	Stiffness constant for the active feedback force acting on the resonator elements, N/m

k_r	Stiffness element between the transmission medium and the resonator elements of the viscoelastic metamaterial, N/m
k_t	Stiffness element within the transmission medium of the viscoelastic metamaterial, N/m
k_h	Stiffness associated with the cavity of a Helmholtz resonator, N/m
m_r	Mass of the resonator elements within the viscoelastic metamaterial, kg
m_t	Mass of the transmission elements within the viscoelastic metamaterial, kg
m_h	Mass associated with the neck of a Helmholtz resonator, kg
n	Denotes the nth layer of a multiple layer metamaterial
n_r	Refractive index
p	Acoustic pressure, Pa
p_n	Acoustic pressure at the nth layer, Pa
$q_{t,n}$	Displacement of the nth transmission mass of the viscoelastic metamaterial, m
r_d	Radius of impedance tube/duct, m
r_{neck}	Radius of Helmholtz resonator neck, m
u_n	Acoustic volume velocity in the nth layer, m^3/s
z	Acoustic impedance, rayls/m^2
z_0	Characteristic acoustic impedance, rayls
z_d	Acoustic impedance of a duct, rayls/m^2
G_{ls}	Actuator dynamics within the active Helmholtz resonator, m^{3}s^{-1}V^{-1})
G	Dynamics of the control plant
H	Controller dynamics
P	Dynamics of the primary plant
Q_{ls}	Q-factor of the actuator in the active Helmholtz resonator

ω_a	Natural frequency of the actuator in the active Helmholtz resonator rad/s
$\widehat{G}$	An estimate of the dynamics of the control plant
ξ_a	Damping ratio of the actuator in the active Helmholtz resonator
d	Disturbance signal
e	Error signal
g_a	Gain constant of the actuator in the active Helmholtz resonator
u	Control signal
x	Reference signal for the FxLMS feed-forward algorithm
y	The ’local’ noise signal in the geometric control design method

Chapter 1

Introduction

1.1 Electromagnetic metamaterials

Metamaterials for elastic waves have attracted considerable research interest in the past decade due to the numerous novel potential applications for the technology, however the idea originally spawned from the area of electromagnetic metamaterials. The concept of a material with electrodynamic properties similar to that of modern electromagnetic metamaterials first arose through the work of Veselago in 1968 [17]. Although the physical structure of the material was not described at the time, it was supposed that were it possible to create a material that exhibits negative permeability, μ, and negative permittivity, ϵ, then novel behaviour would arise not seen in natural materials. The refractive index (n_r) of a medium is defined as the ratio of the wave speed in a medium over its speed in a vacuum, and can be related to the relative permeability and permittivity such that $n_r = \sqrt{\epsilon\mu}$. These 'left-handed' materials, as they would come to be known, would exhibit a negative group velocity, and as such the phase vector would travel in the opposite direction to the wave vector. Applying this property to known wave phenomena leads to the conclusion that a wave travelling through such a medium would retain many common behaviours, but reversed. A commonly cited example of this is negative refraction; here Snell's law still applies, however the refracted wave lies to the opposite side of the incident normal to that would occur in regular, 'right-handed' media. Negative Doppler shift would also occur. Veselago noted that although negative permittivity occurred in certain natural materials, materials did not exist which exhibited negative permeability, and therefore at the time such a material was not realisable.

A viable route to achieving left-handed behaviour was first proposed by Pendry *et al.*, where it was shown that structures such as split ring resonators (SRR) and so called 'swiss roll' elements could produce tunable values of magnetic permeability [18]. This followed previous work that had demonstrated a periodic lattice of wires produced a material which could achieve negative permittivity [19]. Building on Pendry's work, Smith later demonstrated [20, 21] that it was possible to tune a lattice of wires such that the frequency region of negative permittivity overlapped with a region of negative

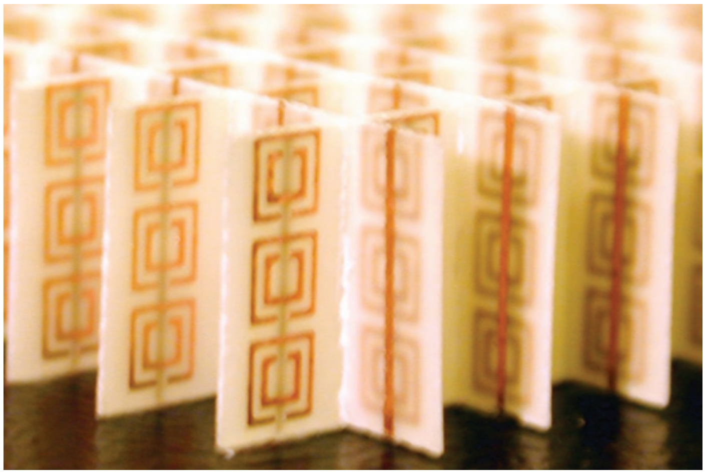

Figure 1.1: An electromagnetic metamaterial formed by split ring resonators and wires assembled on standard printed circuit board, produced by Shelby *et al* [1]

permeability, tuned using the resonant frequency of co-located SRR elements. Experimental results showed that whilst the two components created their single negative (SNG) behaviours independently, the net effect was DNG behaviour within the material. Later experiments [1] verified that negative refraction occurs in these materials, validating Veselago's original hypothesis. Following the experimental validation of these materials Smith *et al.* published an informative review of the prior work, providing a qualitative description of the mechanisms involved in electromagnetic left-handed metamaterials [22]. A photo of a SRR based metamaterial is shown in Figure 1.1

A periodic arrangement of dielectric material such as the wire lattice described above is often referred to as a photonic crystal, which have long been studied due to their being employed to control the propagation of electromagnetic waves [23, Pg. 2-3]. Photonic crystals exhibit a phenomenon known as photonic band gaps, where wave propagation is forbidden in a certain frequency range related to the periodicity of the crystal lattice. The structure of the material leads to a periodically changing dialectric constant, and therefore a periodic index of refraction. At each interface within the crystal the electromagnetic wave is partially reflected, so at certain frequencies, related to the spacing of the crystal elements, these multiple reflections create destructive interference and eliminate the travelling wave. This is a well known phenomenon and was first explained by Lord Rayleigh in 1897 [24], and is often referred to as Bragg scattering since Bragg's Law describes the angle required for incoherent and coherent scattering that will occur for a wave incident on a crystal structure. It was Pendry *et al*'s groundbreaking work that paired these photonic crystal structures with resonator elements to achieve double negativity and hence realise left-handed materials.

1.2 Phononic Crystals

More recently, applying the wave analogy between elastic and electromagnetic waves, the same principle has been applied to viscoelastic media, and the area of viscoelastic metamaterials has created considerable research interest over the last 15 years. Here the mechanical equivalent of permeability is material density, ρ, and the analogue of permittivity is the modulus of elasticity, B. It follows that the refraction of a pressure wave in a homogenous medium is related to the sound speed, which can be expressed as $c = \sqrt{B/\rho}$. Like their electromagnetic counterparts, much of the early work on viscoelastic metamaterials was built upon the idea of periodic materials, called phononic crystals.

Phononic crystals are just periodic arrangements of a material, such as epoxy spheres arranged in a cube, or metal rods arranged in a periodic fashion. Phononic crystals have been studied in the literature for their potential use in waveguide and noise isolation applications, and as a result a variety of analytical tools have been developed for dealing with periodic media, including the variational method (VM) [25], plane wave expansion (PWE) [26], finite difference time domain (FDTD) [25, 27], local interaction simulation approach (LISA) [28] and the lumped mass approach [29].

Phononic crystals have been shown to be effective acoustic isolators, where at certain frequencies wave propagation is forbidden. These regions of high levels of attenuation are called 'band gaps', and are due to scattering caused by the periodic inclusions and the resulting Bragg scattering. An demonstration of a wave attenuation due to the Bragg gap in a phononic crystal is shown in Figure 1.2 [2].

In the work of Goffaux *et al* [26] a novel application for a 2 dimensional phononic crystal was examined using the FDTD method, where a 2-dimensional array of steel rods in air is examined. In the frequency range where Bragg scattering occurs the material is shown to be a very effective acoustic insulator, with the experimental results achieving attenuation of up to 30dB. The paper analyses the performance/cost ratio of the phononic crystal in this application by comparing the results to traditional building materials and the attenuation they achieve due to the mass law. The results show that at lower

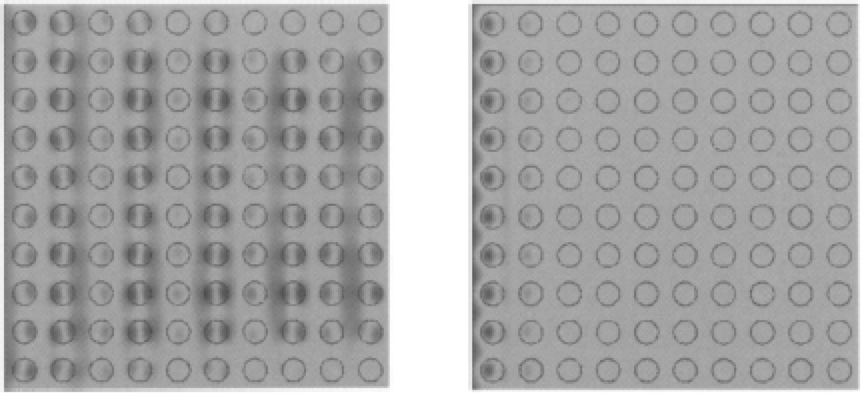

Figure 1.2: Within a phononic crystal frequencies outside the band gap propagate freely (left) but at the Bragg band gap wave attenuation is high (right), [2]

thicknesses (in this case below 9 periods) the crystal is outperformed by traditional materials, but above this the crystal is a much more effective insulator, whilst also providing a potential solution where air flow is required across an acoustic insulator, in a duct for example. This is an important observation and perhaps one that some of the earlier literature neglects; that phononic crystals (and, as will be shown later, metamaterials) have many potentially powerful real world applications, but it is important to ascertain in what situations they offer a significant performance advantage over more traditional methods.

A key paper in the development of viscoelastic metamaterials is that of Liu *et al* [30], who, whilst studying phononic crystals, derived a mathematical method based on well established multiple scattering theory (MST), creating a convenient tool for calculating the response of phononic crystals to elastic waves. Band structures were calculated for gold spheres arranged in a face centred cubic (FCC) structure in a silicon transmission strata, demonstrating regions of the frequency domain where there is no valid wave number solution, k, and wave propagation is forbidden. Further simulations were carried out on an hexagonal closed packed (HCP) arrangement of steel beads immersed in water when subjected to ultrasonic waves. The resulting measured wave field showed good agreement with the predicted results at low frequencies, validating the mathematical process used in this frequency region. At higher frequencies the results are not as accurate, and it was assumed that this is due to imperfections in the crystal being more significant at shorter wavelengths. Within this study Liu *et al* noted the appearance of a second band gap, located at lower frequencies, at a wavelength too large to be attributed to the crystal structure. It was presumed that this is due to the steel spheres resonating; they were therefore acting like the SRR or swiss roll elements that provided resonant behaviour in Pendry *et al* and Smith *et al*'s electromagnetic (EM) metamaterials. This additional resonant effect is studied in more detail by Liu *et al* [3] in a paper of huge significance to in the development of viscoelastic metamaterials, and discussed in Section 1.3.

King and Cox [31] created a periodic waveguide using aluminium insertions within a duct, and predicting the response of the setup using the transfer matrix transfer matrix (TM) method similar to that described by Pestel and Leckie [32, Pg. 51-54]. The results are shown to agree well with the measurements, however an interesting side effect of the acoustic set up is that due to the change in radiation impedance created by the change in cross sectional area at each, junction additional band gaps occur between the expected Bragg gaps. This is caused by the radiation impedance changes causing waves to reflect back up the wave guide, and when in phase with the incident wave setting up standing waves that do not propagate; the TM method has to be modified to accurately predict this. This phenomenon does not occur with electromagnetic waveguides and is an important reminder that the acoustic domain is not a direct analogue of the electromagnetic case.

Since phononic crystals rely on Bragg scattering the band gaps and wave guide effects that they produce are by their very nature high in frequency, or require very large physical dimensions. In addition traditional phononic crystals are, alone, not enough to provide DNG behaviour, and are not metamaterials using the classic Pendry/Smith definition. To extend the behaviour of phononic crystals to achieve DNG material parameters and to be classed as metamaterials resonant elements must be incorporated into the structure.

1.3 Locally Resonant Phononic Crystals

Whilst phononic crystals provide a periodic structure with a wave scattering behaviour similar to EM metamaterials, they are unable to provide negative effective material parameters and lack the resonant elements associated with EM metamaterials. Therefore, to extend the performance of the phononic crystals and introduce negative effective material parameters resonant elements must be introduced into the crystal inclusions. A common way of achieving this is to surround the inclusions in a resilient layer so the inclusions act not only as scatterers for elastic travelling waves but also are able to

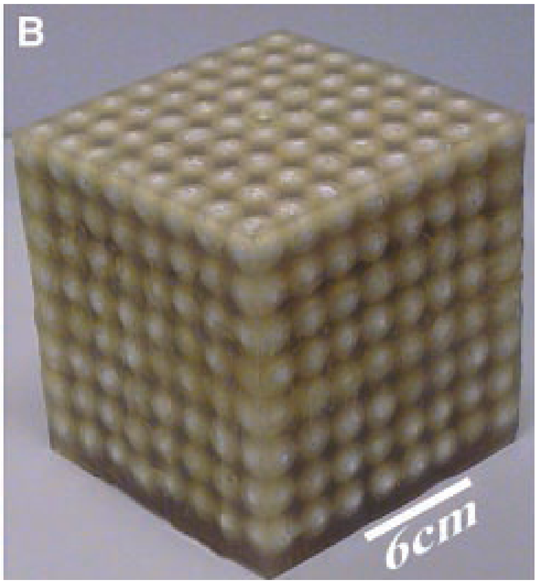

Figure 1.3: A viscoelastic metamaterial formed by rubber coated lead spheres suspended in resin, one of the first viscoelastic metamaterial structures, Liu *et al* [3]

resonate on their compliant surrounding. This approach was first proposed in a ground breaking paper by Liu *et al*. [3] building on their previous work [30]. In this later paper Liu *et al* created a material consisting of lead spheres in epoxy resin, but this time coated the spheres in rubber; a resilient layer that allows the spheres to resonate within the resin structure. The work presents both theoretical calculations and experimental results of the band structure of the material, and demonstrates how these new resonant materials exhibit a band gap at frequencies much lower than those that occur due to Bragg scattering, in this example at wavelengths that are 300 times greater than the lattice constant of the crystal. A photo of Liu *et al*'s viscoelastic metamaterial is shown in figure 1.3.

Liu *et al* noticed two additional gaps that appear in the band structure of the resonant material, and by plotting the displacements of the resonant elements it is shown that one dip is associated with the resonance of the lead sphere on the stiffness of the rubber, whilst the second dip is associated with the rubber itself and the sphere is stationary. Liu *et al* noted that these resonances are localised and therefore occurs even in a single layer with a random arrangement of resonant elements. The attenuation is much larger than one would expect through the mass law alone. This supports the idea that the attenuation is due to the resonant elements alone and not the periodicity or the mass density of the material. The fact that at the wavelengths in question the material is effectively homogenous also supports Liu *et al*'s conclusions. The effective bulk modulus of the material as a function of frequency is calculated, and since the region of low frequency transmission blocking coincides with the region where the effective bulk modulus is shown to be negative, it is concluded that the transmission blocking effect is related to this, analogous to the reflection of electromagnetic waves by a material with a negative dielectric constant. The work of Liu *et al* raised two important points - It is possible to create an viscoelastic material that had the same periodic and resonant structure as EM metamaterials, and that if the viscoelastic metamaterials are to be used for their transmission blocking characteristics the resonances provide a more realistic method to achieve this than the Bragg gaps, where at audible frequencies the wavelengths, and therefore lattice constants required, are far too large to be viable.

The two resonant mechanism described by Liu *et al* were the dipole and monopole resonance respectively, and provide the mechanism for achieving negative material parameters within the metamaterial [33]. Chan *et al* [34] provide a physical analysis of the concept of negative parameters in viscoelastic metamaterials. During a monopolar resonance the volume dilation of the resonant inclusion is out of phase with the pressure field of the surrounding transmission media. The physical upshot of this is the resonant element expands as it is squeezed by the surrounding media, the opposite to what would be expected from Hooke's law, hence the effective stiffness is negative. During bipolar resonance the mass of the inclusion is oscillating out of phase with respect to the transmission medium. Since the resonances occur at long wavelengths the material is considered homogeneous and, if the momentum of the resonating inclusions is larger than that of the surrounding medium, the net momentum of the material as a whole will be negative, and hence the effective mass of the material must be negative. The physical upshot of this behaviour is that when the material is excited by vibration in this frequency region, the centre of the mass of the material moves to the left when it is being pushed to the right, opposite to what would be expected by Newton's second law of motion. It is important to distinguish this double negative behaviour, and its associated negative refraction from the negative refraction that occurs within a phononic crystal, which is due to band folding caused by Bragg scattering leading to negative group velocity.

Criticisms of the idea of negative material parameters exist within the literature. Sun *et al* [35] describe a system consisting of mass-spring units arranged in a one dimensional lattice, where each mass unit contains an internal 'hidden' resonator mass and spring, to illustrate the theory behind negative effective mass. The authors use the model to highlight the fact that negative effective mass is a consequence of attempting to model a two mass system using one mass element. According to Newton's second law of motion the movement of the mass would be in the opposite direction to the applied force, and Sun *et al* consider this to be an inefficient description of the general motion/deformation of the material as a continuous, homogeneous medium. Despite this, it is generally understood within most metamaterial literature that negative effective material parameters are a dynamic effect, and constitute the density/stiffness of the material *as experienced by the travelling wave*, and not a literal description of the physical elements. It is an effective and useful description within the long wavelength limit.

From the analysis above it is clear that, unlike EM metamaterials, which require two different resonant structures within the material to achieve the two negative parameters, in acoustic metamaterials both B and ρ can become negative using a single type of resonant element. It is the structure of this single resonant inclusion that will determine whether the material is capable of achieving SNG or DNG behaviour. Mei *et al* [36] provide a rigorously derived mathematical proof backed up with experimental data that the effective mass density of an inhomogenous material can differ from its static equivalent when considered in the long wavelength limit. In a traditional composite material the effective density of the medium is calculated using an intuitive volume averaged mass density (VAMD). Berryman [37] had developed a more rigorous approach demonstrating that the dynamic density of a composite may differ from its static, volume averaged, value. Mie *et al* demonstrate that the VAMD expression for density is a special case of the Berryman equations, and is only valid when the difference between the mass densities of the components is small.

The work of Liu *et al* lead to a great deal of interest in periodic, resonant viscoelastic materials, now referred to as viscoelastic or acoustic metamaterials. Goffaux and Sanchez-Dehesa [25] applied extended the application of the VM, previously used on phononic crystals, to metamaterials consisting of rubber coated gold spheres in epoxy,similar to Liu *et al*. Using a lumped parameter representation of the resonant material, it is demonstrated how the onset of the resonant behaviour is related to the material parameters of the resonant elements and independent of the lattice material. An interesting aside to come from this work was the observation that there is weak interaction between the resonant states, and by closing the filling fraction this interaction can cause the onset edge of the resonant behaviour to change. This goes against the original observation of Liu *et al*, that the resonant states act independently of each other and can therefore be arranged randomly and will still produce attenuation in a single layer material. Whilst this is practically true in most cases, there is some weak interaction, and this can be exploited, such as in the work on acoustics metamaterials carried out by Cheng *et al* [38], discussed later in Section 1.6.1. Alternative metamaterial structures have since been proposed and investigated. For instance Li and Chan showed how rubber spheres submerged in water [33] could produced a double negative resonant material, and Ding *et al* simulated water spheres containing bubbles to create a dipole resonance and rubber coated gold spheres to create a monopole resonance in an epoxy matrix, tuning the parameters to overlap these two resonances and achieve DNG behaviour [27]. Huang and Sun [39] demonstrated that by including multiple resonators acting on one cell, multiple band gaps can occur at different frequencies, and that these band gaps each create a region of negative effective mass.

Farzbod and Leamy [40] have applied Bloch's method (a common analytical method for studying wave propagation in crystal structures) to lumped parameter models; later Farzbod extended this analysis to include energy dissipation in the model [41]. Here it was shown that Bloch's method can be used to calculate the band structure of metamaterials, but since the maximum displacement can occur within the interior of a Brillouin zone, following the standard Bloch method and limiting the analysis to the boundaries of a single irreducible Brillouin zone can lead to inaccuracies in the prediction of the magnitude of the band gap.

1.4 Resonant Band Gap Profile

Whilst resonant metamaterials provide a mechanism for producing band gaps and negative behaviour at low frequencies is clear the viability of this approach is dependent on the profile of the band gap in frequency; specifically, the width of the frequency region and the magnitude of these effects. Goffaux *et al*. [42] noted the similarities between the characteristics of low frequency band gaps in viscoelastic metamaterials with similar band gaps seen in solid state physics materials, which arise due to what is known as Fano interference. Therefore, like these atomic systems, the location of band gaps can be calculated by studying the band structure of the metamaterials. However the theoretical band structure does not accurately represent the shape of the band gap that will occur in a real material, and is it noted that the low frequency band gaps in viscoelastic metamaterials exhibit a similar asymmetric profile seen in certain scenarios in semi conductor physics. The low frequency band gap is typically characterised as having a very sharp dip in transmissibility at resonance, which quickly recovers in an asymmetric nature such that for much of the band gap region, the magnitude of attenuation is relatively low. The discrepancy between the complete band gap in the calculated band structure and the asymmetric band gap seen in real materials is due to the calculations being based on an infinitely long theoretical material. The differences between finite and infinite structures create a slight mismatch in edge frequencies between the band gap predicted by the band structure and the dip in the transmission of the finite, modelled system. From Goffaux *et al*'s observations about the creation of these band gaps, it can be concluded that the gap will become more symmetrical as the order of the crystal tends to infinity and the gap approaches infinite attenuation; the gap is not completely formed in finite systems.

Wang *et al* [43] reduced the model to a 1-dimensional chain of lead-rubber-resin elements to further study the displacement behaviour of each layer during resonant behaviour, and showed that at each eigenmode of the system displacement only occurred inside certain layers of the material, showing that the band gap at each eigenmode was associated with the resonance of that element. This work was extended to a 2 dimensional model in a subsequent paper [44], where it was found that the fundamental mode of the resonators is identified as the beginning edge of the band gap. At this frequency the vibration is concentrated in the region of the resonant elements with little movement in the transmission media. Over the width of the band gap the vibration of the media increases until it is approximately equal to the resonators, but out of phase; this frequency denotes the upper limit of the band gap. Wang *et al* describe the mechanism that leads to the creation of the band gap as the forces from the oscillators as they move out of phase with the transmission medium causing a 'split (of) the original dispersion curve', although this hints towards the description given by Huang *et al*, exactly what this means in terms of a physical process is not clear. By examining the behaviour of the band gap onset frequency as a function of the filling fraction of the crystal it is demonstrated that the lower edge remains constant, and as such the band gap will occur regardless of periodicity, as predicted previously by Liu *et al* [3].

This phenomenon of resonant and Bragg band gap profiles, shown in Figure 1.4, was

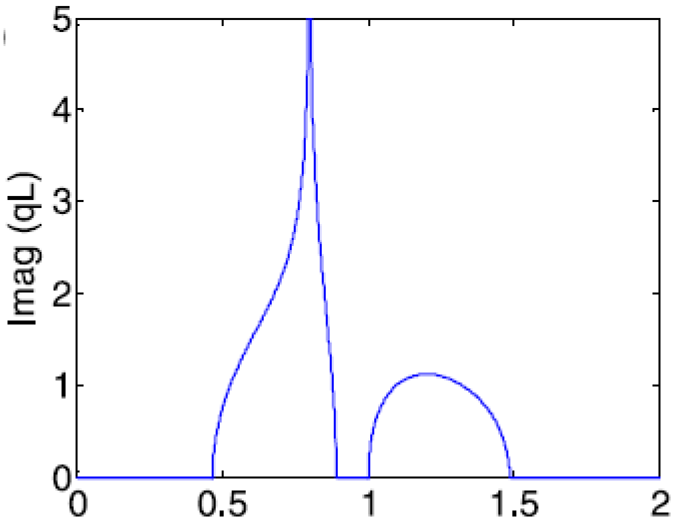

Figure 1.4: Xiao *et al* [4] examined the band structures of the asymmetric resonant band gap (located to the left) and the symmetric Bragg gap (located to the right)

investigated further by Xiao *et al* [4] using a model of a simple, 1 dimensional, metamaterial consisting of an infinite string with a periodic array of mass-spring resonators attached. The focus of the work was to investigate the physical processes behind the formation of the resonant and Bragg band gaps. Building on earlier work carried out by Mead on periodic structures [45], Xiao *et al* demonstrate that the low frequency band gap behaviour is associated with the resonant modes of the resonant element, and more specifically, the fundamental frequencies of a single cell of the periodic material when subject to fixed-fixed or free-free boundary conditions. By examining the mode shapes of these fundamental cells it is shown that the Bragg gap edge frequencies occur where an integer number of half wavelengths occur between the linearly spaced resonant elements, such that the mode shapes are asymmetric and the displacement of the string at the resonant element is zero; the behaviour is not dependent on the resonator material constants. Alternatively, the resonant band gap lower and upper edge frequencies are given by the fundamental modes of the fixed-fixed and free-free unit cells respectively. Here the mode shapes are symmetric and the modal frequencies are dependent purely on the resonator parameters, and not on the periodic constant, therefore the resonant behaviour is present regardless of periodicity. An interesting conclusion to come out of the paper was the phenomenon where the Bragg and resonant band gaps are tuned to coincide, and it was found that the coupling between the two gaps results in a super-wide, symmetrical band gap profile. A similar conclusion relating the resonant band gap edge frequencies to the properties of the resonant elements material properties was found by Diaz *et al* [46] as part of a theory developed to assist the design of periodic resonant structures.

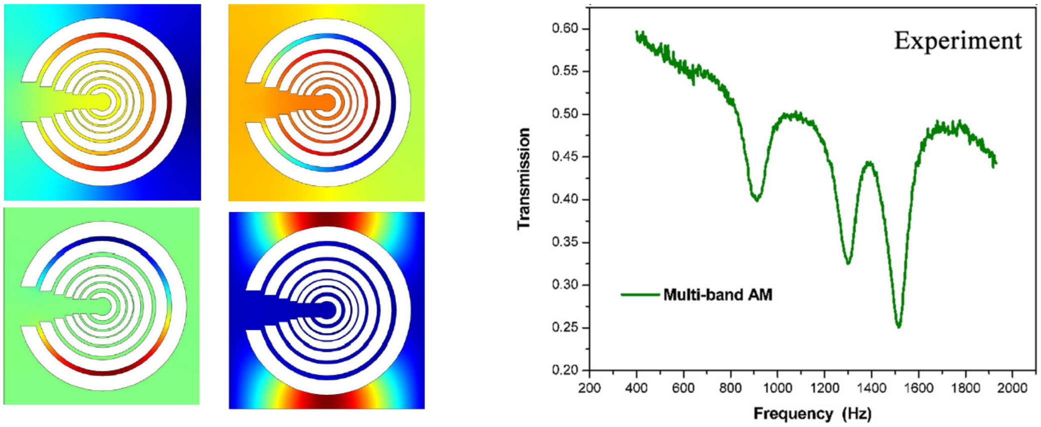

(a) **(b)**

Figure 1.5: (a) Elford *et al* [5] demonstrate how the acoustic field is concentrated at different frequencies using multiple, nested split resonators. (b) Multiple band gaps created at different resonator frequencies by Ding *et al* [6] (© IOP Publishing. Reproduced with permission. All rights reserved)

There have been few attempts at creating a wider band gap by changing the natural frequencies of the resonant inclusions. Ding and Zhao [6] created a 3D material, tested in an impedance tube, consisting of a transmission medium containing split hollow sphere resonator elements, where the resonant frequency of the elements is related to the size of the hollow spheres. By making each layer of resonators a different size the band gap frequency for each layer changes, creating attenuation at successive frequencies, shown in Figure 1.5b. Since each frequency only has the relatively small number of resonators acting on it, the level of attenuation is reduced, but by overlapping the frequencies at which the resonances occur a wideband region of attenuation is achieved. It is also shown that at the resonant frequencies the effective modulus of the material approaches negativity. Although the small number of resonators is not enough in the example studied to overcome the static constants of the material and achieve negativity, presumably the addition of extra resonators would achieve this. A similar configuration was investigated by Elford *et al* [5], who, in this case, created a finite element model of a 2D crystal consisting of steel rods in air. Each scattering rod consists of several C-shaped resonators of different sizes, nested inside of each other like a Russian doll, shown in Figure 1.5a. The result is, again, that the different resonators each act at independent frequencies, leading to resonant band gaps occurring at each of these frequencies and, where they overlap, creating a broadband region of attenuation. Exploiting this staggering of resonances is also the subject of the work of Yang *et al* [47] where a latex wall panel is created using resonances to increase levels of transmission loss, and by Tan *et al* [48] to widen the region of negative effective mass.

Published work here is limited, and whilst the work described above has attempted to address this, these passive solutions have drawbacks To achieve a useful level of attenuation over a wide frequency range, or to achieve negative material parameters over a wide frequency range, requires a large number of resonators and whilst the region at which the resonant behaviour occurs is widened it remains static, so achieving truly broadband band gaps, or SNG/DNG behaviour remains difficult. It is this gap in the currently published material that is the motivation for much of the work carried out in this thesis on using active control to widen the band gap region.

As seen in Section 1.3, negative effective material parameters and the resonant band gap are both due to the dynamic response of the resonant elements within the metamaterial, and as such the resonant band gap is often described in terms of SNG behaviour using logic borrowed from solid state physics. From the refractive index equation $n_r = \sqrt{\rho/B}$ it is clear that in a SNG region the solution to this equation is purely complex. In electromagnetic literature a complex index of refraction, $\tilde{n}_r = n_r + i\beta$, consists of the refractive index, n_r, and an imaginary part, $i\beta$, where β is referred to as the extinction coefficient, which describes the loss within the medium experienced by the travelling wave. This can be related to the wave vector, k, by $k = \frac{2\pi n_r}{\lambda}$ (where λ denotes wavelength), so when a material is SNG the wave vector is purely imaginary. Inserting this result into the wave equation yields a result that consists only of an evanescent wave decaying with distance from the source, with no travelling wave component; hence the wave does not travel through the structure. For viscoelastic waves the experimental results of Lee *et al* support this view, where an acoustic metamaterial that exhibited negative density [49] and an acoustic metamaterial that exhibited negative bulk modulus [50] were created, and when the two structures were combined [51] the band gaps that previously existed in the respective SNG regions became transparent where these regions overlapped to create DNG behaviour.

Whilst the above description provides a mathematical explanation of the band gap phenomenon it does not give a satisfactory description of the physical processes that create the band gap regions. Huang and Sun to describe the process in terms of energy transfer and work done in their paper [52], where a mass in mass system capable of achieving negative effective mass is modelled. In a material with no losses energy carried by the wave cannot be dissipated and the conservation of energy denotes that when work is done on the metamaterial in the form of a excitation force, if the wave is attenuated spatially within the material (such as in the band gap region), the energy must be transferred and stored somewhere inside the system. It is shown that at resonance since the response of the effective material and the excitation force are out of phase, the work done by the external excitation force is totally transferred to and stored in the resonator elements, so energy does not transfer through the material. This energy is then taken out by the excitation force in subsequent cycles in the form of negative work, as it moves out of phase with the resonant masses. By studying the behaviour away from but close to resonance, still within the negative effective mass region, it is shown that the effect still occurs, however now energy transfer to the resonant elements is not complete and some energy leaks into the system, meaning some wave propagation takes place but is attenuated. Whilst it is not explicitly stated in the paper, it appears that a similar drop in effectiveness of the energy storage within the resonators would occur if other real world factors are introduced to the model, such as a limit to the displacement that the resonator element can experience, damping within the system, etc. Since the model studied is not sufficient to produce negative effective stiffness, this is also not mentioned within the work.

However these final two descriptions of band gap formation are not complete, suggesting that band gap formation is due simply to SNG behaviour, and in the absence of losses. Part of the work contained in Chapter 3 considers other mechanisms through which a resonant band gap can occur even in a double negative region, with or without dissipation present.

1.5 Acoustic Cloaking and Superlenses

1.5.1 Superlenses

As well as the potential of metamaterials within isolation applications, the tunable effective material parameters and the possibility of negative refraction lead to two novel concepts; the acoustic cloak and the acoustic superlens. Whilst these applications are not of direct consequence to the motivation of this project, they both could require broadband resonant effects, and are therefore potential beneficiaries of the work to be presented within this thesis.

Acoustic superlenses are able to use negative refraction to achieve sound focusing beyond the normal wavelength limit, termed 'sub-diffraction'. Zhang *et al* [53] investigated the idea of a practical acoustic lens. It was demonstrated experimentally and through simulation how a 2D network of channels with Helmholtz resonators can be used to achieve negative effective material parameters and hence negative refraction. The negative refractive index of the network is exploited to focus sound from a point source, although it was noted that the focal point achieved was not small enough to be classified as sub-diffraction imaging in this case. This is attributed to the set up not being able to provide the necessary growth of evanescent waves to achieve sub-diffraction, however it is as a possibility with an expanded experimental set up.

Negative refraction can also occur in non resonant phononic crystals, such as in the work of Yang *et al* [54]. Here 3 dimensional crystal is analysed using MST to provide a simulated response to a given sound source and comparing this to experimental results on an actual crystal. The set up was shown to focus a diverging ultrasonic beam to a small focal spot. By studying a ray traced diagram of the acoustic paths required to achieve focusing of the divergent sound source using a flat lens, it is clear that negative refraction must take place inside the crystal. Acoustic metamaterials of this kind are not curved and therefore do not have a central axis, unlike a traditional optical lens. This means that as the acoustic source is moved laterally, in parallel to the lens surface, the acoustic image moves with it by the same amount and is not distorted. The focal length of such a crystal is dependent on frequency, and to achieve identical focal lengths for different frequencies passively would require alternative crystal dimensions, potentially limiting the effective of using passive materials like these in focusing applications.

1.5.2 Acoustic Cloaking

Due to the ability of viscoelastic metamaterials to provide DNG behaviour and tunable material parameters they have been cited as a potential route to achieving the acoustic cloaking of objects. Much of the work on acoustic cloaking builds on the previous work of Pendry *et al* [55], who investigated the creation of electromagnetic cloaks using metamaterials. The basis of the metamaterial design is to transform the electromagnetic field around an object such that an electromagnetic wave incident on the cloaked object bends around the object and leaves the cloaked region unperturbed, as if the object was not there. This approach has been shown experimentally to be valid by Schurig *et al.* [56]. Similar transformation mathematics have more recently been applied to acoustic waves by Milton *et al* [57], with it being shown that it is possible to create a set of elastodynamic equations of a special case that have a form such that they are invariant when subject to curvilinear space transformations.

Schurig has since collaborated with Cummer [58] on extending the idea of cloaking to acoustic waves using the mathematical tools from Milton *et al* to produce a theoretical acoustic cloak that consists of an anisotropic cloaking material of varying mass density and bulk modulus that is the analogue of the electromagnetic cloaks that came before it. FDTD simulations were created, validating the effectiveness of the cloak. Achieving such a cloak experimentally would be challenging due to the extremes of material parameters required and the way the material parameters are required and also to vary through the material are not seen in naturally occurring media. Should a limited bandwidth solution be required, however, and by utilising metamaterials it is feasible that such a cloak could be produced experimentally. This Cummer-Schurig scheme of cloaking has been shown by Cai and Sanchez-Dehesa [59] to be independent of the shape of the wave front that is incident on the cloak, but performance is reduced when the object to be cloaked is non-rigid. Building on the transformation approach, Norris and Parnell [60] have devised a theory to prestress a material to perform the transformation of the acoustic field elastodynamically.

Further work by Liu *et al* [7] has lead to theoretical, imperfect cloaks where the continuously varying materials that would constitute a Cummer-Schurig cloak are approximated using discrete layers of isotropic material where the properties change layer to layer. These discrete layered cloaks have wave bending properties similar to perfect cloaks however still exhibit some wave reflection if the impedance of the outer

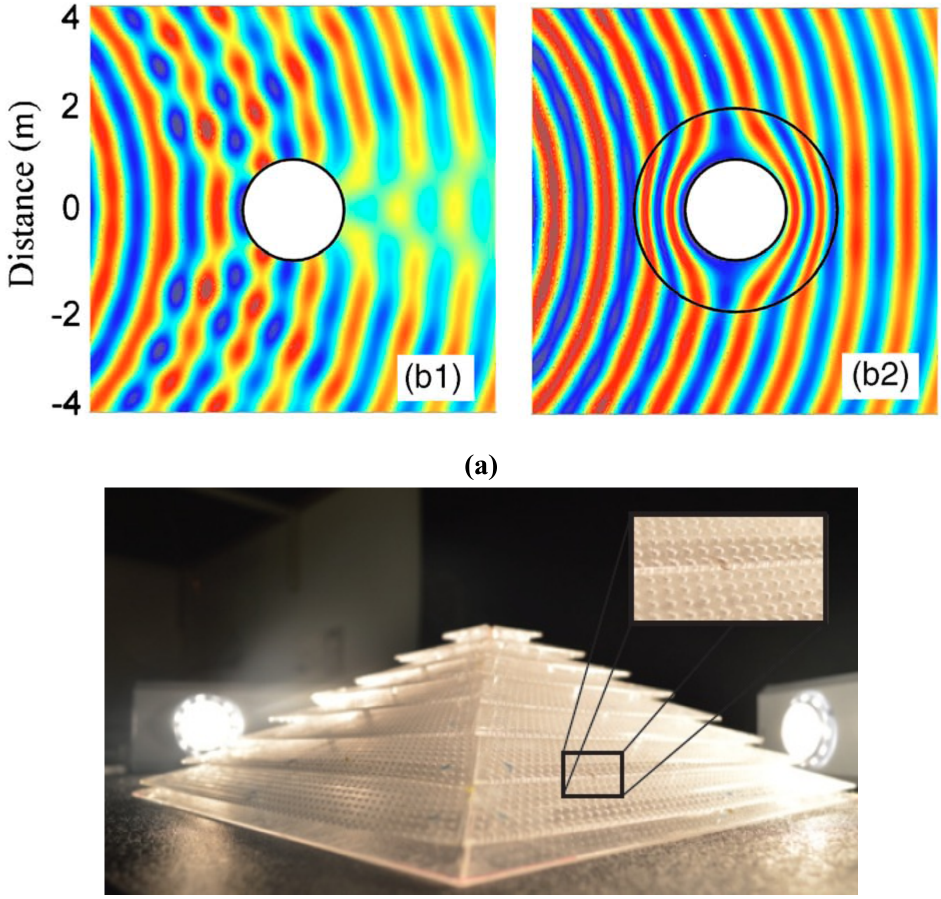

(a)

(b)

Figure 1.6: (a) Liu *et al*'s [7] demonstration of sound field scattering of an object without (left) and with (right) and acoustic cloak. (b) The acoustic ground cloak realised by Zigoneanu *et al* [8]

layer is not matched with the surrounding medium, and small levels of scattering will occur both around all sides of the cloaked object. These effects are shown in Figure 1.6a. Whilst this approximation brings the acoustic cloak one step closer to realisation, the material parameters required to achieve a cloak are still currently impractical, a limitation acknowledged by the authors. The work of Liu *et al* [61] proposes a variation where the device cloaks a scattering object external to it, rather than surrounded by the cloak, by a cancelling effect of the scattered waves from the object to be concealed and the scattered waves from the cloaking device. This presents a particularly useful result, as it would allow the cloaked object to still 'hear' the outside acoustic field.

Most recently Zigoneanu *et al* [8] realised a near perfect 3 dimensional omnidirectional cloak that work for objects placed on a solid surface; a ground cloak. This was shown to work experimentally, and is the most promising development in the area of acoustic cloaking. The authors consider that this achievement combined with the ability to manipulate the effective material parameters using metamaterial structures mean that the range of realisable cloaking devices should improve in the near future.

Whilst the works described above demonstrate the case for using viscoelastic metamaterials to achieve acoustic cloaking devices, realising many of these devices in the literature would require material parameters that are impractical, and even in the Cummer realisation then the cloak is dispersive, only working over a narrow frequency band. Outside of this band the object will not be cloaked, and the scattered acoustic field could potentially even be enhanced. This is an area where the active metamaterials presented in this thesis could be useful components in future developments.

1.6 1-Dimensional Vibration Metamaterials

The area of viscoelastic metamaterials grew out of research into phononic crystals and based on the advances being made in solid state physics, and 1 dimensional metamaterials have been investigated in this context as a means of creating simple examples that provide insight into the fundamental processes that occur in metamaterials, some of which have been highlighted in previous sections. However, they are also of particular interest due to their potential in situations where 1D propagation is the phenomenon that is of interest, such as in simple vibration structures that will be discussed here, or in the acoustic ducts that are discussed in the subsequent section (1.6.1). The majority of machinery used in modern industry for propulsion, pumping, movement etc. requires high speed rotating parts, and since those rotating parts can never be perfectly balanced the machinery will vibrate. Therefore vibration isolation is historically an area of considerable research interest and one in which the band gap behaviour of metamaterials could have an obvious impact. Since traditional vibration isolation methods have been studied for many years more than metamaterials, there are areas where the two research threads have overlapped with vibration isolator designs within the literature often being similar in structure to acoustic metamaterials, some examples of which are described here

Huang *et al* [62] created a periodic structure mechanical filter consisting of alternating, paired mass-stiffness elements connected to a flexible base plate that can radiate acoustic sound as a function of a vibration excitation at the top of the structure. The paper shows how by changing the resonant frequency of one set of the paired mass-stiffness elements the band gap due to this resonance can be moved in frequency, lowering the resonance at the expense of narrowing the band gap range. By reducing transmission through the material for a given frequency the resulting acoustic field at that frequency radiated from the base is reduced.

Milton and Willis [63] proposed a material that consisted of a rigid body with ’hidden’ resonant inclusions, and used this as a basis to modify Newton’s second law to develop a mathematical framework with which to describe the dynamic behaviour of these types of materials, the upshot of which is a framework for formulating the effective material parameters when designing such metamaterials. Yao *et al* [64] then took this further and created a 1 dimensional mass-spring system based on the theory Milton and Willis. The experimental system consisted of metal elements connected by metal springs and the response of the material measured using high speed digital cameras to examine the displacement of each element as a function of time. The results from this experiment demonstrate that the band gap occurs due to the resonant elements; as the material enters the region of negative effective mass the resonant elements move out of phase with the transmission medium. The idea of ’zero-mass’ was also investigated, where the momentum of the resonant inclusions is such that it exactly cancels out the momentum of the transmission medium and the effective mass is zero. At this frequency the set up oscillates as a perfectly rigid bar - all the elements are in phase with no spring deformation. Using the wave vector calculations of the Milton and Willis method, this is explained as the system effectively consisting of massless springs only, and the wave vector being zero. Hence, at this frequency the wave vector has an infinite wavelength, and all the units have equal displacement.

The work of Gao *et al* [65] focuses on vibration neutralisers on a beam, positioned so as to reduce the transmission efficiency of flexural waves along a beam. The beam-like resonant vibration neutralisers are fitted in a periodic array along a length of the beam creating, in effect, a 1-dimensional metamaterial although this term is never used by the authors. Various configurations of neutralisers is compared, and it is found that the effectiveness of the neutralisers can be increased by reducing the array spacing so the neutralisers are close enough to be subject to coupling effects due to near field waves. It is noted that the distance between the vibration neutralisers must be relatively small compared to the wavelength being considered otherwise this coupling effect will not occur. This result is analogous to the independent resonator phenomenon described by Liu *et al* [3] and small amount of coupling described by Goffaux *et al* [25] that was described in Section 1.3.

1.6.1 Ducted Acoustic Metamaterials

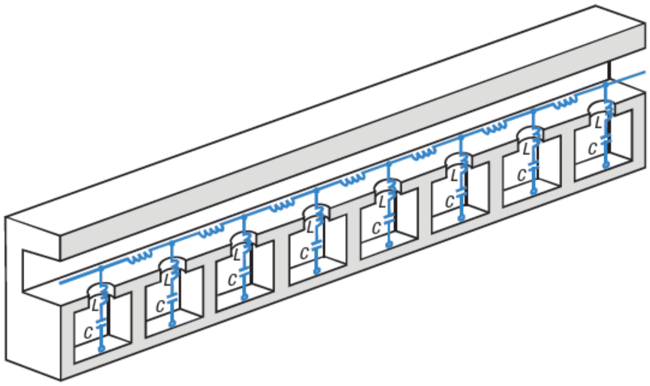

Figure 1.7: An acoustic duct fitted with an array of Helmholtz resonators, by Fang *et al* [9]

With potential applications in noise isolation within ducted systems and on a smaller scale as microelements within a larger 'macro' material such as a cloak or lens, ducted acoustic metamaterials are a common feature of the literature. Fang *et al.* [9] produced one of the seminal initial papers on the subject, demonstrating experimentally such a duct, in this case an ultrasonic rig measuring acoustic waves in water. By comparing the transmission characteristics of a duct fitted with an array of Helmholtz resonators, shown in Figure 1.7, to that of a regular duct when incident with ultrasonic sound waves a distinct region of attenuation is found around the resonance frequency of the Helmholtz array, and calculating the dispersion characteristics shows the band structure 'bending back' upon itself, leading to an antiparallel relationship between group and phase velocities. In an infinite, theoretical material with no losses, the band structure in this region would become a discontinuity, leading to a complete band gap. An expression for the effective bulk modulus is also presented, and appears to have been derived by substituting analogous quantities for acoustic parameters into expression for the effective permeability of an electromagnetic material derived by Pendry *et al* [18]. The calculations closely match the results of the experiment, however no rigorous derivation of the expression is offered. In addition, Fang does not mention the effective density of the system, and whether this is constant or dispersive.

Insight into this last point is offered by Cheng *et al* [66] who state that such a metamaterial is actually inevitably dispersive in both effective bulk modulus and density, and can therefore become double negative. Cheng states that in electromagnetic materials it is possible to induce resonances in the electric and magnetic (E and H) fields independently, and in double negative viscoelastic metamaterials such as that presented by [27, 33] the acoustic properties of the transmission and resonant mediums have a sharp contrast, however in the acoustic metamaterials such as this where the same component fluid is contained in the waveguide and the resonator, this is not the case. In the acoustic field the fluid within the duct is synchronised with that of the resonator, and the resonances of the two constituent acoustic properties, pressure and volume velocity, are not induced separately. Therefore the elastic and inertial properties must resonate simultaneously. Cheng notes that the results of both finite element method (FEM) simulations and experiment suggest this is the case.

In addition, the expression that Cheng and Fang cite, governing the dispersive effective bulk modulus is a direct analogue of that given by Pendry *et al* [18] for electromagnetic metamaterials, and no formal derivation of the expression in the acoustic domain is offered. Whilst the expression is shown to correlate with experimental results, Akl and Baz [67] offer a more formal derivation for the effective bulk modulus of such a material, however do not approach the problem of the effective density. In fact in a separate paper Baz [68] uses a different mechanism (a diaphragm located within the duct itself) to control the effective density of the metamaterial. This leads to a somewhat unsatisfactory state of affairs where Cheng *et al* state that a Helmholtz resonator based material must be dispersive in both inertial and elastic properties, however much of the key literature neglects the dispersive density component of this set up.

In another study Cheng *et al*. [38] also investigated multiple resonators connected in parallel to the same ’cell’ of the material and how this effects the magnitude and profile of the band gap. The addition of extra resonators is shown to have an affect of not only deepening but significantly widening the band gap, with the addition from 1 to 4 resonators leading to an increase of a factor of three in the full-width half-maximum (FWHM) of the band gap. The magnitude of the effect is attributed to the coupling of the closely spaced resonators within each cell of the material, which creates a mutual impedance between the neck openings and an additional additive term to the radiation impedance. This coupling occurs due to multiple resonators acting on the same ’cell’ of the acoustic duct, whereas the coupling that was observed by Goffaux in resonant phononic crystals, or in the case of the beam fitted with an array of vibration isolators studied by Gao, was due to near field wave interaction between separate cells of the periodic material. Therefore in these higher dimensioned materials it is not possible to get the same degree of coupling as in this 1D acoustic case.

The aforementioned work of Lee *et al* [51] demonstrated an acoustic duct metamaterial with double negative effective parameters without the need for traditional Helmholtz resonator elements. Diaphragms between each cell provide a spring element to react to the movement of the air within each cell. The resonant system created in each cell therefore has a natural frequency related to these two elements, and the resulting change in phase that occurs as the excitation frequency moves above this resonance frequency leads to negative acceleration, and therefore effective negative mass [49] (this is similar to the mechanism used by Baz, described above). Then, side holes are created within these cells such that as air oscillates within the cell, some air is pumped in and out of the side hole and energy is dissipated through radiation and drag, creating a sink in the system [50]. This alters the continuity equation of the tube such that the effective bulk modulus becomes dispersive, and can become negative at certain frequencies.

1.6.2 Active Metamaterials

Whilst acoustic metamaterials have been shown to have some remarkable properties, this novel behaviour is for the most part restricted to very narrow frequency bands dictated by the lattice constant of the material (when considering Bragg effects) and by the material constants of the resonant elements (when considering resonant effects). Also, some applications, such as acoustic cloaking, require material constants that are just impractically extreme. This has lead to work investigating the possibility of incorporating active elements into metamaterials to potentially adapt and enhance the performance such that it occurs over a wider frequency band or can recreate the behaviour of extreme values of density and modulus whilst utilising commonly available materials. This is a relatively recent development in viscoelastic metamaterials, and therefore the amount of published material in this area at present is limited, and a large portion of the work presented in this thesis focuses on this area.

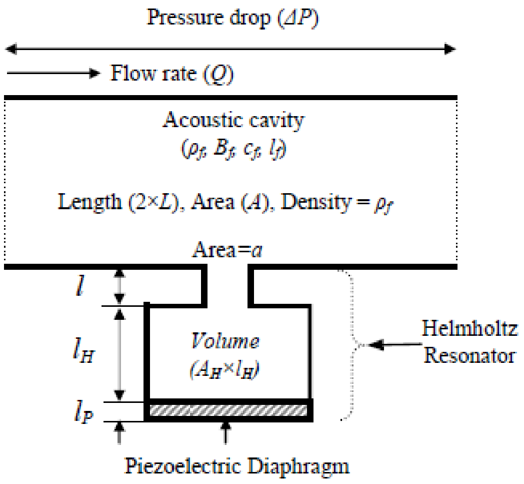

Figure 1.8: A Helmholtz resonator with a piezoelectric diaphragm controlled by a local shunt circuit [10] © IOP Publishing. Reproduced with permission. All rights reserved

The work of Akl and Baz has demonstrated the potential of tuning the effective material parameters of a ducted acoustic metamaterial. By adapting the classic acoustic metamaterial configuration consisting of a duct with an array of Helmholtz resonators so the back wall of the resonators is replaced with a piezoelectric patch [69], it is demonstrated that by tuning the stiffness of the piezo patches using electrical shunts, the effective bulk modulus of the material is tuned in turn. A subsequent paper by the authors [69] introduces an adaptation to the system so the resonant elements of the system are created purely by a duct fitted with a periodic array of piezoelectric patches flush mounted to the duct walls, replacing the Helmholtz resonators. Here the programmable bulk modulus is provided by direct acoustic pressure feedback. Comparing the two systems reveals the design challenges that must be considered if the metamaterial is to be applied to a practical use. The flush mounted panels are found to require a much lower control voltage compared to the Helmholtz resonators if a bulk modulus is required that is above the ambient value of the fluid in the duct, whereas for values lower than the ambient the opposite is true. Therefore to create a practical material with manageable control voltages, if values above and below ambient are required both resonator systems would be as part of the material. The active system is shown to have regions of instability due to the required stiffness of the piezoelectric diaphragm becoming zero, and the stability of the system is investigated in a later paper by Akl and Baz [10].

Alongside the above work, an alternative acoustic metamaterial is proposed by Baz [68] that is capable of providing tunable effective density. In this material an acoustic duct is split into cells by way of a flexible diaphragm, similar to the passive material proposed by Lee *et al* [49], however the diaphragms consist of piezoelectric material such that their stiffness can be tuned using an electric shunt circuit. This work has also been extended into a circular geometry [70] and a single cell has been demonstrated experimentally [71]

The purpose of the above work by Akl and Baz is to create a material where each cell can be tuned to give a constant value of effective bulk modulus or density across a large range of frequencies, addressing the dispersive issues that would impede the construction of an acoustic cloak from passive elements. In each of the configurations discussed above the piezoelectric patches are self sensing actuators. Although the response is examined for a range of tunings, the electrical shunts considered are static components, as such the material could not be adaptive and would only work in a fixed frequency range, albeit one of enhanced width. Since the focus is on developing components for an acoustic cloak, the work does not assess the band stop performance of the material, and how that may be enhanced by the active arrangement. Also, since all the material parameters presented in the papers are positive, the possibility of achieving negative parameters is not investigated. The materials presented are 1 dimensional, and due to the ducted nature of the material there may be difficulty encountered when trying to scale the material up to higher dimensions.

This active control work in ducts can be considered to have an overlap, in spirit at least, with work carried out investigating impedance matching in acoustic ducts by Collet *et al*. [72], who created a distribution of transducers on the skin of an acoustic duct to actively control the acoustic impedance of the duct such that no acoustic wave propagates down the duct. This system has been verified through both finite element simulation and experimental results. The system uses distributed control, which is demonstrated within the work to be more energy efficient at achieving the control objective than classic feedforward control methods, whilst also being ripe for future exploitation by emerging micro electromechanical systems (MEMS) technologies.

The work of Airoldi and Ruzzene [11] describes a 1 dimensional waveguide metamaterial constructed from a metal beam with shunted piezoelectric patches attached

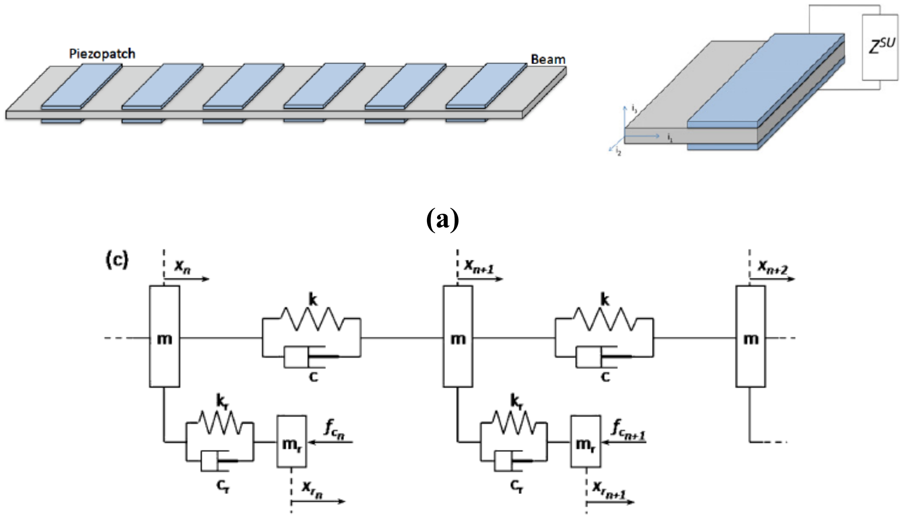

(a)

(b)

Figure 1.9: (a) The active waveguide metamaterial by Airoldi and Ruzzene [11] (left) consisting of locally shunted piezo patches (right). (b) The active metamaterial structure proposed by Pope and Daley [12]

either side at periodic intervals. The shunts are resonant Antiniou circuits such that the patches form resonant elements, creating a periodic resonant material. The response of the material is predicted mathematically and measured using a laser Doppler vibrometer, with results showing a band gap due to the patches occurring at the resonant frequency of the shunting circuits, which disappear under ’open circuit’ conditions, leaving the expected behaviour of a homogeneous beam. The equivalent material parameters are calculated from the experimental data and the dispersive sound speed demonstrated by examining the propagation of pulse inputs into the system.

One of the drawbacks of ducted acoustic metamaterials may be the difficulty in scaling the structures up to multiple dimensions. Therefore the work carried out by Pope and Daley has focused on a lumped parameter approach to acoustic metamaterials, simulating the response of materials with physical mass, spring and damper elements. Pope and Daley [12] showed that it is possible, using a lumped parameter approach, to create an active material that had behaviour equivalent to that of a ducted array of Helmholtz resonators. Then by applying active feedback forces to alter the behaviour of the resonant elements so their motion was a function of the motion of neighbouring cells of the material, it was possible to create a material that exhibited DNG behaviour for a given, adaptable frequency band. This model was later extended by Pope *et al* [73] to consider impedance matching of the active material such that the acoustic impedance of the material was matched to the surrounding media over a controllable range of frequencies; an important aspect of creating non-scattering acoustic cloaks. Whilst these initial simple control architectures produced adaptable double negative and impedance matching behaviour, they were later found to be inherently unstable, so have since been adapted in later work to stabilise the system whilst also taking into consideration the actuator dynamics issues that will occur when attempting to produce such materials [74, 75], and a process has been developed to design these metamaterials and define their regions of stability [76]

1.7 Thesis Structure and Objectives

This thesis presents several advancements to the prior literature presented above, particularly focusing on the resonant band gap profile. From the proceeding literature review it is evident that the resonant nature of the band gap leads to narrow bandwidths of attenuation or double negative behaviour, and whilst there have been attempts to address this using the passive methods described this requires large number of resonators to achieve a modest performance. By incorporating active elements into metamaterials the band gap can become much wider and become more flexible.

The goal of this thesis is to develop the, so far mostly theoretical, ideas of active elastic metamaterials and move closer towards an end goal of producing practical, working metamaterials that have the potential to be used as high performance isolators or an element within an acoustic cloaking device. In particular, the work demonstrates the high levels of performance and flexibility that be achieved by incorporating active control techniques into a passive metamaterial structure, and the high level of performance that results from a unified design process that incorporates the best features of active and passive functionality. The number of examples of active metamaterials in the literature are limited, and the most significant of these examples, the work of Akl and Baz, does not address the isolation properties of the band gap. Indeed this work focuses on using static local shunt circuits to create specified range of effective material parameters and does not address the adaptive potential of traditional active control.

The main focus of the research is on isolation applications, however metamaterials are also of interest due to their ability to provide dispersive effective material parameters which can create behaviour not seen in naturally occurring media. Using resonant structures to achieve extreme, and even negative, effective values of bulk modulus and density is a vital component in the development of acoustic cloaking systems. Therefore, whilst cloaking applications are not explicitly considered within the thesis, part of the research focusses on the effective material parameters of the materials created, and how these parameters can be manipulated by design of the active and passive components of the structures. Indeed, it is shown that the band gap behaviour and the material parameters are intrinsically linked. In the future as acoustic cloaking and manufacturing ability develops the metamaterials presented here could be miniaturised and developed to be components within a cloaking application.

The structure of the thesis is as follows -

Chapter 2 - Uncoupled Locally Resonant Viscoelastic Metamaterial Design

Building on the work of Pope and Daley [12] a model for an ’uncoupled’ viscoelastic metamaterial is described. Pope and Daley previously demonstrated that such a metamaterial exhibited a resonant band gap, where vibration transmissibility across the metamaterial is extremely low, and that the material was passively single negative (it had negative effective mass at resonance). It was also shown that applying an active force could adjust the location of the band gap within the frequency domain, or by using active control to couple resonators to adjacent masses, double negative behaviour could be induced. In this chapter the behaviour of this metamaterial is explored further and two key advances are made. It is demonstrated that as the number of layers of the metamaterial increases the maximum displacements of the elements of the metamaterial is reduced, and subsequently the individual maximum forces required from the active control architecture is also reduced. It is also demonstrated within this chapter that active control can be applied in such a way to stagger the resonant frequency of the inclusions from layer to layer, ’smearing’ the band gap in frequency and creating broadband effects.

Chapter 3 - Coupled Viscoelastic Metamaterial Design

Pope and Daley previously showed that active control can be used to couple the resonant elements of the viscoelastic metamaterial from Chapter 2 to adjacent transmission elements, achieving negative behaviour in both the effective mass and stiffness. In this chapter the metamaterial model is developed further by adding additional elastic connections and achieving this double negativity passively and the active control architecture is also developed to incorporate reactive forces rather than point forces, simplifying the controller design. Using Bloch analysis a method is developed for analysing the width and form of the passive band gap, and from this a condition identified to achieve a wide, symmetric band gap. A concept design is then developed to realise this new ’coupled’ viscoelastic metamaterial, with a particular focus on vibration isolation applications, and a experimental prototype of the active metamaterial is designed and produced. Laboratory measurements then confirm that the prototype behaves as predicted by the model and a resonant band gap region is confirmed.

Chapter 4 - Actively Enhancing the Band Gap of the Coupled Viscoelastic Metamaterial

To enhance the region at which attenuation occurs around the passive band gap, in this chapter active control is applied to the metamaterial produced in Chapter 3. Initially a single channel Filtered-x Least Mean Squared algorithm is implemented to demonstrate the efficacy of using an active control to enhance band gap attenuation of the metamaterial. The algorithm is applied to both tonal and broadband disturbances and is shown to effectively attenuate vibration transmission through the structure. Next several feedback controllers are implemented using Finite Impulse Response filters optimised using a constrained, non-linear optimisation algorithm to minimise transmission through the metamaterial over a given frequency range. Several controller structures are implemented, including single channel (SISO) and multichannel (MIMO) examples. The results suggest that active control can be used to greatly enhance the bandwidth over which attenuation occurs in and around the passive band gap, as well as suppressing out of band resonances.

Chapter 5 - A Passive Locally Resonant Acoustic Metamaterial

A duct lined with an array of Helmholtz resonators is a common metamaterial structure, as described in Section 1.6.1. The metamaterial presented in this Chapter is based on this concept. The design consists of an array of split hollow sphere elements acting as Helmholtz resonators suspended in a circular sample. The material is then produced using additive layer manufacturing techniques, since one future aim for these metamaterial structures is to move into higher degrees of freedom and smaller dimensions, and therefore 3D printing technology is likely to be the most viable route to production. To predict the performance of the metamaterial presented in this Chapter the acoustic transmission line method is used with a transfer matrix approach. Combining a transfer matrix formulation with an impedance representation of the Helmholtz resonator allows the transmission coefficient to be determined. Next, a lumped parameter equivalent circuit representation of a Helmholtz resonator within a duct is derived and it is shown that both the effective bulk modulus and density parameters are dispersive. The metamaterial samples are then tested in the laboratory and the model is shown to accurately predict the transmission coefficient and dispersive material parameters. Finally the effect of differing the number of resonators is investigated.

Chapter 6 - Design of an Active Helmholtz Resonator For Use in an Acoustic Metamaterial

Before active control can be applied to enhance the band gap of the acoustic metamaterial described in Chapter 5 it is necessary to investigate the performance of a single active Helmholtz resonator. In this chapter a model of an active Helmholtz resonator is introduced and its performance regarding band gap attenuation and dispersive material parameters is investigated. First the formal stability limits of a second order control loop are derived and the performance at these limits examined. Next, to develop a practical feedback controller, constrained non-linear optimisation is used to design FIR filters designed to minimise sound transmission over a specified frequency range. The affect on transmission coefficient and the effective material parameters of these controllers is then examined. This process is then repeated using simple 2nd order pole-zero type controllers.

Chapter 7 - Implementation of an Active Helmholtz Resonator

Based on the active Helmholtz resonator model introduced in Chapter 6 a prototype active Helmholtz resonator is produced and its performance measured in the laboratory. Based on the results from the previous chapter, both simple 2nd order controllers and optimised FIR filters are designed and applied to the resonator. Finally, to assess the potential level of control that could be achieved by the single active resonator the system is reformulated as a remote control problem and analysed using a geometric control strategy developed by Daley and Wang [77].

Chapter 8.1 - Conclusions

The final chapter presents a summary of the conclusions drawn from the work presented in the rest of this thesis, and suggestions for future work are provided

1.8 Contributions

The main contributions of this thesis are:

1. Using the active viscoelastic metamaterial structure proposed by Pope and Daley [12] it is demonstrated that metamaterials have advantages over traditional active isolation materials, with smaller elemental displacements and individual control forces. A simple active control technique can be used to stagger the natural frequency of each resonator element and widen the region at which attenuation occurs.

2. A new viscoelastic metamaterial has been proposed that achieves double negativity passively and has a deep resonant band gap coinciding with this double negative region. A novel method for predicting the form of this band gap and for achieving a wide symmetric band gap is derived

3. A concept design is developed of the metamaterial as a vibration isolator, and a prototype of this concept is produced and tested in the laboratory. The passive band gap is confirmed.

4. Using active control techniques it is demonstrated how the passive band gap can be enhanced and attenuation can be extended over a wide frequency region. Both feedforward and feedback controllers have been tested, including multi-input, multi-output (MIMO) optimised feedback filters.

5. An acoustic metamaterial consisting of an array of small Helmholtz resonators is developed that exhibits a band gap in its transmission coefficient at resonance. The majority of the literature on the material parameters of these types of metamaterials

focus on the effective bulk modulus, but it is shown here that both the effective bulk modulus and the effective density are dispersive.

6. The acoustic metamaterials described above have been produced using additive layer manufacturing (3D printing) techniques, and tested in the laboratory to confirm the behaviour described.
7. As a first step in integrating active control into the acoustic metamaterial an active Helmholtz resonator model is introduced and by combining the model with optimised feedback controllers, the potential for manipulating the band gap and effective material parameters is investigated.
8. Finally a prototype active Helmholtz resonator is produced, its passive performance confirmed in the laboratory and the band gap attenuation is manipulated using feedback controllers. An indication of the maximum level of attenuation available from the active resonator is then achieved using a geometric approach [78] to the control problem.

Chapter 2

Uncoupled Locally Resonant Viscoelastic Metamaterial Design

2.1 Introduction

As described in Section 1.6.1, a duct fitted with a periodic array of Helmholtz resonators is a common example of an acoustic metamaterial [9, 38, 66, 68, 69], an example of which is shown in Figure 2.1a. Pope and Daley [12] used this structure as an inspiration for a theoretical viscoelastic metamaterial structure consisting of a chain of masses connected by viscoelastic connections, each of these masses is then connected to its own dynamic vibration absorber unit, shown in Figure 2.1b. It is this structure that will form the basis of the investigations within this chapter. The Pope and Daley work demonstrated that the metamaterial structure presented exhibited resonant band gaps in the transmission spectrum. The material is also SNG, with a region of negative effective mass coinciding with the resonant band gap.

Pope and Daley propose the addition of active forces, denoted as f_c in Figure 2.1b, and propose using an active spring and damping constant to mimic the effect of extra viscoelastic connections between the resonator masses, m_r, and a virtual earth to actively adjust the frequency at which the band gap occurs online. The active architecture also facilitates additional coupling between the resonator masses and other elements of the material. It is shown by adding virtual viscoelastic connections between the resonator masses and adjacent transmission masses, m_t, the effective stiffness of the material also becomes dispersive and the material can become double negative. The Pope and Daley work proposes a novel metamaterial structure and is a theoretical investigation into its potential, however it does not attempt to present a realisable metamaterial design, nor focus on a particular practical use for the metamaterial. A follow up paper by Pope *et al* [79] attempts to address some of the practical issues of implementation, particularly highlighting issues with stability and the chosen controller design, and complications due to actuator dynamics.

The work described in this chapter builds on the foundation described above. The

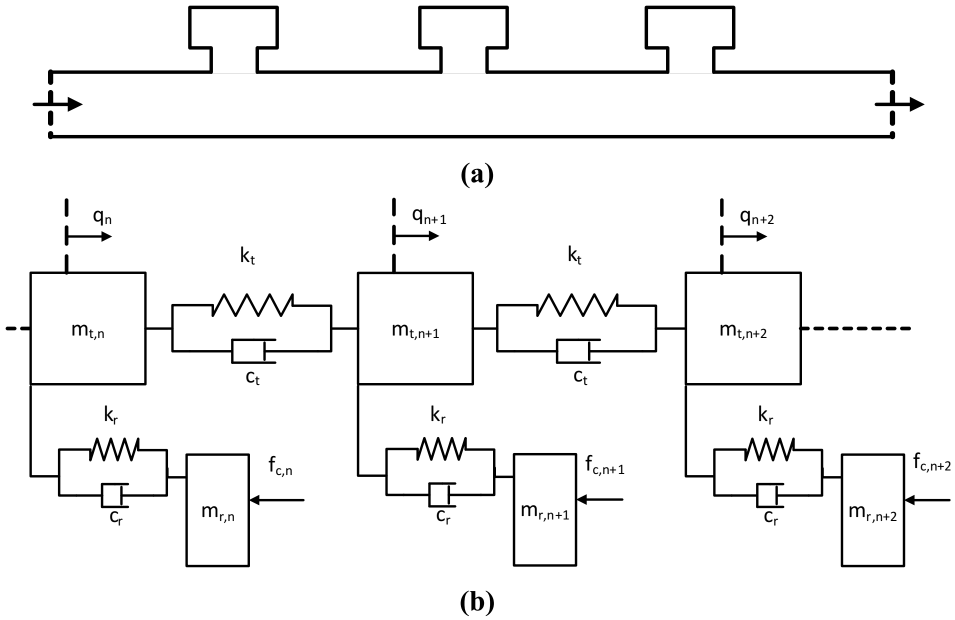

Figure 2.1: (a) An array of Helmholtz resonators fitted to a duct constitutes a periodic locally resonant metamaterial. (b) Using a mechanical analogue a design for a viscoelastic metamaterial can be imagined

same metamaterial structure as proposed by Pope and Daley is investigated theoretically; the mechanism behind the negative material parameters is investigated as well as its potential use as a vibration isolator. Whilst there are known faults with the practicality of the design (described in [79] and mentioned above), the model is used to highlight possible advantages such an approach may have over traditional vibration isolation techniques. It is demonstrated that as the number of layers of the metamaterial increases the maximum displacements of the elements of the metamaterial is reduced, and subsequently the maximum individual forces required by the active control architecture is also reduced. This is a key factor in reducing the form factor of future active metamaterials, as well as providing an advantage for using active metamaterials over more traditional active control techniques in isolation applications.

Whilst the resonant structure means metamaterials have the potential to greatly outperform traditional isolation techniques at low frequencies, a key drawback of passive metamaterials is that the interesting behaviour they exhibit is limited to narrow bandwidths around the resonant frequency. It is demonstrated within this chapter that active control can be applied in such a way to stagger the resonant frequency of the inclusions from layer to layer, ’smearing’ the band gap in frequency and creating broadband effects.

2.2 The Metamaterial Structure

A chain of single Helmholtz resonator elements within or attached to a duct is a common example of a simple acoustic metamaterial [9, 38, 66, 68, 69], and is represented in Figure 2.1a. Within the long wavelength limit ($ka \ll \lambda$, where k is the wavenumber and a is the periodic constant of the metamaterial), using a lumped parameter approach allows a mechanical analogue to be applied [12], creating the model shown in Figure 2.1b. Here the mass of the air within the tube is represented by the m_t mass elements, and the compliance by the stiffness and damping elements represented by k_t and c_t respectively. The mechanical analogue of a Helmholtz resonator is represented by the mass, stiffness and damping elements m_r, k_r and c_r respectively.

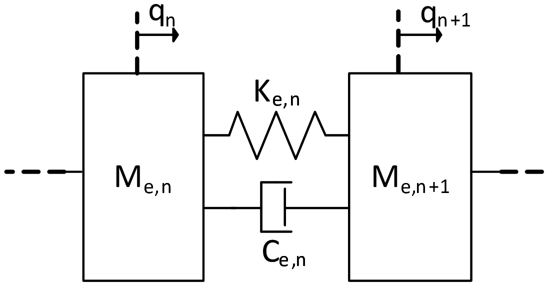

Figure 2.2: A simple representation of a metamaterial chain using equivalent material parameters

This lumped parameter model now serves two functions, first it is mathematical device for assessing the response of the ducted acoustic metamaterial, but in addition it provides a potential design for a viscoelastic metamaterial built from physical mass and spring elements. The model shown in Figure 2.1b can be extended to incorporate an active control architecture, where point forces are applied to the resonator masses, denoted as f_c. Such a material would have potential applications in vibration isolation as well as a potential building block of an acoustic cloaking device, and was first proposed by Pope and Daley [12]. By representing the material by a simple chain of effective material elements, as shown in Figure 2.2 then, presuming harmonic motion, the dynamics of this material can be expressed as

$$-M_e q_n \omega^2 = (C_e j\omega + K_e)(q_{n-1} + q_{n+1} - 2q_n) + f_n \tag{2.1}$$

Where f_n is a harmonic disturbance force applied to the nth transmission mass of the material and $q_{t,n}$ is the displacement of the nth transmission mass. M_e, K_e and C_e are the effective mass, stiffness and damping coefficients of the material respectively. If there are no active forces (i.e. $f_c = 0$ for all resonators), and all layers of the metamaterial are identical ($m_{t,1} = m_{t,2}... = m_{t,N}$ etc.) formulating and rearranging the equations of motion for the explicit material model in Figure 2.1b yields

$$-\omega^2 \left(m_t - \frac{-m_r\omega^2(c_r j\omega + k_r)}{\omega^2(-m_r\omega^2 + c_r j\omega + k_r)} \right) q_n = (k_t + j\omega c_t)(2q_n - q_{n+1} - q_{n-1}) + f_n \tag{2.2}$$

It is clear from comparing Equations 2.2 and 2.1 that the equivalent mass, M_e of the system has become dispersive. The expressions for the effective mass and the real part of that expression are given below.

$$M_e = m_t - \frac{-m_r\omega^2(c_r j\omega + k_r)}{\omega^2(-m_r\omega^2 + c_r j\omega + k_r)} \tag{2.3}$$

$$\text{Re}(M_e) = m_t - \frac{m_r(m_r k_r - c_r^2)\omega^2 - m_r k_r^2}{m_r^2\omega^4 + (c_r^2 - 2m_r k_r)\omega^2 + k_r^2} \tag{2.4}$$

The equivalent stiffness, K_e, and damping, C_e, remain equal to their static counterparts, k_t and c_t respectively. Equation 2.3 shows that for the passive material the effective mass, M_e, is complex. The real part of M_e represents the equivalent inertial mass of the dynamic system, whilst the imaginary part represents an additional loss component within the system, introduced by damping terms associated with the resonators. At resonance or at low frequencies the dispersive term on the right hand side of Equation 2.4 can become larger than the static term m_t and the effective mass of the system becomes negative. Within this region the material is said to be SNG, as the effective stiffness of the material remains static and positive. Within the literature [3, 4, 9] SNG regions have been shown to create band gaps, where wave transmission is forbidden, and this is true for the material considered here, where the SNG region coincides with a deep, asymmetric band gap. These are caused by the wave vector becoming imaginary and therefore waves within the structure being purely evanescent.

This behaviour is discussed in Section 2.3. The work of Pope and Daley [12] considers use of an active force, f_n, to extend and adapt the performance of the passive material. By applying an active control force in proportion to the displacement and velocity of the resonant element such that $f_{c,n} = k_c q_n + c_c \dot{q}_{t,n}$ it is possible to change the natural frequency of the resonant elements by varying the constants k_c and c_c. This is a simple method for adapting the location of the band gap, and is referred to in this thesis as the 'local' control strategy.

Whilst the passive and active system described above provide a mechanism for achieving negative mass, they do not contain the necessary frequency dependent stiffness term to achieve double negativity. It was shown in [12] that the control force can be extended to be a function not only of the dynamic motion of the resonator mass but of neighbouring mass elements, in this case the $(n-1)th$ and $(n+1)th$ transmission masses. This modified control force, $f_{c,n} = k_c(q_{t,n-1} + q_{t,n+1} - 2q_{r,n}) + c_c(\dot{q}_{t,n-1} + \dot{q}_{t,n+1} - 2\dot{q}_{r,n})$ results in an expression for the effective mass and a combined expression for the effective damping-stiffness of the system, given by Equation 2.5 and Equation 2.6 respectively.

$$M_e = m_t + \frac{m_r(c_r j\omega + k_r)}{-m_r\omega^2 + (2c_c + c_r)j\omega + 2k_c + k_r} \tag{2.5}$$

$$K_e + j\omega C_e = c_t j\omega + k_t + \frac{(c_c j\omega + k_c)(c_r j\omega + k_r)}{-m_r\omega^2 + (2c_c + c_r)j\omega + 2k_c + k_r} \tag{2.6}$$

Equation (2.6) is a complex expression describing the combined effective damping and stiffness. As such the real part represents the pure stiffness elements within the system, and the imaginary part the dissipative damping elements within the system. So calculating the real and imaginary part of Equation (2.6) yields the effective stiffness, K_e and the effective damping, C_e of the system.

$$\text{Re}(M_e) = m_t + \frac{m_r((-m_r k_r + c_r(2c_c + c_r))\omega^2 + k_r(2k_c + k_r))}{m_r^2\omega^4 + ((-2m_r(2k_c + k_r) + 2c_c + c_r)^2)\omega^2 + (2k_c + k_r)^2} \tag{2.7}$$

$$K_e = k_t + \frac{m_r c_c c_r \omega^4 + (-m_r k_c k_r + 2c_c^2 k_r + c_r^2 k_c)\omega^2 + k_c k_r(2k_c + k_r)}{m_r^2\omega^4 + (-2m_r(2k_c + k_r) + (2c_c + c_r)^2)\omega^2 + (2k_c + k_r)^2} \tag{2.8}$$

$$C_e = c_t + \frac{(c_c c_r(2c_c + c_r) - m_r(c_c k_r + c_r k_c))\omega^2 + 2c_r k_c^2 + c_c k_r^2}{m_r^2\omega^4 + (-2m_r(2k_c + k_r) + (2c_c + c_r)^2)\omega^2 + (2k_c + k_r)^2} \tag{2.9}$$

This new extended control force, described from herein as ’distributed’ control, now provides a mechanism for negative effective stiffness, since at certain frequencies it is possible to make the dispersive term on the right hand side of Equation 2.8 negative and larger than the constant k_t.

2.3 Modelling the Transmission Response

Modelling the dynamic behaviour of a chain of metamaterial layers requires determining the equations of motion of the material. The equations of motion and related mass, stiffness and damping matrices of the system can be constructed using D’Alembert’s principle. Assuming harmonic motion, the equations of motion are

$$[-\omega^2\mathbf{M} + j\omega(\mathbf{C} + \mathbf{F_c}) + (\mathbf{K} + \mathbf{F_k})]\mathbf{q} = \mathbf{f} \tag{2.10}$$

Where **M**,**C** and **K** are the mass, damping, stiffness matrices, $\mathbf{F_k}$ and $\mathbf{F_c}$ are the matrices containing the active k_c and c_c coefficients respectively, **f** is the disturbance force vector, and ω is angular frequency in rad/s. The vector **q** contains the displacement terms for both the transmission and resonator mass elements of the system. By assuming a harmonic excitation force on the first mass and solving for the displacement of the last mass, the transmission characteristics of the system are attained.

	Parameter	Value
Transmission Media	m_t	$0.01kg$
	k_t	$3000Nm^{-1}$
	c_t	$0.01Nsm^{-1}$
Resonators	m_r	$0.1kg$
	k_r	$1000Nm^{-1}$
	c_r	$0.002Nsm^{-1}$
Equivalent feedback parameters	k_c	$1000Nm^{-1}$
	c_c	$0.01Nsm^{-1}$

Table 2.1: The material parameters used to simulate the metamaterials described in Section 2.3

The material parameters used for the simulations in this chapter are given in Table 2.1. These parameters do not reflect a particular use case, but mirror those used by Pope and Daley [12]. The dynamic response of a 3-6 layer active material with local and distributed feedback applied can be seen in Figure 2.3, where the transmission is defined as the magnitude of the acceleration of the final layer as a function of the acceleration of the first layer.

Both materials exhibit a deep, asymmetric region of attenuation at the frequency associated with the resonant elements (the resonant band gap), that coincides with the onset of negative mass. The location of this region remains stationary with an increased number layers but becomes deeper. This deepening of the band gap leads to the total amount of attenuation over the band gap to increase, however due to the asymmetric nature of the band gap, for much of the band gap region attenuation is relatively low compared to the peak attenuation levels.

2.3.1 Negativity and the Band Gap

Figure 2.3b shows K_e and M_e becoming negative simultaneously, leading to a region of double negativity. The double negative region also coincides with the region of attenuation known as the band gap. Previous studies have suggested that the resonant band gap occurs when the metamaterial becomes single negative, causing the wave vector, k, to become imaginary, leading to an evanescent rather than travelling wave solution to the wave equation. When the material is made to be double negative, the solution becomes negative real and a passband occurs in what is now a 'left-handed' material [21] [51]. However, this explanation neglects dissipative losses within the material. The presence of a band gap within this double negative region can be explained using the acoustic transmission line method (ATLM) representation of the material

The metamaterial consists of a number of periodic layers, therefore it is possible to consider the material as a series of 4-pole linear ported networks connected together in a transmission line [32, Pg. 51-54]. Here, a transfer matrix is formulated to describe the transform from one state vector to another across the chain of masses (e.g. $q_n \rightarrow q_{n+1} \ldots \rightarrow q_N$). To formulate the transfer matrix the state vectors representing the force (f) and displacement (q) of each 'cell' of the chain are considered, where in this case these state vectors are scalar values and each cell consists of a single set of equivalent mass-spring-damper elements. Now, the relationship between the force and displacement across a multiple layer material can be considered in terms of the transfer matrices, $\boldsymbol{T}$, such that

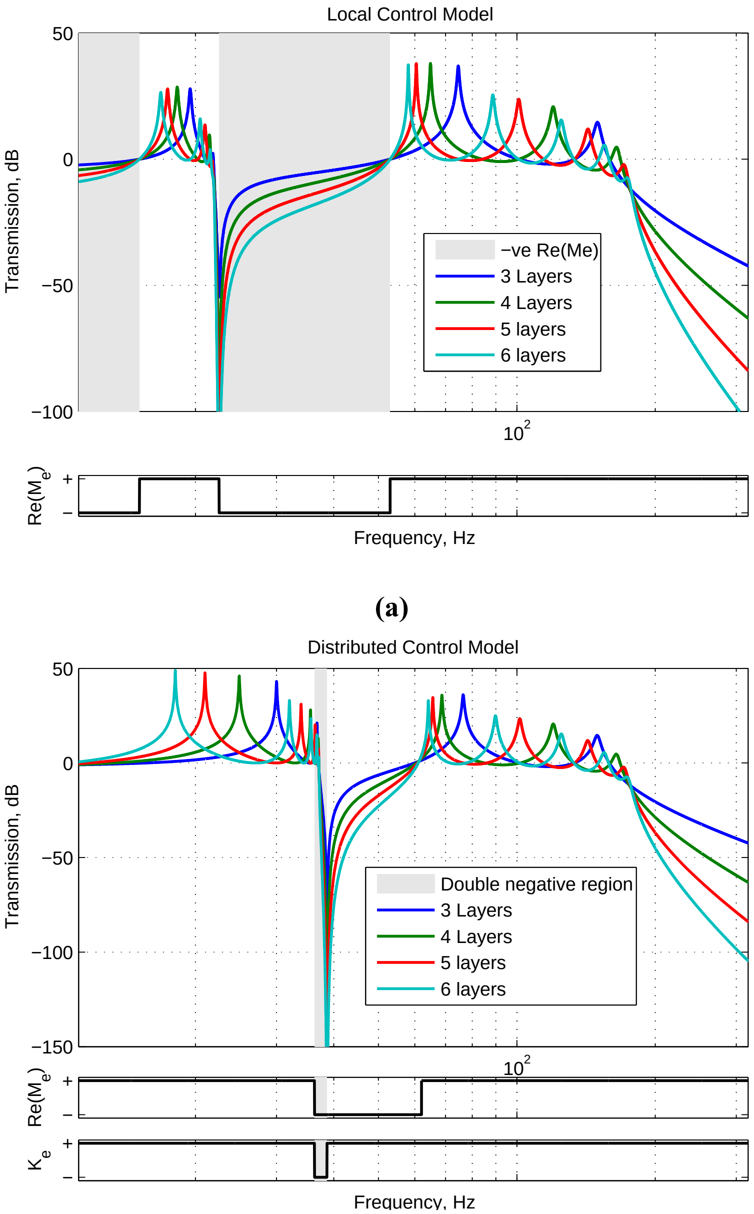

(a)

(b)

Figure 2.3: The transmission response and region of negative effective parameters of the local control (a) and distributed control (b) active metamaterials consisting of 3-6 layers. The grey area denotes the SNG region of the local control material and the DNG region of the distributed control material

$$\begin{Bmatrix} q_N \\ f_N \end{Bmatrix} = \prod_0^N \boldsymbol{T}_n \begin{Bmatrix} q_0 \\ f_0 \end{Bmatrix} = \boldsymbol{\tau} \begin{Bmatrix} q_0 \\ f_0 \end{Bmatrix} \tag{2.11}$$

$$\boldsymbol{T}_n = \begin{bmatrix} 1 - \frac{\omega^2 M_e}{K_e + j\omega C_e} & -\frac{1}{K_e + j\omega C_e} \\ \\ \omega^2 M_e & 1 \end{bmatrix} \tag{2.12}$$

Note that if the multiple layers are identical, as is the case with a periodic metamaterial, the product of transfer matrices reduces to $\boldsymbol{\tau} = \boldsymbol{T}^N$. Also note that $|\boldsymbol{T}| = 1$, which is a property of reciprocal systems, and more specifically a constraint of passive, linear, 2-port networks [80]. By applying the initial condition $f_N = 0$ the transmission transfer function, H, of the material from the first to the last mass is given by Equation 2.13 where the subscript (p, q) denotes the pth and qth column of $\boldsymbol{T}^N$.

$$H_T = \frac{q_N}{q_0} = \left(\boldsymbol{T}^N_{1,1} - \frac{\boldsymbol{T}^N_{1,2}\boldsymbol{T}^N_{2,1}}{\boldsymbol{T}^N_{2,2}} \right) \tag{2.13}$$

Bloch theory can be used to describe how waves move through periodic structures by calculating the dispersion characteristics of the material [81]. When applied to an infinitely long viscoelastic metamaterial described by the transfer matrix above, the relationship between displacements of adjacent transmission masses is

$$q_{n+1} = q_n e^{jkd} \tag{2.14}$$

Where k is the wavenumber, and d is the lattice constant. In its general form, the theory states that wavenumbers come in pairs $\pm k$, representing waves travelling in the positive and negative direction, however only the positive travelling wave shall be considered here. By substituting this expression into Equation 2.1 the Bloch dispersion relationship can be derived as

$$\cos kd = 1 - \frac{\omega^2 M_e}{2(K_e + j\omega C_e)} \tag{2.15}$$

If no dissipation is present, (i.e. M_e is pure real and C_e is zero), then in a SNG region the left hand side of the equation will become greater than one and create a purely imaginary wave vector and, hence, a band gap. If the material is DNG then, under the condition that

$|M_e/2K_e| < 1$, the wave vector will become real once more. However, when losses are present, as in Equation 2.15, it is clear that the solution will be complex even for a DNG material since the M_e and C_e parameters are complex themselves, leading to a travelling (real) wave with an attenuation (imaginary) envelope. When the relationships governing the effective material parameters resonate, the magnitude of imaginary terms becomes large, leading to high levels of attenuation. Whilst not a ’complete’ band gap (since there is still a travelling wave component) attenuation levels are so high as to effectively behave as a band gap. Solving Equation 2.15 for kd reveals the dispersion characteristics of the material, plotted in Figure 2.4, and it is clear that the region where the magnitude of the imaginary part of the wave number becomes large coincides with the band gap of the material response. Note that due to the restricted domain of the $\cos^{-1}$ function, the calculated real part of the dispersion characteristic is limited to $0 \leq \mathrm{Re}(kd) \leq \pi$; in reality the wave number is not bound in this way. This demonstrates that band gaps in the transmission response of this type of metamaterial occur even in regions of double negativity.

The transitions shown in the graphs which define the bounds of the band gap and high frequency roll off regions are functions of the mechanical properties of the system, with the band gap onset occurring at a frequency related to the ratio of the resonator mass and associated stiffnesses connected to it, and the high frequency roll off occurring at a frequency related to the ratio of the transmission mass and associated stiffnesses. The relationship between these transition points and the mechanical properties of the material is explored in greater detail in Section 3.4 of this thesis.

2.4 Physical Properties of the Uncoupled Metamaterial

The double negative behaviour of the material means that it has potential applications in the construction of an acoustic cloak or sub-wavelength acoustic lens. The high levels of attenuation available from the low frequency band gap mean that the material also has applications in isolation scenarios. However, if the such a design is to be successful it is essential that the metamaterial can be built to practical and useful dimensions and also affords advantages over more ’traditional’ methods, such as applying active control to existing isolation mounts. In the following section the practicality and potential advantages of such a design are explored.

A significant contribution to the form factor and performance of the metamaterial is

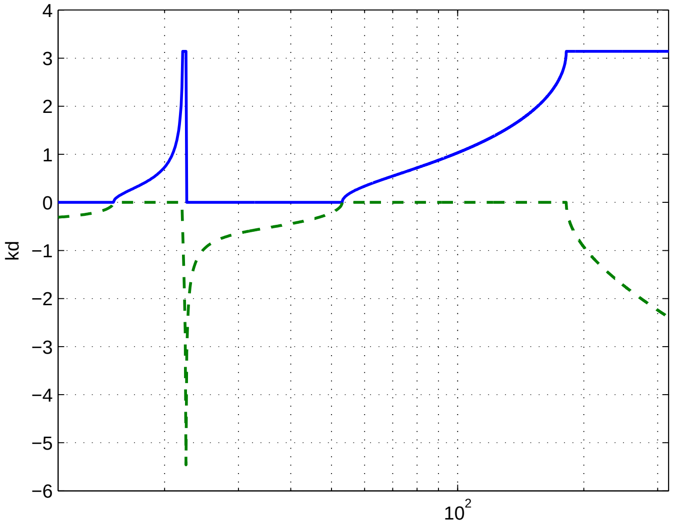

(a)

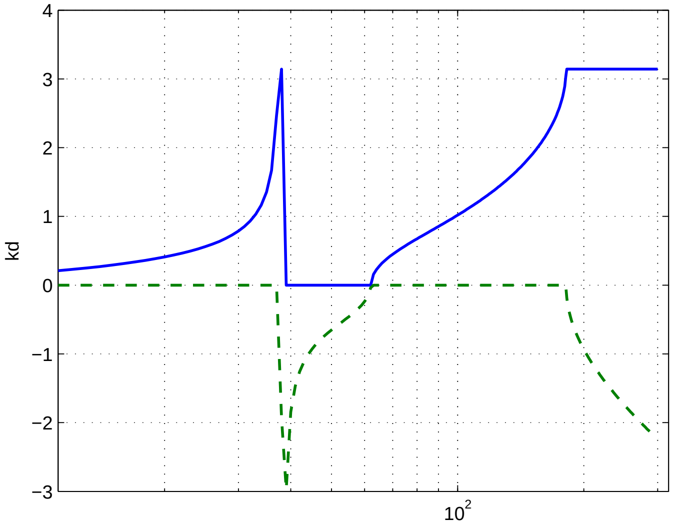

(b)

Figure 2.4: The Bloch dispersion relationship of the local control (a) and distributed control (b) active metamaterials. (blue) The real component, (green dotted) the imaginary component

the clearance required between the elements of the material and the size of the transducers that will be required to produce the active functionality required. The first factor will be related to the maximum displacement experienced by each element of the material as it vibrates and the second will be a function of the magnitude of the forces required in the active control system. An insight into these properties can be gained by utilising the equations of motion. For the examples presented in this section a circular cross section metamaterial is considered with a diameter of 100mm, incident with an acoustic plane wave with a sound pressure level (SPL) of 90dB (ref. 20μPa) (calculated as Force $=$ Pressure $\times$ Area, however for the purposes of this investigation the absolute value for force here is arbitrary), and it is assumed that the values calculated would remain within the linear limits of the material. The material constants used are the same as those in Section 2.3, contained in Table 2.1. The maximum displacement of elements occur at modal frequencies. Since the magnitude of the feedback force is proportional to the magnitude of the motion this also leads to the largest feedback forces being required in this region under the local and distributed control architectures. Therefore, since it is the low frequency band gap region that is of most interest and the band gap itself is the product of modal resonance, it is this region that is critical when designing a material and for which results are presented.

Figure 2.5a shows the maximum displacement within the low frequency band gap region for the local control and distributed control materials, both consisting of 4 layers. There is a large peak in displacement of elements in the local control material within the resonant band gap of an order of 1mm. The distributed control material exhibits a displacement much smaller in this region, suggesting that this type of active architecture could be used to reduce displacements and potentially increase the performance efficiency of the material with respect to the overall material thickness. However, outside this region it can be seen that the distributed control material has an increased displacement at other frequencies, likely to be a consequence of the waterbed effect [82, pg. 165-169]. The maximum displacement within the band gap decreases with the addition of more layers to the metamaterial, as shown in Figure 2.5b, however this appears to tend towards a finite value, meaning that the addition of further layers offers diminishing returns on reducing the maximum displacement. It is also of interest to note that the local control model demonstrates maximum displacement in the first transmission mass. This is because, in these materials, each layer can be considered to be

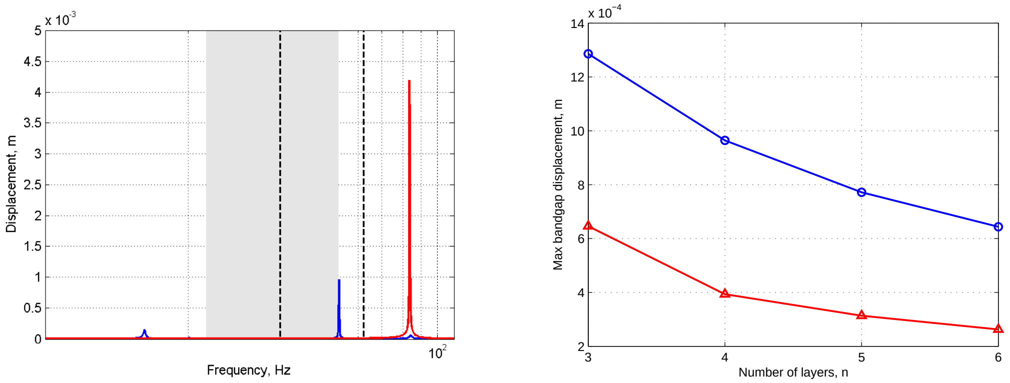

(a) **(b)**

Figure 2.5: (a) The maximum elemental displacement of a 4-layer active metamaterial with local active control (blue) and with distributed active control (red). The resonant band gap region is indicated by the shaded area (local control) and dotted lines (distributed control). (b) The maximum elemental displacement within the region of the resonant band gap as a function of the number of metamaterial layers, local control (blue) and distributed control (red)

acting independently as a vibrating mass with the resonator acting as a mechanical filter. As energy passes through each layer it is attenuated by the filter, so the amount of energy passed on to the next layer is reduced, and therefore the amplitude of vibration is reduced, layer to layer. The distributed control introduces extra coupling between the adjacent masses, effectively creating energy transfer between a transmission mass and the resonators of the adjacent layers, this makes the behaviour of the material more complicated and the layers can no longer be considered as simply independent. The distributed control model shows the maximum displacement alternating between the first and last transmission mass, dependant on whether there are an odd or even number of layers. Insight into the physical nature of this behaviour may be gained by examining the mode shapes of the material, and this requires further investigation.

Since both the local and distributed feedback schemes consist of virtual stiffness and damping terms they produce forces proportional to, and can be calculated using, the displacement and velocity of the material elements. Results are shown in Figure 2.6. The magnitude of the feedback force required by the distributed control material within the low frequency band gap is over an order of magnitude higher than that required in the local control material. Since the feedback forces are proportional to the motion of the

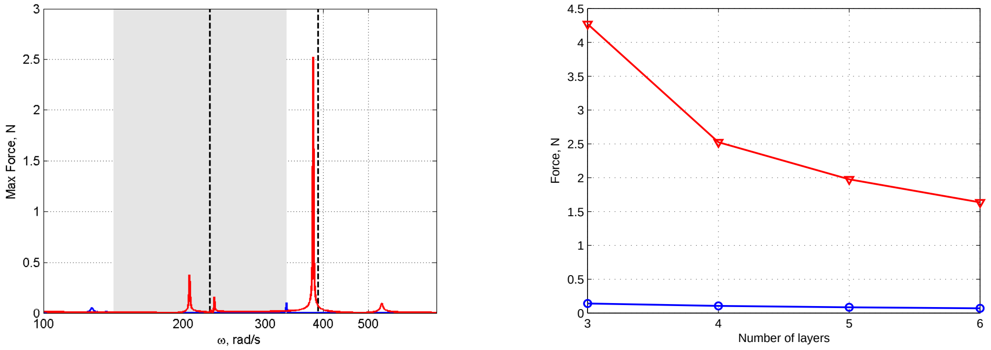

(a) **(b)**

Figure 2.6: (a) The maximum feedback force required in the low frequency band gap in a 4-layer active metamaterial with 'local' active control (blue) and with 'distributed' active control (red). The regions of negative effective mass are given by the shaded area (local control) and the region between the dotted lines (distributed control) (b) The maximum feedback force required within the region of the resonant band gap as a function of the number of metamaterial layers. Local (blue) and distributed (red) control

metamaterial elements, a peak in feedback force is seen within the band gap region, however it was also noted that for the distributed control material, at frequencies approximately 2 octaves below the resonant band gap, there was a large peak in feedback force almost twice that experienced within the band gap itself, this is important to note should the material be required to operate outside of the band gap region. As with the elemental displacements, increasing the number of layers of the material reduces the maximum amount of feedback force required, however this too tends towards a finite value as additional layers are added.

The physical form factor of the material will be related to the size of the displacements and active forces required, and the results above demonstrate that when designing such a metamaterial investigating these properties is possible using the equations of motion and feedback force equations. The levels of force required and displacements experienced is of course related to the disturbance force experienced, as well as levels of damping present in the material (something that was chosen arbitrarily here). However these results highlight an important point, in that the addition of extra layers reduced both the displacements and control forces experienced. For isolation applications this demonstrates an advantage of using a periodic layered material over more traditional active methods; specifically that higher levels of performance can be achieved with smaller local control forces.

2.5 Heuristically Widening the Region of Attenuation

The metamaterials described in this chapter have the potential to be used as high performance isolators, however, as shown in previous sections the low frequency resonant band gap has a deep but asymmetric and narrow attenuation profile, meaning in their current form they would only be useful at isolating disturbances of a discrete and stationary frequency. To make the metamaterials viable solutions for vibration isolators they will need to provide useful attenuation over a wider frequency range. This section will show that there is potential to achieve this using both passive and active means. The active architecture in particular has the potential to provide materials with band gaps that are not only cover a wide frequency range, but can adapt the frequency range of that band gap as required. This section will focus on the local active architecture.

The material as a system has numerous poles and zeros that dictate its frequency response characteristics, with zeros associated with the resonator elements creating the region of attenuation within the band gap. Whilst they have not been explicitly calculated here, considering these poles and zeros gives an insight into the behaviour of the band gap as more layers are added to the metamaterial.

By considering the transfer matrix, Equation 2.12, from Section 2.3.1, the region of attenuation that makes up the band gap will be associated with zeros appearing in the transfer function 2.13. These zeros are associated with resonator element on each layer of the metamaterial, and for a material of identical layers are located in the same location on the complex plane. This is what creates the behaviour seen in Firgure 2.3, where the addition of extra layers leads to more zeros at the same point, making the band gap attenuation deeper, but not wider, and remaining stationary in frequency. A strategy for achieving a wider, more symmetric, band gap profile is to adjust the location of these zeros so they do not occur at the same frequency but at adjacent frequencies, meaning the attenuation profile is ’smeared’ in the frequency range, leading to a wider region of useful attenuation at the expense of maximum attenuation levels.

As stated in Section 2.4, the local control material can be considered to act like a succession of independent layers each attached to a mechanical filter. The resonators in the material act like traditional vibration absorbers, with additional viscoelastic terms, k_c and c_c, that changes their resonant frequency, and hence the frequency at which they

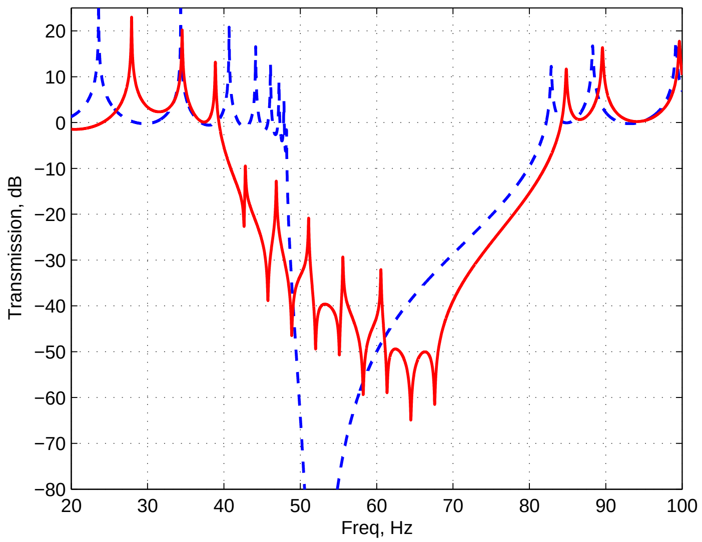

Figure 2.7: The transmission response of a 10 layer local control metamaterial with staggered resonators with the step-size frequency gap between resonators set to 6%(red) and identical resonators (blue dotted)

absorb energy. By adapting vibration absorber theory [83, pg. 150], the frequency at which energy is absorbed is

$$\omega_n \approx \sqrt{\frac{k_r + k_c}{m_r}} \tag{2.16}$$

Therefore it is clear that by changing the feedback constant k_c the natural frequency of the resonator element will change, changing the zeros associated with that resonance and hence the region of attenuation. The value of ω_n can be changed from layer to layer, by changing k_c as a function of n, and the region at which significant attenuation is achieved can be widened. Figure 2.7 shows an example of this, where a 10 layer material whose ω_n values have been staggered over a frequency range in steps of 6% of the passive natural frequency, increasing the region where attenuation of over 10dB is achieved by $\approx$ 10Hz. This approach could also be achieved by manufacturing the layers to have varying values of k_r, however using an active approach has the advantage of each layer being identical, simplifying the mechanical design, and also allowing the frequency region at which the attenuation occurs to be adjusted online.

Whilst this approach can be used to widen the region of attenuation, designing such a

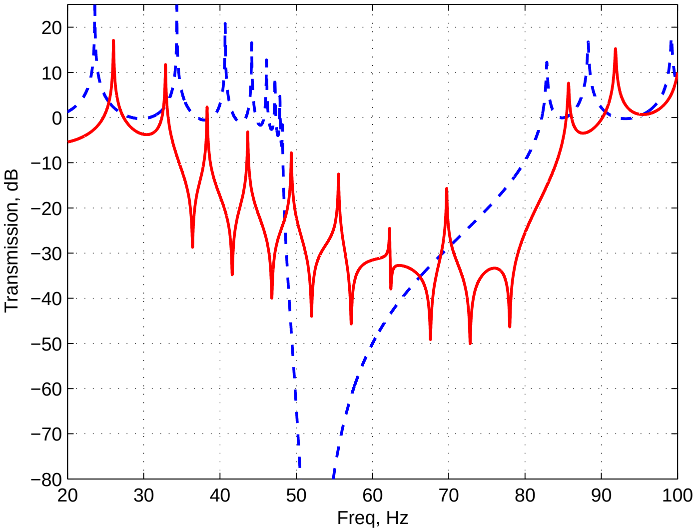

(a)

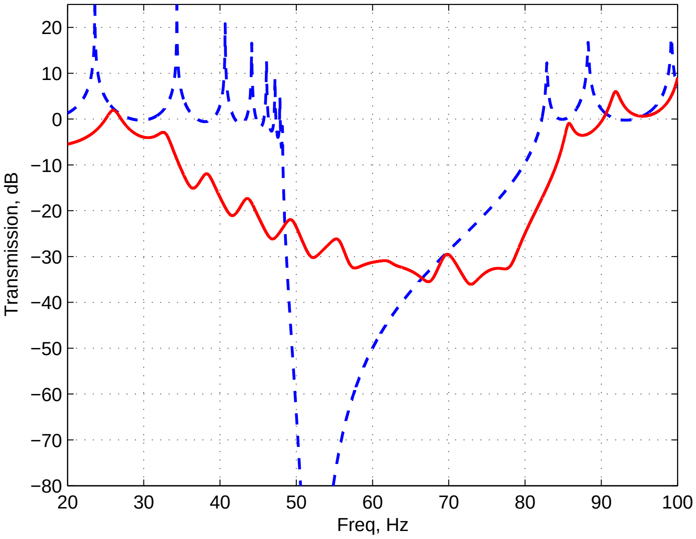

(b)

Figure 2.8: (a) Transmission response of a 10-layer, staggered resonator local control material where the step-size frequency gap between resonators is set to 10% of the passive natural frequency, with the active damping constant, $c_c = 0.1$ (red) compared to a material with identical resonator frequencies (dotted blue). (b) The same material with the active damping constant increased to $c_c = 1$

material poses some potential problems. It is not clear at what intervals the resonators should be spaced in frequency to achieve the optimum band gap. Too narrow and the material is not attenuating in the widest possible frequency range, too wide and resonant peaks start to appear in the spaces between the resonators natural frequencies, as shown in Figure 2.8a. In addition, achieving a level of symmetry, possibly a desirable characteristic in the band gap profile, is not trivial due to each resonators individual asymmetric profile. These undesirable characteristics can be tempered by adding additional damping using the c_c coefficient, shown in 2.8b, however this will require greater control force and the bandwidth of the attenuating region remains modest. Greater performance can be achieved by taking a more sophisticated control approach than the static, local controllers considered here, and will be investigated as part of Chapter 4

2.6 Conclusion

The viscoelastic metamaterial presented in this section was designed using a lumped parameter analogy of a ducted array of Helmholtz resonators. It was shown that passively this metamaterial is single negative, exhibiting negative effective mass, and has a deep, asymmetric band gap at the natural frequency associated of the resonant elements. The location of the band gap can be manipulated using a local control strategy. In addition, using a distributed control strategy it is possible to couple the motion of the resonator elements to mass elements of adjacent cells, creating a dispersive effective stiffness and therefore allowing the material to become double negative at resonance. This work has also been described by Pope and Daley [12].

The DNG behaviour and high levels of attenuation available from the low frequency band gap mean that the material has potential applications in acoustic cloaking, superlens and isolation scenarios. However, the success of the material in these applications is dependent on their scalability (particularly for cloaks and lenses) and advantages over current technologies (for the case of isolation applications). In this chapter the physical form factor has been explored by investigating the orders of displacements experienced by the material elements, and the active forces required to create the local and distributed control strategies. It was shown that elemental displacement around the resonant band gap can be reduced by increasing the number of layers of the material, and therefore the material can be scaled to smaller form factors. Smaller displacements also result in smaller feedback forces being required, suggesting that such materials would be advantageous over existing active isolation technologies. By adjusting the control gains as a function of the layer of the material, it is possible to ’smear’ the band gap over a wider frequency range.

However, the model presented in this section is not without its shortcomings. The bandwidth achievable by actively staggering the resonator frequencies is modest, and a strategy for optimally tuning these constants is not trivial. In addition, the material requires the application of point forces to masses, normally achievable using inertial actuators. This introduces additional complexity and limitation into the design of the material; the force delivered by an inertial actuators is related to its size, and smaller actuators will tend to have a higher natural frequency, below which they are ineffective - This limits the scale of the material. In addition, the potentially large displacements of the resonator elements may approach that of the inertial element of the actuator. In this scenario the actuator can no longer be considered to be delivering a pure force, but is instead must be considered as additional mass and stiffness elements coupled to the material model. Therefore an alternative method of delivering active feedback forces would be preferable.

These shortcomings are addressed in Chapter 3, where the material is developed further to deliver active control through reactive forces rather than point forces, and Chapter 4, where control strategies are developed to increase the performance of the resonant band gap. Additionally, it is noted that the distributed control method to attain DNG behaviour was shown to be unstable by Pope *et al* [74]. Whilst Pope *et al* addressed these issues in their work it would be preferable if the material exhibited a double negative region passively, one that could then be manipulated using active control techniques. Therefore the new metamaterial presented in Chapter 3 has passive coupling, allowing the material to achieved double negativity passively.

Chapter 3

Coupled Viscoelastic Metamaterial Design

3.1 Introduction

Chapter 2 introduced the metamaterial structure first investigated by Pope and Daley [12], who showed that such a material would be SNG, but could be made to be DNG with the addition of active elements that couple the motion of the resonator masses to the adjacent transmission layers of the material. The results from Chapter 2 also demonstrate that using a periodic metamaterial structure within an active isolation scenario has advantages over a traditional single layer approach, producing smaller element displacements and lower individual active forces, meaning that the form factor of the material could be reduced. However, the previous chapter dealt only with the theoretical material structure, and acknowledges that there would be practical challenges into realising such a metamaterial.

The work presented in this chapter develops the metamaterial further to address these issues and produce a practical metamaterial design for production. Additional passive viscoelastic connections are incorporated, inspired by the distributed active approach from Pope and Daley and investigated in Chapter 2, to produce a material which achieves double negativity passively. The active control architecture is also adjusted to incorporate reactive forces rather than point forces, simplifying the control architecture design and removing the need for inertial actuators. The presence of a resonant band gap and double negativity is confirmed through the theoretical model, and a novel wavenumber based approach for determining the width and form of the band gap is developed and the condition for a wide, symmetric band gap identified. Next, the concept is developed into a practical experimental design, which is then produced using steel machining techniques, and the passive isolation performance is confirmed within the laboratory.

The viscoelastic metamaterial design presented here and in Chapter 4 is an original approach to creating a vibration isolation device, and is the subject of a patent (pending, application number GB1304500.0).

3.2 The Coupled Metamaterial Structure

The metamaterial model described in Chapter 2, referred to as the ’uncoupled viscoelastic metamaterial’, was based on a lumped-parameter mechanical analogue of an array of Helmholtz resonators within a duct. The resulting viscoelastic metamaterial is identified as a potential building block within an acoustic cloak or superlens, or for use in vibration isolation applications, however several shortcomings with the design are highlighted in 2.6. For the purposes of creating an experimental realisation of a metamaterial and to address some of these shortcomings the model was developed further and the resulting alternative metamaterial is presented within this section.

Whilst Pope and Daley demonstrated that a distributed control strategy produced double negative behaviour in the uncoupled metamaterial, it was later shown by Pope *et al* [74] that this original approach was unstable. This is readily addressed, and indeed was resolved in [74] however it would be preferable if the material exhibited a double negative region passively; one that could then be enhanced using active control techniques. For the material presented in this chapter, building on the logic of the distributed active control strategy employed in Chapter 2, additional passive viscoelastic connections are used to couple each resonator element to the transmission mass in the adjacent cell as well as its own, such that each resonator mass now has two spring connections. This is shown to create the required dispersive effective stiffness.

In addition, the uncoupled design required point forces which would require inertial actuators, the desire to scale the material down in the future and the requirement to effect control at low frequencies make the use of inertial actuator impractical, as described in Section 2.6. Therefore the structure has been adapted to facilitate the ready incorporation of reactive control forces, applied between resonator masses, so each force is now incident on two resonator masses. This simplifies the implementation of active control on the model at the expense of restricting the nature of the control forces that can be applied. This new structure is referred to as the ’coupled’ viscoelastic metamaterial, and is pictured in Figure 3.1a.

As before, m_t, k_t, and c_t are the mass, stiffness and damping components respectively of what is considered the transmission elements of the material, and m_r, k_r and c_r are the mass, stiffness and damping elements of what are considered the resonator elements. However, like the distributed control active material presented in Chapter 2, the coupling

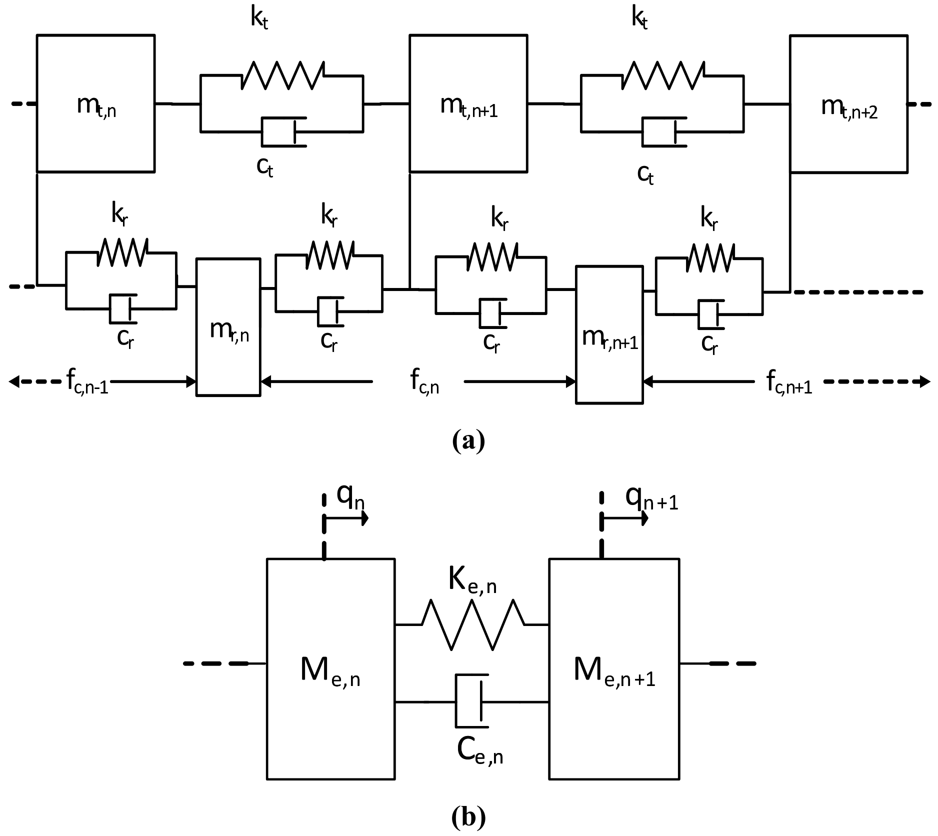

Figure 3.1: (a) Lumped parameter model of the coupled viscoelastic metamaterial. (b) A simple chain of equivalent masses and viscoelastic connections

of the resonator elements to multiple transmission elements means that the material can no longer be considered as a simple chain of masses fitted with vibration absorbers, and therefore the distinction between the transmission path and resonator elements is blurred somewhat. However, as will be shown in this section, the principles of operation and the dynamic response of the material retains the desirable band gap properties of the 'uncoupled' material. To provide active control reactive forces are applied between the resonator elements, denoted by f_c.

As before, the material can be considered as the equivalent chain of masses connected by viscoelastic connections shown in Figure 3.1b, the equation of motion of which can be written as Equation 3.1.

$$-\omega^2 M_e q_n + (j\omega C_e + K_e)(2q_n - q_{n+1} - q_{n-1}) = f_n \tag{3.1}$$

By formulating and rearranging the equations of motion for the explicit material model in Figure 3.1a yields Equation 3.2. The detailed derivation of this is contained in Appendix A

$$\begin{aligned} &-\omega^2\left(m_t+\frac{2m_r(k_r+j\omega c_r)}{-\omega^2 m_r+2(k_r+j\omega c_r)}\right)q_n\dots \\ &\qquad +\left(k_t+j\omega c_t+\frac{(k_r+j\omega c_r)^2}{-\omega^2 m_r+2(k_r+j\omega c_r)}\right)(2q_n-q_{n+1}-q_{n-1})=f_n \end{aligned} \tag{3.2}$$

Comparing these two expressions it is evident that the effective mass, M_e and stiffness and damping $K_e{+}j\omega C_e$ are given by

$$M_e=m_t+\frac{2m_r(k_r+j\omega c_r)}{-\omega^2 m_r+2(k_r+j\omega c_r)} \tag{3.3}$$

$$K_e+j\omega C_e=k_t+j\omega c_t+\frac{(k_r+j\omega c_r)^2}{-\omega^2 m_r+2(k_r+j\omega c_r)} \tag{3.4}$$

These expressions are complex, where Im(M_e) is an additional dissipative term introduced by the presence of damping within the resonator elements, whilst Re(M_e) is the effective inertial mass of the system and the quantity of interest. Likewise the real part of $K_e+j\omega C_e$ is the effective stiffness of the system, with the imaginary part being the dissipative effective damping. The purely real effective mass and stiffness of the system are therefore

$$\text{Re}(M_e)=m_t+\frac{4k_r^2 m_r+\omega^2(4c_r^2 m_r-2k_r m_r^2)}{m_r^2\omega^4+4\omega^2(c_r^2-k_r m_r)+4k_r^2} \tag{3.5}$$

$$K_e=k_t+\frac{2k_r^3-m_r\omega^2(k_r^2-c_r^2\omega^2)+2c_r k_r\omega^2}{m_r^2\omega^4+4\omega^2(c_r^2-k_r m_r)+4k_r^2} \tag{3.6}$$

The dissipative terms are then

$$\text{Im}(M_e)=\frac{-(2c_r m_r^2\omega^3)}{m_r^2\omega^4+4\omega^2(c_r^2-k_r m_r)+4k_r^2} \tag{3.7}$$

$$C_e = j\omega c_t + \frac{2j\omega c_r(c_r^2\omega^2 + k_r^2 - m_r k_r \omega^2)}{m_r^2\omega^4 + 4\omega^2(c_r^2 - k_r m_r) + 4k_r^2} \tag{3.8}$$

In contrast to the uncoupled passive system presented in Chapter 2, both terms for the effective stiffness and mass for this coupled material are now dispersive. Both of these two equations have the same denominator, and therefore 'resonate' at the same frequency. This means the effective mass and stiffness can become negative simultaneously, allowing the material to become DNG. The behaviour of a typical passive coupled metamaterial has been calculated in the Following sections of this Chapter using the parameters in Table 3.1. The transmission response (the motion of the last transmission mass related to the first) of a 4 layer metamaterial, including the sign of each of the material parameters is shown in Figure 3.2 along with the Bloch dispersion relationship.

	Parameter	Value
Transmission Media	m_t	$0.553kg$
	k_t	$282353Nm^{-1}$
	c_t	$0.1Nsm^{-1}$
Resonators	m_r	$0.671kg$
	k_r	$76667Nm^{-1}$
	c_r	$0.1Nsm^{-1}$

Table 3.1: The material parameters used to simulate the response of a typical coupled viscoelastic metamaterial

Comparing the coupled material response to the uncoupled material from Chapter 2 and it is clear that the coupling, whilst producing DNG behaviour, has not hindered the desirable band gap properties - the high levels of attenuation at resonance is retained, caused by the imaginary part of the dispersion relationship becoming large in magnitude. As with the calculations from Chapter 2, note that this is calculated using a $\cos^{-1}$ function, and therefore the domain of the real part is restricted to $0 \leq \text{Re}(kd) \leq \pi$. In reality the dispersion relationship is not bound in this way and can span multiple 'branches' of this function.

3.3 Finite and Inhomogeneous viscoelastic metamaterials

When the physical properties of the metamaterial vary in different transmission units, the transfer matrix method described in Section 2.3 can still be adopted to study wave

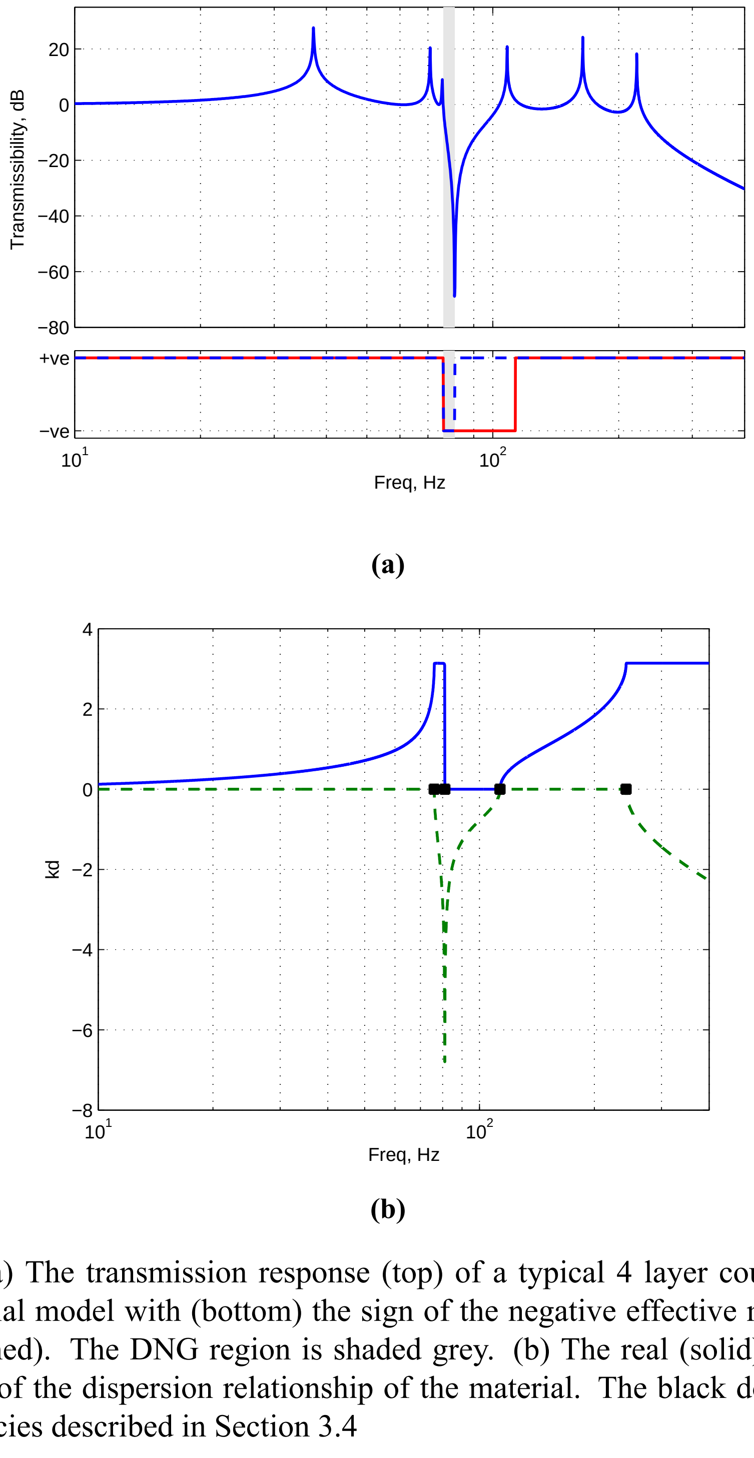

(a)

(b)

Figure 3.2: (a) The transmission response (top) of a typical 4 layer coupled viscoelastic metamaterial model with (bottom) the sign of the negative effective mass (solid) and stiffness (dashed). The DNG region is shaded grey. (b) The real (solid) and imaginary (dashed) part of the dispersion relationship of the material. The black dots denote the 4 break frequencies described in Section 3.4

propagation behaviour through the transmission medium. And it has been demonstrated that creating an inhomogeneous material, as in Section 2.5, can create advantages in relation to broader band gap behaviour.

However, the effective material parameters described above are derived presuming a periodic material of infinite length. In reality the design illustrated in Figure 3.1a cannot be truly homogeneous because the new coupled design means that the layers at each end of the material are not the same as the middle layers. This means the effective mass of the outer layer differs from the interior layers, and is given by

$$M_e = m_t + \frac{m_r(k_r + j\omega c_r)}{-\omega^2 m_r + 2(k_r + j\omega c_r)} \tag{3.9}$$

i.e. the dispersive component of the effective mass it is half that of the interior layers. The effective stiffness and damping elements remain the same as defined in Equation 3.4. Accordingly the response of the metamaterial can still be determined using the effective material parameters with the appropriate modification to the the component of the outer layer. As N becomes large, the effect of the boundary conditions on the dynamic properties of the metamaterial becomes negligible.

3.4 Dispersion Relationship

As Figure 3.2a shows, the double negative region also coincides with the region of attenuation commonly referred to as the band gap. Previous studies have suggested that the resonant band gap occurs in a single negative region where the wavenumber, k, becomes imaginary, since this leads to an evanescent rather than travelling wave solution to the wave equation. When the material is made to be double negative, the solution becomes negative real and a passband occurs in what is now a ’left-handed’ material [51]. However, this explanation neglects dissipative losses within the material, which become large at resonance. The Bloch dispersion relationship of a the periodic metamaterial of infinite length remains the same as that given for the uncoupled material from Chapter 2.

$$\cos kd = 1 - \frac{\omega^2 M_e}{2(K_e + j\omega C_e)} \tag{3.10}$$

Here even for a DNG material, if the effective material parameters are complex themselves the result will be complex, leading to a travelling (real) wave with an attenuation (imaginary) envelope. At resonance the magnitude of imaginary terms of the effective material parameters become very large leading to high levels of attenuation.

In fact, in the case of the coupled metamaterial the wave number can become complex even in the absence of dissipative elements when $|\cos kd| > 1$. This occurs when $\alpha > 2$ or $\alpha < 0$, where $\alpha = \omega^2 M_e/(2K_e)$. Considering these conditions, combining Equations 3.10, 3.3 and 3.4 leads to 3 inequalities that define the band gap. Taking the first condition, α will be positive only if both the numerator and denominator are of the same sign, i.e. if both of the following inequalities are simultaneously true or false

$$\omega^2 < \frac{(m_t + m_r)k_r}{m_t m_r} \tag{3.11}$$

$$\omega^2 < \frac{(2k_t + k_r)k_r}{k_t m_r} \tag{3.12}$$

These expressions represent the numerator and denominator respectively. Taking the second condition, the third inequality defines where $\alpha > 2$ and can be written as a quadratic expression in ω^2

$$-\omega^4 m_t m_r + \omega^2(2(m_t + m_r)k_r + 4m_r k_t) - 4(k_r(2k_t + k_r)) > 0 \tag{3.13}$$

which has two positive solutions

$$\omega_{0,r}^2 = \frac{2k_r}{m_r} \tag{3.14}$$

$$\omega_{UL}^2 = \frac{2k_r + 4k_t}{m_t} \tag{3.15}$$

Combining 3.14 with the inequalities 3.11 and 3.12 yields two more break frequencies

$$\omega_{mid}^2 = \omega_{0,r}^2 \left(1 + \frac{k_r}{2k_t}\right) \tag{3.16}$$

$$\omega_{end}^2 = \omega_{0,r}^2 \left(1 + \frac{m_r}{m_t}\right) \tag{3.17}$$

Both the numerator and denominator of Equation 3.10 are positive as $\omega \to 0$, which allows the use of these four frequencies to describe the form of the transmissibility of the material and, crucially, determine the position and width of the band gap. $\omega_{0,r}$ would be the natural frequency of the resonator elements if they were single cells with fixed-fixed boundary conditions, and is the point at which (3.13) becomes true, denoting the lower edge of the band gap. As ω increases the left hand side of (3.13) becomes larger as the denominator governed by (3.12) becomes smaller and attenuation increases. At ω_{mid} the denominator becomes zero, $\omega^2 M_e/(2K_e)$ resonates and the band gap attenuation peaks. As ω increases further the denominator (3.12) becomes negative, α becomes negative and kd remains complex. Now the magnitude of the denominator $2K_e$ gets larger, reducing the magnitude of the α and limiting band gap attenuation. Finally, at ω_{end}, the numerator inequality (3.11) becomes false and the wave number becomes pure real, denoting the upper band gap edge. The fourth break frequency, ω_{UL}, defines the dynamic limit of the lumped parameter system, above which response rolls off as a low pass mechanical filter, and is independent of the resonator mass.

This method of wavenumber analysis provides a useful tool in determining the width and form of the resonant band gap, and from the above expressions it is clear that it is possible to adjust the total width of the band gap by adjusting the ratio of the resonator and transmission masses, and the location of the midpoint by manipulating the ratio of the resonator and transmission stiffnesses.

The four break frequencies are shown on the dispersion relationship shown in Figure 3.2b as black dots. Note there is a small discrepancy between $\omega_{0,r}$ and the onset of the band gap and ω_{UL} and the onset high frequency roll off present in the transmissibility plot, Figure 3.2a. This is due to the finite nature of the 4 layer metamaterial plotted. The wave number analysis assumes an infinite number of material layers, and as previously described the effective material parameters of the first and last layers differ slightly from Equations 3.3 and 3.4 and effect the transmission performance. As the number of layers, N, increases these onset frequencies tend towards the calculated values given by Equations 3.14 and 3.15, as demonstrated by the transmissibility of a 20 layer metamaterial, shown in Figure 3.3. Note that the first two break frequencies coincide with the edges of the double negative region.

3.4.1 Significance of the Relationship Between the Band Gap Frequencies and the Onset of High Frequency Roll-Off

As described above, by examining the dispersion relationship of the material it is possible to describe the band gap location and profile using the variables $\omega_{0,r}$, ω_{mid} and ω_{end}, and

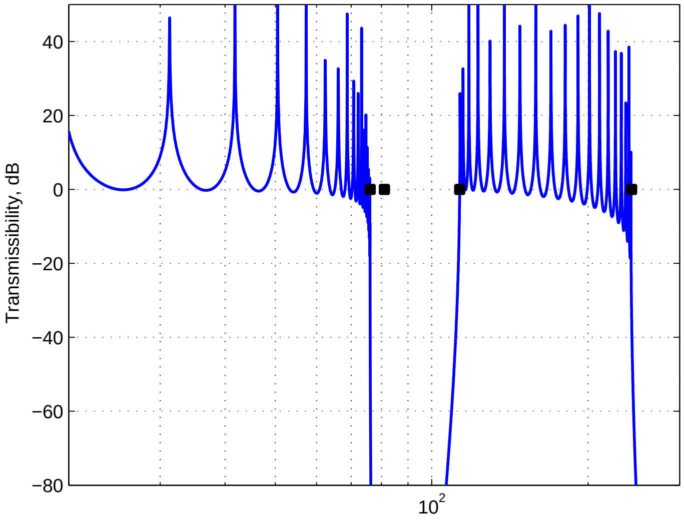

Figure 3.3: The calculated transmissibility of a coupled metamaterial consisting of 20 layers, with the calculated break frequencies marked with black dots

the frequency above which high frequency roll off occurs using ω_{UL}. In its 'normal' mode of operation, one would expect that the band gap be tuned such that $\omega_{0,r} < \omega_{mid} < \omega_{end} < \omega_{UL}$, although this does not need to be the case. However, depending on the location of the band gap in relation to the onset of high frequency roll-off the shape of the band gap changes.

Consider the transmissibility of four examples of the coupled metamaterial, each where the value for k_t is reduced relative to the previous case. The transmissibility of four such materials, each consisting of 4 layers, is shown in Figure 3.4a. As the Figure shows, the onset frequency of the band gap, $\omega_{0,r}$, remains constant, as would be expected from Equation 3.14. The mid-point and end-point frequencies however, increase, widening the band gap, and creating a more symmetrical profile. Examining Equation 3.17, this increase in band gap end-point appears to contradict the equation for ω_{end}, however it is important to remember that the calculated break frequencies are for a material of infinite layers - for a material of few layers the inhomogeneity makes the equations are less accurate and it is this that leads to this discrepancy. Figure 3.4b shows the same scenario with metamaterials consisting of 20 layers, which all share the same value for ω_{end}.

A key result is shown by the light blue response, where the band gap is wide and

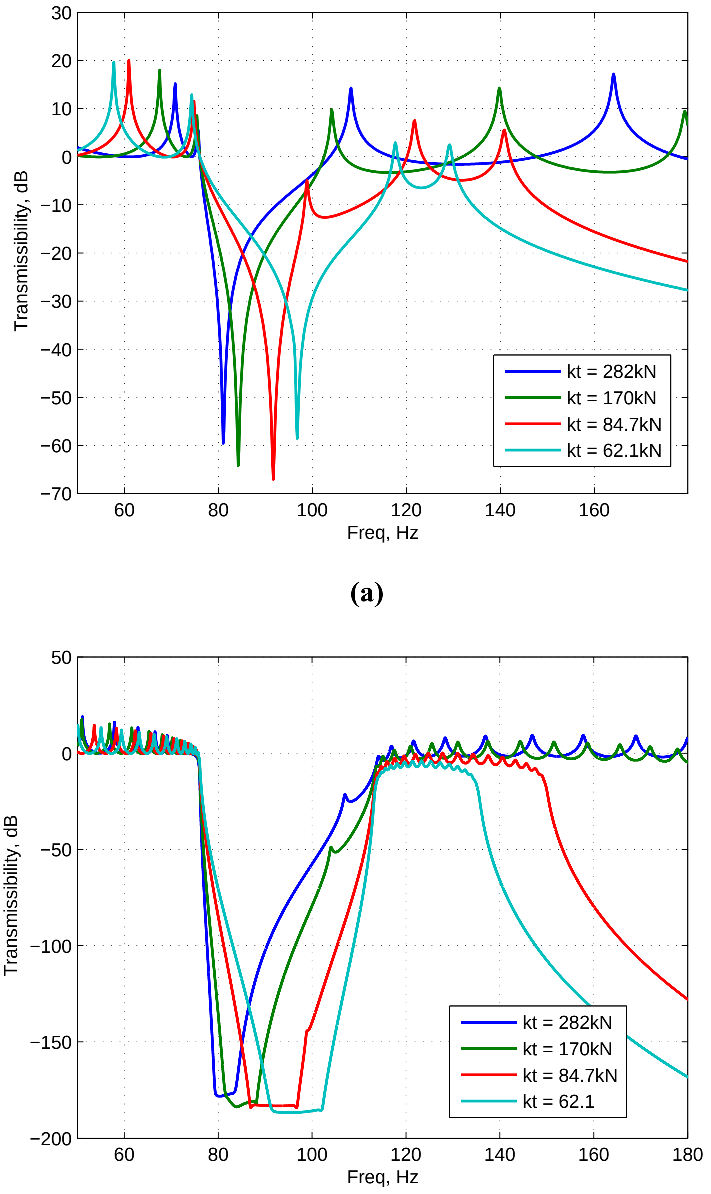

(a)

(b)

Figure 3.4: (a) A comparison of the transmissibility 4 metamaterials consisting of 4 layers, with decreasing values of k_t and (b) The transmissibility of 4 metamaterials again, with decreasing values of k_t, but consisting of 20 layers.

symmetrical. In this case the metamaterial has been tuned such that $2k_r/m_r = 2k_t/m_t$. This scenario can be considered as being when the natural frequency of a resonant element with fixed-fixed boundary conditions ($\omega_{0,r}$) is equal to the natural frequency of a transmission element with fixed-fixed boundary conditions. In a phononic crystal based metamaterial the Bragg scattering based band gap occurs when the wavelength of the incident sound coincides with twice the periodic constant, $\lambda = 2d$. It has been shown by Xiao *et al* [4] among others that when the Bragg gap of a metamaterial is tuned with to coincide with the (often narrow and asymmetrical) resonant band gap then the two couple together to create a wide, symmetrical band gap. In the lumped parameter model used for the coupled metamaterial the concept of a periodic constant and wavelength do not apply, since the model has no physical dimensions or sound speed. However, it seems reasonable to equate the natural frequency of a single fixed-fixed transmission cell with the 'natural wavelength' of a single layer of a periodic crystal. Therefore the phenomenon shown here can be considered analogous to the behaviour seen in phononic crystal based metamaterials when the Bragg and resonant band gaps are coupled to create a wide, symmetric 'super' band gap.

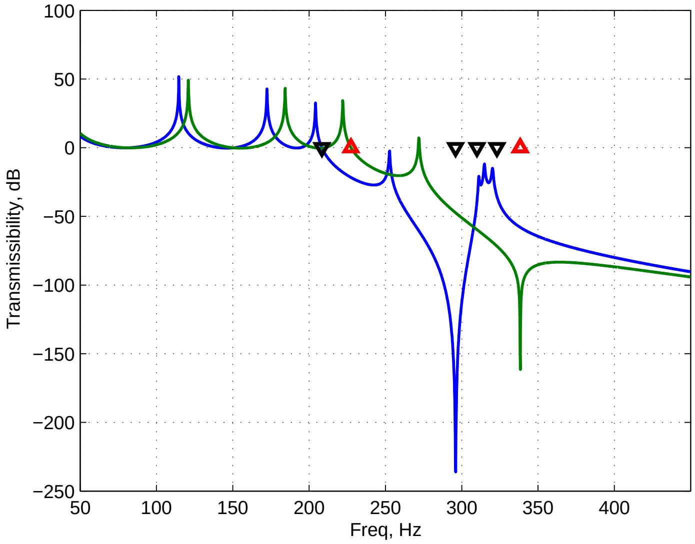

Figure 3.5: The transmissibility of 4 layer metamaterials where the band gap is tuned above the Bragg 'coupling point' (blue) and such that ω_{mid}, ω_{end} and ω_{UL} are equal (green). The break frequencies for the metamaterials are denoted by the black and red triangles respectively

As the band gap frequency is increased higher, above this Bragg 'coupling point', the difference between the band gap frequency and high frequency roll off point, ω_{UL}, reduces further. The band gap mid point and end points begin to converge, making the band gap narrow and asymmetrical once more with a form that is a mirror image of band gaps tuned below this Bragg point, behaviour shown by the blue line of Figure 3.5, with 4 break frequencies denoted by black triangles. Again this behaviour was noted by Xiao *et al* in phononic crystals at frequencies above the Bragg frequency. Eventually, as the band gap frequency increases higher, a point is reached where ω_{mid}, ω_{end} and ω_{UL} are all equal. At this scenario the band gap all but disappears into the high frequency roll off region of the material, and the metamaterial would no longer function in its intended purpose, as demonstrated by the green line of Figure 3.5. The break frequencies are shown as red triangles; since 3 of the break frequencies overlap, in this case only 2 triangles are visible. By equating Equations 3.16, 3.17 and 3.15 a quadratic equation is derived the roots of which are given by Equation 3.18, the positive root of which is this high frequency limit of operation of the metamaterial.

$$k_{r,limit} = \frac{-2(m_r^{-1} - m_t^{-1}) \pm \sqrt{4(m_r^{-1} - m_t^{-1})^2 + 16(m_r m_t)^-1)}}{2(k_t m_r)^{-1}} \tag{3.18}$$

3.5 Design Concept of an Experimental Coupled Metamaterial

Using this model as a basis, an experimental demonstrator concept was developed to achieve the dynamic behaviour of the model whilst fulfilling certain design objectives. The ideal material concept would be flexible enough to incorporate multiple, parallel resonators attached to each transmission mass; something that could be desirable in future iterations. It must also be able to be utilised as both a passive and an active material. As metamaterials development continues towards a commercially viable solution it will be necessary to create a higher density of resonant elements and increase the degrees of freedom. As densities increase conventional manufacturing techniques are impractical on such scales, and additive layer manufacturing (3-dimensional printing) is likely to be a viable solution. Therefore the concept was designed for existing additive layer manufacturing techniques to be printed in titanium. (A prototype was produced, however it became clear during production that the 3D printing technology currently

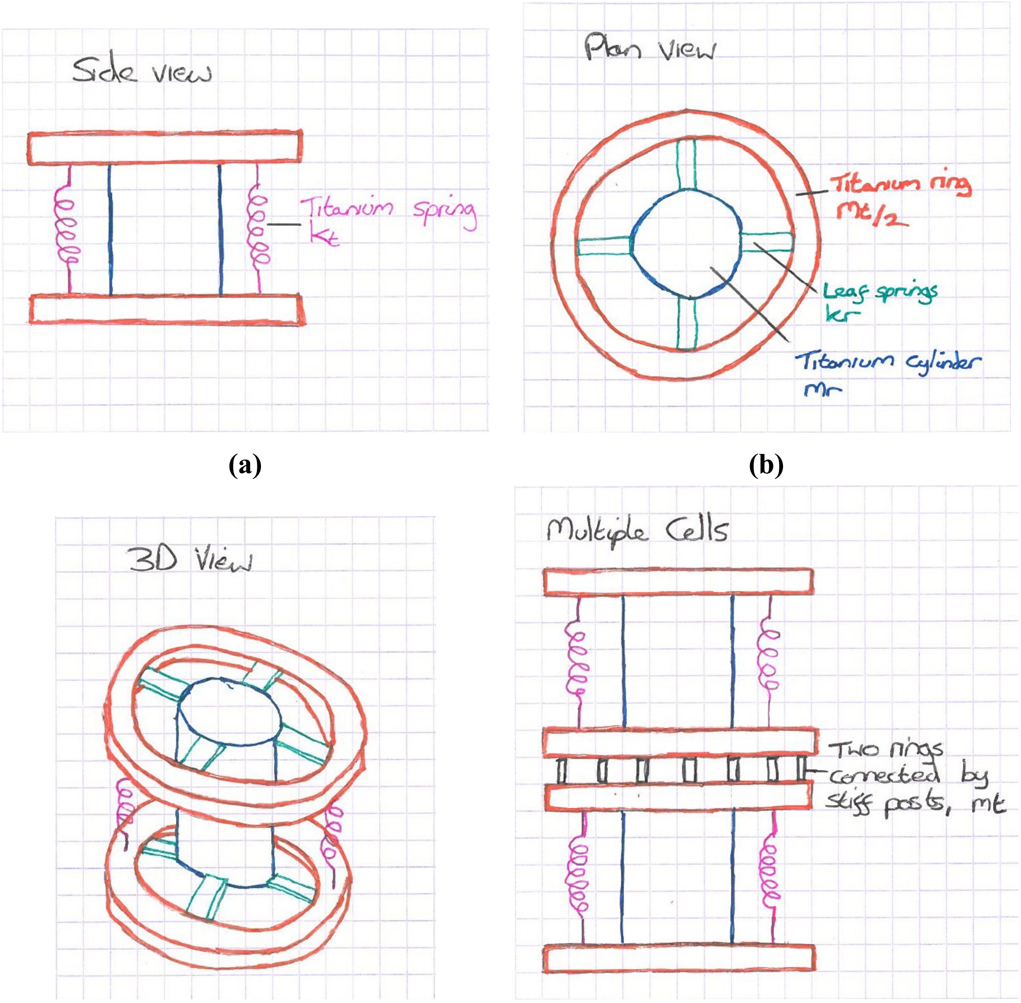

(a) (b) (c) (d)

Figure 3.6: Sketches of the coupled metamaterial production concept, plan view of a cell (a), side view of a cell (b), 3-dimensional view of a cell (c) and multiple cells connected together (d)

available was not sufficiently advanced, and several production problems were experienced, therefore the final metamaterial was produced from mild steel using traditional machining techniques, as described in Section 3.6. Therefore, whilst the concept design described here features integrated coil springs, in the final production these were replaced with purchased, natural rubber springs.)

The original concept sketches of the design are shown in Figure 3.6 (CAD representation of the final design were developed later for production). The concept consists of a chain of double metal discs which act as the transmission masses; these discs are separated by coil springs, which provide a viscoelastic connection, k_t and c_t , whilst maintaining separation between the layers to accommodate the resonant elements. Each transmission disc is connected to a resonant element via leaf springs, providing the k_r and c_r elements through their lateral stiffness and inherent damping.

Each transmission layer consists of two metal discs bolted together. This configuration allows a modular production of cells, with each cell consisting of a resonant mass connected to a transmission ring, $m_t/2$, at each end. This modular construction facilitates easy access between cells to fit and access reactive actuators, and in addition, should extra space be required to accommodate the displacement of the resonant elements, posts/washers can be used in lieu of regular bolts to separate the two discs. Once these cells are connected together the two connected discs make up a single m_t element. Additional free standing discs can be bolted onto each end of the metamaterial to bring the first and last transmission masses up to the appropriate weight. As well as the production convenience of the modular configuration, it means that materials of different numbers of layers can be constructed easily without the need to produce each metamaterial separately.

Since the dynamic behaviour of interest is governed by the mass and stiffness elements, the material dimensions were chosen to coincide with the desired m and k values, with damping in the material being purely a function of the inherent damping within the metal elements. The proposed configuration has the additional advantage of enabling the resonator masses to be greater than the transmission masses thereby facilitating the achievement of negative effective material parameters. The design was also developed to have the form of and functionality of a vibration isolation mount that could readily be extended for practical application. It is also feasible that MDOF resonators could be incorporated into each layer, as shown in Figure 3.7, which would

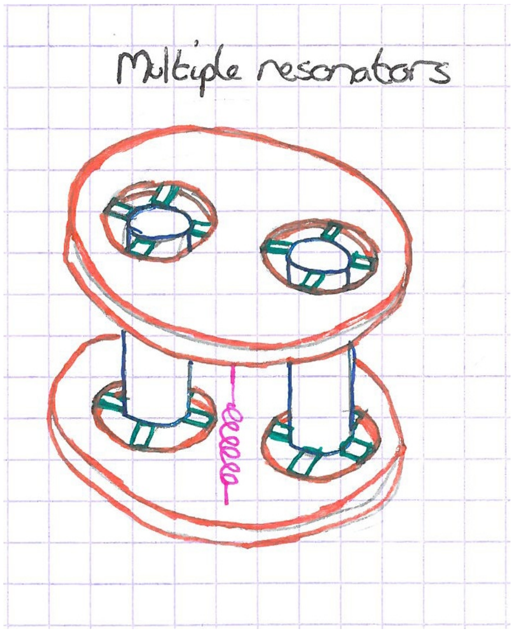

Figure 3.7: A modification to the design would allow multiple parallel resonators

lead to a broader passive region of attenuation, as described in 2.5.

3.6 Metamaterial Design For Production

The dimensions of the experimental demonstrator were chosen to provide a low frequency band gap and region of double negativity, taking into account additional mass of the actuators and to provide a dimensions within the capability of currently available manufacturing processes. The original concept design described in Section 3.5 was developed with 3D printing technology in mind, however an initial attempt was made to produce a metamaterial out of titanium using laser sintering based additive layer manufacturing met with limited success. The limitations of the technology at present make it unsuitable for the production of the metamaterial design, therefore it was decided to produce the metamaterial using traditional steel machining techniques. This means the final design differs from the concept design in that commercially available rubber springs are used in place of the coil springs for the k_t and c_t viscoelastic elements.

The dimensions chosen for the transmission elements are detailed in Table 3.2, and the resonator elements in Table 3.3. The resonator stiffness elements k_r are governed by the stiffness of the leaf springs, which are calculated using Equation 3.19 [84].

Transmission disc outer radius, m	Transmission disc inner radius, m	Transmission disc thickness, m
0.080	0.060	0.004

Table 3.2: Dimensions of the transmission elements

Width of leaf spring, m	Thickness of leaf spring, m	Length of leaf spring, m	Radius of resonator cylinder, m	Height of resonator cylinder, m	Number of leaf springs
0.010	0.001	0.030	0.030	0.030	4

Table 3.3: Dimensions of the resonator elements

Material layers, N	m_t, kg	k_t, N/m	m_r, kg	k_r, N/m	Band gap frequency, Hz
4	0.27	280000	0.36	43000	$\sim$ 85

Table 3.4: Resulting material properties of the experimental metamaterial

$$k_{leaf} = \frac{3E_S I_b}{l_b^3} \tag{3.19}$$

where E_S is the Young's modulus of steel, l_b is the length of the beam element, and the second moment of area of the beam, $I_b = w_b t_b^3/12$, where w_b and t_b are the width and thickness of the beam respectively. The values for transmission and resonator stiffness were chosen using Equations 3.14-3.17 from Section 3.4 to provide a low frequency band gap whilst ensuring the high frequency limit ω_{UL} is sufficiently high. The resulting material properties are contained in Table 3.4. The rubber springs used were AVA 164/20 rubber mounts, with 4 springs used per transmission layer. The 164/20 rubber mount has one male, one female thread connection, and is quoted by the manufacturer as being the same in composition as the 164/1 which has 2 male connections. The 164/1 mount has an individual stiffness of approximately 71kN/m, however the manufacturers say in the datasheet that mountings with female fixings 'tend to be considerable stiffer than those with male fixings', therefore the actual stiffness of the mounts used is unknown and a nominal stiffness of 71kN/m is used for simulations. The datasheet for the rubber mounts is included in the Appendix E.

The resulting *passive* metamaterial response, along with the regions of negative effective mass and stiffness, are shown in Figure 3.8. Note the band gap profile has a 'double spike' at its lowest point, this is due to the resonator containing the coils and the resonators containing the magnets have slightly different masses, however the effect is

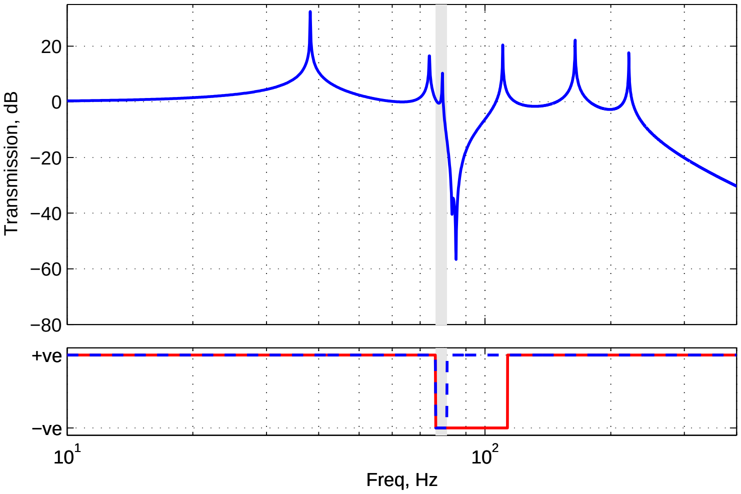

Figure 3.8: The modelled passive transmission response of the coupled viscoelastic metamaterial experimental design

small.

3.7 Manufacture of the Experimental Demonstrator

The material was produced as 3 cells in machined steel such that each cell consists of 2 discrete steel halves connected together. The cells then bolt together to produce a continuous, periodic material. The resonator masses contain hollows to accommodate voice coil type reactive actuators, such that control forces can be applied. The cell designs were produced using the `Solidworks` three dimensional Computer Aided Design (3DCAD) package.This 3D representation was then used to export 2D drawings from which production could take place. The translation from the 2D engineering drawings to a finished steel product was undertaken by the Engineering Design and Manufacturing Centre at the University of Southampton. Some representative images showing more detail of the design can be seen in Figure 3.9.

The overall demonstrator design is comprised of three cells with four transmission plates and three resonators. The resonator mass in the upper and lower sections has a large recess to take the body of a voice coil that will provide the active force that reacts between adjacent resonator masses.

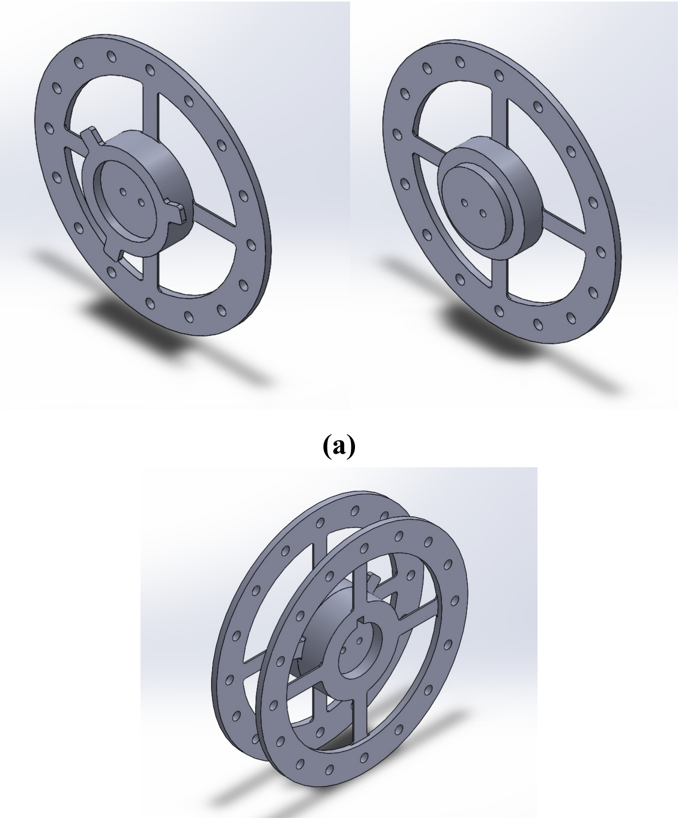

(a)

(b)

Figure 3.9: 3DCAD representations of the metamaterial design. (a) A single cell produced in two sections which are bolted together. (b) Shows an assembled cell

3.8 Post Manufacture Machining and Assembly

To provide active functionality, reactive actuators were fitted into the resonator elements. The 4 layer metamaterial has 3 resonant elements and requires 2 actuators. Reactive actuators consist of 2 parts, a coil and a magnet. The middle resonator element is connected to the coil elements of both actuators, whilst the magnets are connected to the top and bottom resonators. The top and bottom resonators are hollowed out so the magnets are hidden within the resonator body, whilst the middle resonator is also shaped to accommodate some of the coil housing. Due to the additional weight of the magnet/coil, this hollowing has a negligible effect on the total weight of the resonator masses.

The model of actuator used in the material is the LVCM-032-025-02 manufactured by

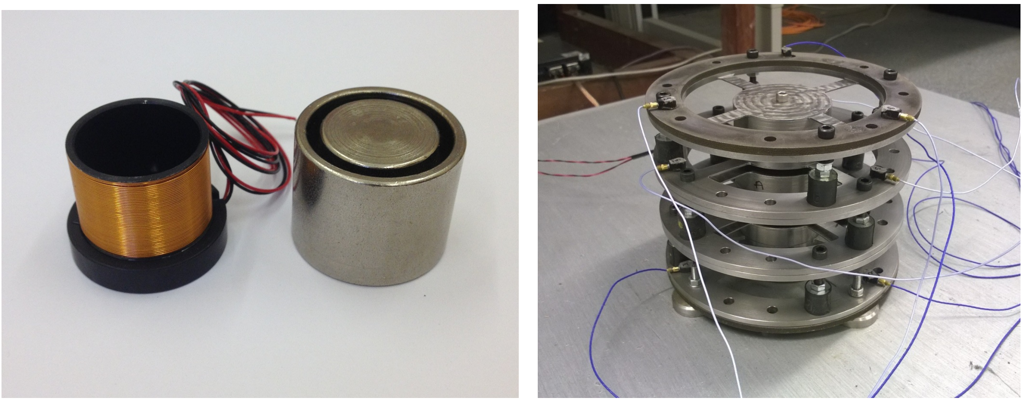

(a) (b)

Figure 3.10: (a) The LVCM-032-025-02 actuator used for active control, consisting of separate coil (left) and magnet (right) sections. (b) The fully assembled metamaterial. Note the attached accelerometers positioned at 120 degree intervals for testing

Moticont. This is shown in Figure 3.10a and a datasheet is included in Appendix D. The fully assembled viscoelastic metamaterial is shown in Figure 3.10b. The assembly also has provision for 21 accelerometers to be fitted (3 for each transmission mass and 3 for each resonator mass) for control and monitoring purposes.

3.9 Evaluation Method

To perform transmission testing of the metamaterial, the assembled unit is attached to the centre of a heavy steel plate approximately 10mm thick. Fitted to the centre of the underside of the plate is an inertial shaker. The resonant frequency of the inertial shaker is approximately 40Hz which sets the lower frequency limit of the measurements, since the shaker is inefficient at frequencies below this and cannot impart enough energy into the structure to achieve an acceptable signal level. The bottom and top transmission plate of the material are fitted with 3 accelerometers, positioned 120 degrees apart. Orientating the accelerometers in this way allows the vertical motion of the plate to be extracted merely by taking the average of the 3 measured signals (and thereby decoupling the axial motion from rotational modes). The 2 higher order rotational modes can also be measured by combining the signals using simple trigonometry, detailed in Appendix C.

A dSPACE rapid prototyping system is used to excite the steel plate via the inertial shaker and to capture the accelerometer signals so that a transfer function between the motion of the bottom and top layers can then be constructed from the recorded time series. The dSPACE unit also allows active control to be applied with real-time capture of the accelerometer signals, processing these signals according to the appropriate algorithm, and application of a control signal to the actuators within the resonator masses. The application of active control to the metamaterial will be explored in Chapter 4; the rest of this chapter shall focus on the passive performance of the metamaterial. The full measurement set up is Figure 3.11. The disturbance signal used for passive measurements was white noise, which is band limited to 1kHz using a reconstruction filter.

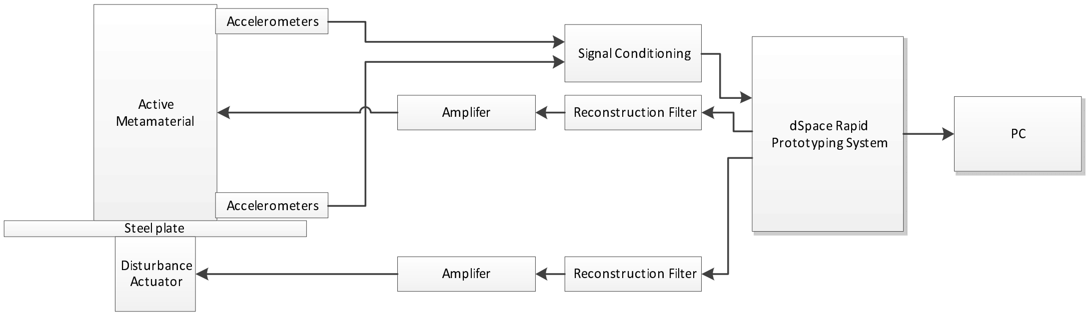

Figure 3.11: A block diagram of the measurement setup

3.10 Passive Metamaterial Response

3.10.1 Transmissibility

The open loop transmissibility is determined by calculating the transfer function between the acceleration measured at the first transmission mass to the acceleration at the last transmission mass as a result of a white noise disturbance being placed through the disturbance actuator. The measured transmissibility is shown by the blue line in Figure 3.12a, and the coherence between the vibration at the two plates is shown in Figure 3.12b. The measured response has a deep resonant band gap situated around 170Hz, and a high frequency roll-off occurring above 400Hz as the material acts as a low pass structural filter. The band gap and roll off frequency are higher than the values for $\omega_{0,r}$ and ω_{UL} predicted by Equations 3.14 and 3.15.

The discrepancy in the predicted and achieved band gap frequencies is perhaps not surprising. Of particular consequence is the specification of the leaf springs, the stiffness of which is very sensitive to the thickness of the springs ($k_r \propto t_b^3$) and the length

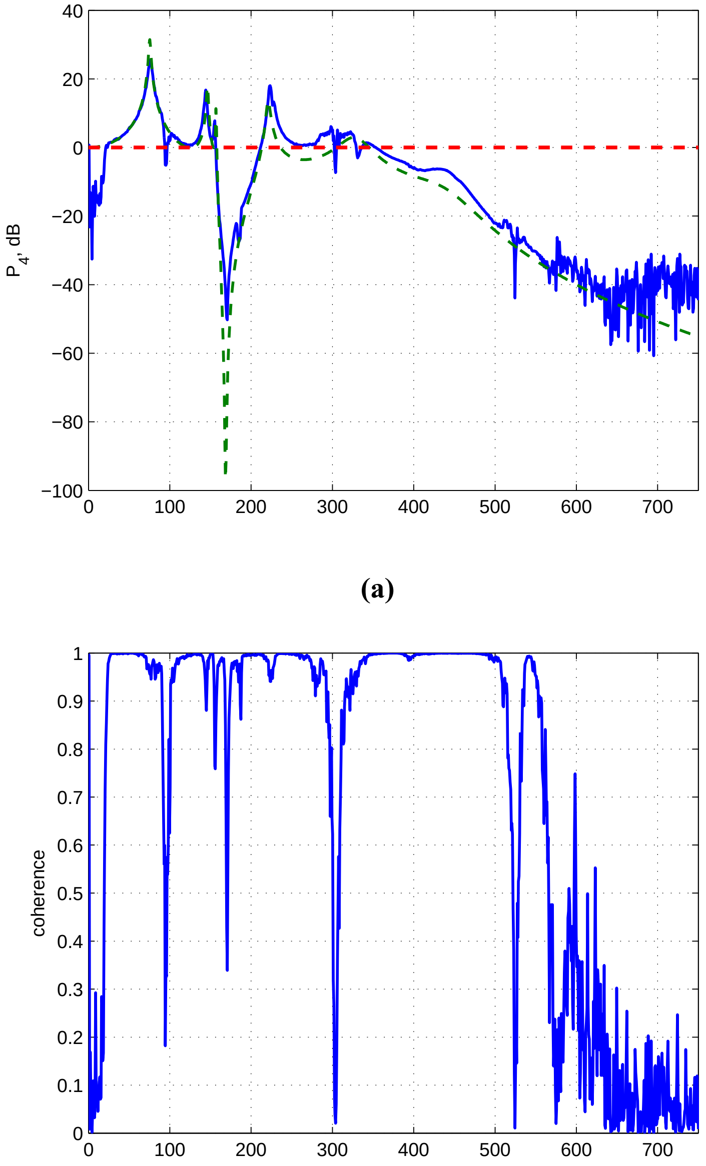

(a)

(b)

Figure 3.12: (a) Measured vertical transmissibility of the metamaterial (blue) compared to the response of the model adapted for best fit (green dotted). (b) Coherence between the vibration measured at the first and last transmission plate

($k_r \propto 1/l_b^3$). The thickness of the leaf springs have been produced to specification, however there is a degree of tolerance in their manufacture. Perhaps more importantly, the beams are specified to be 30mm in length, however it was necessary in their manufacture to include a radius at their termination points at the resonator and transmission masses, meaning their effective length is shorter than this, increasing their stiffness. The specified stiffness of the rubber mounts is provided by the manufacturer as a guide only, and it was noted that since the rubber bungs used have a female thread connection, they will be stiffer than that given in the datasheet. In addition when assembling the material care was taken to ensure that the rubber springs were tightened such that the transmission layers were parallel, the leaf springs not pre-deformed or slanted, and the rubber springs where not twisted, however these are all sources that could lead to an increase in the actual stiffness of the transmission and resonator stiffness elements. Lastly, the material parameters for steel are variable, and can change depending on the grade of steel used, therefore the value used in the model may not be an exact match for the material used.

The green dotted line of Figure 3.12a shows the response of the metamaterial model where the k_t and k_r values have been changed to best fit the measured data. Which was achieved by reducing l_b (the length of the leaf springs) to 22mm from 30mm, and increasing their thickness from 1mm to 1.15mm. Accounting for a 4mm radius at each end of the leaf springs, manufacturing tolerances, uncertainty about the properties of steel and slight twisting or warping that may have occurred in construction this seems a reasonable adjustment, and highlights the sensitivity of the leaf spring stiffness to its dimensions. The stiffness of the rubber mounts was changed from a nominal 71kN/m to 350kN/m, 5 times larger. This is a large change, however, as stated in Section 3.6, the manufacturers state that rubber mounts with female connections are 'considerably stiffer' than the nominal values for mounts with male connections given in the datasheet, and therefore could lie within the manufacturers tolerance.

The coherence of the measurements is close to 1 across a large portion of the frequency range, with an expected drop around the band gap where the response of the material becomes much smaller. There are additional regions where coherence is expected to be small; in the very high frequencies where the response of the material is rolling off above ω_{UL}, in the very low frequencies below the natural frequency of the disturbance actuator (approx. 40Hz) and therefore signal power is low. At 99Hz there is a

Figure 3.13: The transmissibility measured with increasing levels of disturbance gain

small inconsistency in the response where one would expect the response to descend smoothly from the resonant peak at 77Hz, and another around 300Hz where the response would be expected to change smoothly there appears to be some noise/inconsistencies. The coherence also drops at these points. Figure 3.13 shows the transmissibility of the metamaterial measured over 6 measurement runs, where in each case the disturbance gain was increased linearly (from 0.002 to 0.007 in the dSpace model, although these numbers are arbitrary). The transmissibility is identical over much of the range, demonstrating that the metamaterial is operating within its linear range. However at the aforementioned points there are clear non linearities in the metamaterial response. A possible source of these non linearities is misalignment in the voice coil assembly leading to levels of stiction, also there is likely to be a significant air-spring effect in the base of the armature assembly.

Overall the measured response of the metamaterial shows good agreement with the adjusted model. Specifically the metamaterial exhibits a deep resonant band gap that provides a peak attenuation of almost 60dB, and over 10dB of attenuation over a bandwidth of approximately 50Hz. The production of the metamaterial was a success and provides a platform to demonstrate the effectiveness of added active functionality.

3.10.2 Rotational Modes

The metamaterial was designed to study 1-dimensional wave propagation, and vibrate purely in the vertical direction, however some rotational motion is inevitable. For the prototype to be a valid tool for investigating the behaviour of the metamaterial structure it is important that this rotational motion is small compared to the vertical motion. The three modes to consider are the axial/vertical mode (the mode of interest), and two orthogonal rotational modes, the pitch and the roll. The axial motion is calculated by adding the three accelerometer signals together, and the two rotational modes using simple trigonometry described in Appendix C. Figure 3.14a shows the motion in all 3-degrees of freedom (DOF) of the final transmission plate in response to vertical excitation in the bottom plate. Note the focus is on the frequency range surrounding the band gap, between 50 and 300Hz. This figure demonstrates that the majority of the motion of the plate is in the vertical mode. This is the mode of vibration that the vertical motion of the plate most readily couples into. The 3 modes have a similar form, suggesting that the dominant vertical mode weakly couples into the other modes and dominates their response. The magnitude of the other modes is at least 20dB below that of the vertical mode.

Figure 3.14b shows the response measured at each of the three accelerometers, showing that all three accelerometers have approximately the same magnitude response, again suggesting that they are moving predominantly in a vertical motion. The bottom half of the Figure shows the magnitude of the phase gap between each pair of accelerometers, calculated as $||\phi_a| - |\phi_b||$ where ϕ is the measured phase angle, such that a value close to zero suggests that the accelerometers are moving in phase with each other, and a value of 180 degrees means the accelerometers are out of phase. Over the frequency range of interest the phase gap between the accelerometers is mostly very small suggesting that vertical motion is the dominant mode. Within the band gap there a spike where some out of phase motion is measured. However, this is perhaps to be expected considering the metamaterial has been designed such that response here in the vertical mode is very small, and indeed the largest out of phase value within the band gap region coincide with the largest drops in measured coherence (Figure 3.12b), and therefore this should not be considered to invalidate the performance of the prototype.

The evidence provided by the calculations presented above, together with the good level of agreement between the measured response and the axial motion model suggests

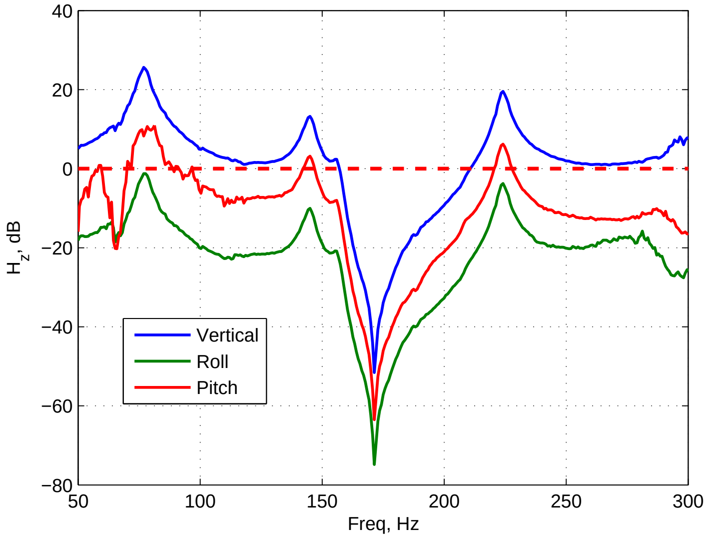

(a)

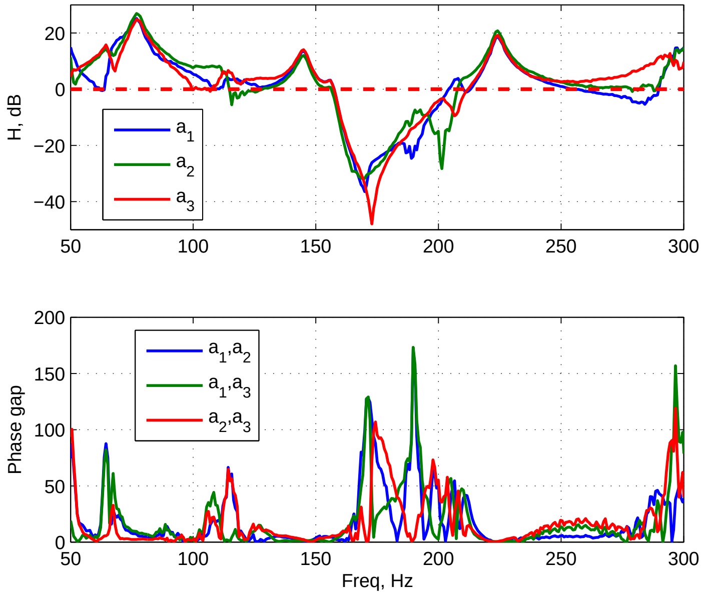

(b)

Figure 3.14: (a) The transmission response of the last plate of the metamaterial in the vertical, roll and pitch modes due to vertical input. (b) The response of individual accelerometers and the magnitude of the phase gap between them

that motion in the rotational modes is not significant and is not adversely affecting the measured response.

3.11 Conclusion

In the previous Chapter 2, an active uncoupled viscoelastic metamaterial design was proposed based on the work of Pope and Daley [12]. Whilst this active viscoelastic metamaterial model was a useful theoretical tool it had several drawbacks that made it unsuitable for developing into a practical device. Therefore the model was used as an inspiration for a new metamaterial structure designed to address these shortcomings, presented in this chapter. The new metamaterial concept has additional viscoelastic connections that mean it achieves double negativity without the need for the distributed active system described in Chapter 2. The active control architecture has also been developed to use reactive rather than point forces. This simplifies the design process since it mitigates the need for inertial actuators, which at the displacements likely to occur at resonance could complicate the control design process since the actuator dynamics will need to be incorporated into the material model. With reactive actuators this is not an issue, however it does restrict the nature of the control forces that can be applied.

This metamaterial concept was then developed into a design that was produced from mild steel using machining techniques. The design was developed to mimic the form factor of traditional vibration isolators found on heavy machinery such as diesel generators etc. and is modular, so extra layers could be added as required for different use cases. The metamaterial was then tested in the laboratory and the presence of a resonant band gap confirmed. The band gap did not appear at the specified frequency due to the limited accuracy of the specification of the rubber mounts, and the requirement for their to be radii on the edge of the leaf springs shortening their effective length. However, these are things that could be changed if the metamaterial was to be produced for use commercially, and once the model of the metamaterial was altered to take these factors into account there is a good agreement between the predicted and the measured response. Therefore the aim to produce a metamaterial with a resonant band gap was a success, and a valuable tool to investigate how that band gap could be enhanced using active control. Such a metamaterial could be extremely useful in isolation applications.

Note that for isolation purposes the negative material parameters are of little importance, however these are relevant in the work being carried out in other areas on the use of metamaterials for acoustic superlenses or cloaking devices. Whilst the form of the metamaterial produced here was for isolation purposes, the concept could equally be applied on a smaller scale in these aforementioned scenarios.

Chapter 4

Actively Enhancing the Band Gap of the Coupled Viscoelastic Metamaterial

The coupled viscoelastic metamaterial introduced in 3 was shown to have a deep narrow band gap due to the presence of the resonator elements. The attenuation of vertical vibration through the material means the metamaterial has potential applications in vibration isolation scenarios, however since the band gap is due to a resonant mechanism it only occurs over a narrow bandwidth. It was shown in Section 2.5 that by adjusting the natural frequencies of the resonant inclusions such that they occur in adjacent frequency band it is possible to ’smear’ the band gap over a wider frequency range at the expense of band gap depth. Similar strategies have been investigated in the by Ding *et al* [6] and Elford *et al* [5] among others [47, 48], as discussed in Section 1.4. Whilst this strategy can successfully widen the region of attenuation a large number of resonant elements is required to achieve relatively limited bandwidth and once constructed the band gap remains static.

Studies into active metamaterials are relatively few in number, and so far much of the literature focussing on adding active elements to metamaterial structures has focused on controlling the effective material parameters. Most notable of these is the contributions of Akl and Baz, published either in collaboration, alone or with contributions from others [10, 67–71]. In addition this work, and of others such as the work of Airoldi and Ruzzene [11], has focused on using local, static shunt circuits to manipulate the resonant behaviour of the metamaterial rather than any sort of digital or adaptive system that one would associate traditionally with active control. The work of Pope and Daley [12] introduced the idea of an active viscoelastic metamaterial with an arbitrary control force, and provided the basis for the work contained in Chapter 2 of this thesis. Subsequent studies then focused on further investigating this configuration [73–76], but these studies are mostly theoretical, and none of these specifically focused on designing controllers to widen the region of attenuation associated with the resonant band gap.

The work presented in this chapter applies active control to the metamaterial produced in Chapter 3. Initially a single channel Filtered-x Least Mean Squares (FxLMS) algorithm is implemented to demonstrate the efficacy of using an active control to enhance band gap attenuation of the metamaterial. The FxLMS algorithm was chosen as it is a well established active control algorithm that could be readily implemented and is well suited for systems with complex and higher order dynamics.

Next several feedback controllers are implemented using optimised finite impulse response (FIR) filters. The filters are optimised using a constrained, non-linear optimisation algorithm to minimise transmission through the metamaterial over a given frequency range. The optimisation routine is constrained to ensure that stability and power constraints are obeyed, and the controllers are implemented within the laboratory. Several controller structures are implemented, including single channel (single-input, single-output (SISO)) and multichannel (multi-input, multi-output (MIMO)) examples, and the results presented.

The purpose of work in this Chapter is not to ascertain best active control algorithm for use with metamaterials of this kind but to prove the concept of using active metamaterials for isolation, as well as to highlight any limitations. The results suggest that active control can be used to greatly enhance the bandwidth over which attenuation occurs in and around the passive band gap. Out of band resonances can also be suppressed.

4.1 Applying a Filtered-x Least Mean Squares Feed-forward Controller

There are many potential strategies that can be employed when designing an active control system. First and foremost the system must achieve the design goal whilst remaining stable, however it is often necessary to compromise performance for reasons of robustness, computational capability and complexity. Initially, to demonstrate the efficacy of using active control to enhance band gap attenuation of the metamaterial, a single channel FxLMS controller was applied [85, 86]. This is a well established robust active control technique that is well suited to the control of systems with complex and high order dynamics. A block diagram describing the FxLMS algorithm is shown in Figure 4.1. FxLMS is an adaptive feedforward algorithm that minimises an error signal $e(n)$ using a reference signal $x(n)$. The algorithm iteratively updates the control filter

$\boldsymbol{w}(n)$ using a 'gradient of steepest descent' approach to shape the control signal $u(n)$ such that it cancels out the disturbance $d(n)$. The algorithm updates the filter using the product of the instantaneous reference signal filtered by $\widehat{G}(z)$ and the instantaneous error signal, where $\widehat{G}(z)$ is an estimate of the control plant response, $G(z)$.

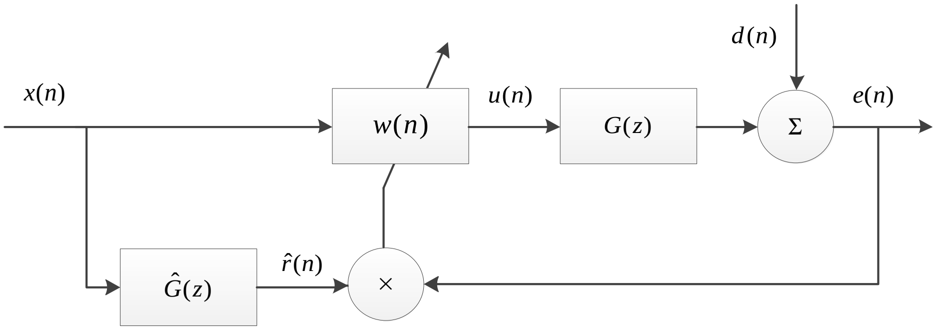

Figure 4.1: A block diagram of the FxLMS algorithm used for active control of the metamaterial

Figure 4.2a shows a schematic of the metamaterial, highlighting the designation of the mass elements and the actuators, for reference. For these experiments the algorithm was employed to minimise the acceleration of the top transmission plate ('trans 4' in Figure 4.2a) due to an excitation force being applied at the bottom transmission plate ('trans 1' in Figure 4.2a), effectively minimising transmissibility through the structure. The measured acceleration of the bottom plate was used as a reference signal, and for these initial investigations only the top actuator (actuator A, Figure 4.2a) was used creating a SISO control architecture. How this then relates to the components of the FxLMS algorithm is then shown in Figure 4.2b.

Using the dSpace rapid prototyping system described in 3.9, it is possible to input a disturbance signal, measure the vibration of the top transmission plate (trans 4 in Figure 4.2a) and bottom transmission plate (trans 1 in Figure 4.2a) and implement the FxLMS algorithm in real time. Initially, measurements were taken of the plant response $G(z)$ using the dSpace system and then a 512 coefficient FIR filter was fitted to the measured frequency response using the `MATLAB` function `fir1` (based on [87], algorithm 5.2); this could then serve as the model of the plant $\widehat{G}(z)$ within the algorithm. A weighting function was used to maximise the model accuracy between 50Hz and 400Hz, since the disturbance actuator is inefficient below its resonance of 40Hz meaning there is little vibration energy to control below this frequency, and the metamaterial acts like a passive low pass mechanical filter above approximately 400Hz. The most critical issue for the model response is that the phase is accurate to within 90 degrees of the true control response to ensure that the algorithm remains stable [85, pg. 135]. Figure 4.3a compares the FIR model obtained to the measured plant response. The model is highly accurate and therefore suitable for control purposes over the frequency span of interest.

The algorithm was initially used to control tonal disturbances and applied at a number of discrete frequencies across the range of interest. The algorithm was then applied for a band limited white noise disturbance (limited to 100Hz < f < 300Hz using digital filters within the dSpace environment). In both instances the convergence gain was adapted heuristically to achieve the best results whilst retaining stability and a sampling frequency of 1.5kHz was used. The tonal control is achieved using two filters of 1 coefficient, controlling the amplitude of an in-phase and a quadrature version of the reference signal to cancel out the disturbance. To control a broadband disturbance, a single control filter of 1024 coefficients is shaped by the FxLMS algorithm. An illustration of the achieved performance is shown in Figure 4.3b. This shows the passive transmissibility curve of the material due to the band limited input compared to the transmissibility when broadband control is applied and allowed to converge. The equivalent levels of transmissibility achieved using tonal control are also plotted, calculated by taking the level of control achieved on a tonal disturbance at this frequency and subtracting it from the passive broadband level at this frequency. The tonal results can be considered a guide to the optimum level of performance that could be achieved at each frequency using a more powerful broadband control strategy, such as FxLMS with a longer control filter, or a different control algorithm.

It should be noted that in the figure the disturbance is band limited such that excitation only occurs over the 100Hz-300Hz range. Over this frequency span the broadband controller shows an improvement over the passive isolation performance. The detrimental out of band resonances that appear either side of the band gap have been suppressed and the band gap has been broadened from approximately 50Hz for the passive case with attenuation being achieved over an approximately 100Hz band once control has been applied. The peak level of band gap attenuation has been reduced but remains over 20dB. The algorithm attempts to minimise the broadband error signal; since the error signal at band gap frequencies is already very low the filter can reduce out of band levels at the expense of the band gap whilst still reducing the broadband level. The

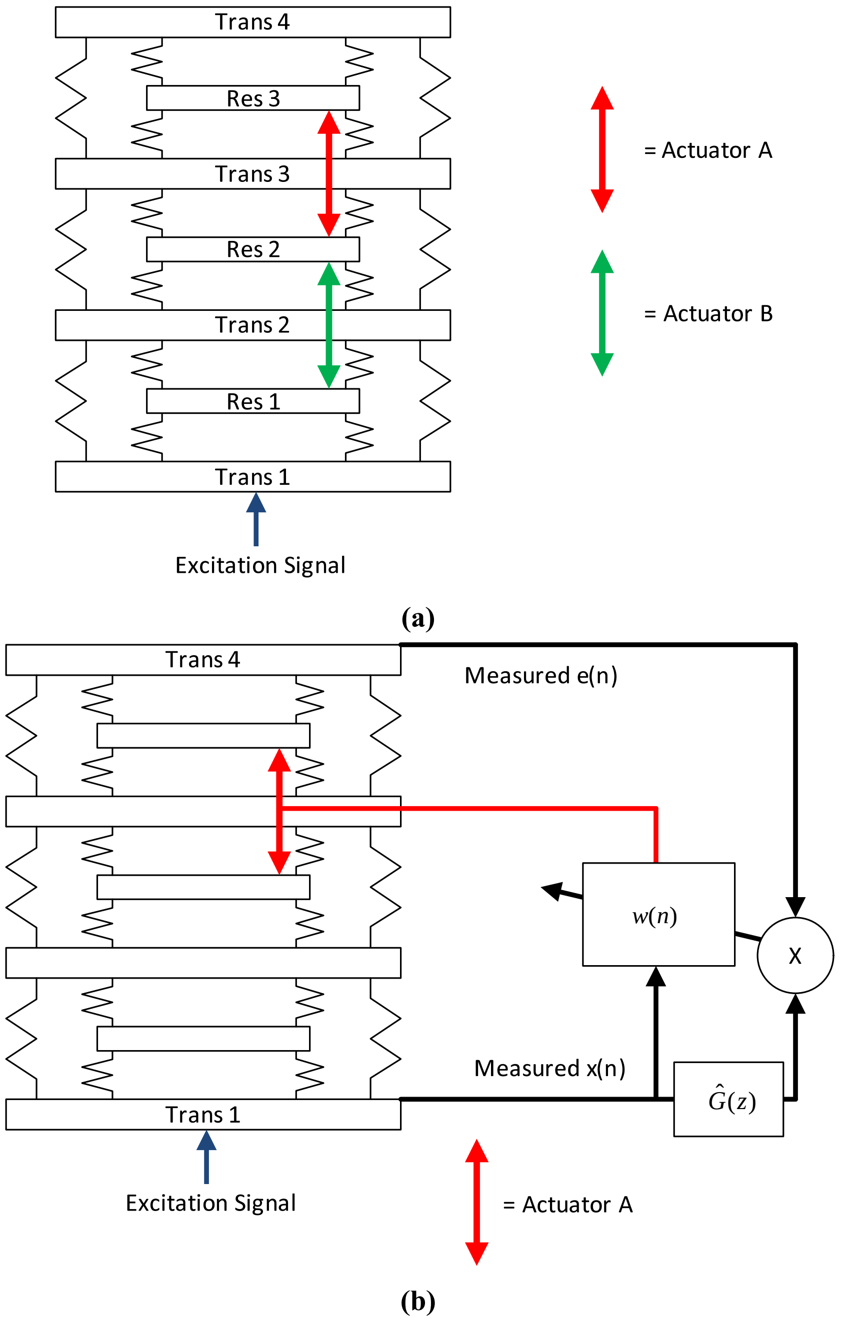

Figure 4.2: (a) A schematic of the active viscoelastic metamaterial showing the naming convention for the mass elements and actuators. (b) A schematic of the FxLMS implementation on the active viscoelastic metamaterial

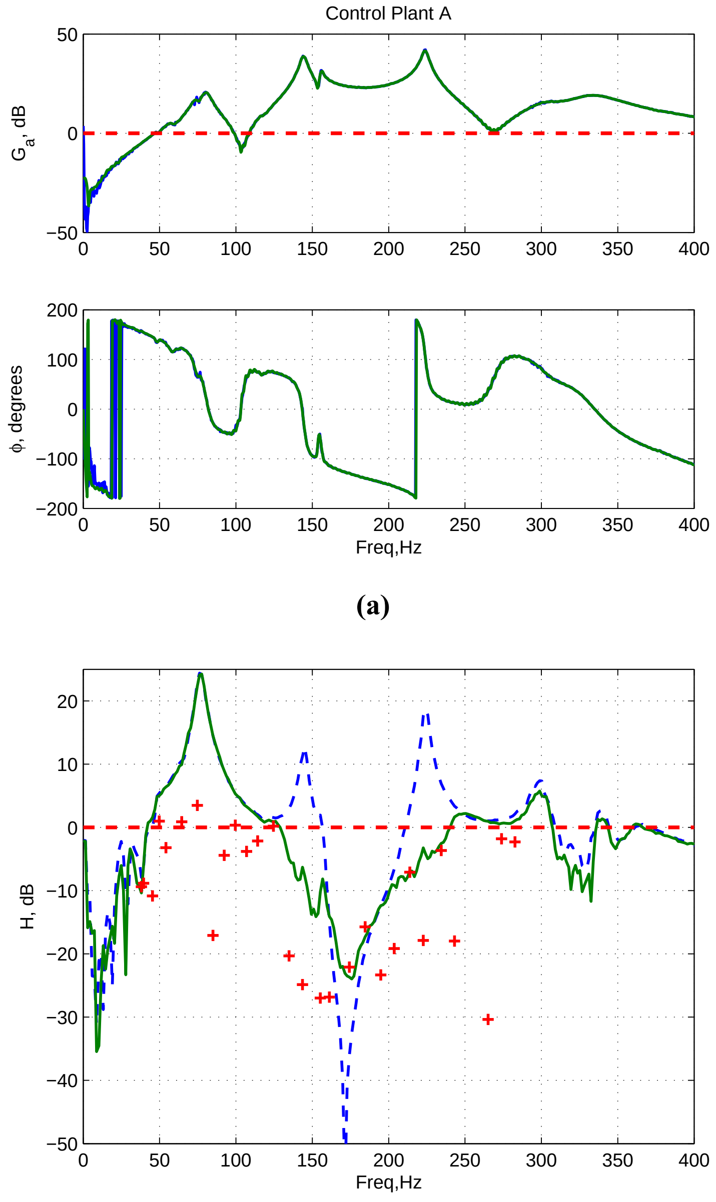

(a)

(b)

Figure 4.3: (a) The measured transfer function between the input actuator A and transmission plate 4 (blue) compared to the FIR filter modelling that response (green). The model perfectly covers the original response apart from at very low frequencies. (b) The transmissibility of the passive material (blue) compared to when broadband FxLMS control is applied (green). The red stars show the equivalent level of attenuation achieved by the tonal controller

broadband controller performance is limited by the filter length and the tonal results provide a better indication of the limits of achievable performance with this specific arrangement. It is clear from Figure 4.3a that Actuator A has the largest influence in the approximate frequency range of 130-230Hz, and indeed it is in this range in which the largest amount of attenuation is achieved. The tonal results suggest that as well as creating this wider band gap a more optimum broadband filter could also suppress the resonance at 76Hz.

One could envisage a scenario where the active system applied here could be deployed practically, such as a piece of rotating machinery with a strong tonal vibration component. The passive design of the metamaterial could be tuned to the region at which the tonal component occurs, the active broadening of the band gap could account for small changes in that tonal component due to load, temperature etc, whilst also suppressing out of band resonances, ensuring other frequencies are not enhanced.

4.2 Negative Feedback Control Theory

The FxLMS algorithm implemented above provides a useful proof of concept of the active metamaterial. However, one of the drawbacks of using the FxLMS algorithm for broadband disturbances is it can take a long time to converge, and the algorithm also does not naturally focus on a specified bandwidth but attempts to minimise the magnitude of the broadband error signal. In many situations it may be more desirable to focus on a particular frequency range. Examples include a broadband vibration source but connected to a radiating structure, where only the modes within a limited frequency range effectively propagate acoustically, or rotating machinery that has a strong tonal component which theoretically can be matched with the passive band gap but varies in frequency based on load and therefore requires a wider band gap region. In the example above this latter issue was sidestepped by band limiting the disturbance signal to frequencies surrounding the passive band gap, however in practice this may not be possible. Whilst these issues have potential solutions, such as preconditioning the filter to speed up convergence, or adding extra band pass filter to the inputs to the algorithm, it was decided to investigate the use of fixed feedback filters that could be designed to target transmission reduction in specified frequency ranges.

With a negative feedback system applied the active metamaterial can now be represented in the continuous time domain using the block diagram contained in Figure

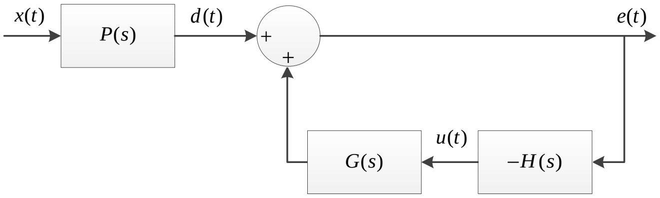

Figure 4.4: The block diagram of the viscoelastic metamaterial subject to disturbance $x(t)$, with the transmission path dynamics $P(s)$, and a negative feedback control system consisting of plant dynamics $G(s)$ and controller $H(s)$

4.4, where now the passive transmission path is represented by $P(s)$, subject to a input $x(t)$. The negative feedback loop consists of measurements of the vertical motion of the last transmission mass, $e(t)$, with a feedback loop consisting of the plant dynamics, $G(s)$, and the controller to be designed $H(s)$. Note that the block diagram shows a single channel case, however the metamaterial has 2 actuators, and therefore 2 control paths. When both paths are used $G(s)$ and $H(s)$ become matrices, and the control signal u(t) becomes a vector. In the Laplace domain the relationship between the disturbance and error signals for the SISO system can be expressed as

$$E(s) = D(s) - E(s)G(s)H(s) = X(s)P(s) - E(s)G(s)H(s) \tag{4.1}$$

Rearranging gives the transfer function of the system, which is equal to $P(s)$ multiplied by the sensitivity function $S(s)$

$$\frac{E(s)}{X(s)} = P(s)S(s) \tag{4.2}$$

where

$$S(s) = \frac{E(s)}{D(s)} = \frac{1}{1 + G(s)H(s)} \tag{4.3}$$

One of the major performance limitations of feedback systems is often the need to maintain closed loop stability and, focussing on a single channel system for the time being, the closed loop system will be stable providing that the positions of the poles of the transfer function are in the left half of the s-plane [88, pg. 234]. However in the case of the metamaterial a pole-zero model of the system in the s-plane is not directly measurable and a more convenient and accurate method for assessing the stability is to make the substitution $s = j\omega$ and examine the system in the frequency domain. Stability can now be assessed using the Nyquist Stability criterion [89, pg. 246]. The Nyquist stability criterion is a well established graphical method for establishing the closed loop stability of a feedback system by plotting it's open loop frequency response ($G(j\omega)H(j\omega)$) on a Nyquist plot; plotting the real part against the imaginary part. Note that up until this point nothing has been said about open loop stability, but in the case of the passive metamaterial the plant is guaranteed to be stable, and for the purposes of this investigation it shall be assumed now that controller is stable. The complete Nyquist method has several criteria that are not to be detailed here, but can be simplified by making this assumption. Now the 'simplified Nyquist condition' can be summarised as the closed loop system shall remain stable providing there are no encirclements of the Nyquist point (-1,0) on the Nyquist diagram.

In addition to the sensitivity function $S(s)$ there is a quantity described as the complimentary sensitivity function $T(s)$ [85, pg. 276], called such because $S(s) + T(s) = 1$.

$$T(s) = \frac{G(s)H(s)}{1 + G(s)H(s)} \tag{4.4}$$

This expression is introduced here since it is useful for assessing the stability of the closed loop system and its robustness to variations in the plant response, and will be employed to in the next section for ensuring robust stability.

4.3 Designing a Single Channel Feedback Filter

The theory detailed in the previous section provides the framework in which to analyse the performance and stability of a feedback filter as it is applied to the viscoelastic metamaterial. To begin with a single channel feedback system was designed, to form the feedback loop containing actuator A. The controller itself consists of an FIR filter whose coefficients are optimised to minimise the transmission of vibration through the metamaterial over a given frequency range using a constrained non-linear optimisation (CNO) routine. An FIR filter was chosen since it is inherently stable, so when paired with the passive plant dynamics of the metamaterial, will be open loop stable as described in the previous section. The CNO was performed using the `fmincon` function that is included as part of the optimisation toolbox for the `MATLAB` computing environment. This uses an interior point optimisation algorithm based on [90, 91]. The optimisation routine attempts to minimise the output of a cost function $\Gamma(\boldsymbol{w})$ whilst satisfying the constraint function $\boldsymbol{c}(\boldsymbol{w}) \leq 0$, where the constraint function $\boldsymbol{c}$ is a function of the filter coefficients, $\boldsymbol{w}$, and can be chosen to achieve the required design objectives. Formally,

$$\min_{\boldsymbol{w}} \Gamma(\boldsymbol{w}) \text{ such that } \boldsymbol{c}(\boldsymbol{w}) \leq 0 \tag{4.5}$$

The optimisation successfully terminates when the gradient of $\Gamma(\boldsymbol{w})$ with respect to $\boldsymbol{w}$ is smaller than a predefined tolerance and the constraints are all satisfied. For the purposes of this investigation, all tolerances used were the default values allocated by `MATLAB`. The algorithm was used to optimise the coefficients of the FIR feedback filter, with the cost function to minimise being the mean square value of the transfer function between transmission plates 1 and 4 (with reference to Figure 4.2a), evaluated only in the frequency band of interest. Figure 4.5 shows a schematic representation of the single channel feedback controller applied to the metamaterial.

$$\Gamma(\boldsymbol{w}) = \frac{1}{\omega_{ul} - \omega_{ll}} \sum_{\omega_{ll}}^{\omega_{ul}} |P(\omega) S(\boldsymbol{w}, \omega)|^2 \tag{4.6}$$

The optimisation routine is designed to find the local minimum of the cost function, however the cost function here represents a physical system, and without appropriate constraints the route will return a solution that is practically useless. Here, there are two governing constraints to the active metamaterial problem, maintaining closed loop stability, and the physical constraints of the components used in the system. Of the five mathematical constraints available to the function and shown in Equation 4.5, for this investigation only the first constraint was used, $\boldsymbol{c}(\boldsymbol{w}) \leq 0$, with the output of the function $\boldsymbol{c}(\boldsymbol{w})$ a vector containing the results of three functions; $c_{stab}(\boldsymbol{w})$ which is set to ensure nominal closed loop stability, $c_{rob}(\boldsymbol{w})$ which is set to ensure that the closed loop stability is robust to plant uncertainties, and $c_W(\boldsymbol{w})$ which ensures that the power output of the active system is does not exceed appropriate limits.

4.3.1 Robust Stability Constraints

Stability is ensured using the Nyquist criterion described above in Section 4.2. To ensure that no encirclements of the Nyquist point occur, the constraint is set such that the real part of the open loop response must remain greater than -1.

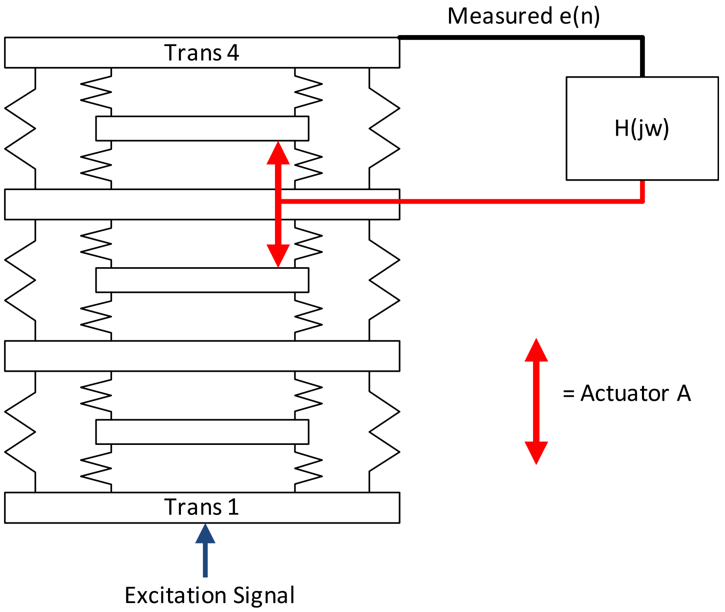

Figure 4.5: A schematic representation of the active viscoelastic metamaterial with a single channel feedback filter applied

$$-1 \leq \text{Re}(G(j\omega)H(j\omega)) \tag{4.7}$$

$$\therefore c_{stab}(\boldsymbol{w}) = -\text{Re}(G(j\omega)H(\boldsymbol{w}, j\omega)) - 1 \leq 0 \tag{4.8}$$

This condition may be considered more conservative than is strictly necessary, since when the magnitude of the imaginary part of $G(j\omega)H(j\omega)$ is non zero, the real part could become less than -1 but an encirclement of the Nyquist point still be avoided. However, the above condition is simple to apply, and it will be shown in subsequent sections that significant levels of attenuation are still achieved. Therefore, whilst more optimal stability conditions may exist, for the purposes of this investigation this simple condition is adequate.

Considering the graphical construct of the Nyquist diagram it is clear that the above restraint will prevent any encirclement of the Nyquist point, however it is also clear that the condition is still satisfied should the open loop gain be 0dB at -180 degrees, the point at which the system becomes unstable. The plant response is likely to be subject to numerous uncertainties related to measurement error, change over time and temperature, and small non linearities, therefore an additional stability constraint is required to ensure *robust* stability is achieved.

To formally determine the robust stability of a system a model of the uncertainties in the plant response is required. In this case such a model is unavailable; the system under test is a prototype and whose specific use case is undetermined. The motivation of the investigation is merely to determine the efficacy of combining metamaterials with active control for isolation applications, and therefore a specific model of plant uncertainties is unnecessary, and instead a general robust stability condition can be applied. It was assumed that the plant model was subject to unstructured uncertainties such that, whilst the exact nature of the uncertainties are unknown their magnitude is such that they can be described using the following approach [85, pg. 281]

$$G(j\omega) = G_0(j\omega)[1 + \Delta_G(j\omega)] \tag{4.9}$$

where $G_0(j\omega)$ is the nominal plant response and $\Delta_G(j\omega)$ is the multiplicative plant uncertainty at each frequency whose value is unknown but whose magnitude is bounded to be no greater than $B_u(\omega)$. Such an approach creates a 'disc of uncertainty' at each frequency point along the locus, in which the true plant response may lie. An arbitrary example of such a system is represented by the Nyquist plot shown in Figure 4.6a, where the nominal plant response has substantial stability margins, yet the radius of the disc of uncertainty at the chosen frequency point suggests that the true margins may be much smaller.

Assuming such uncertainties exist, then to achieve robust stability it is necessary to design the controller such that the distance from the centre of the circle to the Nyquist point is greater than the radius of the circle such that

$$|1 + G_0(j\omega)H(j\omega)| > B_u(\omega)|G_0(j\omega)H(j\omega)| \tag{4.10}$$

therefore

$$\frac{B_u(\omega)|G_0(j\omega)H(j\omega)|}{|1 + G_0(j\omega)H(j\omega)|} < 1 \tag{4.11}$$

$$\therefore B_u(\omega)T(j\omega) < 1 \tag{4.12}$$

In the case of the active metamaterial means that the robust constraint component c_{rob} is set to Equation 4.13, leading the optimisation routine to create control loop dynamics that, accounting for this uncertainty, remain a given distance from the Nyquist point and

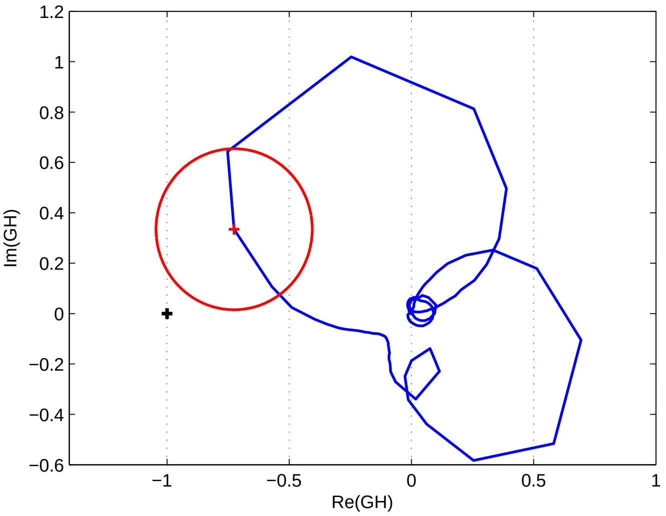

(a)

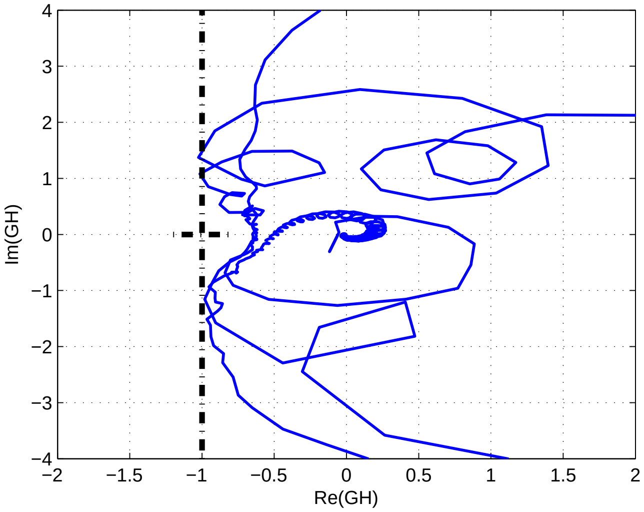

(b)

Figure 4.6: (a) The Nyquist diagram of this arbitrary plant response demonstrates how the gain and phase margins may be much smaller than is initially apparent in the face of multiplicative unstructured uncertainties, represented by the red disc of radius $B_u(\omega)|G_0(j\omega)|$. (b) A typical Nyquist diagram of $G(j\omega)H(j\omega)$ after the filter has been optimised using the stability and robust stability constraints. The black dotted line highlights the stability constraint and Nyquist point

thus are robustly closed loop stable.

$$\therefore c_{rob}(\boldsymbol{w}) = \frac{B_u(\omega)|G_0(j\omega)H(j\omega,\boldsymbol{w})|}{|1+G_0(j\omega)H(j\omega,\boldsymbol{w})|} - 1 \leq 0 \tag{4.13}$$

To achieve a gain margin of approximately 3.5dB and a phase margin of approximately $30°$ the value for multiplicative uncertainty was set to $B_u(\omega) = 0.5$ [85, pg. 283]. A typical example of the Nyquist diagram when this robust stability constraint is applied is shown in Figure 4.6b.

4.3.2 Power Constraint

The final constraint to be applied to the optimisation routine concerns the maximum amount of power applied to the actuators, effectively a constraint on control effort. For a practical implementation of a system it is important to ensure that under specified operating conditions signal levels are such that they are within the saturation and power handling limits of the components used. Since the metamaterial is a prototype and is not being tested under a specific use case, the operating conditions are unknown and any power limit set for these investigations is somewhat arbitrary, however, to protect the actuators installed within the prototype and for completeness such a constraint was applied. The maximum noise signal, $x(t)$, at the first transmission plate is assumed to be white noise with an amplitude of $0.1V_{rms}$ in each frequency bin, such that the disturbance signal at the last mass, $d(t)$ can be formulated in the discrete frequency domain as $D(j\omega) = 0.1 \times (-H(j\omega)S(j\omega))$. Since power, $W = V^2/R$ then the electrical power at the actuator can be formulated as

$$W = \sum_{\omega=0}^{\omega=\omega_{max}} \frac{|0.1 \times (-H_a(j\omega)S(j\omega))|^2}{\Omega_a} \tag{4.14}$$

where $\Omega_a = 2.5$ Ohms, the nominal impedance of the actuator, and $\omega_{max} = 2\pi.750$, where 750Hz is the Nyquist frequency. The constraint is then set so as not to exceed half of the maximum continuous power rating of the actuator of 14W.

$$c_W(\boldsymbol{w}) = \sum_{\omega=0}^{\omega=\omega_{max}} \frac{|0.1 \times (-H_a(j\omega,\boldsymbol{w})S(j\omega,\boldsymbol{w}))|^2}{\Omega_a} - \frac{14}{2} \tag{4.15}$$

4.3.3 Applying the Optimisation Routine

One can envisage two use cases for the prototype isolator for which this active control approach may be useful. First for the suppression of tonal disturbances where the band gap provides the required attenuation of the disturbance tone but suppression of the out of band resonances is desirable to stop the enhancement of any out of band noise or to prevent large excursions during machine run up. Or second for band-limited disturbances where the band gap must cover a wider range of frequencies. With this in mind the optimisation routine was applied over four different frequency bands to assess its performance.

- Suppressing the resonance between 50 and 100Hz
- Extending the band gap over lower frequencies from 70 to 170Hz
- Extending the band gap over higher frequencies from 200 to 250Hz
- Simultaneously extending the band gap over both lower and higher frequencies from 100 to 250 Hz

The optimisation routine is computationally expensive; each iteration of the algorithm requires the calculation of the estimates of the ’gradient of the objective’, in this case $\Gamma'(\boldsymbol{w})$; there are as many gradient estimates as there are filter coefficients. In addition to this the input $\boldsymbol{w}$ is a vector of filter coefficients, and therefore defined in the time domain, yet Γ is calculated in the frequency domain, meaning each cost calculation requires a transformation between domains. Since the calculations are in the discrete domain, to ensure the calculated Nyquist stability translates to stability in practice at all frequencies the granularity of the frequency bins must remain small, and therefore the length of the vector used in a discrete Fourier transform (NFFT) must be high. With these factors in mind for each frequency range two filters were designed of relatively modest length of 128 and 256 coefficients, using an NFFT of 1024 and a sampling frequency of 1.6kHz. The starting coefficients of the filter, $\boldsymbol{w}_0$ were all set to 0. Additional runs were then carried out from two other starting points, a vector of ones, and a vector of random numbers between -0.5 and 0.5, to ensure that the start point did not lead to a different minimum being discovered. Whilst this does not prove that $\Gamma(\boldsymbol{w})$ is a convex function, it increases the likelihood that the local minimum found may be the global minimum.

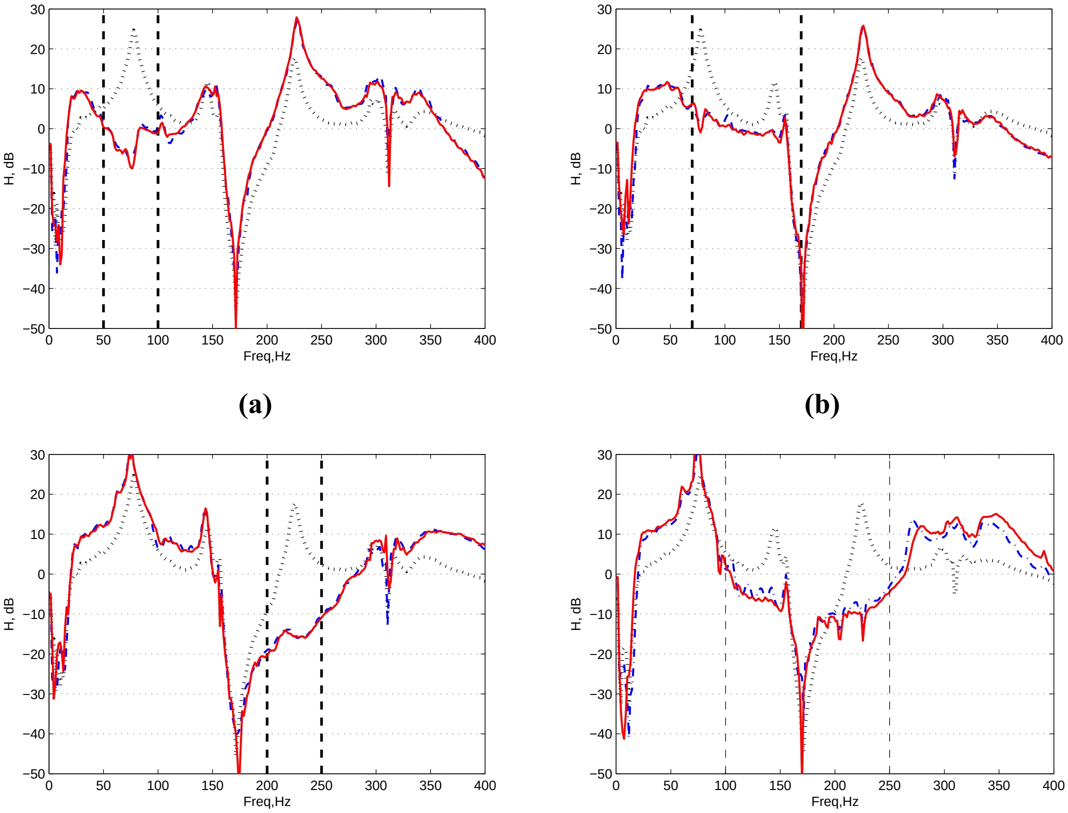

(a)

(b)

(c)

(d)

Figure 4.7: The measured closed loop transmission coefficient when the filter was optimised over 50-100Hz (a), 70-170Hz (b), 200-250Hz(c) and 100-250Hz (d), for a 128 coefficient (blue dashed) and 256 coefficient (red solid) filter. The upper and lower frequency bounds of the optimisation are shown by the vertical dashed lines and the open loop transmission coefficient is shown as the black dotted line

The eight resulting filters were applied to the metamaterial prototype, with the measured closed loop transmission coefficients presented in Figure 4.7. The results for the filters optimised over 50-100Hz (Figure 4.7a) demonstrate that the large resonance in this region can be effectively suppressed, even achieving a small amount of attenuation with a peak level of control of over 30dB. There is inevitable enhancement in other areas of the frequency response due to the waterbed effect, including a small narrowing of the passive band gap, and enhancement of the resonance at the high frequency edge of the band gap. However, a deep band gap remains, and may still be serviceable in isolating well defined tonal disturbances. Minimising the response in the 70-170Hz region (Figure 4.7b) also shows that the out of band resonances at 70Hz and at 150Hz can be effectively suppressed with the response reduced to 0dB across almost the entire target range. Considering the plant response G from Figure 4.3a, the actuator has a low degree of coupling into the final transmission plate at these lower frequencies, meaning a large amount of control effort is required here to influence the motion of the plate. This could potentially limit the performance here in the 70-170Hz region, so to achieve effective suppression of the out of band resonances is encouraging. The opposite is true in the frequency range above the band gap, where the actuator enjoys a good degree of coupling, meaning that control in the 200-250Hz region (Figure 4.7c) is very successful, not only suppressing the resonance at 220Hz but extending the band gap, doubling the bandwidth over which attenuation of over 10dB is achieved from ~50Hz to ~100Hz.

The results show that attempts to widen the band gap over a wider frequency range of 100Hz to 250Hz (Figure 4.7d) achieves is successful, particularly above the band gap region where the level of attenuation is approximately 6-10dB, an overall level of control of around 20dB. The attenuation achieved in the frequency range below the passive band gap is smaller than in the higher frequency range due to the lesser degree of coupling from the actuator, however a useful level of 3-6dB is still achieved. The Nyquist diagram of $G(j\omega)H(j\omega)$ for the 128 coefficient filter is shown in Figure 4.8b, and demonstrates how the open loop response is at the limit of the stability constraint. The power limit was found not to be reached, and it is this stability constraint that limits the performance of the system.

The results for all 4 design objectives show very little improvement when doubling the length of the filter from 128 coefficients to 256 coefficients. This suggests that increasing the length of the filter in further would not lead to large amounts of

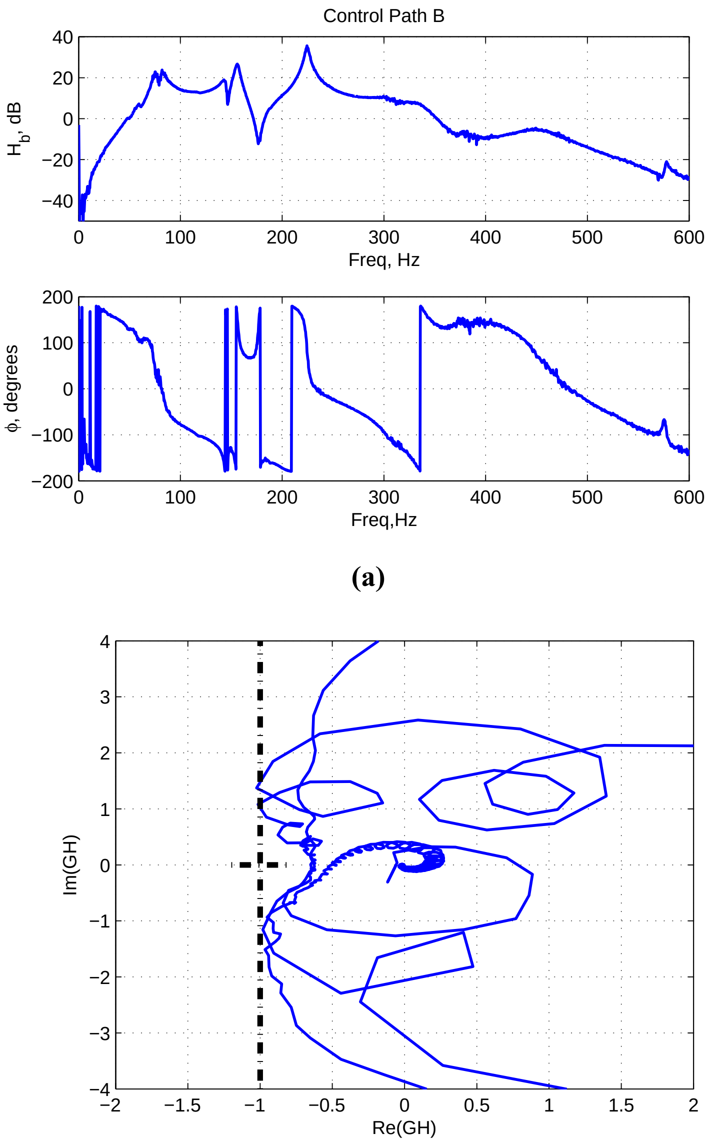

(a)

(b)

Figure 4.8: (a) The plant response of actuator B, G_b, showing the response between the input signal and the acceleration of the final transmission mass. (b) The Nyquist diagram showing $G(j\omega)H(j\omega)$ of the 128 coefficient filter optimised to minimise transmissibility between 100-250Hz

performance gain, and another strategy must be sought to improve the transmissibility performance. Therefore to achieve a broadband band gap with large levels of attenuation a multiple channel solution was sought. A multichannel controller would use both actuators, and therefore have the flexibility of accessing two plant responses, G_a and G_b, which could lead to achieving greater levels of control. The plant response between the input signal and the final transmission mass, G_b, is plotted in Figure 4.8a and, compared to G_a (previously shown in Figure 4.3a), shows a greater degree of coupling into the 100-150Hz region, which may assist with extending the band gap into the lower frequency region. A multichannel solution also requires more error sensors, and therefore has the advantage of having more information available to it with which to construct the control signals.

4.4 Designing a Multichannel Feedback Filter

The design of a multi-channel controller is subject to the same performance goals and constraints as the single channel case already described. However, the addition of extra channels means that some of the conditions applied in the single channel case are no longer valid and must be adapted. The active metamaterial contains 2 actuators and a single output/error signal to be minimised (the vertical motion of the final transmission mass). In this new scenario the number of actuators M, is larger than the number of error signals to be minimised, L. Such a system is said to be 'under-determined' since, mathematically speaking, there are fewer equations of the form $e_l = d_l + \sum G_{lm} u_m$ than there are unknowns u_m, (here u_m represent the M control signals) [85, pg. 183]. In an under-determined problem there are an infinite number of solutions to the minimisation problem, and the optimisation routine will not converge. To avoid this problem an additional error signal was included on the 3rd transmission mass (the layer before the final transmission mass), creating a vector of error signals, $\boldsymbol{e}$, creating a fully determined system. A 2x2 matrix is then used to weight the error signals and ensure that when an optimal solution is found it still achieves the goal of greatly reducing the vibration levels at the final transmission mass. The resulting vibration of the 3rd transmission mass is of little consequence to the design objective of the system. A schematic representation of the MIMO feedback controller applied to the viscoelastic metamaterial is shown in Figure 4.9, where the subscripts '3' and '4' denote the measured error signals from transmission plate 3 and 4, and the subscripts 'A' and 'B' denotes actuator A or B respectively.

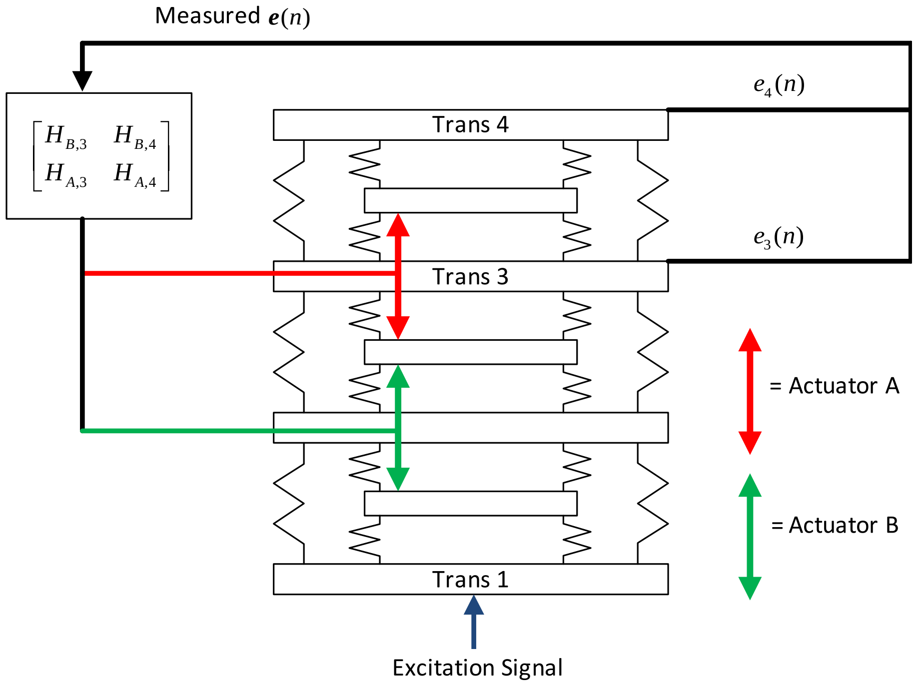

Figure 4.9: A schematic representation of the active viscoelastic metamaterial with the MIMO controller applied

After several test runs of the optimisation routine on this new 2x2 scenario, it was decided to include a regularisation parameter [85, pg. 183] as it was found to further assist convergence. The regularisation parameter, β is applied to alter the cost function such that what is minimised is not only the magnitude of the error signal but also the weighted mean-square effort term using the control signal u. Now, with reference to the sensitivity function, Equation 4.3, $\boldsymbol{H}(j\omega)$ is an $M \times L$ matrix, $\boldsymbol{G}(j\omega)$ is an $L \times M$ matrix and $\boldsymbol{P}(j\omega)$ becomes a vector with two elements, $\boldsymbol{P}(j\omega) = [P_3, P_4]'$. The function to be minimised, Γ now becomes

$$\Gamma(\boldsymbol{w}) = \frac{1}{\omega_{ul} - \omega_{ll}} \sum_{\omega_{ll}}^{\omega_{ul}} \boldsymbol{S}(\boldsymbol{w}, \omega)^H \boldsymbol{Q} \boldsymbol{S}(\boldsymbol{w}, \omega) + \sum_{\omega_0}^{\omega_N} \boldsymbol{u}(\boldsymbol{w}, \omega)^H \boldsymbol{R} \boldsymbol{u}(\boldsymbol{w}, \omega) \tag{4.16}$$

$\boldsymbol{Q}$ and $\boldsymbol{R}$ are weighting matrices, which were heuristically changed with each optimisation attempt to achieve the best results, however a typical set of weighting matrices would consist of a large number corresponding to the error measurement of the final transmission mass and small numbers otherwise, as shown below.

$$\boldsymbol{Q} = \begin{bmatrix} 10^{-3} & 0 \\ 0 & 10^{3} \end{bmatrix} \qquad \boldsymbol{R} = \beta \begin{bmatrix} 1 & 0 \\ 0 & 1 \end{bmatrix} = \begin{bmatrix} 10^{-6} & 0 \\ 0 & 10^{-6} \end{bmatrix} \tag{4.17}$$

The simple Nyquist condition used in the single channel case can no longer be applied to the multichannel case, instead the generalised Nyquist criterion is used [92, pg. 59]. Now the system will be closed-loop stable if the eigenvalues, $\lambda_i(w)$, of $\boldsymbol{G}(j\omega)\boldsymbol{H}(j\omega)$ do not encircle the -1 point on the complex plane. For the 2x2 system here therefore there will be 2 eigenvalues, the characteristic loci of which must not encircle the Nyquist point. The updated stability constraint is shown below, where $i = 1, 2$, representing the two eigenvalues of the matrix.

$$\therefore c_{stab}(\boldsymbol{w}) = -\operatorname{Re}(\lambda_i(\omega, \boldsymbol{w})) - 1 \leq 0 \tag{4.18}$$

In addition to adapting the stability constraint to achieve multichannel stability, the robust stability constraint must be updated to be valid in the multichannel case. Sticking with the multiplicative, unstructured uncertainty that was used in the single channel case, by using the small gain theorem it can be shown [85, pg. 315] that a sufficient condition for robust stability can be defined as

$$||\boldsymbol{T}_0 B_u||_\infty < 1 \tag{4.19}$$

where here $\boldsymbol{T}_0$ denotes the multichannel version of the complementary sensitivity function, Equation 4.4, and $||\ ||_\infty$ denotes the infinity norm. The robust stability constraint is adapted accordingly and shown below. Although the concept of gain and phase margins are not applicable in the multi-channel case, to remain consistent with the single channel case a multiplicative uncertainty of 0.5 is used.

$$\therefore c_{rob}(\boldsymbol{w}) = ||\boldsymbol{T}_0(\omega, \boldsymbol{w}) B_u||_\infty - 1 \leq 0 \tag{4.20}$$

The power constraint is kept as with the single channel case, Equation 4.15, except that now the control signal, $\boldsymbol{u}$, is a vector containing two control signals, both of which must satisfy the maximum power constraint. Figure 4.10 shows a typical plot of the loci of the two eigenvalue and the value of $||\boldsymbol{T}_0(\omega, \boldsymbol{w})B_u||$ after filter convergence, illustrating the effect of the stability and robust stability constraints.

4.4.1 Applying the Multichannel Optimisation Routine

The results above show the single channel controller can effectively suppress out of band resonances as well as widen the band gap, creating a larger region of attenuation. The amount of attenuation achieved in the lower frequencies below the band gap is limited by the plant response of actuator A. A multiple channel solution using both of the actuators means two plant responses are available to the algorithm, and could help overcome this problem. To design the multichannel controller the CNO routine was applied to the wideband scenario tested in the single channel case, targeting the transmissibility between 100-250Hz.

Three different configurations were tested - a fully populated 2-in 2-out controller consisting of 4 FIR filters, referred to as 'centralised'; a second controller with a diagonal structure consisting of 2 FIR filters, with zeros at the off diagonal elements, referred to as 'decentralised'; the final configuration has the same structure as the decentralised example, however the controller consists of 2 *identical* FIR filters, referred to as the 'periodic' controller. The three structures are shown in Table 4.1, where the subscript A/B and 3/4 represent control output to actuator 'A' or 'B' due to an error signal from the 3rd and 4th (final) transmission mass respectively, and the 'CC', 'DC' and 'PC' subscripts refer to the centralised, decentralised and periodic controllers respectively. The dependence on $j\omega$ omitted for clarity.

Centralised	Decentralised	Periodic
$\boldsymbol{H} = \begin{bmatrix} H_{B,3,CC} & H_{B,4,CC} \\ H_{A,3,CC} & H_{A,4,CC} \end{bmatrix}$	$\boldsymbol{H} = \begin{bmatrix} H_{B,3,DC} & 0 \\ 0 & H_{A,4,DC} \end{bmatrix}$	$\boldsymbol{H} = \begin{bmatrix} H_{PC} & 0 \\ 0 & H_{PC} \end{bmatrix}$

Table 4.1: The three MIMO controller structures to be designed

The three structures were chosen to represent a range of different design approaches. The centralised controller offers the greatest amount of flexibility, and for the case of using the metamaterial in its current form as a 2-sensor, 2 actuator vibration isolator, is perfectly practical. As the metamaterial design is expanded, incorporating more

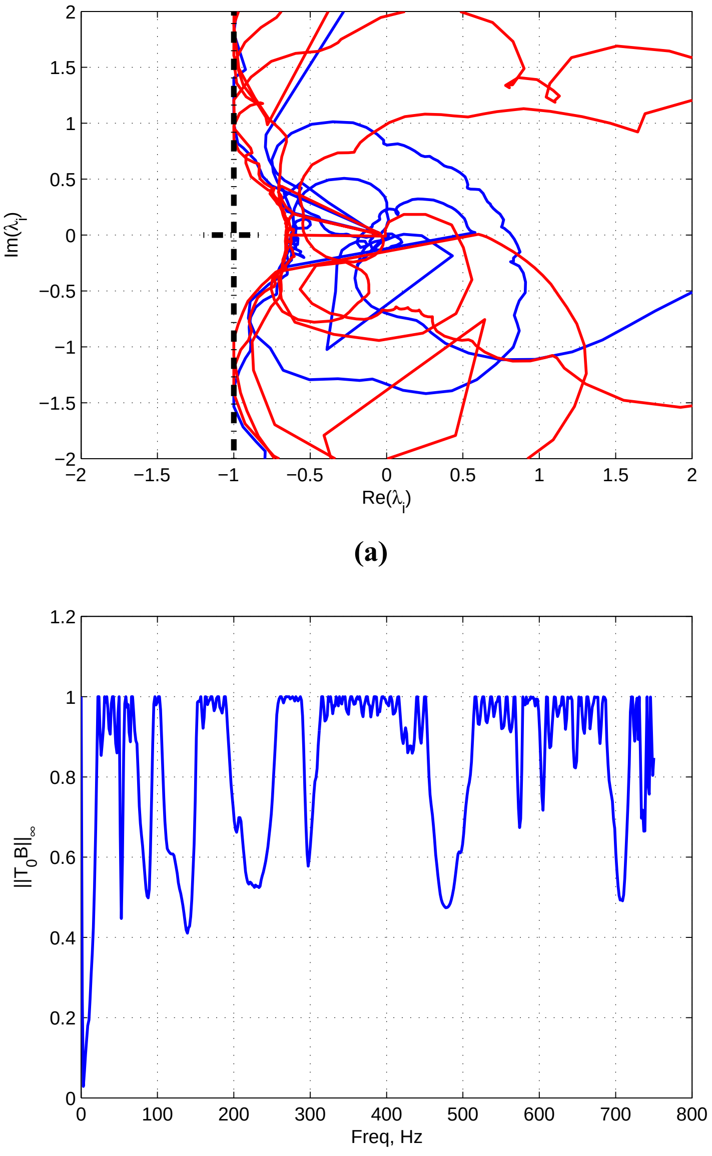

(a)

(b)

Figure 4.10: Typical plots of the loci of (a) the 2 eigenvalues of $G(j\omega)H(j\omega)$ after convergence, the black dotted line highlights the stability constraint and Nyquist point. (b) The robust stability constraint $||\boldsymbol{T}_0(j\omega)B_u||$ after convergence

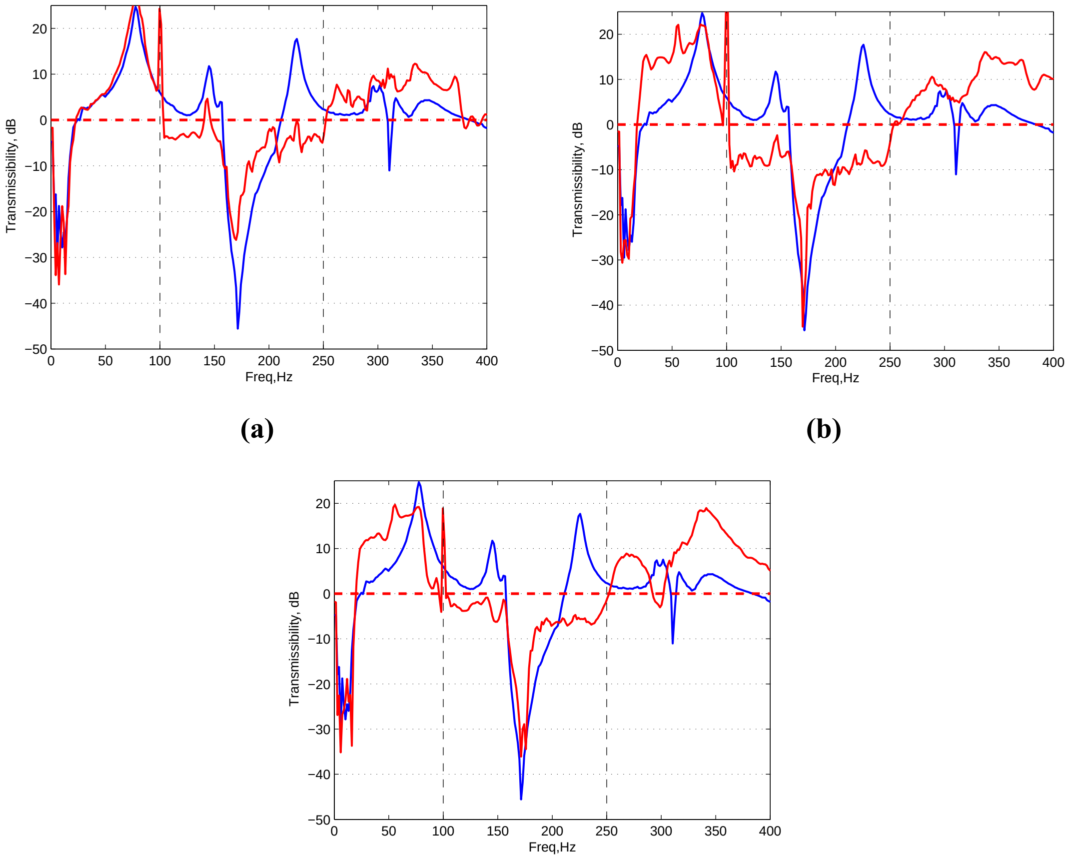

(a)

(b)

(c)

Figure 4.11: The passive (blue) and active (red) measured transmissibility of the viscoelastic metamaterial when 128 coefficient filters were optimised over 100-250Hz, and the MIMO feedback controller has a (a) centralised, (b) decentralised and (c) periodic structure

numerous and smaller elements, a centralised system would not be suitable and a decentralised control scheme would be required with each layer of the metamaterial having its own discrete control hardware. Finally, staying true to the strict definition of a metamaterial as being periodic, the periodic controller means each section of the metamaterial is both physically and *electronically* identical to the others. In the future one could envisage a modular design and production process where each identical cell is mass produced on a small scale and used as a building block of an isolation or wave guide scheme, perhaps even with local passive control loops to reduce complexity further.

Figure 4.11 presents the measured results for the three controller structures after the optimisation routine was allowed to converge and was then applied to the active metamaterial. The periodic filter structure, Figure 4.11c, manages to successfully suppress the resonances either side of the band gap, and achieves attenuation in the higher frequencies of the target region of approximately 5-7dB. Overall in the lower frequencies the attenuation is lower at 1-3dB. The centre of the band gap is preserved, however the overall passive band gap profile is narrowed somewhat. This performance is comparable to, if slightly outperformed by, the single channel case from Section 4.3.3. This is perhaps to be expected; having to apply two identical feedback signals to the two actuators each with its own plant response could be considered a more onerous constraint than designing a single filter and making the 2nd feedback signal zero. Removing the periodic constraint leads to a large improvement in the performance of the metamaterial, as shown in the results for the decentralised controller, Figure 4.11b. Here again the centre of the band gap is conserved, and the attenuation across the vast majority of the rest of the targeted frequency range is in the 7-10dB. The small exception is the region at approximately 145Hz, corresponding to the resonant peak at the lower edge of the band gap, where attenuation drops to approximately 2dB. This control structure shows great potential if employed in an isolation scenario.

The measured results for the centralised controller are less impressive. It would be expected that since this configuration has the most flexibility it would produce the best results; at the very least the optimisation should be able to produce results equal to the decentralised case by converging to the same solution, with the off diagonal elements remaining at 0. When applying the optimisation routine to this scenario the `fmincon` function often would not converge, or could not find a feasible solution (i.e. a solution that satisfies the constraints). This is particularly surprising since all the constraints can be satisfied by reducing the gain of the filters towards zero, regardless of their response. To assist convergence the initial filter coefficients were then set to final the decentralised solution - a subset of the possible solutions to the centralised problem, and therefore the minimum one would expect the centralised scenario to achieve - however even then the algorithm would diverge from this solution and fail.

By adjusting the weighting matrices of the cost function a solution was eventually achieved, however during convergence the output of the function would often give a warning about poor matrix conditioning, and it is thought that this conditioning may be the reason for the failure of the function to converge to a satisfactory solution. The nature of the warning messages provided by the function mean that it was not clear during which process of the optimisation step that the matrix conditioning was an issue. The centralised control structure has greater degrees of freedom than the periodic or decentralised case, and it may be expected that using a fully populated controller may allow the variance of GH to increase, reducing the conditioning of the matrix, although a formal proof is of this is outside the scope of this research and not offered here. For the purposes of demonstrating the potential of the active metamaterial as a vibration isolator it is enough to say that the problem can be avoided in this case by constraining the controller to follow the decentralised structure.

4.5 Conclusion

The results presented in this Chapter demonstrate how the application of active control to the viscoelastic metamaterial presented in Chapter 3 can enhance the passive band gap performance and create a system that has the potential to outperform traditional passive isolation methods. Both SISO feedforward FxLMS and SISO optimised feedback filters were implemented and shown to be effective in suppressing out of band resonances and increasing the bandwidth at which wave attenuation occurs when compared to the passive case. The amount of attenuation achievable at frequencies below the band gap region was limited in part due to the small magnitude of plant response of Actuator A at these frequencies.

Greater performance could be achieved by implementing a MIMO controller consisting of optimised feedback filters, where three controller structures were investigated. First a 'periodic' controller was chosen to be true to the periodic structure of metamaterials, and could be considered a route towards creating active metamaterials with a modular structure, mass produced as distinct cells that could be combined as required. The periodic structure showed promise but its performance is constrained by the need for each filter to be identical. When this constraint is relaxed to create a decentralised controller the performance increases, achieving nearly 10dB of attenuation across the target frequency whilst retaining the peak passive band gap performance.

The final multichannel controller structure was a fully centralised system consisting of 4 distinct filters. Since this controller is the least constrained of the three structures it would be expected to achieve the best results, however it became clear during the filter design process that there was an issue with filter convergence, probably due to matrix conditioning issues. This meant that whilst a feasible solution was eventually achieved, the performance of the controller is not as good as that of the more highly constrained periodic and decentralised structures. Alternative techniques must be sought in the future to address this and produce a greater level of performance. This could be to investigate other control design techniques, or it could be taking measures to improve the conditioning of the system. Although no investigation of the factors governing the conditioning issue has been carried out in this study, it is likely that adding damping into the structure would help.

The results demonstrate the ability to either suppress out of band resonances or enhance the bandwidth over which attenuation occurs either side of the band gap whilst retaining the majority of the passive band gap performance. Even when using the FxLMS algorithm, where a wide range of frequencies were targeted, it is of significance that the greatest levels of attenuation are achieved where the natural band gaps occur, and a unified design process that matches the best features of both active and passive functionality can provide impressive levels of attenuation over wide bandwidths. This, combined with the findings from Chapter 2, supports the argument for using, where appropriate, active periodic materials in vibration isolation applications over more traditional active isolation mounts.

As with Chapter 3, the focus here has been on improving the band gap performance with respect to isolation applications. In the future the concept could also be applied on a smaller scale with respect to an acoustic superlens or cloak design, and the active control used to manipulate the material parameters to achieve negativity over a broad frequency range.

Chapter 5

A Passive Locally Resonant Acoustic Metamaterial

A duct lined with an array of Helmholtz resonators is a common metamaterial structure, as discussed in Section 1.6.1, and was the inspiration behind the uncoupled viscoelastic metamaterial from Chapter 2 by way of a acoustic-mechanical analogy. The metamaterial presented in this Chapter is based on this concept, and is similar in design to the metamaterial presented by Ding *et al* [6]. The design consists of an array of split hollow sphere (SHS) elements acting as Helmholtz resonators suspended in a circular sample, effectively providing 7 resonators attached in parallel at one point along the duct. The passive material differs from Ding *et al* in that the Helmholtz resonators are suspended within a fine mesh that has been designed to be, as far as possible, acoustically transparent; in Ding *et al*'s work air filled hollow spheres are suspended in a sponge. Therefore in the example presented here both the transmission and resonant medium are as much as possible the same; air. In addition, the material presented here is designed for and produced using additive layer manufacturing techniques, the only viable production technique to produce the required fine mesh suspension, and therefore provides a validation of the design and manufacturing process of acoustic metamaterials in this way and experimental validation of their performance. As metamaterial structures are developed into higher degrees of freedom and smaller dimensions 3D printing technology such as this is likely to be the most viable route to production. The metamaterial presented in this chapter also serves as a useful starting point for the development of an active acoustic metamaterial as discussed in later chapters.

The material is considered only in 1 dimension. Indeed the materials are designed to be tested within an impedance tube, where the frequencies of interest are within the plane wave working limits of the impedance tube and therefore the propagation can be considered 1-dimensional. Whilst there are not many real world environments where 1 dimensional sound propagation is valid, it is a convenient environment to study the fundamental physical properties of these materials, facilitating further research considering the problem in higher dimensions.

Previous studies into acoustic metamaterials based on Helmholtz resonators have led to alternative expressions for the effective bulk modulus of the system. One of the key initial studies into such materials, by Fang *et al* [9], provides an expression for the bulk modulus using a direct analogy between electromagnetic and acoustic metamaterials, taking the expression for the effective permeability derived by Pendry *et al* [18] and substituting equivalent acoustic parameters in place of the parameters for an electromagnetic split ring resonator. The resulting expression describes the effective bulk modulus in terms of the natural frequency ω_0 of the resonators and Fang *et al* note that the form of results given by this equation appear to agree with experimental measurements for an array of Helmholtz resonators. However, this analogous acoustic expression is not given any formal derivation within the paper, and indeed it seems unlikely that the subtleties of the resonator behaviour could be described simply using the resonant frequency alone when it is known that the Q factor of a Helmholtz resonator can be expressed as a function of the ratio of the cavity volume and the neck area [93, pg. 285], different values of which can yield the same resonant frequency.

Akl and Baz [69] derive an expression for the effective bulk modulus of the acoustic metamaterial by creating an equivalent circuit and examining the volume flow into the resonator element. The resulting expression is in terms of both the physical dimensions of the tube and resonator elements, and it is noted in the article that results calculated using the resulting equation follow the form of those of the Fang expression, although no formal comparison is carried out.

Both the Fang and Akl and Baz papers refer to the effective bulk modulus being dispersive, however, whilst they do not explicitly state that the effective density is static, the chance of the density being dispersive also is not explored. Indeed further work as Akl and Baz [70, 71] and by Baz [68] as a sole author investigate using a membrane structure to control the effective density of the metamaterial cell, suggesting that this is otherwise presumed to be static. However, this contradicts the work of Cheng *et al* [66] who calculate the effective density from the effective impedance and effective bulk modulus, and demonstrate a dispersive result. Indeed, Cheng *et al* state that, unlike in electromagnetic materials where resonances within the electrical and magnetic fields are induced through separate structures, in purely acoustic medium where the transmission and resonant elements of the material contain an identical fluid then the resonances of the acoustic pressure and volume velocity, p and u, are intrinsically linked and will resonate simultaneously

To predict the performance of the metamaterial presented in this Chapter a model is developed based on the acoustic transmission line method (ATLM) using a transfer matrix approach. Combining a transfer matrix formulation with an impedance representation of the Helmholtz resonator allows the transmission coefficient to be determined. Next, a lumped parameter equivalent circuit representation of a Helmholtz resonator within a duct is derived. The circuit differs from that used in the work of Akl and Baz [69] in that it considers multiple layers of the metamaterial to show that *both* the effective bulk modulus and density parameters are dispersive, and provides mathematical expressions to calculate them.

The calculations from this model are compared to those measured in the laboratory with the produced metamaterial samples and the model is shown to accurately predict the transmission coefficient, effective bulk modulus and wave number of the metamaterial. The dispersive nature of the effective density is also accurately predicted, however occurring at frequencies slightly higher than those seen through experiment. Finally the effect of differing the number of resonators is investigated, and it is shown that the presence of multiple resonators subtly increases the frequency at which the resonant behaviour occurs, possibly due to mutual coupling between the resonators. It is shown that this can be predicted by adapting the transfer matrix model to use the effective material parameters to determine the dispersive sound speed of the metamaterial.

5.1 Helmholtz Resonators

A Helmholtz resonator is a common acoustic device [93] consisting of a rigid walled cavity of volume V_H, with an opening or neck with an area S_n and length L_{neck}, such as the SHS shown in Figure 5.1a. Providing that the wavelengths of interest are such that they are much greater than the dimensions Helmholtz resonator, it can be considered as a lumped mass system as shown in Figure 5.1b. At these frequencies the air in the neck of the resonator acts like a solid mass, reacting on the viscoelastic properties of the air within the resonator cavity. By considering the device in this way it is clear that the mechanical impedance of the system is given by Equation 5.1, and this then leads the acoustic impedance Z_h related to the area of the resonator opening

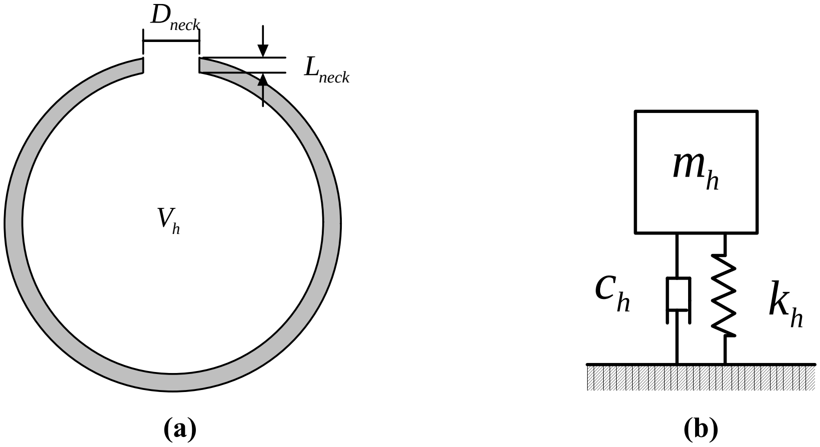

Figure 5.1: A split hollow sphere element as a Helmholtz resonator (a) and its lumped mechanical model (b)

$$Z_{mech} = c_h + j(\omega m_h - \frac{k_h}{\omega}) \tag{5.1}$$

$$Z_h = \frac{Z_{mech}}{S_n^2} \tag{5.2}$$

Here ω is angular frequency in rad/s. The mass can be calculated as $m_h = \rho_0 S_n L'_{neck}$, where ρ_0 is the ambient density of air, and L'_{neck} is the effective length of the resonator neck (approximately $1.6 \cdot L_{neck}$) [93, pg. 284]. The stiffness $k_h = \rho_0 c_0^2 S_n^2 / V_h$, where c_0 is the ambient sound speed. c_h represents the viscoelastic losses of the resonator, and this has two sources, the thermoviscous resistance due to motion of air within the resonator and friction as the mass of air the neck, R_v, and the radiation resistance due to sound radiating into the surrounding medium R_r [94].

$$R_r = \frac{\rho_0 k^2 S_n^2}{4\pi} \tag{5.3}$$

$$R_v = \left[2 \cdot 0.00083 \sqrt{\frac{\omega}{2\pi}} S_n (L_{neck} + r_{neck})\right] / \rho_0 c_0 r_{neck} \tag{5.4}$$

where r_{neck} is the radius of the resonator neck. The natural frequency, ω_0, of the resonator occurs when the reactance (imaginary) part of this impedance becomes zero

$$\omega_0 = c_0\sqrt{\frac{S_n}{L'_{neck}V_h}} \tag{5.5}$$

5.2 Dispersive Material Parameters of a Helmholtz Resonator within a Duct

The impedance based model of the Helmholtz resonator can be combined with a lumped parameter model of an acoustic duct to determine the effective material parameters of a Helmholtz resonator based metamaterial. The method for deriving expressions for the effective material parameters uses an equivalent circuit approach. An equivalent circuit is used to represent the acoustic elements [95, pg. 50], where the compliance of air is represented by capacitance C, and inertia through inductive elements, L. Now the current flow represents the volume velocity, and the voltage represents acoustic pressure. The resonator elements themselves are kept as ’black box’ impedances Z_h. For simplicity the duct is assumed to have zero losses.

An equivalent circuit for 3 consecutive empty sections of acoustic duct, length $2l$, is shown in Figure 5.2b, where $2L_d$ and C_d represent the inertance and compliance respectively of the air within the duct [93, pg. 288], and are functions of the ambient density ρ_0 and bulk modulus B_0 respectively.

$$L_d = \frac{\rho_0 S_d l}{S_d^2} = \frac{\rho_0 l}{S_d} \tag{5.6}$$

$$C_d = \frac{S_d^2 2l}{B_0 S_d} = \frac{S_d 2l}{B_0} \tag{5.7}$$

Figure 5.2c shows the same circuit with the inclusion of a Helmholtz resonator within each layer, representing 3 layers of an acoustic metamaterial. The impedance of the resonator is Z_h. Using Helmholtz resonator theory [93, pg. 284] the impedance of a Helmholtz resonator is defined as $Z_h = sL_h + 1/(sC_h) + R_h$, where L_h, C_h and R_h are the inertance, compliance and resistance respectively of the resonator. The inertance is defined as $L_h = m_h/S_n^2$, the compliance as $C_h = S_n^2/k_h$, and the resistance $R_h = (R_v + R_r)/S_n^2$.

Using Kirchoff’s voltage law it is possible to derive the equations of motion of each model. For a single section of empty duct the equations of motion become

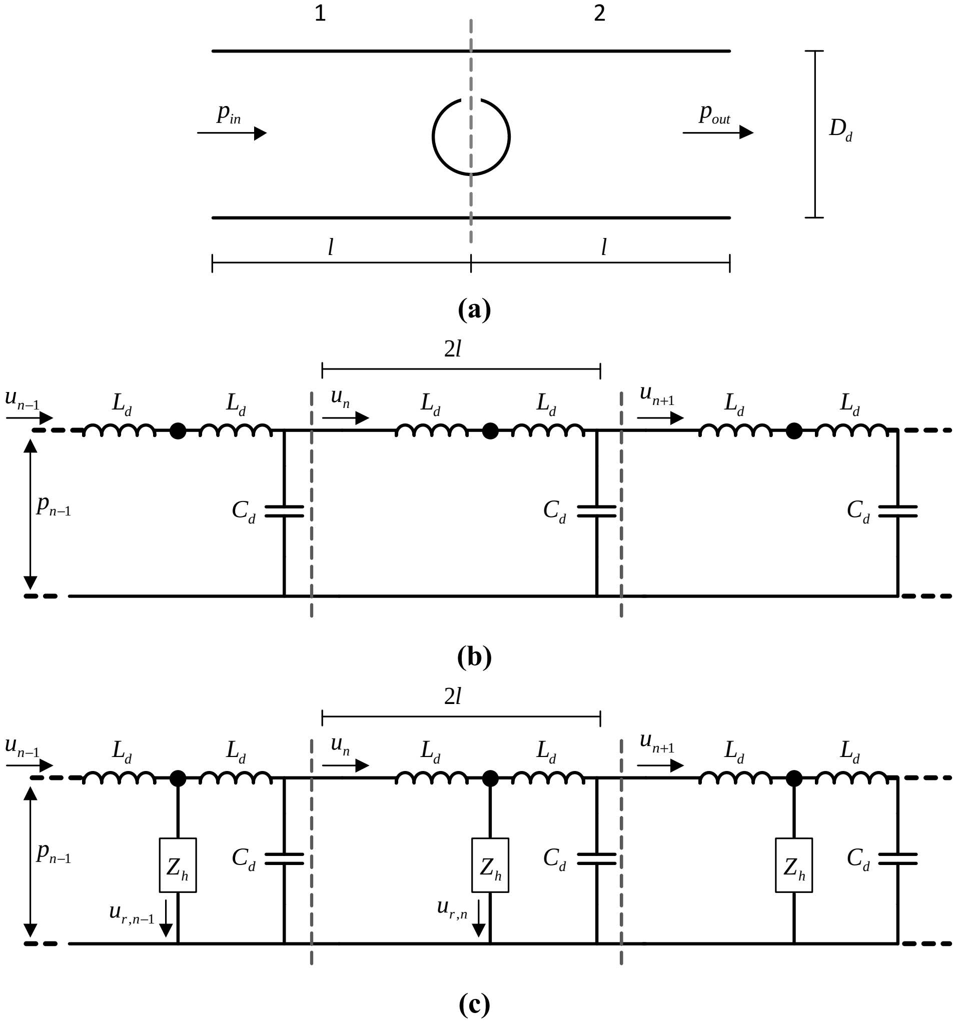

Figure 5.2: (a) A Helmholtz resonator within a duct, (b) Equivalent lumped parameter circuits of 3 sections of empty duct and (c) 3 layers of a metamaterial consisting of a duct containing a Helmholtz resonator

$$s^2 2L_d u_2 = \frac{1}{sC_d}(u_{n-1} + u_{n+1} - 2u_n) \tag{5.8}$$

where s is the Laplace variable. The acoustic metamaterial consists of several layers of the Helmholtz resonator circuit shown in Figure 5.2c, the equations of motion of which are given by Equation 5.9. Detailed derivation of this equation is given in Appendix B.

$$s^2 L_d \left(1 + \frac{Z_h + \frac{1}{sC_d}}{Z_h + sL_d + \frac{1}{sC_d}}\right) u_2 = \frac{Z_h}{sC_d(Z_h + sL_d + \frac{1}{sC_d})}(u_{n-1} + u_{n+1} - 2u_n) \tag{5.9}$$

Comparing Equations 5.8 and 5.9, it is clear that the effective inertance and compliance of the lumped parameter model of the acoustic metamaterial are given by

$$L_e = L_d \left(1 + \frac{Z_h + \frac{1}{sC_d}}{Z_h + sL_d + \frac{1}{sC_d}}\right) \tag{5.10}$$

$$C_e = \frac{C_d(Z_h + sL_d + \frac{1}{sC_d})}{Z_h} = C_d \left(1 + \frac{sL_d + \frac{1}{sC_d}}{Z_h}\right) \tag{5.11}$$

Examining Equations 5.10 and 5.11, it is clear that in the absence of a resonator (i.e. $Z_h = \infty$) then the values for L_e and C_e revert to their static values of $2L_d$ and C_d. For an element of an acoustic medium length $2l$ and cross sectional area S_d, effective inertance and compliance are related to the effective density, ρ_e, and bulk modulus, B_e, respectively of the fluid, which can be calculated using Equations 5.12 and 5.13 [93].

$$\rho_e = \frac{L_e S_d}{2l} \tag{5.12}$$

$$B_e = \frac{2lS_d}{C_e} \tag{5.13}$$

The effective material parameters of an acoustic metamaterial consisting of a Helmholtz resonator (or indeed any other suitable acoustic element) within a duct can now be readily ascertained from its acoustic impedance. In the case of multiple resonators in a single layer the material parameters can be determined by considering the elements positioned in parallel, and combining their impedances accordingly. For a collection of N identical resonators, the impedance $Z_{h,N} = Z_h/N$.

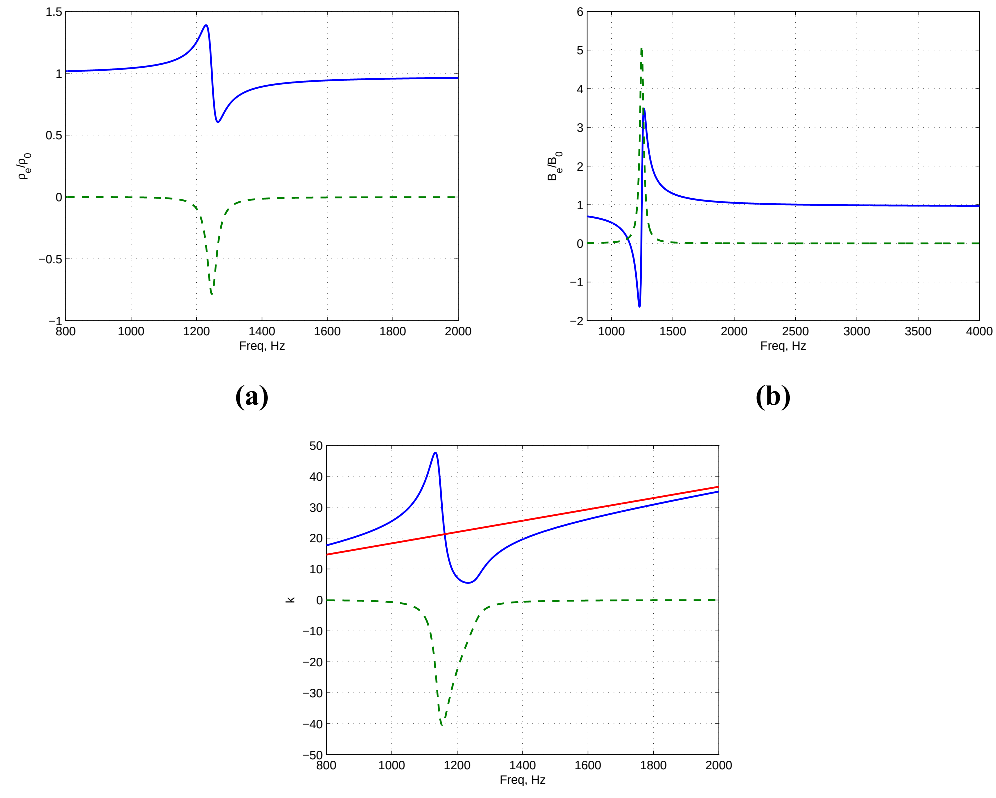

(a) **(b)**

(c)

Figure 5.3: (a) The effective density, (b) bulk modulus and (c) resulting wavenumber of an example of the acoustic metamaterial consisting of 7 Helmholtz resonators tuned to 1145Hz within a duct. Real part (blue) and imaginary part (green). The wavenumber is compared to the wavenumber of an empty acoustic tube (red)

A typical numerical example of the effective material parameters and resulting acoustic wavenumber of a metamaterial consisting of 7 resonators tuned to 1145Hz are plotted in Figure 5.3. The wavenumber plot includes the wavenumber in air of the empty duct, included for comparison. Once the effective bulk modulus and density have been determined it is possible to calculate the dispersive sound speed of the metamaterial $c_n = \sqrt{B_e/\rho_e}$ and the wavenumber $w_n = \omega/c_n$.

5.3 Transmission Behaviour of A Helmholtz Resonator Within a Duct

As shown above, the effective material parameters described in Section 5.2 govern the sound speed of plane waves passing through the metamaterial and are functions of the resonator impedance. The impedance can also be combined with a 2-port network based transmission line approach (the ATLM) to model the transmissibility of the metamaterial.

Consider a plane wave moving through a medium that is split into discrete layers of thickness d_n, a 2-port network can be derived [96] relating the acoustic pressure, p_n, and volume velocity, u_n, at each layer of the system. Each layer has an acoustic impedance Z_n such that as each pressure disturbance, p, travels from layer to layer the change in acoustic impedance would lead to a proportion of the wave being transmitted and a proportion reflected, such that in the nth layer there shall be two travelling pressure waves; an incident wave, $p_{i,n}$ and a reflected wave $p_{r,n}$, as shown in Figure 5.4.

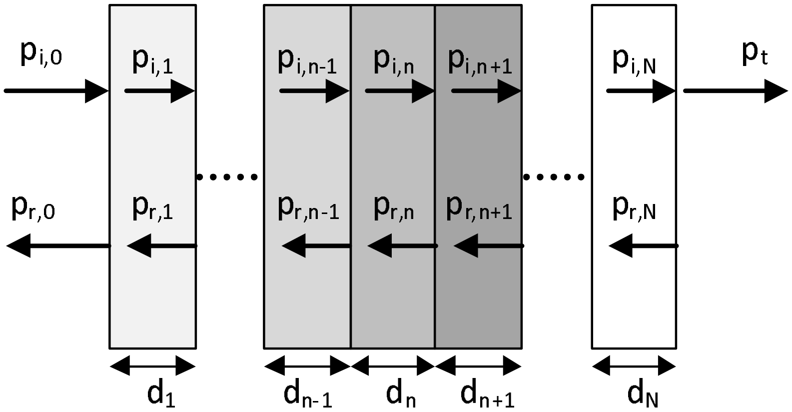

Figure 5.4: The reflection and transmission of plane waves within multiple homogeneous medium layers

Within a duct, presuming that the frequencies are such that propagation is purely planar, the relationship between the acoustic pressure, p_n and particle velocity u_n across each layer can be modelled in the frequency domain as using a transfer matrix $\mathbf{T}$ such that

$$\begin{Bmatrix} \mathbf{P}_{n-1} \\ \mathbf{U}_{n-1} \end{Bmatrix} = \mathbf{T}_n \begin{Bmatrix} \mathbf{P}_n \\ \mathbf{U}_n \end{Bmatrix} \tag{5.14}$$

The transfer matrix for a layer of a material is expressed as a function of its acoustic impedance, z and the wave number, k, within the nth layer such that

$$\mathbf{T}_n = \begin{bmatrix} \cos(k_n d_n) & j z_n \sin(k_n d_n) \\ \dfrac{j \sin(k_n d_n)}{z_n} & \cos(k_n d_n) \end{bmatrix} \tag{5.15}$$

Therefore a pressure wave travelling through multiple material layers can be modelled as

$$\begin{Bmatrix} \mathbf{p}_0 \\ \mathbf{u}_0 \end{Bmatrix} = \prod_{n=1}^{N} \mathbf{T}_n \cdot \begin{Bmatrix} \mathbf{p}_{N+1} \\ \mathbf{u}_{N+1} \end{Bmatrix} = \boldsymbol{\tau} \begin{Bmatrix} \mathbf{p}_{N+1} \\ \mathbf{u}_{N+1} \end{Bmatrix} \tag{5.16}$$

Note that if the multiple layers are identical, as is the case with a periodic metamaterial, the product of transfer matrices, $\boldsymbol{\tau}$, reduces to $\mathbf{T}^N$.

The acoustic impedance of a fluid within a duct is $z = z_0/S_d$ [93, pg. 288], where the cross sectional area of the duct $S_d = \pi r_d^2$. z_0 is the characteristic acoustic impedance, and is a function of the material parameters, $z_0 = \rho_0 c_0$. Viscous losses are proportional to the radius of the duct r_d, and accounted for in the imaginary part of the complex wave number.

Now a Helmholtz resonator mounted within a duct, as that pictured in Figure 5.5a can be represented as the equivalent circuit shown in Figure 5.5b, where Z_1 and Z_2 represent the complex impedance of the duct, and Z_h the resonator. The duct impedances can be replaced with 2-port networks representing an empty duct, using the transfer matrix Equation 5.15, with the appropriate values for acoustic impedance and wavenumber, where the thickness of the layer $d_n = l$; here (neglecting losses) the transfer matrix becomes a pure delay term. The transfer matrix for the resonator impedance can be inferred from Equation 5.14, noting that $z = p/u$

$$\mathbf{T}_h = \begin{bmatrix} 1 & 0 \\ \dfrac{1}{Z_h} & 1 \end{bmatrix} \tag{5.17}$$

The transfer matrix for the metamaterial can now be created by combining the ’duct’ transfer matrices, $\boldsymbol{T}_d$, with the ’resonator’ transfer matrix, $\boldsymbol{T}_h$

$$\tau = \boldsymbol{T}_d \boldsymbol{T}_h \boldsymbol{T}_d \tag{5.18}$$

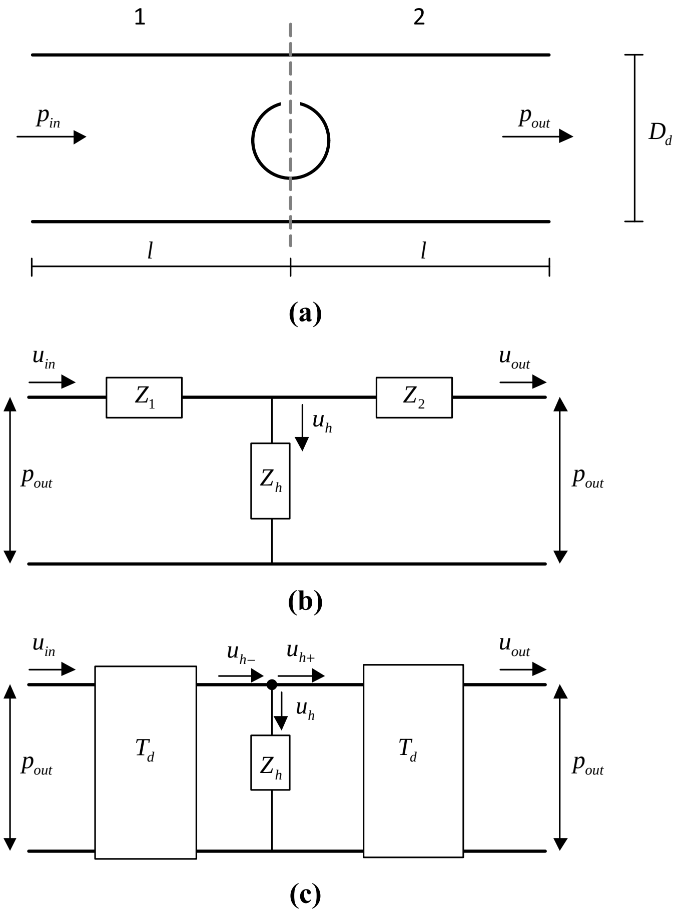

(a)

(b)

(c)

Figure 5.5: A Helmholtz resonator in a duct (a) can be represented as the equivalent circuit shown in (b), where the complex impedances associated with the duct can be modelled using 2-pole linear networks (c)

The transmission coefficient, T, of a metamaterial consisting of a resonator within a section of tube can now be calculated by substituting $\boldsymbol{U}_n = \boldsymbol{P}_n/z_n$ into the transfer matrix model and rearranging.

$$T = \frac{P_t}{Pi,0} = \frac{2}{\boldsymbol{\tau}_{1,1} + \dfrac{\boldsymbol{\tau}_{1,2}}{z_{N+1}} + z_{N-1}\boldsymbol{\tau}_{2,1} + \dfrac{z_{N-1}}{z_{N+1}} + \boldsymbol{\tau}_{2,2}} \tag{5.19}$$

where $z_{N-1} = z_{N+1} = z_d$, the acoustic impedance of the air within the duct. This provides a simple way of modelling the transmission behaviour of the metamaterial using the impedance of the Helmholtz resonators. Where multiple resonators are present within one layer of the metamaterial they can be considered to be positioned in parallel, and therefore can be combined in the usual manner for parallel impedances.

5.4 Metamaterial Sample Design and Manufacture

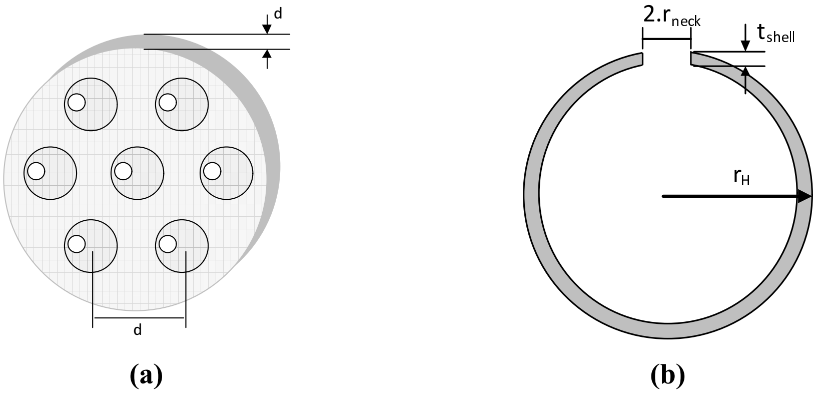

Figure 5.6: The schematic design of the metamaterial samples (a) the dimensions of the SHS resonators (b)

To validate the theory described above designs for a series of locally resonant acoustic metamaterials were produced and tested in an impedance tube set up using a 4 microphone method as proposed by Song and Bolton [97] and described in Section 5.5. As future metamaterial design moves into multi-degree of freedom devices and smaller dimensions traditional manufacturing techniques will be insufficient, emerging 3-dimensional printing techniques such as additive layer manufacture will become the only viable option. Therefore the metamaterials presented here, as well as confirming the acoustic performance of this type of material, serve as a validation of the 3D printing design approach for the production of small scale acoustic metamaterials.

The designs consist of individual circular samples, made up of a triangular porous mesh that contains an hexagonal array of 7 SHS hollow spheres, a schematic of the split hollow sphere and complete sample design is shown in Figure 5.6. The mesh is to provide structural integrity only and is designed to be, as far as possible, acoustically transparent. To provide additional structure integrity the samples are surrounded by a 1mm thick solid band of diameter 99.5mm (to fit into a 100mm diameter impedance tube), and the thickness of the samples and spacing of the resonators, both of which dictate the lattice constant, d, of 30mm. The samples have designed to be produced out of

Polyamide 6, using existing 3D printing technology. The material specification is to produce the highest possible modulus of elasticity, to ensure that the measured results are due to the effect of the metamaterial form on the propagation of sound through the air, and not due to resilience in the polymer structure itself.

In all, four types of metamaterial sample were specified[a]; three structures with arrays of SHS resonators of differing neck diameter, $2r_{neck}$, (types A-C in Table 5.1) and one structure with mixed resonators (two resonators of type A, three of type B, two of type C). In addition two control structures were specified; one a plain mesh with no SHS elements, and one with an array of solid (non resonant) spheres.

Type	$2r_{neck}$, m	r_H, m	t_{shell}, m	$\omega_0/(2\pi)$, Hz
A	0.0030	0.0125	0.0007	960
B	0.0040	0.0125	0.0007	1145
C	0.0060	0.0125	0.0007	1451

Table 5.1: Dimensions of the metamaterial samples

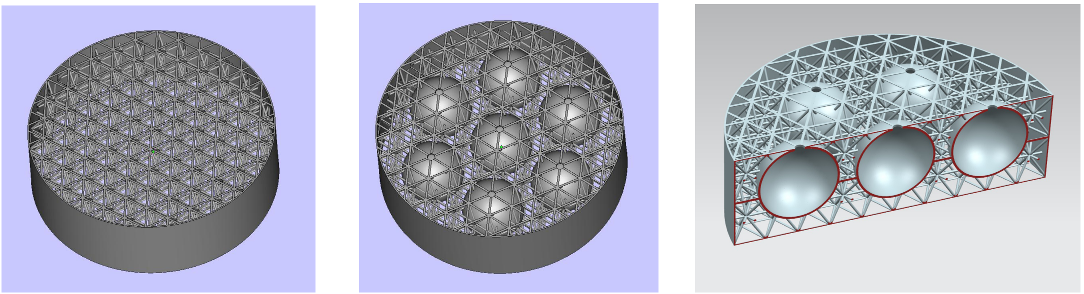
(a) (b) (c)

Figure 5.7: 3DCAD representations of the lattice structure (a) the hollow spheres embedded in the lattice (b) and a cutaway showing the interior of the hollow spheres (a)

The additive layer manufacturing (ALM) system used for these polymeric samples was an EOS P390 laser sintering system[b]. Laser sintering (LS) is a technique that utilises polymeric powder as a feedstock material to produce components in an additive manner.

---

[a] Specifying the detailed design and dimensions of these samples was carried out by Dr Gao Yan of the Institute of Sound and Vibration Research (ISVR), University of Southampton

[b] Transferring the concept design to a CAD representation and manufacture of the samples was undertaken by the EPSRC National Centre for Innovative Manufacturing in Additive Manufacturing, Nottingham University, with assistance of Dr Chris Tuck and Prof. Richard Hague

The LS system feeds the powdered polymer that is spread over the build area by a hopper and blade arrangement; this gives a layer of normally 100µm in thickness. The powder bed is heated close to the melt point of the material (175°C) and then a laser scans the bed with a single layer slice of the desired geometry taken from the CAD file. The process then repeats until all the remaining geometry has been completed and the system left to cool.

For the passive structures the complexity of the design, particularly with respect to the lattice structure encasing the SHS elements means that a manufacturing method that minimises support structures required for overhangs or island geometries is beneficial. LS is suitable because, as powder is delivered to the powder bed, it effectively forms a support structure around the material consolidated by the laser that will form the component. Once the system has cooled to ambient temperature the loose powder is shaken loose of the geometry and lightly cleaned to reveal the component. A typical manufactured sample (with all SHS having a 6mm neck diameter) is shown in Figure 5.8.

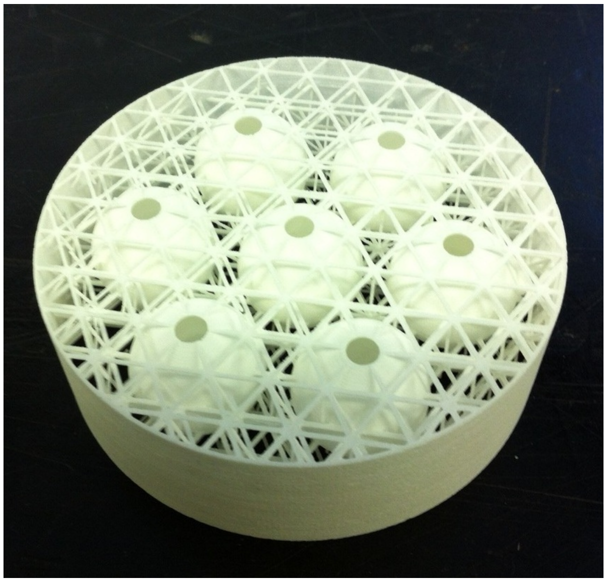

Figure 5.8: A photo of one of the manufactured acoustic metamaterial samples where all resonators have a 6mm neck diameter

5.5 Measurement Method

When testing the samples there are several properties that are of interest, namely the transmission behaviour across the sample, and the effective material parameters of the metamaterial. Song and Bolton [97] identify a method for testing a material sample within an impedance tube to determine the transmission matrix of a material which can be used to determine not only the transmission and reflection properties but the wave number and acoustic impedance of the sample. These values can then be used to determine the effective material parameters. The measurement method will be referred to as the 4 microphone technique. To perform the measurement the sample is placed within an impedance tube with two microphones positioned either side, as shown in Figure 5.9. A disturbance loudspeaker is used at one end of the impedance tube to provide a white noise signal and the measured signals recorded at the 4 microphone positions[c].

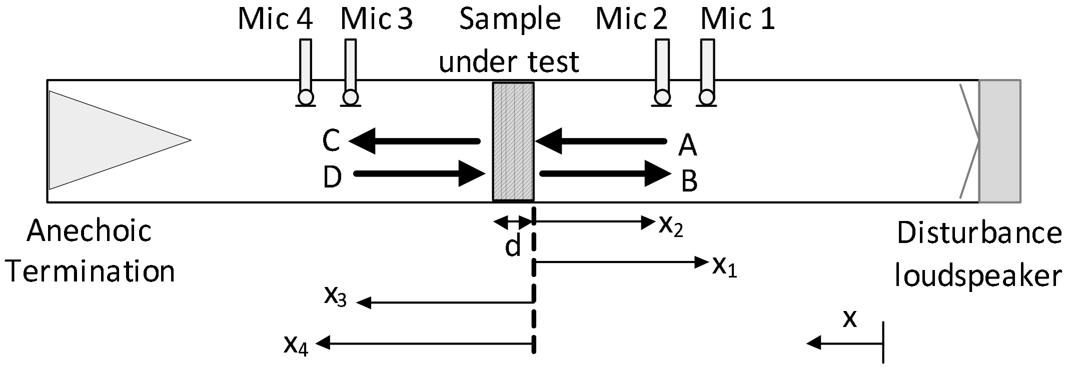

Figure 5.9: Measurement equipment used to measure the response of the acoustic metamaterial samples

Under the measurement set up detailed above 4 travelling waves are defined; a forward travelling wave from the loudspeaker, a backward travelling wave reflected from the sample, a forward travelling wave transmitted through the sample, and a backward travelling wave reflected from the impedance tube termination, labelled A-D respectively in Figure 5.9. Note that since in this case there is an anechoic termination that the amplitude of wave D should be close to zero. Now the signals at each of the 4

---

[c] To carry out the measurements a single microphone can be used and moved between the four positions or 4 microphones can be used at once provided compensators are applied to phase match the microphone array

microphones is a sum of the forward and backward travelling waves, expressed in the frequency domain as

$$P_1 = (Ae^{-jkx_1} + Be^{jkx_1})e^{j\omega t} \tag{5.20a}$$

$$P_2 = (Ae^{-jkx_2} + Be^{jkx_2})e^{j\omega t} \tag{5.20b}$$

$$P_3 = (Ce^{-jkx_3} + De^{jkx_3})e^{j\omega t} \tag{5.20c}$$

$$P_4 = (Ce^{-jkx_4} + De^{jkx_4})e^{j\omega t} \tag{5.20d}$$

Here an $e^{+j\omega t}$ sign convention is used to denote the direction of wave travel and the wavenumber is the complex wavenumber in air. The wavenumber is defined as $k = k_{prop} + jk_{diss}$ where the real (propagation) part of the wavenumber $k_{prop} = \omega/c_0$ and the imaginary (dissipative) element of the complex wavenumber is proportional to the diameter of the tube, r_d, calculated according to British Standard for the determination of sound absorption coefficients and acoustic impedance in impedance tubes [98] (Note that the standard presents this equation as an estimation method for survey purposes and is most accurate at low frequencies. Gaining an accurate representation of tube attenuation requires additional measurements comparing minima from standing waves. However for our purposes it provides a useful rough approximation).

$$k_{diss} = 0.0194\frac{\sqrt{2\pi\omega}}{2c_0 r_d} \tag{5.21}$$

Now by combining and rearranging Equations 5.20(a)-(d) the coefficients A-D can be calculated in terms of the 4 microphone signals.

$$A = \frac{j(P_1 e^{jkx_2} - P_2 e^{jkx_1})}{2 \sin k(x_1 - x_2)} \tag{5.22a}$$

$$B = \frac{j(P_2 e^{-jkx_1} - P_1 e^{-jkx_2})}{2 \sin k(x_1 - x_2)} \tag{5.22b}$$

$$C = \frac{j(P_3 e^{jkx_4} - P_4 e^{jkx_3})}{2 \sin k(x_3 - x_4)} \tag{5.22c}$$

$$D = \frac{j(P_4 e^{-jkx_3} - P_3 e^{-jkx_4})}{2 \sin k(x_3 - x_4)} \tag{5.22d}$$

The transmitted wave and reflected waves can then be easily calculated as $P_T = C/A$ and $P_R = B/A$ respectively. Additionally these coefficients represent the forward travelling and reflected wave amplitudes within the tube, which can then be used to calculate the pressure, P, at the surface on each side of the sample under test, and the particle velocity U.

$$P \mid_{x=0} = A + B \tag{5.23a}$$

$$U \mid_{x=0} = \frac{A - B}{\rho_0 c_0} \tag{5.23b}$$

$$P \mid_{x=d} = Ce^{-jkd} - De^{jkd} \tag{5.23c}$$

$$U \mid_{x=d} = \frac{Ce^{-jkd} - De^{jkd}}{\rho_0 c_0} \tag{5.23d}$$

with reference to the transfer matrix algebra detailed in Section 5.3 the transfer matrix across the sample under test can be used to relate the pressure and particle velocity at $x = 0$ and $x = d_N$. The matrix elements can be defined in terms of the pressures and particle velocities as

$$T_{11} = \frac{P\mid_{x=d_N} U\mid_{x=d_N} + P\mid_{x=0} U\mid_{x=0}}{P\mid_{x=0} U\mid_{x=d_N} + P\mid_{x=d_N} U\mid_{x=0}} \tag{5.24a}$$

$$T_{12} = \frac{P\mid^2_{x=0} - P\mid^2_{x=d_N}}{P\mid_{x=0} U\mid_{x=d_N} + P\mid_{x=d_N} U\mid_{x=0}} \tag{5.24b}$$

$$T_{21} = \frac{U\mid^2_{x=0} - P\mid^2_{x=d_N}}{P\mid_{x=0} U\mid_{x=d_N} + P\mid_{x=d_N} U\mid_{x=0}} \tag{5.24c}$$

$$T_{22} = \frac{P\mid_{x=d_N} U\mid_{x=d_N} + P\mid_{x=0} U\mid_{x=0}}{P\mid_{x=0} U\mid_{x=d_N} + P\mid_{x=d_N} U\mid_{x=0}} \tag{5.24d}$$

Note that $T_{11} = T_{22}$, which is a property of symmetrical systems such as the acoustic sample, and that the determinant of the transfer matrix $|T| = 1$, which is a property of reciprocal systems, and more specifically a constraint of passive, linear, four-pole networks [80, pg. 223]. Now the transfer matrix elements are known, with reference to Equation 5.15, the wave number of the material can be calculated as

$$k = \frac{1}{d}\cos^{-1} T_{11} \tag{5.25}$$

and the characteristic acoustic impedance can be calculated as

$$Z_n = \rho_e c_{met} = \sqrt{\frac{T_{12}}{T_{21}}} \tag{5.26}$$

where ρ_e and c_{met} are the effective density and sound speed of the material sample. The effective bulk modulus can now be determined as

$$B_e = Z_n c_{met} \tag{5.27}$$

5.6 Measurement Results

Although it is not required by the method, for the measurements presented in this thesis the far end of the impedance tube contained an anechoic termination for convenience. To produce the disturbance signals and record the microphone signals the same dSpace system described in Chapter 3 was used. Analysis was then carried out in `MATLAB`.

5.6.1 Transmission of Acoustic Waves

From the transfer matrix approach detailed in Section 5.3, it is clear that as more layers of metamaterial are added the transfer matrix, $\boldsymbol{\tau}$, is raised to a higher power such that $\boldsymbol{\tau} = \boldsymbol{T}_n^N$. There will be zeroes associated with the layer transfer matrix $\boldsymbol{T}_n$ that are responsible for the region of attenuation due to the resonator elements; the band gap. Therefore as more layers are added, the denominator equations that produce these zeroes are raised to the power N, creating additional zeros. These zeroes occupy the same location in the complex plane, which means one would expect the depth of the band gap to increase as more layers are added, but the location of the band gap in the frequency domain to remain constant. Figure 5.10a confirms this behaviour occurring in both simulations and measured results. The frequency of attenuation is consistent with the natural frequencies stated in 5.4 for a 4mm neck diameter, with any small discrepancies attributable to manufacturing tolerances. The level of attenuation achieved and the Q-factor of the notch achieved in the simulations should be viewed with caution, since the width and depth of the band gap achieved is controlled by intrinsic losses in the resonator elements, which in this case have been adjusted to fit the measured results.

Conversely, changing the radius of the resonator neck has a direct effect on the frequency at which the reactance of the resonators equals zero, leading to a change in the location of the resulting band gap. Figure 5.10b shows how the band gap changes location as the resonant frequency of the resonators is changed for both simulated and measured results. As a control, mesh structures containing no resonator elements were also measured, where the lack of resonant behaviour means that the transmission behaviour should be unity (neglecting the propagation loss due to viscous losses within the tube). Figure 5.10c demonstrates this, where the plain mesh produces almost zero transmission loss and phase change across the frequency range. The same result was observed for the control sample consisting of solid spheres, although the result is not presented here.

5.6.2 Effective Material Parameters and Wave Number

The advantage of the 4 microphone technique described in Section 5.5 over more traditional transmission loss measurements is the ability to calculate not only the transmission behaviour of the material but the specific acoustic impedance and the wave

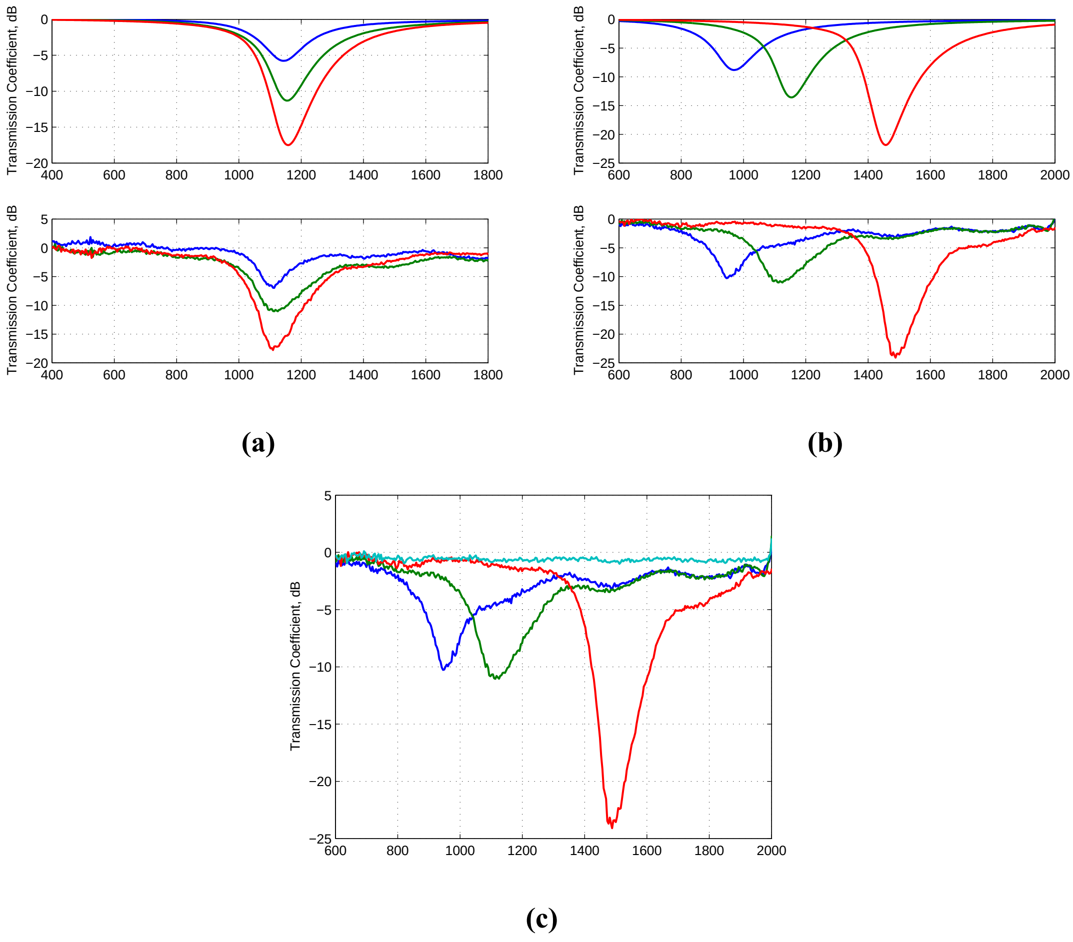

(a)

(b)

(c)

Figure 5.10: (a) The transmission behaviour of 1 (blue), 2 (green) and 3 (red) layers of the 4mm resonator metamaterial, simulated (top) and measured (bottom). (b) The transmission behaviour of 2 layers of 3mm (blue), 4mm (green) and 6mm (red) resonator metamaterial, simulated (top) and measured (bottom). (c) The measured transmission behaviour of 3 layers of 3mm (blue), 4mm (green) and 6mm (red) compared to a plain mesh (light blue) with no resonator elements

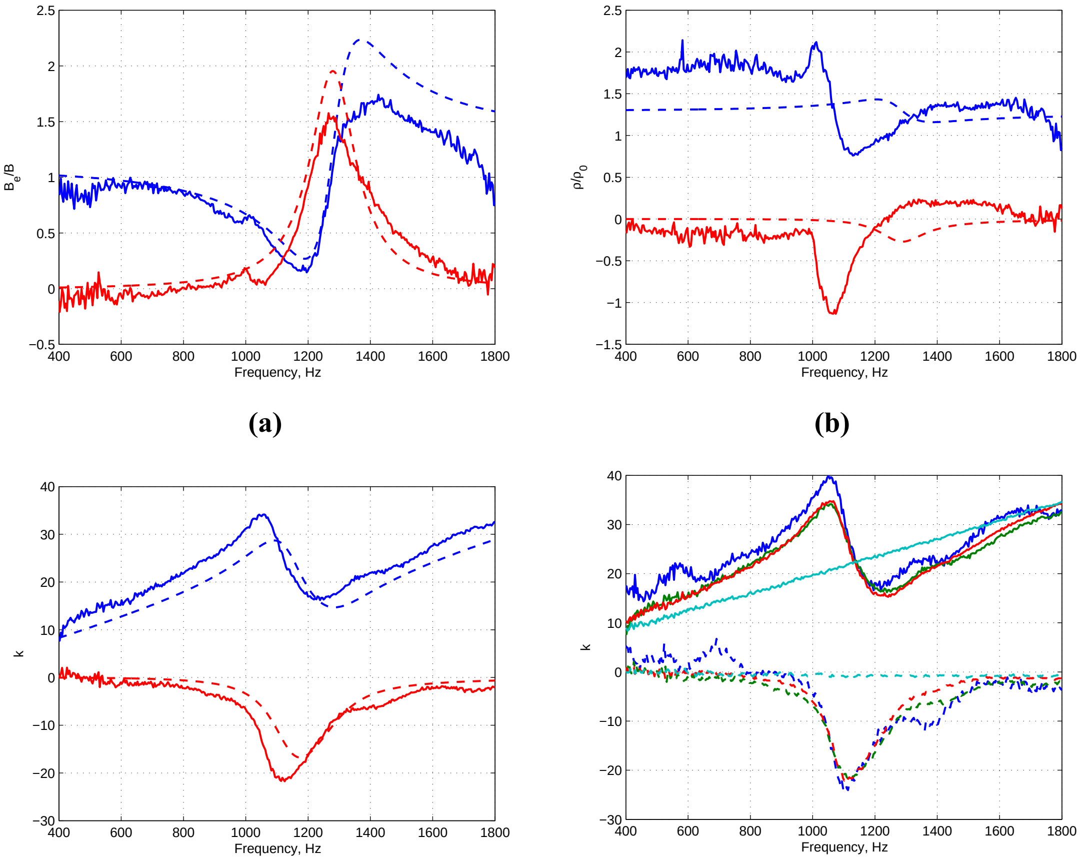

(a) **(b)**

(c) **(d)**

Figure 5.11: The real (blue) and imaginary (red) part of the bulk modulus (a), density (b) and wave number (c) of a 3 layer metamaterial with 4mm type resonators, simulated (dotted) and measured (solid). (d) The measured wave number of a metamaterial of 4mm type resonators consisting of 1 (blue), 2 (red), 3 (green) layers, and an empty mesh (light blue)

number as well. From this it is possible to calculate the bulk modulus and density. This is of particular interest in the study of acoustic metamaterials; achieving controllable and even negative effective material parameters is key to achieving potential powerful applications such as acoustic cloaks or sub-wavelength lenses.

Figures 5.11a, 5.11b and 5.11c show the simulated and measured bulk modulus, density and wave number respectively of 3 layers of a metamaterial with 4mm type resonators. The real part of the wave number has a negative gradient around the resonant frequency of the resonator inclusions, a result of the dispersive effective material parameters shown (note that in the measurements performed the bulk modulus and density are inferred from the measured wave number and impedance, however in reality it is logical to consider the dispersion behaviour a consequence of the dispersive effective material parameters of the material). The bulk modulus calculations provide a good agreement with the measurement results. Whilst the density calculations appear to match the dispersive nature of the measurement results, the model appears to overestimate the frequency at which this dispersive behaviour occurs. This could be a consequence of the lumped parameter model; dividing a continuous system into discrete degrees of freedom has the consequence of constraining the system, and therefore one would expect the natural frequency of the modes of the system to be overestimated. However, this is just conjecture, and the magnitude of this effect suggests that another mechanism might be the cause of this. The measured results of the effective density are also very noisy, further obscuring the true effect and making comparison difficult. This requires further investigation. However, the magnitude of the dispersive component of the density calculations is relatively small, meaning the bulk modulus appears to be the dominant force for creating a dispersive wave number in the metamaterial, therefore the calculated wavenumber still provides an accurate prediction of the measured results. The small magnitude of the dispersive density is due to the relatively low mass of air in the resonator necks, whose out of phase motion being the origin of the dispersive behaviour, is small compared to the mass of air in the duct.

The effective material parameters of the material does not change with the addition of extra layers of metamaterial, as it is function of the ratio of the resonator volumes to the overall volume of the metamaterial, something which will remain constant. This means that the wavenumber remains constant with the addition of extra layers, as demonstrated in Figure 5.11d. The extent of the wave number bending remains approximately the same for measurements of 3mm type resonator metamaterials of 1 to 3 layers. The figure also shows the wave number of the mesh samples which is shown to be equal to that expected in air, with the real part increasing linearly with frequency and an imaginary part of zero.

Whilst the bulk modulus and density are shown to have a dip around resonance in most cases measured the dip is not enough to overcome to the static material parameters of the transmission medium and achieve negativity. Therefore the materials presented here do not achieve SNG or DNG behaviour. As described above, adding more layers to the metamaterial does not increase the dispersive effect since the filling fraction of resonator to ’transmission’ volume remains constant. To achieve negativity the dip must be made deeper. This could theoretically be achieved by reducing the losses within the resonators, however in reality this would be very difficult. More practically, the dimensions of the metamaterial could be changed to increase the volume ratio or the resonators and therefore allow the dispersive bulk modulus components to have a greater influence

Again, as with the levels of transmission loss described in Section 5.6.1 the magnitude of the effects seen are dependent on the losses contained within the metamaterial. It may be possible to attempt to measure and quantify the loss factors involved and improve the simulations however the motivation behind this work is to provide a proof of concept for the metamaterial design, and therefore an accurate representation of losses is not required and the loss factors used in the simulated results were adapted to fit the measured results.

5.7 Mixed Resonators

Whilst the results presented above demonstrate the efficacy of using metamaterials to achieve transmission loss and to affect the effective material parameters, the desired behaviour only occurs in a narrow frequency band around the resonant frequency of the resonant elements. Therefore it is desirable to widen the region where this desired behaviour occurs. One route to achieving this is to combine metamaterials of mixed resonator types, so the effects occur at more than one frequency similar to the effect demonstrated in Section 2.5, and by Ding *et al* [6]. Figure 5.12 compares the performance of 2 such multilayer metamaterials, where one material (’mixed resonator’) has been created by using 2 identical layers that consist of a mix of resonators (2 x 3mm, 3 x 4mm, 2 x 6mm) and another (’mixed layer’) has been created by using 3 distinct layers where each layer has a different resonator type. As the figures show, by mixing the

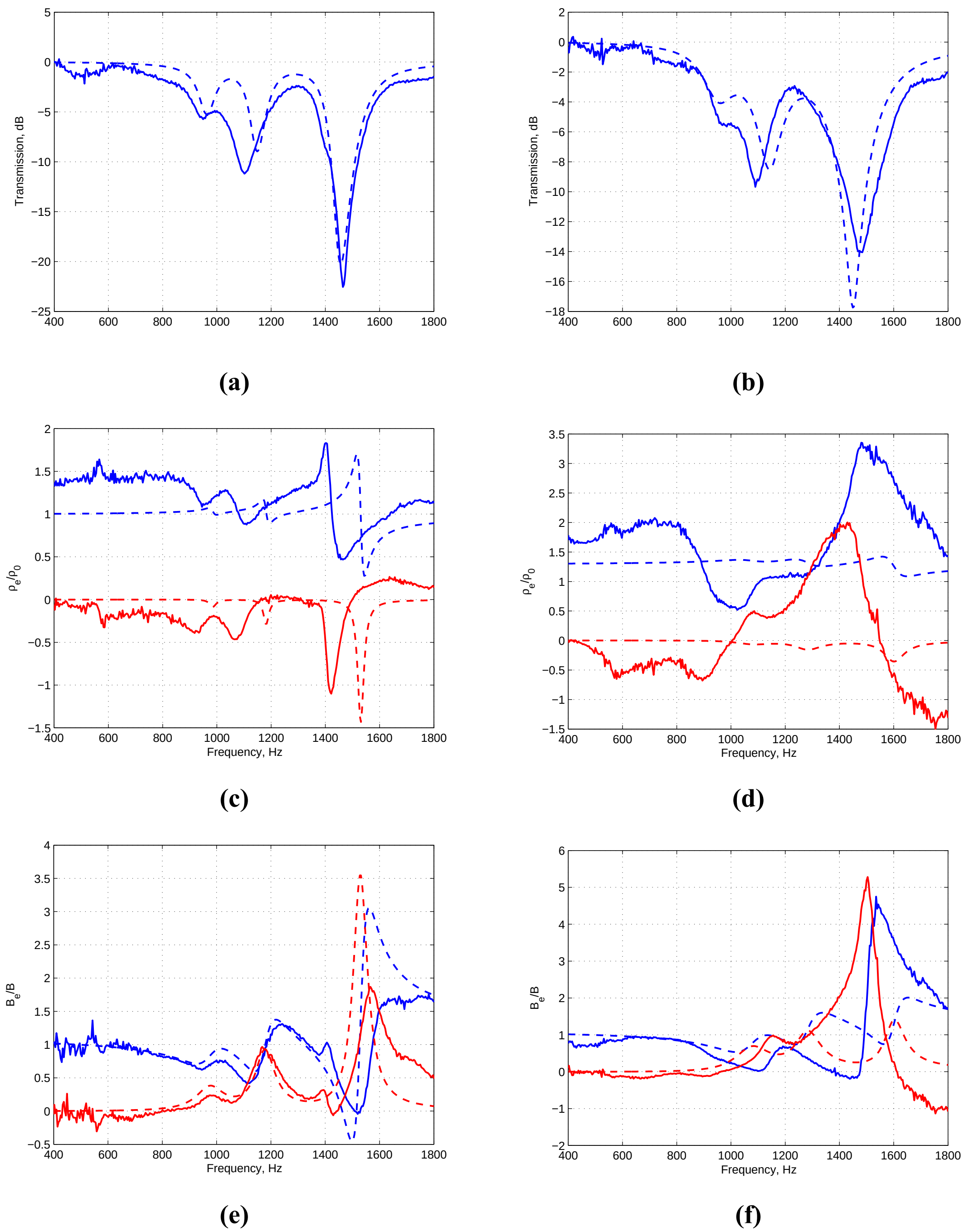

Figure 5.12: The transmission coefficient (a), density (c) and bulk modulus (e) of 3 layers of a mixed resonator material, and of a 3 layer metamaterial consisting of 1 layer of each resonator type (b), (d) and (f) respectively. Simulated (dotted) and measured (solid) performance. The effective material parameters have a real (blue) and imaginary (red) part

resonator types the resonant band gap and the dispersive nature of the bulk modulus and density can now be seen at multiple frequencies. If the resonator frequencies were set such that these regions overlapped then a single, wide band, region of attenuation could be expected. The wave number plots for these measurements is shown in Figure 5.13.

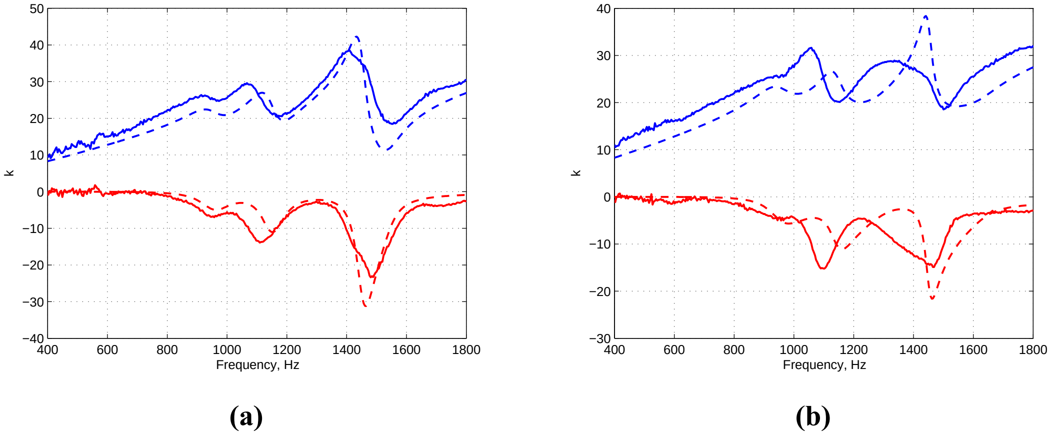

Figure 5.13: The wave number of (a) 3 layers of a mixed resonator material, and (b) a 3 layer metamaterial consisting of 1 layer of each resonator type. Simulated (dotted) and measured (solid) performance, real part (blue) and imaginary part (red)

The form of the predictions for the effective material parameters for the 'mixed resonator' type metamaterial are reasonably accurate, (excepting the over prediction for the frequency at which the density becomes dispersive, as discussed in Section 5.6.2). However for the 'mixed layer' example the predictions are less accurate. Unlike the 'mixed resonator' example where there the different resonators are all located at the same point in the plane wave (i.e. in parallel), each layer in the 'mixed layer' material is different, and it could be that this could cause complex transmission/reflection waves between the layers. The expressions governing the material parameters from Section 5.2 uses the assumption that each layer contains the same Z_h element; when multiple resonators are connected in parallel an equivalent single Z_h impedance element is calculated. When the layers are different this assumption no longer holds, and the expressions will no longer be accurate. The results presented in the figure for the 'mixed layer' material were calculated by taking the average value across the three layers at each frequency. The measured results suggest that the actual behaviour is more complicated than this. One potential solution would be to treat the three layers as one large layer where all the resonators are attached in parallel, however at three layers the material is 90mm thick. This is approximately a third of a wavelength at 1400Hz; such large dimensions stretch the credibility of the long wavelength assumption ($kd \ll 1$), and therefore a different method must be sought to accurately model this type of material.

The above results demonstrate the effect that the resonant elements have on the behaviour of plane waves as they travel through the metamaterial. If it is low frequencies that are of interest, as is the case in audio frequencies for example, then the lattice constants required to take advantage of periodic Bragg effects become prohibitively large, and therefore it is only resonant band gaps are of practical use.

5.8 Number of Resonators

Since this is a metamaterial and not a phononic crystal, the effects described above are due to the resonant nature of the Helmholtz units acting like a lumped mass and spring, and not due to scattering caused by their physical presence. Therefore if the number of resonator units is reduced, even though the number of *physical inclusions* is kept constant, the magnitude of the transmission loss and dispersive behaviour will reduce. In practice this can be tested by blocking the holes of a number of the Helmholtz resonators within the metamaterial.

For the results presented in this section the predictions for the transmission performance of the metamaterial have been calculated using a slightly different method to the results presented previously in this chapter. Rather than calculate a combined transfer matrix (as $\boldsymbol{\tau} = \boldsymbol{T}_d \boldsymbol{T}_h \boldsymbol{T}_d$), a single transfer matrix is used to represent a layer of metamaterial

$$\mathbf{T}_n = \begin{bmatrix} \cos(k_n d_n) & j z_n \sin(k_n d_n) \\ \dfrac{j \sin(k_n d_n)}{z_n} & \cos(k_n d_n) \end{bmatrix} \tag{5.28}$$

where the wavenumber is calculated as $k_n = c_n/\omega$ where $c_n = \sqrt{B_e/\rho_e}$. Z_n is calculated as a Thévenin equivalent impedance of the single layer of the metamaterial, with reference to Figure 5.5b

$$Z_n = Z_1 + \frac{1}{\frac{1}{Z_h} + \frac{1}{Z_2}} \tag{5.29}$$

where $Z_1 = Z_2 = z_0/S_d$. This is referred to herein as the ’wavenumber method’. Results calculated with this model agree well in most cases with that given by the three transfer matrix model used previously, but it has not been used in the previously presented results due to inaccuracies that arise with the wavenumber method under certain conditions, discussed in Chapter 6. The wavenumber method is used for these calculations since the results presented below exhibits a subtle frequency shifting behaviour when the number of resonators changes, explained below. A small effect that is not predicted by the three transfer matrix method, but apparent in the measured results presented here.

Figure 5.14 demonstrates this effect experimentally compared to what would be expected from the wavenumber model, where the number of resonators increases from 1 to 6 inclusions, 1 resonator at a time. As predicted the level of transmission loss as the number of resonators increases.

Of interest is the fact that as the resonator number increases, the centre frequency of the resonant effects on the model of the material parameters appears to shift upwards in frequency (note only the real part is plotted, for clarity). In the measured results this effect is seen on the measured effective bulk modulus, but is not clearly apparent on the density. This effect carries through to the ’downstroke’ of the section of the wave number, and also subtly changes the transmission response centre frequency. Examining the effect for the 6mm neck metamaterial, Figure 5.15 it is clear that this shifting in frequency is more pronounced, so much that it is discernible in the shifting centre frequency of the measured band gap. It is also visible in the measured effective density although the effect is small.

Clearly, there is a mechanism at work here that causes the centre frequency of the resonant effects to change as more resonators are added. The results suggest that a larger neck diameter increases this effect, although it is not clear if this is due to the change purely in the neck size or the change in the natural frequency of the resonator. The most likely culprit for this is the adjacent resonators coupling together such that their mutual presence changes their individual performance. This behaviour is reflected in the results calculated using the effective material parameters model.

Coupling effects have previously been acknowledged in the literature, although the

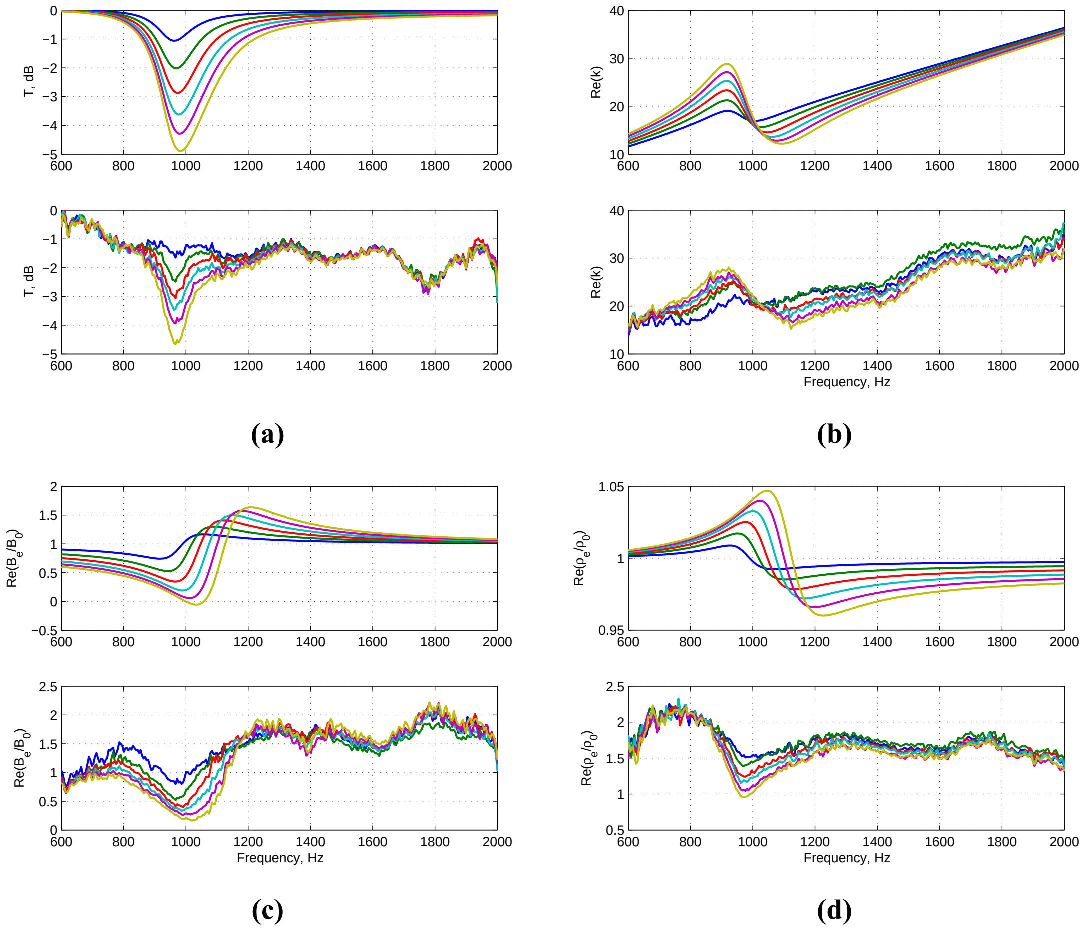

(a) (b) (c) (d)

Figure 5.14: (a) The transmission performance, and real parts of the (b) wave number, (c) bulk modulus and (d) bulk modulus of the 3mm neck diameter acoustic metamaterial where the resonator number varies from 1-6. Theoretical (top) and measured (bottom) results

amount of empirical work is small; Ingard [94] notes that coupling occurs between closely spaced resonators and this reduces the maximum level of absorption of each resonator, and further work by Mechel [99] shows that arrays of resonators will have a wider band of absorption than a single resonator. More recently Johansson and Kleiner [100] investigated the problem from the point of view of mutually coupled pipe organ enclosures, and explicitly modelled two Helmholtz resonators on close proximity, demonstrating the detuning phenomenon that appears in such systems. Johansson and Kleiner show the centre frequency decreasing with increased coupling, and attribute this to the propagation delay between two adjacent resonators in free space. The results here

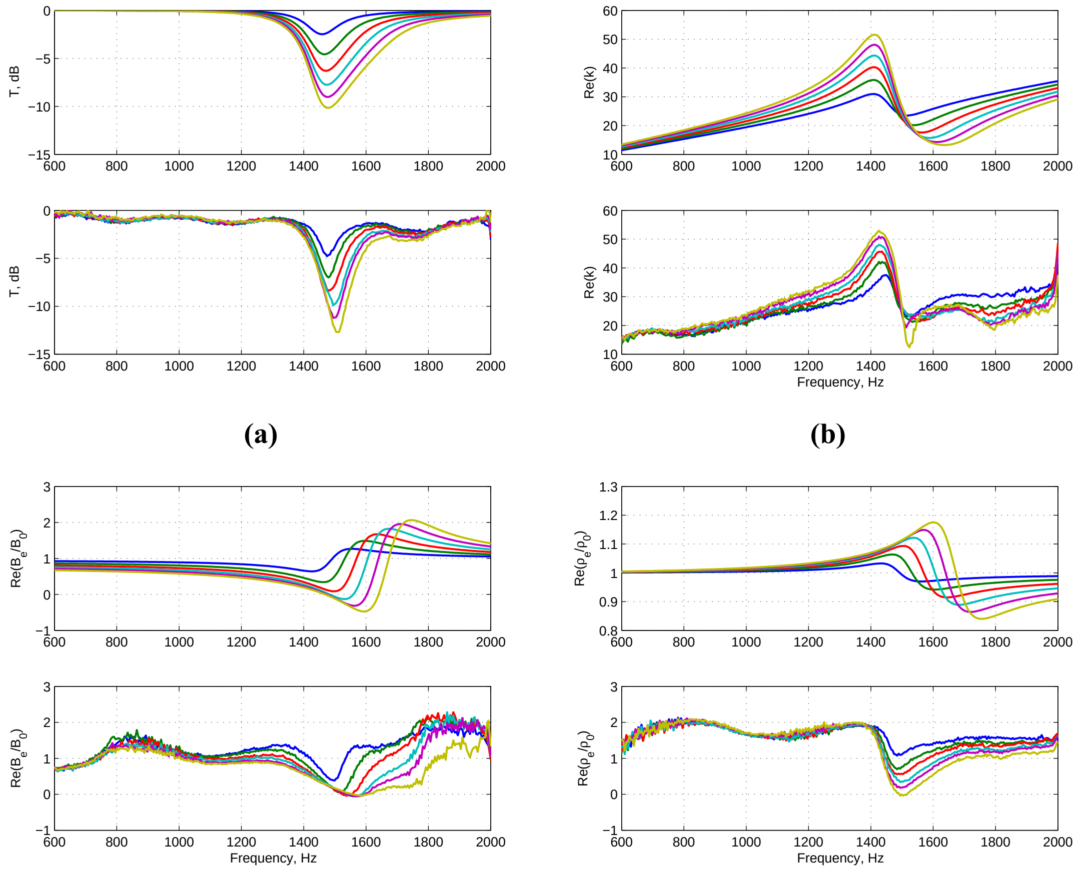

(a) **(b)**

(c) **(d)**

Figure 5.15: (a) The transmission performance, and real parts of the (b) wave number, (c) bulk modulus and (d) bulk modulus of the 6mm neck diameter acoustic metamaterial where the resonator number varies from 1-6. Theoretical (top) and measured (bottom) results

show the centre frequency *increasing*. Since the metamaterial is subject to plane wave propagation, propagation delay cannot be the culprit in this case, instead it may be the effects of mutual impedance between the resonators acting as radiating sources. If the radiation impedance of the resonators is affected this would alter the effective length of the resonator necks, and hence their natural frequency. It would require further investigation, however, to confirm this and accurately model the behaviour, and is beyond the scope of this research. For the purposes of isolation applications the detuning effects from coupling are relatively small compared to the bandwidth of the band gap, and can therefore often be neglected, meaning the three transfer-matrix method for calculating transmission coefficient is valid and accurate.

5.9 Conclusion

The work presented in this Chapter describes a passive acoustic metamaterial consisting of an array of SHS elements acting as Helmholtz resonators. Using a lumped parameter equivalent circuit approach mathematical expressions describing the effective bulk modulus and density were derived and the metamaterial is shown to have the potential to become double negative. Previous studies on similar metamaterials have focused on the effective bulk modulus and neglected the effective density. The model developed in this Chapter demonstrates that both material parameters are in fact dispersive, agreeing with the observations of Cheng *et al* [66]. The effective material parameters were combined with a transfer matrix formulation using the ATLM to predict the transmission coefficient of the metamaterial.

A metamaterial design for production several examples were produced using additive layer manufacturing techniques (3D printing). These samples were tested in an impedance tube and the transfer matrix model was shown to accurately predict the transmission coefficient, effective bulk modulus and wave number of the metamaterial. The form of the effective density is accurately predicted, however the frequency at which the dispersive behaviour occurs is somewhat overestimated, perhaps due to the constrained nature of the lumped parameter assumption.

By combining different resonators within the same metamaterial layer it was demonstrated that it is possible to create multiple or wider band gaps and regions of dispersive material parameters. This is similar to the strategy employed on the uncoupled viscoelastic metamaterial, described in Section 2.5. It was possible also to create multiple band gaps by using several metamaterial layers, where each layer contained a different resonator type. However, this structure violates the periodic assumption used to derive the effective material parameter model, and therefore the predicted material parameters do not match those measured within the laboratory.

Finally the issue of resonator coupling was investigated by changing the number of resonators present in a single layer. There appears to be some degree of coupling between the resonators which changes the frequency at which the resonant behaviour occurs. The wavenumber model appears to capture this behaviour somewhat, but is based on lumped parameter approximation and is inaccurate under certain conditions (discussed in the next

Chapter). Attempts to address Helmholtz resonator coupling in the literature remains rudimental at this time. This could be of particular consequence in the development of active acoustic metamaterials where the coupling effects, if not modelled accurately, could lead to instabilities in the closed loop response.

Overall the method for modelling Helmholtz resonator based metamaterials developed in this Chapter is shown to be useful and accurate, and the experimental results provide a validation of the metamaterial structure and, importantly, a use case of producing acoustic metamaterials using 3D printing techniques, paving the way for materials to be produced on smaller scales and in higher dimensions.

Chapter 6

Design of an Active Helmholtz Resonator For Use in an Acoustic Metamaterial

6.1 Introduction

A passive acoustic metamaterial consisting of an array of Helmholtz resonators was introduced in Chapter 5. The metamaterial provides a passive band gap and region of dispersive material parameters. Multiple regions of attenuation can be achieved by changing the resonant frequency of some of the inclusions, such that several smaller band gaps can be achieved, and by tuning these bands appropriately it is possible to get them to merge. However, to create a wide band gap and still retain an acceptable level of attenuation would require a large number of resonators, therefore a more desirable method to increase the metamaterial performance is to incorporate active control elements into the structure, similar to the active viscoelastic metamaterial described in Chapters 3 and 4.

Helmholtz resonators are traditionally used for narrowband disturbances, and semi-active resonators have been considered in the literature, such as those by Lee *et al* [101] and Hao *et al* [102], where the volume of the resonator is adapted by using water and a mechanical mechanism respectively. Whilst this adds an adaptive function to the resonators, and would allow the region of attenuation to be adjusted, it would not increase the performance of the metamaterial with respect to the level or bandwidth of the dispersive properties and attenuation. Active functionality in this sense has been investigated more recently by Akl and Baz [67], using shunted piezoelectric patches to alter the effective bulk modulus of the metamaterial, however this is using a local analogue control strategy where shunt circuits are used to tune a self sensing piezoelectric actuator. The potential of this approach is limited by the purely dissipative nature of the system. A fully active approach, one that is able to add energy into the system, has the potential to outperform the above strategies. A fully active Helmholtz resonator was designed by Yuan [103] using an acoustic actuator at the base of the resonator cavity to influence the velocity of the fluid within the neck of the resonator. The active resonator was attached to a duct in a ’side-firing’ configuration, and by manually manipulating the poles of a second order feedback controller it was shown that the attenuation of propagating noise could be widened compared to using a passive Helmholtz resonator. The work in this Chapter considers an active acoustic metamaterial consisting of active Helmholtz resonators. The resonators in an active metamaterial are, by necessity, much smaller than one would use for traditional sound isolation applications, such as those studied by Yuan, however building on this model it is possible to investigate the potential levels of performance that could be achieved, and to demonstrate the levels of attenuation that are possible using the optimised control design methods developed in Chapter 4.

Using an impedance model of the resonator the model of the active metamaterial can be constructed using the transfer matrix method described in Chapter 5. Initially, to investigate the performance potential of such a metamaterial, the formal stability limits of a second order control loop are derived and the performance at these limits examined. Next, to develop a practical feedback controller, constrained non-linear optimisation is used to design FIR filters designed to minimise sound transmission over a specified frequency range. The affect on transmission coefficient and the effective material parameters of these controllers is then examined. It is shown that using optimised filters in this way can greatly increase the bandwidth over which attenuation is achieved, or create new regions of attenuation whilst retaining the passive band gap performance. The regions of attenuation coincide with the dispersive nature of the effective material parameters and negative bulk modulus can be achieved.

Next, inspired by the response of the optimised filters created using the above method, which tend to consist of a single resonant peak, the optimisation routine is applied to design simple 2nd order pole-zero controllers. It is shown that a simple resonant structure could create new regions of attenuation, but due to the limit on the degrees of freedom of the system, the bandwidth of these new band gaps is narrower than that achieved with FIR filters. Such a simple system could be achieved with analogue electronics, and used in situations where the reduction in complexity is desirable. However further investigation is required into the performance achievable with these types of controllers is required.

For simplicity the investigations detailed in this chapter are for metamaterials that consist of a single resonator. Note that for the passive case, a single resonator of these dimensions offers a relatively small amount of attenuation, in the region of 1dB. It is important to note that the resonator is intended to be a single part of an array of resonators making up a metamaterial whose performance would be much greater, as shown in Chapter 5. To extend the model to a greater number of resonators may require further development of the model to incorporate coupling effects such as those detailed in Section 5.8.

6.2 An Active Helmholtz Resonator Within a Duct

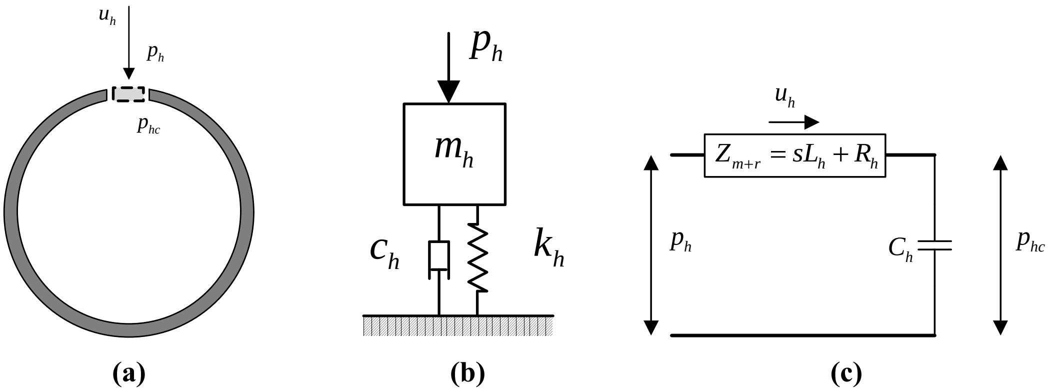

Figure 6.1: A SHS element as a Helmholtz resonator (a) its lumped mechanical model (b) and an equivalent circuit representation (c)

The model of the Helmholtz resonator is built using well established theory [93, pg. 286] previously summarised in Section 5.1. The action of a Helmholtz resonator results from the mass of air within the neck of the resonator moving with a the velocity u_h due to the acoustic pressure incident on the mass, p_h, shown in Figure 6.1a. The air within the cavity acts as a spring, the compression of which induces a pressure within the cavity p_{hc}. The resonator may be considered using a lumped mechanical model, such as that shown in Figure 6.1b. An equivalent circuit representation of this mechanical model is shown in Figure 6.1c, where the inertance of the mass of air within the neck is defined as $L_h = m_h/S_n^2$ and the compliance of the volume of air within the cavity $C_h = S_n^2/k_h$. The mass is calculated as $m_h = \rho_0 S_n L'_{neck}$, and the stiffness $k_h = \rho_0 c_0^2 S_n^2/V_h$. The resistance of the system R_h is a function of the thermoviscous resistance due to motion of air within the resonator and friction as the mass of air the neck, R_v, and the radiation resistance due to sound radiating into the surrounding medium R_r [94].

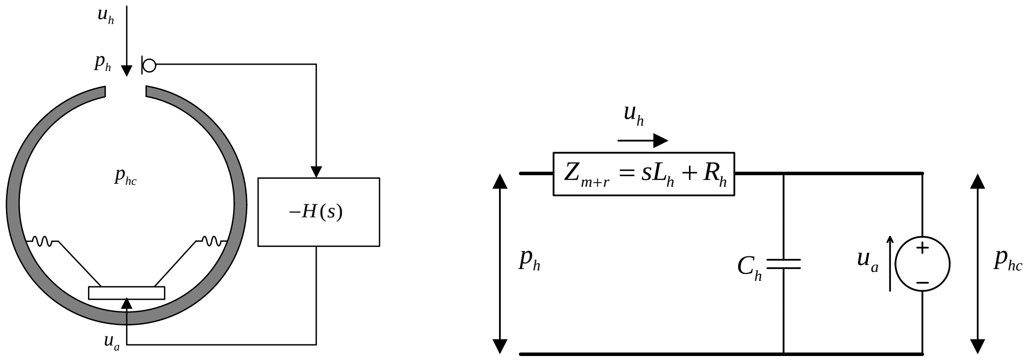

(a) (b)

Figure 6.2: A SHS element as with added active functionality (a) and equivalent circuit of this system (b)

Now consider an active Helmholtz resonator containing an acoustic actuator capable of producing a pressure within the resonator cavity. The actuator is controlled using a microphone to detect the pressure at the resonator neck and a controller $H(s)$. Such a structure is shown in Figure 6.2a and is represented by the circuit shown in Figure 6.2b. The work of Yuan [103] demonstrates how to calculate the acoustic impedance of such an active Helmholtz resonator, reproduced here for reference. The velocity of the mass of air within the resonator neck is proportional to the pressure differential across the neck and the impedance of the mass and loss terms

$$u_h = \frac{p_h - p_{hc}}{Z_{m+r}} \tag{6.1}$$

where the pressure within the acoustic cavity is proportional to the integration (described here using the Laplace operator) of the velocity of the mass of air

$$p_{hc} = \frac{u_h k_h}{s} = \frac{u_h}{sC_h} \tag{6.2}$$

Now, at the base of the resonator an actuator is used to induce an additional volume velocity u_a within the resonator cavity such that the pressure within the cavity is proportional to the integration of the two velocities such that

$$p_{hc} = \frac{(u_h + u_a)}{sC_h} \tag{6.3}$$

where the velocity due to the actuator is defined as

$$u_a = -G_{ls}(s)H(s)p_h \tag{6.4}$$

where G_{ls} represents the dynamics of the actuator. By combining these equations the pressure within the cavity can be expressed as

$$p_{hc} = \frac{1 - Z_{m+r}G_{ls}(s)H(s)}{sC_h Z_{m+r} + 1} \tag{6.5}$$

Combining 6.5 and 6.1 yields

$$Z_a = \frac{p_h}{u_h} = \frac{(sC_h Z_{m+r} + 1)}{sC_h + G_{ls}(s)H(s)} = \frac{(sC_h(sL_h + R_h) + 1)}{sC_h + G_{ls}(s)H(s)} \tag{6.6}$$

Using this impedance representation the transmission performance of an active metamaterial consisting of a single active resonator within a section of tube can now be calculated by combining this expression with the transfer matrix model used to model the passive metamaterial from Chapter 5, and reproduced here

$$T = \frac{P_t}{Pi,0} = \frac{2}{\boldsymbol{T}_{1,1} + \dfrac{\boldsymbol{T}_{1,2}}{z_{N+1}} + z_{N-1}\boldsymbol{T}_{2,1} + \dfrac{z_{N-1}}{z_{N+1}} + \boldsymbol{T}_{2,2}} \tag{6.7}$$

$$\therefore T = \frac{2Z_a}{2Z_a(\cos kd + j\sin kd) + z_d(\cos kd + j\sin kd)} \tag{6.8}$$

where $z_{N-1} = z_{N+1} = z_d$, the acoustic impedance of the duct. Considering the transmission loss of a single layer, the delay term $1/(\cos kd + j\sin kd)$ can be neglected. Substituting in Equation 6.6 and rearranging this expression gives the closed-loop transfer function, T

$$T = \frac{s^2 2L_h C_h + s2R_h C_h + 2}{s^2 M_h C_h + s(2R_h C_h + z_d C_h) + (2 + z_d G_{ls}(s)H(s))} \tag{6.9}$$

The impedance can also be used to calculated the effective material parameters of the resonator within a duct using Equations 5.13 and 5.12 respectively from Chapter 5.

6.2.1 The actuator dynamics, G_{ls} and the plant response, G

As defined in the model of the active Helmholtz resonator, G_{ls} describes the volume velocity induced in the resonator cavity as a function of the pressure measured at the neck. The plant response G describes the plant response of the control loop, and therefore incorporates not only G_{ls} but the dynamics of the resonator linking the actuator at the base of the resonator to the microphone at the neck. For this investigation a loudspeaker is the considered actuator which, assuming that the drive circuit dynamics (i.e. inductance of the coil etc.) are small, can be approximated as a mass (i.e. the cone and coil) on a spring (the cone suspension). Therefore the actuator dynamics can be represented by a simple second order model

$$G_{ls}(j\omega) = \frac{g_a}{-\omega^2 + 2\xi_a\omega_a j\omega + \omega_a^2} \tag{6.10}$$

The parameters of this model were chosen to be representative of the KDMG20008 loudspeaker by Kingstate, which is a small loudspeaker of appropriate dimensions to be fitted in a metamaterial of the scales investigated in Chapter 5. The frequency response of the KDMG20008 is given by the loudspeaker datasheet, contained in Appendix F. The natural frequency of the of the loudspeaker in rad/s is $\omega_a = 2\pi \times 850\texttt{Hz}$. The damping ratio $\xi_a = 1/(2Q_{ls})$ where the Q-factor is determined by 3dB points of the response, which are estimated to occur at 500Hz and 1300Hz, therefore $Q_{ls} = \omega_a/(2\pi(1400 - 500))$. To choose the gain coefficient g_a a monopole model of a loudspeaker in free space is used where the sound pressure $p(r)$ at a distance r can be calculated using a bounded Green's function as [104, pg. 553]

$$p(r) = \frac{j\omega\rho_0 v_{in} G_{ls} e^{-jkr}}{4\pi r} \tag{6.11}$$

The datasheet for the loudspeaker (Appendix F) contains a measured response for the sound pressure level for a given input, of which there are two examples - 1W/1m and 0.3W/0.1m. A gain coefficient of $g_a = 0.6$ was chosen such that the resonant peak of the model approximately matches that of the first resonance in the datasheet for a voltage input, $v_{in} = \sqrt{W\Omega_a}$ where W is the power input and the nominal impedance of the loudspeaker $\Omega_a = 8$ Ohms (the real resistive load of the loudspeaker will not be linear in this fashion, however this is an approximation for the purposes of this study). The

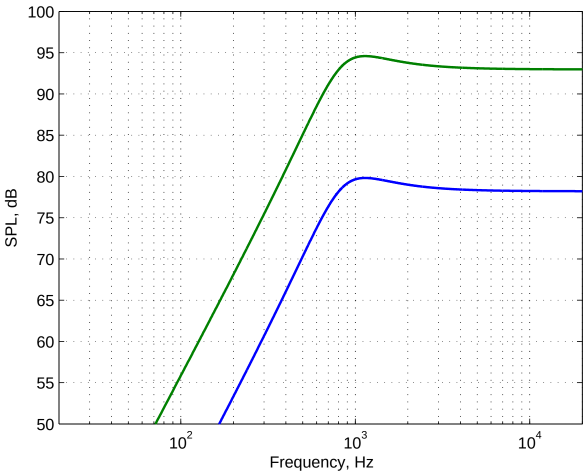

Figure 6.3: The monopole model of the loudspeaker using G_{ls} with a gain constant g_a of 0.6, 0.3W/0.1m (blue) and 1W/1m (green)

resulting responses are shown in Figure 6.3.

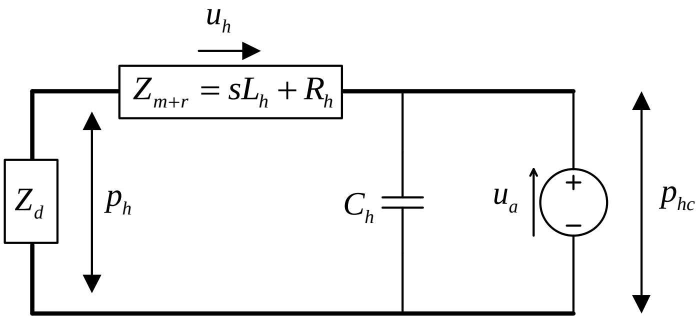

Figure 6.4: An equivalent circuit representation of the active resonator within a duct

When the resonator is placed within the duct it is loaded with the acoustic impedance of the duct, $Z_d = z_0/S_d$ [93, pg. 288] where z_0 is the specific acoustic impedance of air and S_d is the cross sectional area of the duct, leading to the equivalent circuit model shown in Figure 6.4. Using this representation it is possible to relate the volume velocity in the cavity per volt, G_{ls}, to the plant response G. Applying Kirchoff's voltage law to this circuit it is possible to relate the volume velocity of the actuator to the pressure measured at the neck thus

$$\frac{u_a}{p_h} = \left[\frac{1}{Z_d}\left(\frac{sL_h + R_h}{sC_h} + 1\right) + \frac{1}{sC_h}\right] \tag{6.12}$$

The plant response $G(s)$ is defined as the pressure p_h measured at the neck per voltage input to the actuator, whereas the actuator dynamics $G_{ls}(s)$ can be said to be defined as the volume velocity u_a induced in the resonator as a function of the voltage input to the actuator. Therefore the plant response and actuator dynamics can be related using this expression

$$G(s) = G_{ls}\left[\frac{1}{Z_d}\left(\frac{sL_h + R_h}{sC_h} + 1\right) + \frac{1}{sC_h}\right]^{-1} \tag{6.13}$$

In reality the plant and actuator responses would also include the dynamics of the microphone and all amplifiers and signal conditioning stages, however for the purposes of this investigation it is supposed that the microphone has a flat sensitivity profile of -60dB relative to 1V/Pa, and the microphone conditioning and loudspeaker amplifiers provide a total of 60dB of gain, such that this portion of the plant are unity. When implementing this in the laboratory this gain/dynamics will be inherent in the measurement of $G(s)$, from which G_{ls} can be inferred using the impedance model.

6.3 Stability Limits of the Active Helmholtz Resonator

Using the impedance representation of an active Helmholtz resonator means that the transmission performance and effective material parameters can be determined using the transfer matrix and equivalent circuit model respectively. Careful design of the controller $H(s)$ can then be used to manipulate these parameters to achieve a design goal. As with any feedback system maintaining stability is crucial and, physical limitations aside, will define the limits of system performance. This section describes the theoretical stability limits of the transfer function described by Equation 6.9, and the performance that is achieved at those limits.

Using the Routh-Hurwitz stability criterion [105, pg. 119], it can be shown that a closed-loop transfer function with a second order denominator remains stable if all of the coefficients of the characteristic equation are greater than zero. The transfer function of the active Helmholtz resonator in a duct has a second order denominator providing that the control loop dynamics are second order or lower. By considering a simple second order control loop, $G_{ls}(s)H(s) = b_2 s^2 + b_1 s + b_0$, therefore, it is possible to derive by inspection the inequalities below which define the stability limits of the closed-loop system. This control loop is not practically achievable, however serves as a means to explore performance at the limits of stability.

$$\frac{-2}{z_d} < b_0 < \infty \tag{6.14}$$

$$\frac{-(2R_h C_h + z_d)}{z_d} < b_1 < \infty \tag{6.15}$$

$$\frac{-M_h C_h}{z_d} < b_2 < \infty \tag{6.16}$$

Note that for the purposes of this investigation R_h is approximated as a constant rather than a function of frequency, and in the examples presented below $R_h = 1 \times 10^6$ based on the measured results from Chapter 5. The other physical variables are based on the passive Helmholtz resonator dimensions from Chapter 5 with a 4mm neck aperture. In addition, since it is not possible to numerically evaluate infinity, for examples of the positive stability bounds plotted in this section a value of 1 is used. Whilst this appears a small number it is worth noting that generally the absolute value of G_{ls} is very small; for the example described in 6.2.1, the peak response at resonance is in the order of 10^{-4}, with frequencies away from resonance reaching perhaps 3 orders lower than this. Therefore even for a value of $G_{ls}(s)H(s)$ to correspond to gain of 1 at all frequencies the gain of the controller must be very high. Three control loops are considered, a zeroth order loop ($b_1 = b_2 = 0$) and a second order loop ($b_0 = b_1 = 0$) which are purely real, and a first order loop ($b_0 = b_2 = 0$), which is purely imaginary.

6.3.1 b_0 Stability Criteria

Figure 6.5 shows the performance limits for a zero order control loop (i.e. pure gain) whilst remaining within the stability bounds defined by Equation 6.14. Note that for the passive case, a single resonator of these dimensions offers a relatively small amount of attenuation, in the region of 1dB. It is important to note that the resonator is intended to be a single part of an array of resonators making up a metamaterial whose performance would be much greater, as shown in Chapter 5.

At the lower end of the stability bounds (Figures 6.5a, 6.5c and 6.5e), where

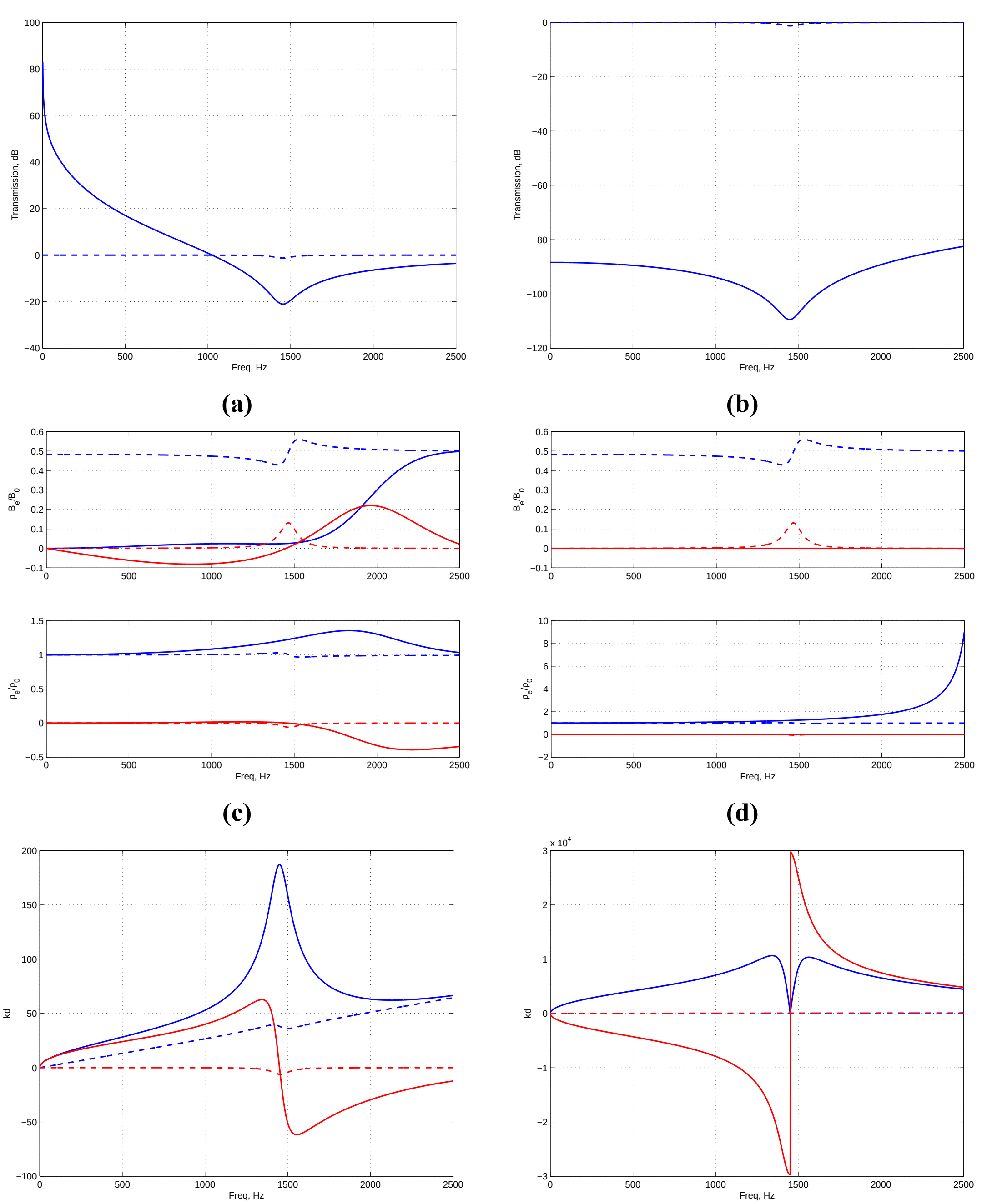

(a) **(b)**

(c) **(d)**

(e) **(f)**

Figure 6.5: The performance of the closed loop acoustic metamaterial with a zero order control loop. Transmission, effective material parameters and wavenumber at the lower ((a),(c) and (e) repectively) and upper ((b),(d) and (f) respectively) stability bounds. Real (blue) and imaginary (red) parts. Where appropriate the open loop response is also shown (dotted)

$G_{ls}(s)H(s) = b_0 = -2/z_d$, the results show that the region of attenuation around the band gap is greatly extended in the higher frequency region, and the depth of the band gap is deepened, as shown in Figure 6.5a. At low frequencies however, the active Helmholtz resonator leads to an enhancement in sound transmission. The dispersive nature of the material parameters is smeared over a very wide frequency range, Figure 6.5c, with the resulting wavenumber shown in Figure 6.5c.

The performance of a controller close to upper stability bound is shown in Figures 6.5b, 6.5d and 6.5f. The transmission coefficient of the system has been greatly reduced across the entire frequency range, and the effective bulk modulus becomes almost zero at all points. The real part of the effective density gets exponentially larger as a function of frequency. An explanation to this behaviour is given by examining the closed loop impedance, Equation 6.6, where any large value for $H(s)$ will lead to an impedance close to zero. A zero impedance will lead to total reflection within the duct, and minimise transmission, given by Equation 6.9. This controller architecture requires impractical gain coefficients, however does suggest that a large gain will lead to good broadband attenuation performance.

Attenuation is normally associated with a negative imaginary component to the wave number, and conversely enhancement with a positive imaginary component, which is a function of the ratio of the two material parameters. Generally attenuation can be seen when Im$(B_e) > 0$ and/or Im$(\rho_e) < 0$, and enhancement can be seen in the contrary case. When these two imaginary components equal zero, there is no attenuation or enhancement. However for the example shown here this is not the case. It is thought that this is due to the fact that the real part of the B_e is close to zero for much of the frequency range. The effective material parameters are derived using a lumped parameter approximation of the duct, whereas in reality the duct is a continuous system. This leads to a discrepancy between the continuous ’three transfer matrix model’ used for most of the simulations in Chapter 5, and the wavenumber model (used to examine the effects of changing the number of resonators in Section 5.8). Under ’normal’ conditions such as the passive examples seen in Chapter 5, this discrepancy is negligible and the wavenumber/material parameter accurately predicts transmission performance, however when the value for bulk modulus becomes very small, and the wavenumber becomes very large (since $k \propto 1/\sqrt{B_e}$) the discrepancy becomes significant. In these situations, the it appears that the lumped parameter model is a poor predictor of metamaterial behaviour.

6.3.2 b_1 Stability Criteria

Figure 6.6 shows the performance of the system with a purely first order control loop set to the lower and upper bound of the stable region as defined by Equation 6.15. At the lower stability bound it can be seen that the system changes from one where a band gap appears at the natural frequency of the passive resonator to a system that enhances the sound transmission in this region; the opposite of the original design objective. At frequencies away from this resonant region the transmission performance is relatively unchanged. The dispersive nature of the material parameters remains, however its form is different. The material parameters appear inverted, the magnitude of the dispersive effect is reduced slightly, and the frequency at which it occurs is reduced, appearing at the onset frequency of the original passive band gap. Unlike for the zero order controller described previously, the value for the effective material parameters remains positive and of reasonable size (i.e. not close to zero), and this inversion of the parameters reflects the enhancement of wave transmission as opposed to the attenuation of the passive band gap; the wavenumber model accurately predicts the transmission behaviour in this case.

The performance of the system at the upper bound mirrors that of the zero order controller, described above.

6.3.3 b_2 Stability Criteria

Figure 6.7 shows the performance of the system with a purely first order controller when the controller is set to the lower and upper bound of the stable region as defined by Equation 6.16. At the lower bound the transmission performance is similar in structure to that seen by the lower bound performance of the zero order controller, however the response is reflected in frequency about the natural frequency of the passive resonator element. Like the b_0 case, the deepness and the width of the band gap region has been increased significantly and there is a region of transmission enhancement outside of this region, however in this 2nd order case the region of enhancement appears at high frequencies instead of low frequencies. Again the dispersive nature of the material parameters has been smeared over a very wide frequency range, however the form of the imaginary part of the wavenumber has similar characteristics to the form of the closed loop band gap, the shapes do not match. As in the previous cases, this is thought to be due to the value of the effective bulk modulus being close to 0 in the band gap region,

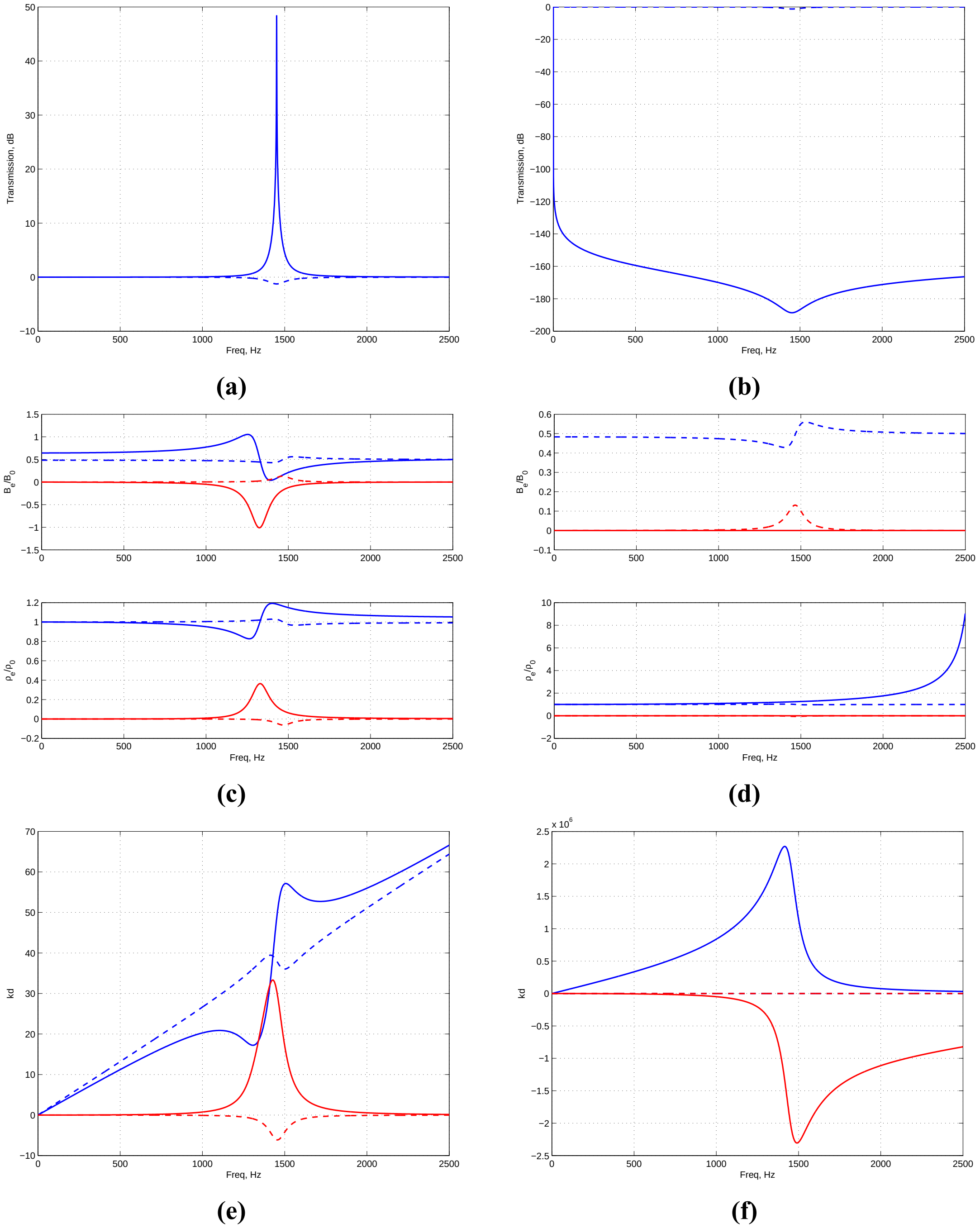

(a) **(b)**

(c) **(d)**

(e) **(f)**

Figure 6.6: The performance of the closed loop acoustic metamaterial with a 1st order control loop. Transmission, effective material parameters and wavenumber at the lower ((a),(c) and (e) repectively) and upper ((b),(d) and (f) respectively) stability bounds. Real (blue) and imaginary (red) parts. Where appropriate the open loop response is also shown (dotted)

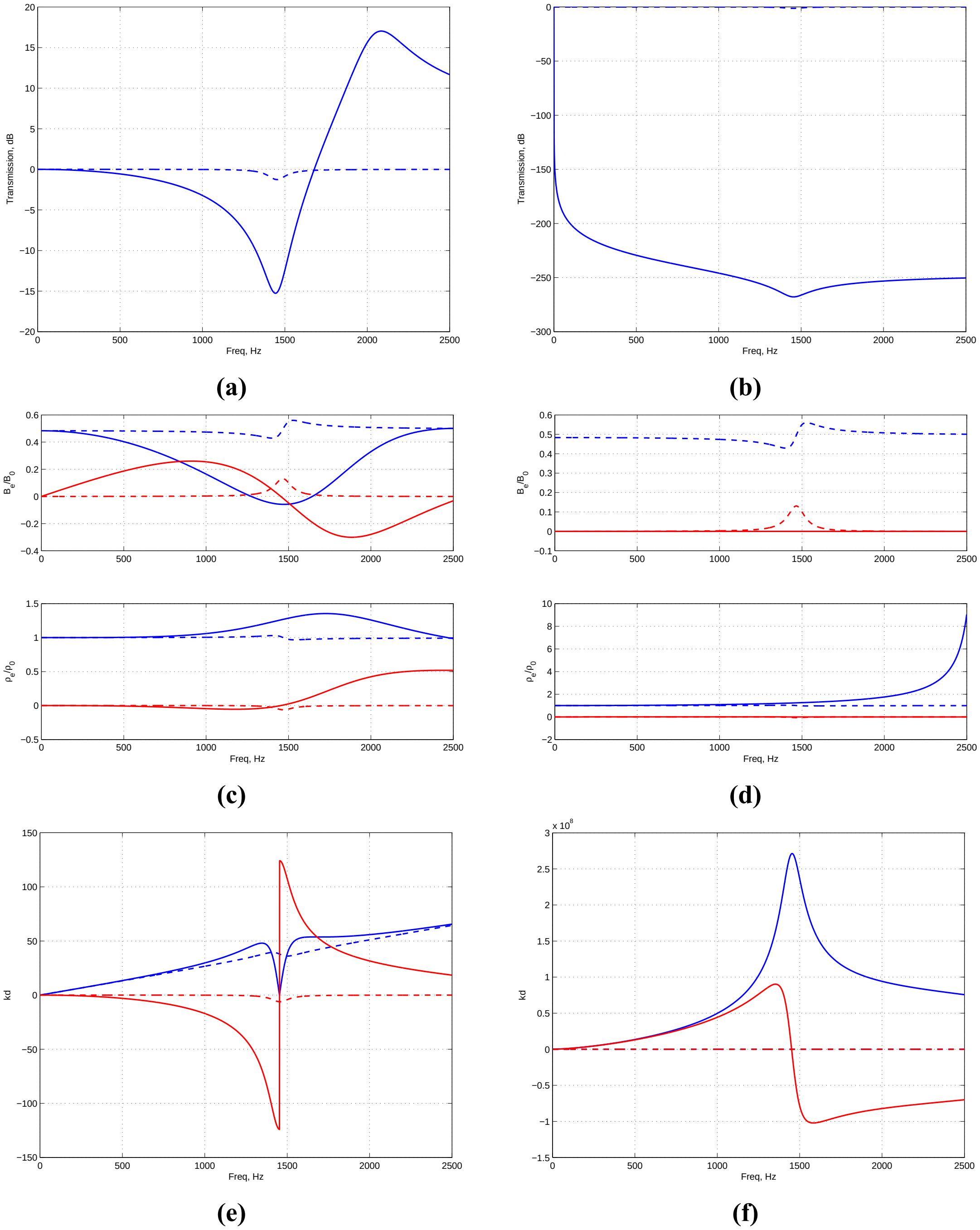

Figure 6.7: The performance of the closed loop acoustic metamaterial with a 2nd order control loop. Transmission, effective material parameters and wavenumber at the lower ((a),(c) and (e) repectively) and upper ((b),(d) and (f) respectively) stability bounds. Real (blue) and imaginary (red) parts. Where appropriate the open loop response is also shown (dotted)

and therefore the wavenumber model becoming inaccurate.

At the upper bound the behaviour once more mirrors that seen in the 1st and 2nd order controllers, with transmission being practically eliminated across the entire frequency range, the bulk modulus being practically zero at all frequencies leading to a very large value for the wavenumber, and the effective density becoming larger with frequency.

6.3.4 Comments

It is clear from the results above that significant performance gains can theoretically be achieved using the active Helmholtz resonator structure compared to a passive resonator. Large increases in both the depth and width of the band gap region can be achieved whilst retaining closed loop stability. The effective material parameters can also be manipulated. However, practically realising such a system will require imposing further constraints.

The control loop dynamics explored above were chosen to illustrate the performance that would occur on the edge of stability, however the 1st and 2nd order systems presented are non causal; the order of the numerator is larger than the order of the zero order denominator. In reality the control loop must be causal, and the actuator dynamics likely to be more complex, therefore these are not realistic conditions. In addition, within a physical system there will be physical limits related to the hardware used, such as the limits of linear operation and power handling of transducers, and the design of the control loop will have to take this into account. Therefore whilst the results from this section give an indication that performance gains are possible in the active system, the degree of performance gain is somewhat overstated, also an alternative method is required to design a practical control loop.

Comparing the transmission performance calculated using the transfer matrix compared to the wavenumber at the stability limits has highlighted a shortcoming in the lumped parameter nature of the wavenumber model. Whilst under passive conditions where the effective material parameters are within ’normal’ parameters an increase in the imaginary part of the wavenumber coincides with the band gap region, however when the value for bulk modulus becomes very small and the wavenumber becomes very large ($k \propto 1/\sqrt{B_e}$) the discrepancy between the continuous system and the lumped model becomes significant and the calculated wavenumber is a poor indicator of band gap location.

6.4 Constrained Nonlinear Optimisation

To design a controller for use within an active Helmholtz resonator, the method described previously in Section 4.3, Constrained Nonlinear Optimisation (CNO), can be used to iteratively shape a control filter to achieve the design objectives whilst satisfying specified constraints. The design of an effective feedback controller involves achieving the maximum possible performance whilst ensuring closed and open loop stability. In addition the system should remain causal and be of a low enough complexity that it would be practical to implement.

The CNO was performed using the same `fmincon` function used in Chapter 4. The function is part of the optimisation toolbox for the `MATLAB` computing environment, and uses an interior point optimisation algorithm based on [90, 91]. The function is applied to minimise the output of a cost function $\Gamma(\boldsymbol{w})$ whilst satisfying the non-linear constraint.

$$\min_{\boldsymbol{w}} \Gamma(\boldsymbol{w}) \text{ such that } \boldsymbol{c}(\boldsymbol{w}) \leq 0 \tag{6.17}$$

The optimisation successfully terminates when the gradient of $\Gamma(w)$ with respect to $\boldsymbol{w}$ is smaller than a predefined tolerance and the constraints are all satisfied. For the purposes of this investigation, all tolerances used were the default values allocated by `MATLAB`. Like in the viscoelastic case described in Chapter 4, the algorithm was used to optimise the coefficients of an FIR feedback filter, ensuring open loop stability and simplifying the design process. The initial coefficients of the filter fed to the algorithm, $\boldsymbol{w}_0$, were all set to 0, and then additional runs were then carried out from 2 other starting points, a vector of ones, and a vector of random numbers between 0 and 1, to ensure that changing the start point did not significantly affect the results, suggesting a global minimum has been reached.

The output of the function $\boldsymbol{c}(\boldsymbol{w})$ is set to ensure closed loop stability and ensure that the power output of the active system is constrained. The system, consisting of a microphone, amplifier, control filter and loudspeaker, is inherently open loop stable, and as such closed loop stability is ensured using simplified Nyquist criterion [85, pg. 278], such that

$$-1 \leq \text{Re}(G(j\omega))H(j\omega) \tag{6.18}$$

$$\therefore c_{stab}(\boldsymbol{w}) = -\operatorname{Re}(G(j\omega)H(\boldsymbol{w}, j\omega)) - 1 \leq 0 \tag{6.19}$$

where the vector $\boldsymbol{w}$ represents the filter coefficients.

For the purposes of this investigation it was assumed that the loudspeaker has a continuous power handling rating of $0.3W$, based on the KDMG20008 loudspeaker by Kingstate, Appendix F. For a disturbance pressure of 2Pa (approx 100dB SPL) white noise, the closed loop pressure at the microphone is

$$d = \frac{2}{1 + G(j\omega)H(j\omega)} \tag{6.20}$$

So, splitting the sound power across N discrete frequency bins, the power output of the control filter is constrained to be less than or equal to half the maximum power handling rating of 0.3W.

$$\boldsymbol{c}_W(\boldsymbol{w}) = \sum_{\omega=\omega_n}^{\omega_N} \frac{1}{N} \frac{|(dH(\boldsymbol{x}, j\omega))^2|}{\Omega_a} - 0.15 \leq 0 \tag{6.21}$$

where Ω_a is the nominal impedance of the actuator. Therefore

$$\boldsymbol{c}(\boldsymbol{w}) = \boldsymbol{c}_{stab}(\boldsymbol{w}, \omega) || c_W(\boldsymbol{w}) \leq 0 \tag{6.22}$$

where the symbol $||$ denotes concatenation of two vectors. $\boldsymbol{c}(\boldsymbol{w})$ is therefore a vector and all elements must be less than or equal to zero to satisfy the constraint. Note the dynamics and power limits described above were chosen using real world values but are somewhat arbitrary. In an experimental implementation the dynamics of the control loop would be measured in situ and must include all equipment within the control path, such as anti-aliasing filters etc.

The cost function for the optimisation is set to minimise the mean-square of the transmission coefficient of the active Helmholtz resonator within a duct

$$\Gamma(\boldsymbol{w}) = \frac{1}{\omega_{ul} - \omega_{ll}} \sum_{\omega_{ll}}^{\omega_{ul}} |T(\boldsymbol{w}, \omega)|^2 \tag{6.23}$$

where the subscripts ul and ll represent the upper and lower frequency limits respectively over which the optimisation takes place, and the closed loop transfer function is now a function of the FIR filter coefficients.

6.4.1 Results

Figure 6.8a shows the transmission response of a single active Helmholtz resonator within a duct when the optimisation has been set to minimise the transmission between 650Hz and 800Hz, Figures 6.8c and 6.8e show the resulting effective material parameters of the system. The results show that transmission is reduced across the target bandwidth extending the band gap into the lower frequency band. Above the target frequency the passive band gap has been replaced with a small enhancement of transmission. Below the target frequency there is a sharp enhancement of 10dB, reducing to 0dB towards the lower frequencies.

Examining Figures 6.8c and 6.8e, it is clear that the presence of active control significantly alters the material parameters of the metamaterial. The effective bulk modulus is negative for a narrow region near the upper end of the target frequency range and therefore the metamaterial becomes single negative. The effect on the effective density is smaller, however the active filter has caused a dispersive effect several times greater than the passive performance.

The widening of the band gap in the lower frequencies coincides with a region where the real part of the effective bulk modulus is close to zero. From an impedance stand point small levels of transmission coinciding with a bulk modulus of zero makes sense, since the acoustic impedance of the system $z_m = \rho_e c_m = \sqrt{\rho_e B_e}$, where c_m is the effective sound speed within the system. A bulk modulus of zero leads to an acoustic impedance of zero; a short circuit in the transmission line, leading to high levels of reflection. Whilst the results appear to support this, as discussed in Section 6.3, the accuracy of the lumped parameter model when the calculated effective material parameters are very small is questionable and requires more investigation.

Figures 6.8b, 6.8d and 6.8f show the results when the filter is optimised to extend the band gap into the upper frequency region, between 850 to 1150Hz. The results mirror that of the previous example optimised to the region below the band gap. The transmission loss is greatly enhanced over the target frequency range, extending the band gap in the higher frequency range, however the passive band gap below 850Hz is lost. Again the effective bulk modulus achieves negativity at the high frequency end of the target range.

Figure 6.9 shows the transmission performance of the system when the filter has been optimised to minimise transmission away from the passive band gap (between 400-500Hz, and between 1200-1300Hz). The transmission has been effectively

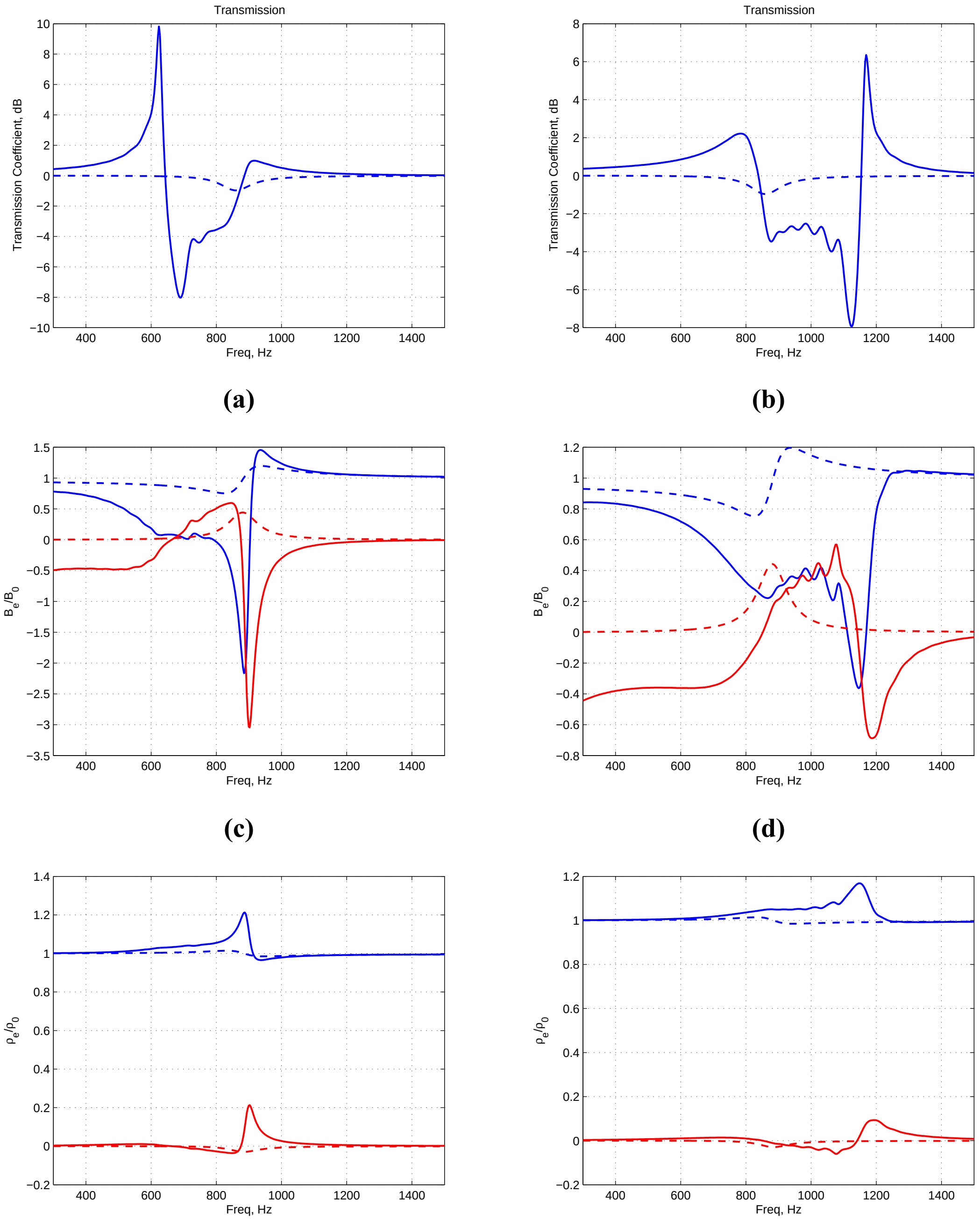

(a) **(b)**

(c) **(d)**

(e) **(f)**

Figure 6.8: The closed loop performance of the transmission performance, effective bulk modulus and density of the active resonator system when the feedback filter has been optimised to minimise transmission from 650-800Hz ((a), (c) and (e) respectively) and from 850-1150Hz ((b), (d) and (f) respectively). Where appropriate the open loop response is also shown (dotted)

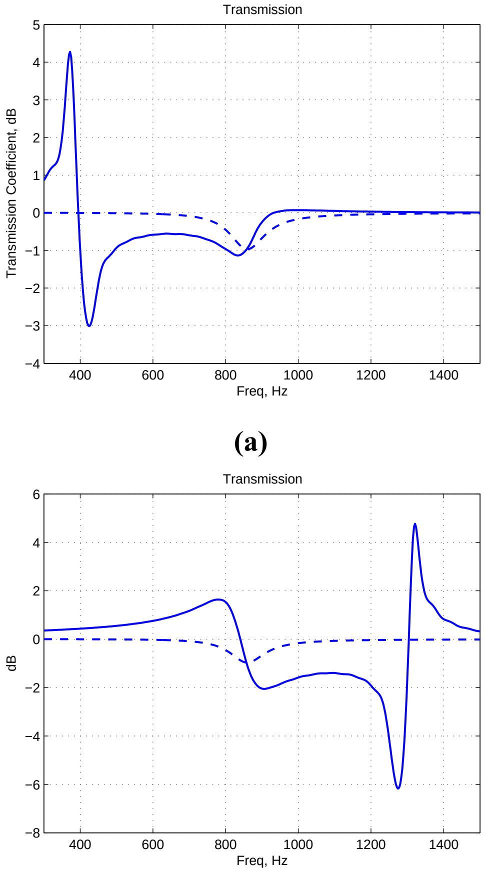

(a)

(b)

Figure 6.9: The transmission coefficient of an active Helmholtz resonator with an FIR feedback filter optimised to reduce transmission between (a) 400-500Hz and (b) 1200-1300Hz, compared to the open loop response (dotted)

suppressed within the optimisation band. In addition there remains a dip in transmission in the region of the natural frequency of the passive resonator. This demonstrates a possible advantage of using resonant metamaterials over traditional active isolation solutions. The passive band gap due to the resonant inclusions can create regions of attenuation that can exist in addition to the active attenuation; performance is gained from both the active and passive elements. This does not appear to occur however when the filter was optimised to extend the band gap, as the results for the filters optimised over 650-800Hz and 850-1150Hz show.

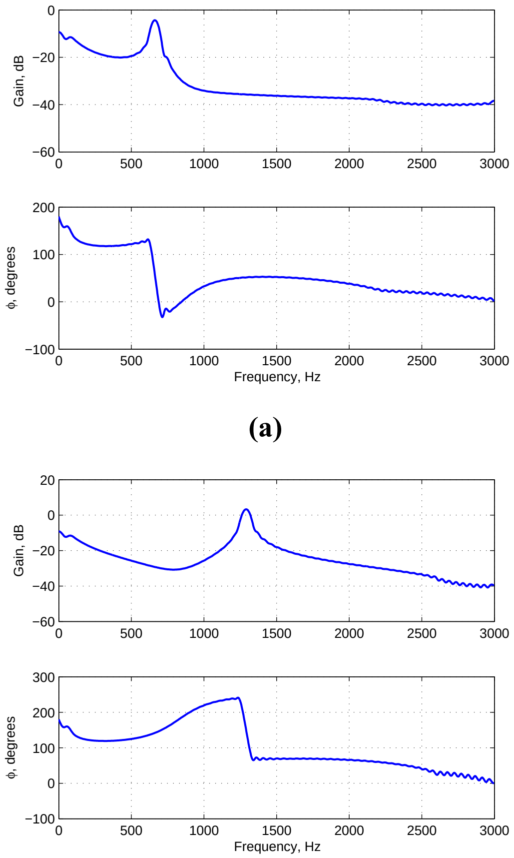

(a)

(b)

Figure 6.10: The magnitude and phase response of filters optimised to reduce the transmission coefficient over (a) 650-800Hz and (b) 1200-1300Hz

6.4.2 Optimised Filter Responses

The FIR filters have a length of 128 coefficients, and therefore the optimisation algorithm has many different degrees of freedom with which to affect the cost function. Therefore it is interesting to note the typical response of the filters created by the algorithm and assess whether a similar response could be achieved using a more simple control structure.

Figure 6.10 shows the response of two optimised filters, one that has been optimised to minimise transmission over 650-800Hz, and the other over 1200-1300Hz (when directly comparing to the closed loop responses shown in the previous section note that the optimisation was carried out with a sampling frequency of 6000Hz, and here the x-axis of the figures covers the entire 3000Hz digital frequency range). The filter responses are not overly complex, consisting of a single resonant peak centred on the target frequency range. This suggests that a similar level of performance may be possible with a much more simple control structure, such as a low order pole-zero controller. For instance, taking the response from Figure 6.10a, a 2nd order system could be tuned to create a resonant peak at 650Hz, with a phase shift of 180 degrees. A simple 2nd order pole-zero controller would not precisely mirror the response shown in the Figure, since it is only able to control the position and size of the resonance, so can only affect the gain and phase in this region; the phase structure of the filters may be of particular importance. However from these results it appears likely that additional, narrow band gaps could achieved whilst greatly reducing the computational burden of the controller - such a system could even be implemented using analogue electronic components. A brief investigation into using simple pole-zero type controllers is presented in the next section.

6.5 Optimised Pole-Zero Controllers

The filter responses designed using the CNO algorithm suggest that it may be possible to enhance the band gap using a simpler control structures. To investigate this possibility the optimisation routine was applied to optimise a second order pole-zero control model to minimise transmission within a specified frequency range. The optimisation routine can manipulate the numerator and denominator coefficients of the following transfer function

$$H(s) = \frac{b_1 s + b_0}{a_2 s^2 + a_1 s + a_0} \tag{6.24}$$

The same optimisation method as with the FIR filter case was used, however since the controller can now become unstable an additional constraint, $\boldsymbol{c}_{OL}(\boldsymbol{w})$ was added to ensure that this was not the case. To ensure open-loop stability the controller is constrained such that the real part of poles of the transfer function $H(s)$, denoted here as $\text{Re}(P_h(s))$, remain negative [105, pg. 197].

$$\boldsymbol{c}_{OL}(\boldsymbol{w}) = \text{Re}(P_h(s)) \tag{6.25}$$

where the poles are calculated using the `MATLAB` function `pole`[d] within the transfer

---

[d] `MATLAB` calculates the poles of the transfer function by determining the denominator roots, which are equal to the eigenvalues of the companion matrix of the polynomial

function object environment. The constraint vector $\boldsymbol{c}(\boldsymbol{w})$ now becomes

$$\boldsymbol{c}(\boldsymbol{w}) = \boldsymbol{c}_{stab}(\boldsymbol{w}, \omega)||c_W(\boldsymbol{w})||\boldsymbol{c}_{OL}(\boldsymbol{w}) \leq 0 \tag{6.26}$$

Note that there are two undesirable cases where the controller stability constraint can be satisfied but the controller is still unsuitable. This first is where $\text{Re}(P_h(s)) = 0$, meaning the controller is marginally stable, and the second is where $\text{Re}(P_h(s)) > 0$ but still within the tolerance of the `fmincon` function. To mitigate this it was decided that when the optimisation returned a solution, the calculated values for the poles were to be checked manually and unsuitable solutions discarded. For the scenarios presented here this situation never arose.

The five coefficients to be optimised are provided to the CNO algorithm, however in the case of a pole zero controller the initial points cannot all be set to zero since this would lead to a divide by zero operation. Therefore the initial coefficients were chosen as 1 in the numerator, and the denominator chosen so it created a resonance similar to that seen in the optimised filter results of Section 6.4.2. The coefficients of the denominator were chosen using a mass-spring-damper analogy where $a_0 = 1/C_h$ and a_2 was adjusted to move the resonant peak within the target region. After several test runs a value for the initial damping coefficient a_1 was given a value 1×10^6. Three optimisation regions were investigated, listed in Table 6.1 along with the initial values for a_2.

Frequency Region, Hz	650-800Hz	850-1150Hz	1200-1300Hz
a_2	500	300	150

Table 6.1: Dimensions of the transmission elements

The Figure 6.11 show the results for three controllers optimised in this way to minimise transmission over 650-800Hz, Figure 6.11a, 850-1150Hz, Figure 6.11b and 1200-1300Hz, Figure 6.11c. Figure 6.11d shows a bode diagram of the filter response for the 650-800Hz case, showing the resonant structure of the controller, for reference. The results for all 3 cases illustrate that a simple resonant controller can create new regions of attenuation at the tuned frequency of the controller. However compared to the results of the optimised FIR filters from the previous section the bandwidth achieved is not as large, with attenuation created only over a narrow frequency range. In addition, the passive band gap is lost in all 3 cases. In fact the passive band gap region away from the

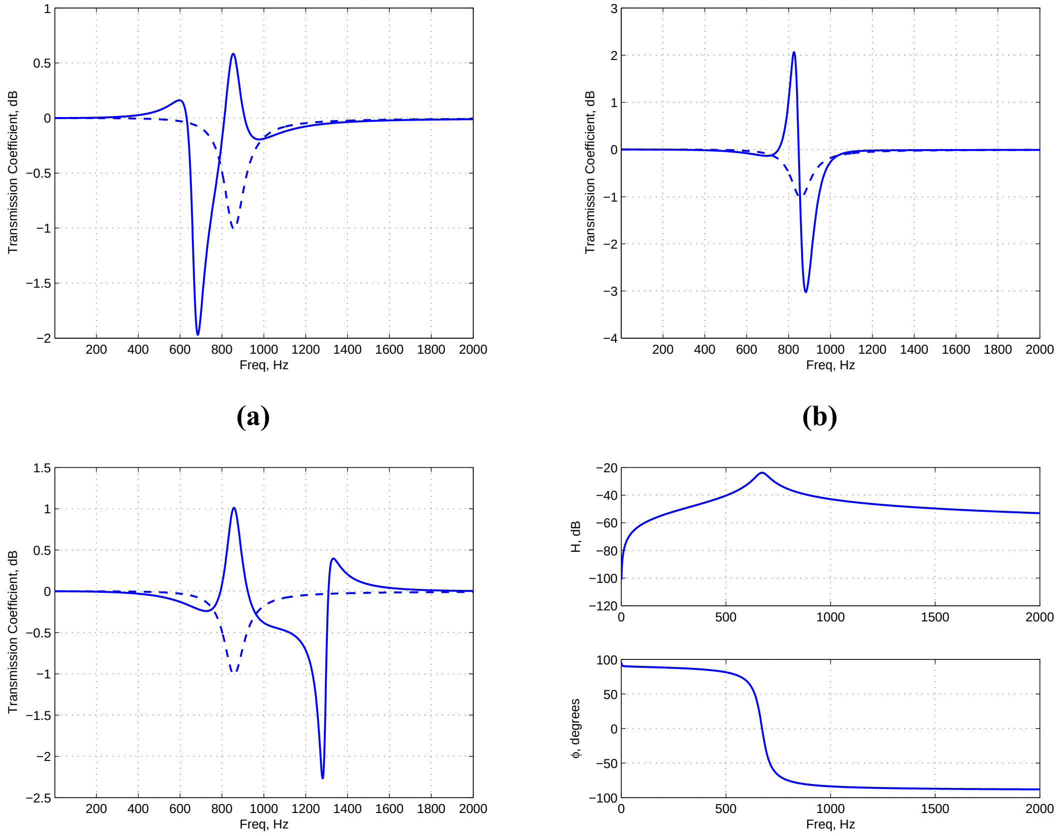

(a) **(b)**

(c) **(d)**

Figure 6.11: The closed loop transmission performance of the active resonator system when a 2nd order pole-zero controller has been optimised to minimise transmission from (a) 650-800Hz, (b) 850-1150Hz and (c) 1200-1300Hz, compared to the open loop response (dotted). (d) A bode diagram of the pole-zero controller optimised over 650-800Hz

target bands becomes a region of enhancement, presumably due to the undesirable phase characteristics of the controller in this region.

With such a low order controller it is only realistic to create a desirable phase/gain at one point around the controller resonance; the degrees of freedom required to influence other frequencies are not available. The phase and gain achieved by the controller is a function of the coefficients chosen to achieve the resonant peak. The consequences of this are highlighted by comparing the performance of the 650-800Hz optimised pole zero controller from Figure 6.11a with the equivalent FIR filter performance, Figure 6.8a. Whilst they both achieve a region of attenuation in the desired range, the FIR filter achieves a wider band gap, with higher, more equal levels of attenuation. This is because it can achieve a more complex phase structure (shown in Figure 6.10a) compared to the single phase shift of the pole zero controller (Figure 6.11d).

To demonstrate the effect of controller order on performance, two additional higher order controllers were designed to minimise transmission between 600-850Hz and compared to the controller above. The first controller, already seen, consists of 2 numerator coefficients and 3 denominator coefficients (i.e. 1 zero, 2 poles) denoted here as 2-3. The order of the additional filters was increased to 3 numerator/4 denominator coefficients (denoted as 3-4) in the second controller and a third 4-5 controller, with the resulting transmission coefficients presented in Figure 6.12.

Performing these optimisations presented several challenges. When the algorithm is dealing with a non-feasible solution (i.e. does not satisfy the constraints) it attempts to move to a feasible region of the error surface and not necessarily minimising the cost function in the process. To begin the optimisation a starting point, $\boldsymbol{x}_0$ has to be provided to the algorithm. In the case of the FIR filters studied in 6.4.2 the controller is inherently internally stable, and the initial coefficients can be set to zero ensuring closed loop stability; pole-zero controllers can become unstable, and restrictions with the mathematical tools used to analyse them within `MATLAB` mean that their coefficients cannot be set to zero. For the simple second order controllers described above this issue was side-stepped by using a mechanical analogy to set $\boldsymbol{x}_0$ such that the controller behaved like a passive system, guaranteeing controller stability. Once the order of the controller is increased it is no longer trivial to relate them to physical systems, and therefore choosing the initial coefficients such that the constraints are satisfied becomes more difficult.

In addition to this, observing the iterative output of the optimisation routine suggested

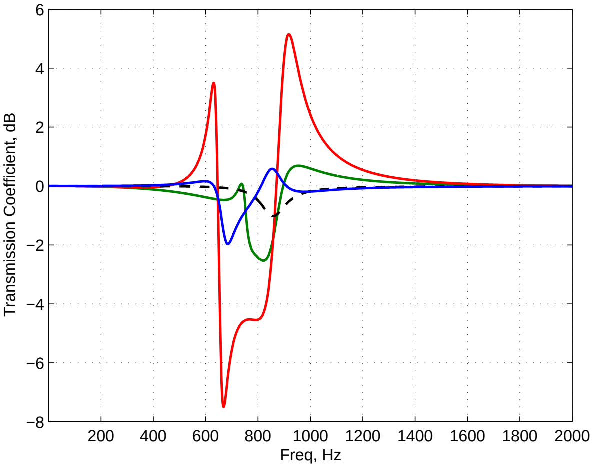

Figure 6.12: The transmission coefficient of the active resonator system when pole-zero controllers of increasing order have been optimised to minimise transmission from 650-800Hz, 2 numerator/3 denominator coefficients (blue), 3 numerator/4 denominator coefficients (green), 4 numerator/5 denominator coefficients (red), compared to the open loop performance (black-dotted).

that the gradient of the error surface was often very small; the change in the cost function, the first order optimality and the feasibility[e] per iteration was very small. This meant that the optimisation would very often terminate without finding a feasible solution, or without achieving attenuation. The termination tolerances can be reduced to stop the algorithm terminating prematurely[f], however setting these tolerances to very small values limits the algorithms ability to effectively converge.

Combining the above knowledge with experience gained using the algorithm in Chapter 4 and in Section 6.4.2 of this Chapter it was apparent that providing the algorithm with a starting point that was both a feasible solution and in a region where the gradient of the error surface is not very small will lead to fast convergence to a feasible, useful solution. However the above issues mean that many optimisation runs had to be performed many times, each from a new starting point chosen through trial and error,

---

[e] These quantities are outputted by the algorithm each iteration. The optimality is a measure the algorithm uses to estimate how optimal the current solution is, and the feasibility represents the degree to which the constraints are being violated. A feasibility output of 0 means the constraints are met

[f] There are two relevant tolerances in the algorithm. `Tolfun` denotes the minimum change in the cost function per iteration, `TolX` denotes the minimum step size per iteration. Since the step size per iteration is related to the gradient of the cost function, these two quantities are related.

before a useful result was achieved. In addition it suggests that the results achieved may not be the global optimum.

However, these issues considered, Figure 6.12 still provides a useful illustration of the effect of controller order on the attenuation achieved. The results show that with each increase in controller order the magnitude and the bandwidth of the attenuation within the target frequencies is larger. The smallest filter order, the 2-3 filter, is represented by the blue line in the Figure and consists of a single dip of approximately 2dB around 650Hz, with enhancement within the passive band gap. When the order is increased to the 3-4 filter a wider dip in transmission of almost 3dB is shown between 850Hz and approximately 700Hz (it does not outperform the lower order filter at all frequencies, but the optimisation routine was attempting to minimise the mean-square of the transmission coefficient). Finally, the largest filter increases the bandwidth and magnitude of the attenuation further, achieving over 4dB of attenuation across the entire target frequency range, peaking at over 7dB.

6.6 Conclusion

By combining an active Helmholtz resonator concept from Yuan *et al* [103] to the acoustic metamaterial presented in Chapter 5 an active acoustic metamaterial is proposed with the potential to create enhanced or multiple band gap regions. For these initial investigations to reduce the model complexity only a single resonator element was considered. This means that the levels of attenuation achieved both passively and actively are small, however it is important to remember that in a metamaterial there would be many elements contributing to a much larger band gap. The passive results from Chapter 5 demonstrate what is achievable with 7 resonators, for example.

Using this active acoustic metamaterial model the limits of stability for the control loop dynamics are determined using the Routh-Hourwitz stability criterion, and the performance of the material at these limits has been investigated. It was demonstrated that if a feedback controller is designed to operate on the margins of stability then very high levels of performance can be achieved with respect to transmission loss. The effective material parameters are also affected significantly. The extreme values achieved at the limits of stability confirm that the active metamaterial could be used to enhance the passive band gaps, however the dynamics suggested are not practical for implementation. Taking practical considerations into account, the performance will be limited by causality constraints, the control plant response and the physical limits of components.

This initial investigation highlighted the limitations of the lumped parameter model of the effective material parameters under certain conditions. When the value for the effective bulk modulus is not close to zero the lumped parameter model is an accurate representation of the continuous system and the wavenumber/material parameter accurately predict transmission performance. However when the value for bulk modulus becomes very small and the wavenumber becomes very large small errors in the model become significant and the lumped parameter model becomes less accurate.

A method for designing practical feedback controllers was then investigated, constrained non-linear optimisation. The feedback controller was chosen to be an FIR filter, so the system is inherently open loop stable, and an appropriate plant model was developed and applied. By applying appropriate constraints closed loop stability is achieved and the control signal remains within a predetermined limit. The results here suggest that under these constraints the levels of transmission loss are more modest, however significant enhancement of the band gap can be achieved. It was shown that it would be possible to increase the bandwidth at which attenuation occurs, and new out of band regions of attenuation can be created whilst retaining the passive band gap attenuation. In this scenario performance is gained from both the active and passive elements, demonstrating an advantage of using resonant metamaterials over traditional active isolation solutions. The regions of attenuation often coincide with an increase in the dispersive material parameters and negative bulk modulus can be achieved. Due to the small relative mass of the air within the resonator neck to the mass of air in the duct, achieving large deviations from the static value of density is more difficult.

The dynamics of the FIR filters achieved by the optimisation routine suggested that the open loop band gap could be improved or additional band gaps created using a more simple control structure. The optimisation routine was applied to 2nd order pole-zero controllers, and it was shown that a simple resonant structure could create new regions of attenuation, however the bandwidth of these new band gaps was relatively narrow and the passive band gap was affected. The complex phase structure needed to achieve wider band attenuation and retain the passive band gap can not be achieved with such a low order system. Such a simple system could be achieved with analogue electronics, and there may be situations where the reduction in complexity afforded in this way may be desirable. It may even be possible to make such systems adaptive to track time variant tonal disturbances, using switched capacitors for example. Increasing the filter order was then shown to improve the bandwidth and level of attenuation that can be achieved.

It is clear that a trade off between controller complexity and performance exists, but that active metamaterials based on active Helmholtz resonators have the potential to achieve high levels of attenuation over wide frequency ranges.

Chapter 7

Implementation of an Active Helmholtz Resonator

The work described in Chapter 6 describes the basis of an active acoustic resonator that could be used as an element within an active acoustic metamaterial. The results from this Chapter combined with the work in Chapter 5 suggest that such a metamaterial could produce wide, deep band gap regions which could be employed in isolation applications. In this Chapter a prototype active resonator is designed based on the resonators studied in Chapters 5 and 6 and produced and tested in the laboratory.

First the active resonator is installed within an impedance tube and its passive band gap confirmed to be within the order of the individual resonators of the passive metamaterial of Chapter 5. Next controllers are designed and applied to the resonator to enhance the passive band gap. Initially simple second order resonant controllers are applied and it is shown that narrow, deep regions of attenuation can be achieved using this method, effectively increasing the degrees of freedom of the resonator. FIR filters are then designed using the constrained non-linear optimisation method developed in Chapter 6 using the measured plant response of the active resonator as an input. These filters are applied and the results show that regions of attenuation can be successfully created in lower frequency regions, however attempts to create attenuation above the passive band gap frequency are less successful. The results show the potential of the approach but more work is needed to develop the method to reliably produce attenuation in a targeted frequency range.

Finally, to assess the potential level of control that could be achieved by the single active resonator the system is reformulated as a remote control problem using a geometric control strategy developed by Daley and Wang [77]. Overall the level of control achievable from the resonator at across much of the frequency range tested is impressive and much higher than the level achieved passively, although the control authority at some frequencies is shown to be limited by reflections occurring in the impedance tube set up.

7.1 Prototype Design

To investigate the potential effectiveness of the active acoustic metamaterial, a prototype active Helmholtz resonator was developed. The prototype was designed to fulfil two design objectives. First it was to have dimensions and performance in the same order as the SHS units contained in the passive metamaterial described in Chapter 5. The second requirement was that the design had to be produced, as far as possible, from off the shelf parts to ensure prompt production of the resonator prototype.

The production concept is detailed in Figure 7.1. The main body of the resonator is cylindrical with an inner diameter of 21mm. The internal cavity between the neck and the loudspeaker diaphragm is approximately 38mm and the neck orifice 6mm wide and 3mm deep.

The theoretical model of the active resonator from Chapter 6 describes the compliance of air within the resonator body to be subject to a velocity input at the neck of the resonator and a velocity input due to the loudspeaker within the resonator base, and the open loop performance therefore equals that of a passive resonator of the same dimensions. However in the case of the prototype this is not going to be the case; the compliance of the air within the cavity will be reacting against the loudspeaker diaphragm, not a solid back wall of a resonator body. This effectively adds a degree of freedom to the resonator, with the mass of the diaphragm and the a stiffness component consisting of the diaphragm suspension and the air cavity behind the loudspeaker. It was decided that for the prototype resonator this air cavity should be kept as small a reasonably possible. This would be a necessary constraint within a metamaterial structure, where the desire would be to have a large number of small resonators. In addition by keeping the overall volume and the volume between the neck and the loudspeaker as similar as possible, the small volume of air behind the diaphragm exerts a relatively high stiffness on the loudspeaker compared to the stiffness within the resonator body, meaning the resonator body is the main source of compliance and minimises the difference between the theoretical passive performance and the measured open loop performance. The small volume behind the loudspeaker has a disadvantage, raising its natural frequency, and increasing the frequency below which force is limited (analogous to the low frequency roll off of a loudspeaker within a cabinet), and reducing the amount of volume velocity that will result from a given input voltage. The cavity behind the

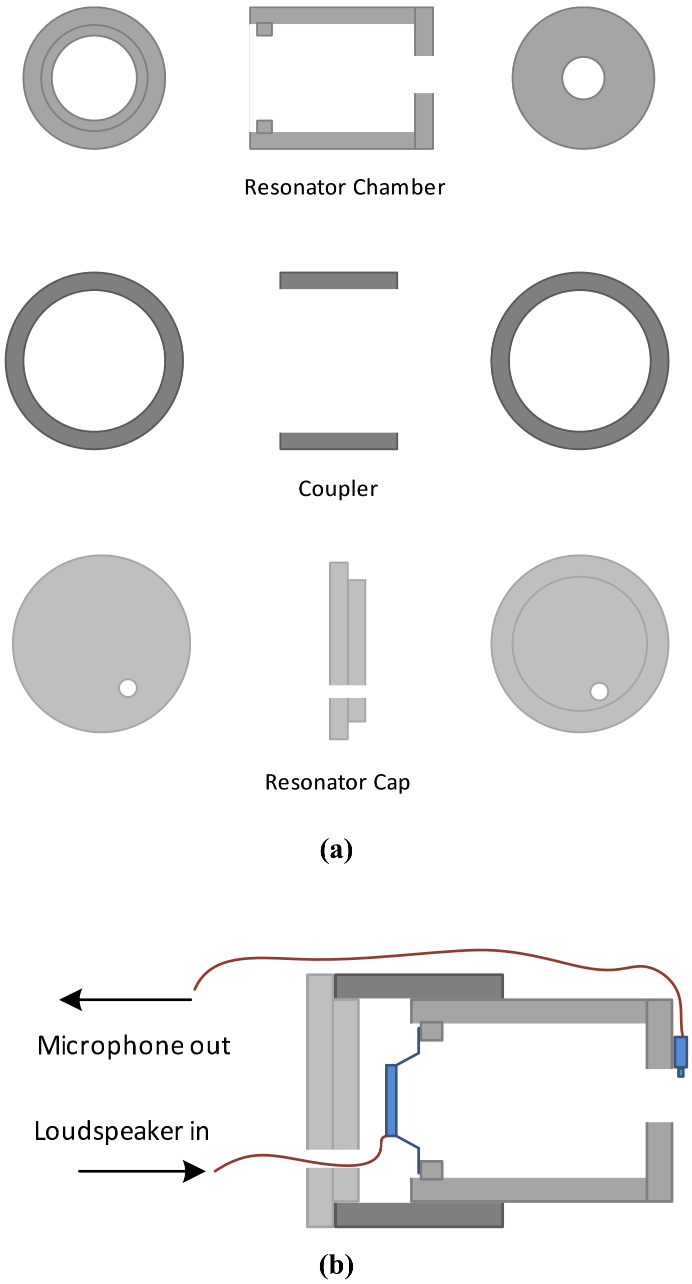

Figure 7.1: (a) Drawings of the constituent parts of the active resonator. (b) The assembled resonator drawing

loudspeaker has a width of 24mm, and a specified length of approximately 5mm (note, this value is at best approximate due to the ’interference fit’ of the rear cavity construction method, detailed below)

The resonator body was produced from a PVC tube normally used as a conduit for electrical cabling, and the rear cavity from a coupling unit, meaning the resonator body and rear cavity readily fit together with an interference fit. Using 3mm PVC sheets, a front end cap was produced with a 6mm neck drilled into the centre, a small lip was attached to the opposite end of the resonator body to attach the loudspeaker, and a rear end cap was produced to be placed over the rear cavity, with a hole to allow the loudspeaker cable to escape. The loudspeaker was attached with adhesive, and the rear end cap sealed into place with putty. The cable hole was also sealed. The loudspeaker used was the KDMG20008 by Kingstate, datasheet contained in Appendix F. The microphone used was a Knowles Acoustics EA-21842-000 1.4mm, datasheet contained in Appendix G, adhered to the front end cap such that the microphone aperture extends over the resonator neck. Photos of the finished prototype positioned in the impedance tube are shown in Figure 7.2.

7.2 Measured Open Loop Transmission Coefficient

The passive band gap of the resonator prototype was measured in situ in the impedance tube setup using the same 4 microphone method employed in Chapter 5. The passive response is shown in Figure 7.3 and confirms the presence of a passive band gap centred at approximately 850Hz. In a passive Helmholtz resonator the back wall can be considered perfectly stiff, leading to a single degree of freedom system. However in this active resonator this is no longer the case; the loudspeaker cone has mass, the loudspeaker cone is compliant on its suspension and then this is backed with another small air cavity. Previous research that employed the same model of loudspeaker [106] estimated the suspension stiffness to be approximately 495N/m, and the rear cavity has a stiffness of B_0A^2/V [93, pg. 284] where A is the cross sectional area and V is the volume of air. The three stiffnesses can then be combined, with the loudspeaker suspension and rear cavity added together in parallel, combined with the resonator cavity in series. Performing this calculation and gives a natural frequency for the resonator of 885Hz, where $f_0 = (2\pi)^{-1}\sqrt{(k/m)}$. This is within 5% of the measured value, which is encouraging considering the uncertainty surrounding the inputs and suggests that using a

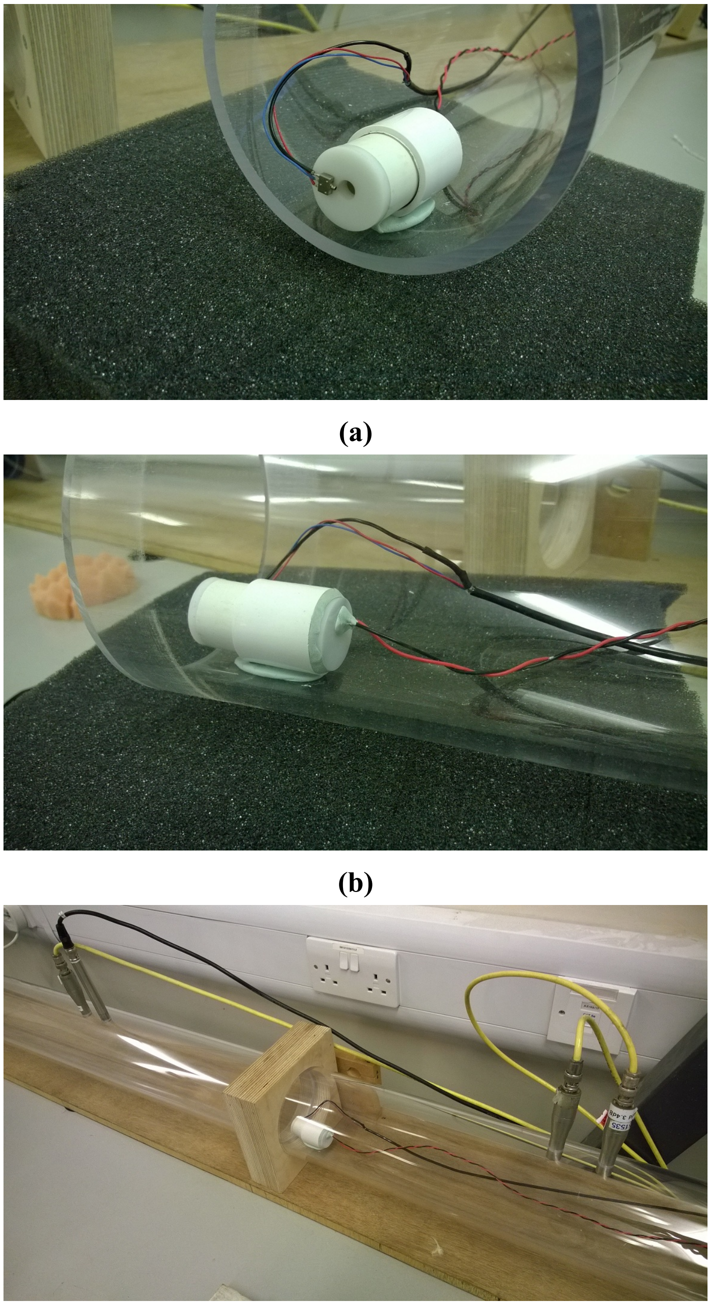

(a)

(b)

(c)

Figure 7.2: The prototype active resonator (a) front view, (b) rear view and (c) situated in the tube

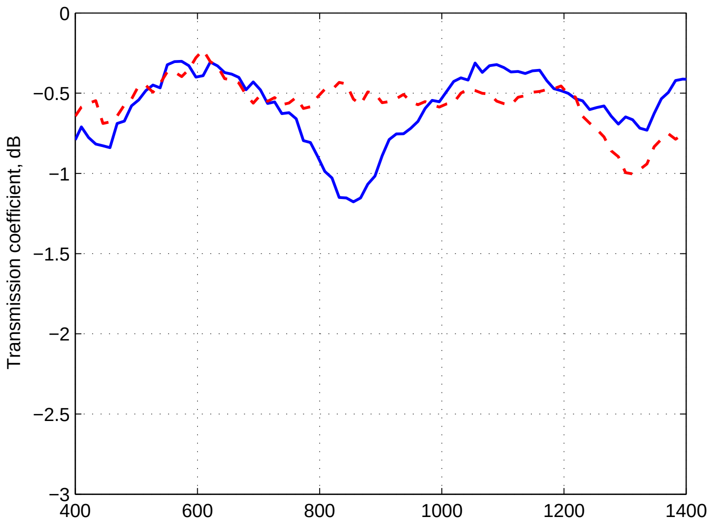

Figure 7.3: (a) The open loop transmission coefficient of the active resonator (blue), and the transmission coefficient when the neck hole is blocked (red dotted)

single degree of freedom model for the resonator and adapting the stiffness to account for the loudspeaker suspension and back cavity can approximate the performance of the active resonator. The magnitude of the attenuation is approximately 1dB, in line with the results of the acoustic metamaterial consisting of a single resonator measured in Section 5.8, Figure 5.15. The level of attenuation of an individual resonator is small however it is important to remember that it would be part of an array of multiple resonators, producing much larger levels of attenuation. The small band gap magnitude and level of measurement noise means that any resonant effects are more difficult to see, however to confirm that the dip in transmission seen at 850Hz is due to the resonator, Figure 7.3 also shows the measurement retaken when the resonator neck has been blocked with electrical tape. The results show that the dip disappears when the resonant mechanism is removed, and therefore is a true resonant band gap and not measurement noise or an effect due to scattering from the resonator body.

7.3 Measured Plant Response

During the course of the testing presented in this Chapter the resonator had to be dismantled and rebuilt due to a loudspeaker failure, during these rebuilds it was found

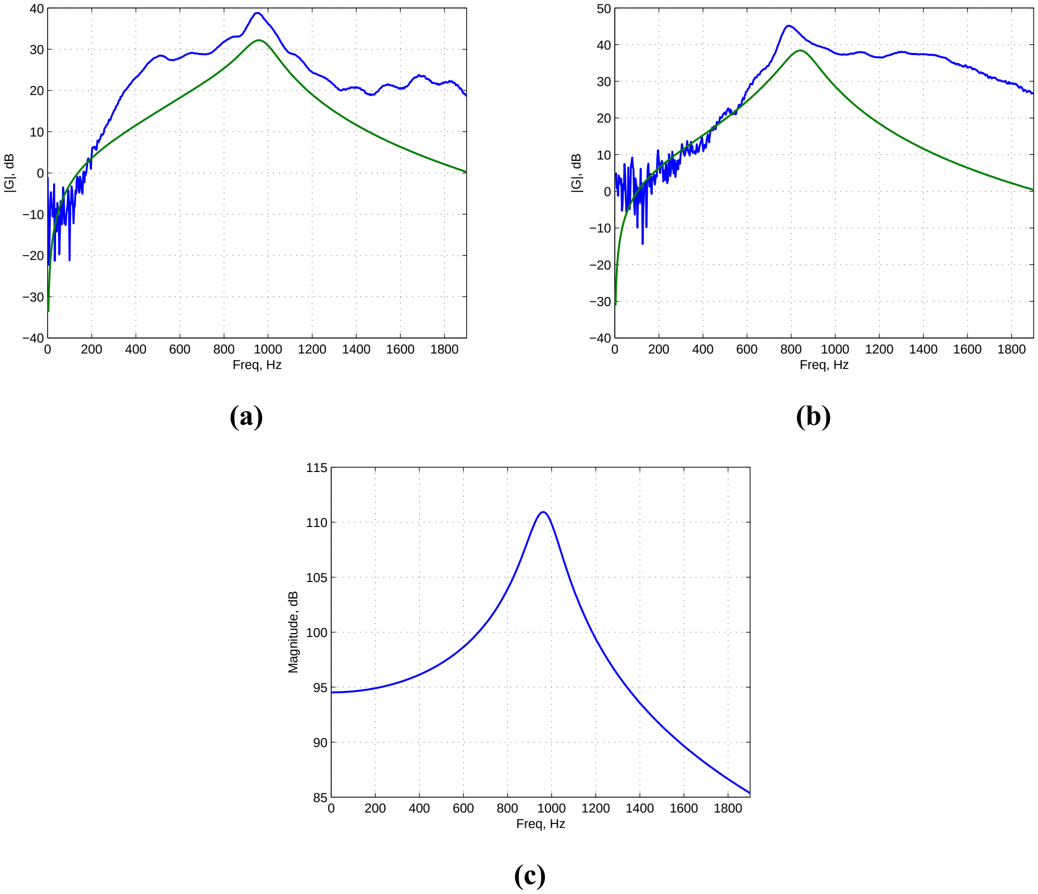

(a) **(b)**

(c)

Figure 7.4: The measured plant response G (blue) compared to the modelled G (green) from Chapter 6 for the two iterations of the active resonator where the natural frequency was approximately (a) 900Hz and (b) 850Hz. (c) The modelled transfer function between G_{ls} and G

that the resonant band gap moved between approximately 850Hz and 900Hz. This variance is thought to be due to a change in the distance between the neck and the loudspeaker diaphragm, variance in loudspeaker construction, and a change in the size of the cavity behind the loudspeaker when refitting the end cap. The plant response of both of these active resonators is shown by the blue lines in Figures 7.4a (900Hz) and 7.4b (850Hz). The analysis presented in this section focusses on the 900Hz case, Figure 7.4a, however the general form of the response is similar for both cases.

The measured plant response is dominated by a resonant peak at 900Hz with a steep low frequency roll off below that of approximately 30dB per octave. Above the resonant peak the response rolls off initially by approximately 10dB before levelling off for much of the higher frequency band. The response in Figure 7.4a is the product of the dynamics of the loudspeaker and the resonant response of the Helmholtz resonator. The loudspeaker response (given in the datasheet, Appendix F) features a resonant peak at approximately 900 Hz, below which the response rolls off dramatically towards the low frequencies. Above this resonance the response dips slightly, but remains relatively flat up to 2kHz. The loudspeaker induces a volume velocity within the resonator cavity which produces a pressure at the neck, where the relationship between the plant response and actuator dynamics is governed by the impedance relationship first derived in Section 6.2.1 and can be represented as

$$\frac{G(s)}{G_{ls}(s)} = \frac{1}{\left[\frac{1}{Z_d}\left(\frac{sL_h+R_h}{sC_h}+1\right)+\frac{1}{sC_h}\right]} \tag{7.1}$$

This expression is plotted in Figure 7.4c, and combined with the response of the loudspeaker, it is clear to see the origins of the form of the measured plant response G. The upshot of this is that both the loudspeaker and resonator response lead to a very steep roll off in the low frequencies below resonance. The green lines in Figures 7.4a and 7.4b are calculated using Equation 7.1 and the simple 2nd order model of G_{ls} from Chapter 6, and shows that the model used previously is a good approximation of the measured plant, although it underestimates the magnitude of the peak by approximately 6dB.

7.4 2nd Order Controllers

Initially to test the active resonator simple 2nd order controllers were designed manually based on the observations made in Sections 6.4 and 6.5 of this thesis. The controllers were designed to emulate a simple resonant circuit, where the denominator coefficients were chosen to represent an inductor, resistor and capacitor respectively, analogous to a mass, damping and stiffness in the mechanical domain. The controller essentially increases the degrees of freedom of the passive resonator, and the transfer function for the controller can be expressed as

$$H(s) = \frac{g \times (1.5 \times 10^4)}{\left(sL + R + \frac{1}{sC}\right)} \tag{7.2}$$

The values for L, R and C were chosen heuristically to create a resonance at a specified frequency and g is a gain constant that is adjusted online. As a reference point, the values L_h, C_h and R_h determined in Chapter 5 and typical values from the pole zero controllers designed in Chapter 6.5 were consulted. Measurements were taken at linearly increasing magnitudes of g until the closed-loop active resonator became unstable. The internal stability of $H(s)$ is ensured since the coefficients of the denominator are chosen to reflect a real-world dissipative system, therefore as long as the values remain physically reasonable (i.e. positive-real), the controller should remain stable. The values chosen are detailed in Table 7.1

Resonant Freq., Hz	738Hz	855Hz	1178Hz	1345Hz
L	420	400	420	420
C	1.11×10^{-10}	8.65×10^{-11}	4.35×10^{-11}	3.33×10^{-11}
R	1×10^5	1×10^5	1×10^5	1×10^5

Table 7.1: Coefficient values for the 2nd order resonant controllers

The measured results for the closed loop transmission coefficient of the active resonator within the impedance tube are shown in Figure 7.5. The predicted attenuation calculated using the model developed in Chapter 6 is also presented in Figure 7.6. Examining the measured results for the two controllers tuned to 738Hz (Figure 7.5a) and to 845Hz (Figure 7.5b), in both examples a narrow, deep band of attenuation has been created at the resonant frequency. In both cases the bandwidth of the attenuation created is modest, however the magnitude is larger than the passive band gap, at over 2dB in both

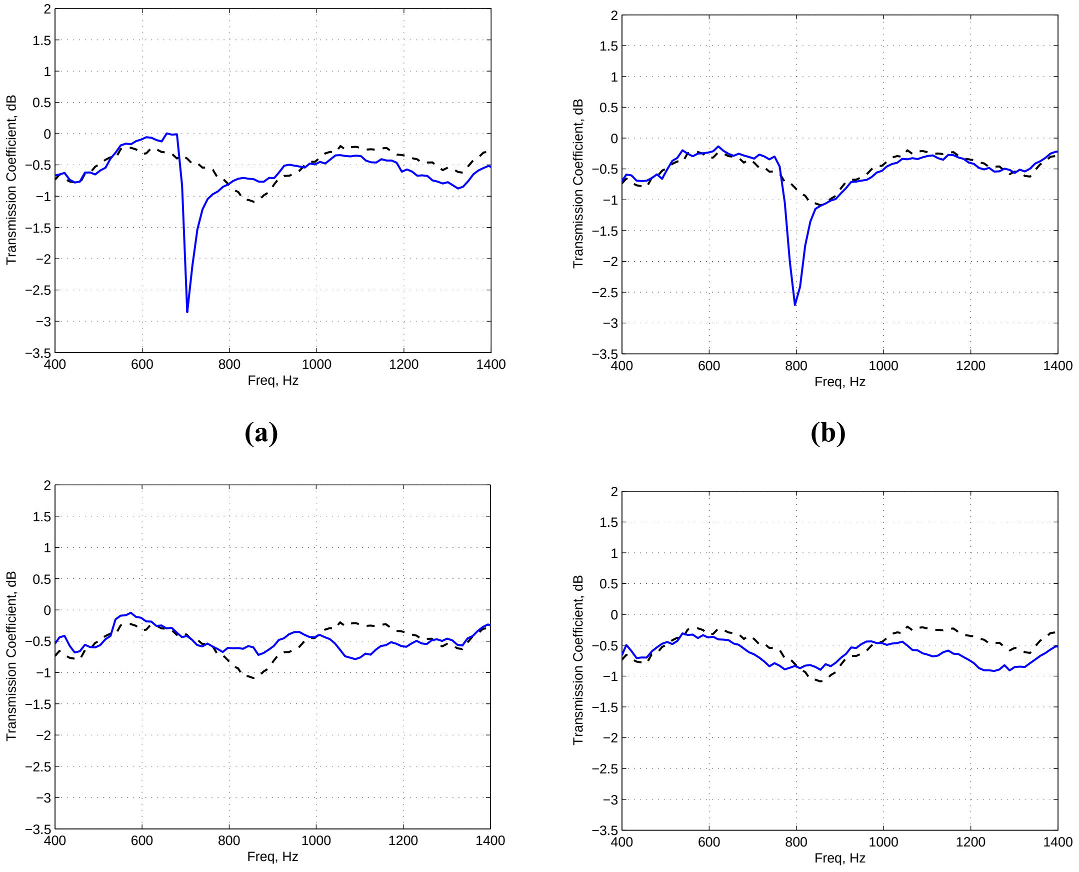

(a) **(b)**

(c) **(d)**

Figure 7.5: The measure transmission coefficient of the active resonator (blue) with a 2nd order feedback controller tuned to (a) 738Hz, (b) 855Hz, (c) 1178Hz and (d) 1345Hz, compared to the open loop response (black)

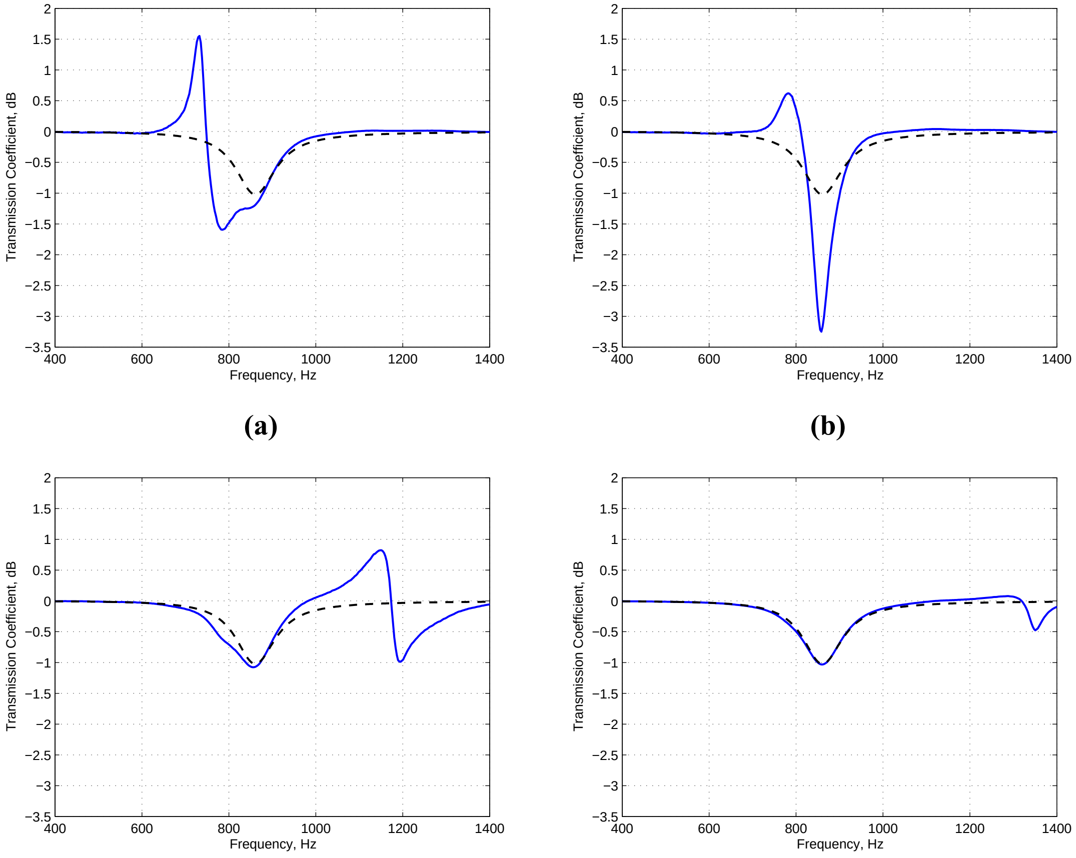

(a) **(b)**

(c) **(d)**

Figure 7.6: The modelled transmission coefficient of the active resonator (blue) with a 2nd order feedback controller tuned to (a) 738Hz, (b) 855Hz, (c) 1178Hz and (d) 1345Hz, compared to the open loop response (black)

cases. Comparing these results to what is predicted by the model there is good agreement with the location of the attenuation, although the magnitude is inaccurate by approximately 0.5-1dB, with an under-prediction in the 738Hz case and an over-prediction in the 845Hz case. It should be noted that the depth of the attenuation can be altered by a limited amount by changing the amount of damping within the model. The parameters for damping have been adapted to match the measured passive performance as much as possible, however since the magnitude of the passive behaviour is so small, there is likely to be a significant degree of possible error here.

The measured results at frequencies above the passive band gap, where the controller has been tuned to 1178Hz (Figure 7.5c) and 1345Hz (Figure 7.5d), also create attenuation at the tuned frequency, however the magnitude is lower, peaking at approximately 0.8dB in each case. The predicted results shown in Figures 7.6c and 7.6c respectively, predict these regions of attenuation, predicting that the magnitude would be less than that below the band gap. To create attenuation it was necessary to apply a positive gain constant g for the controllers targeted below the passive band gap, and a negative g for those above the passive band gap; probably due to the phase shift that occurs passively at the natural frequency of the Helmholtz resonator.

The controllers presented here are fast and simple to implement and in that way served as a good initial proof of operation for the active resonator, however they are in no way optimal and a more formal design method is preferable.

7.5 Using Constrained Non-Linear Optimisation to Design the Feedback Controller

To design a controller in a more formal fashion to the 2nd order examples above the optimisation method employed in Chapters 4 and 6 was revisited. Using the same steps described in Section 6.4 control filters were designed, using the model of the active resonator to assess the predicted resulting transmission loss. The difference between the optimisations carried out here and those described in the previous chapter, Section 6.4 are that the value for $G_{ls}(j\omega)$ is inferred from the measured plant response $G(j\omega)$ using Equation 7.1 and the measured plant response is used to assess stability. Also, an additional constraint is applied to account for measurement errors and ensure robust stability. The robust stability constraint used is identical to that described in Section 4.3.

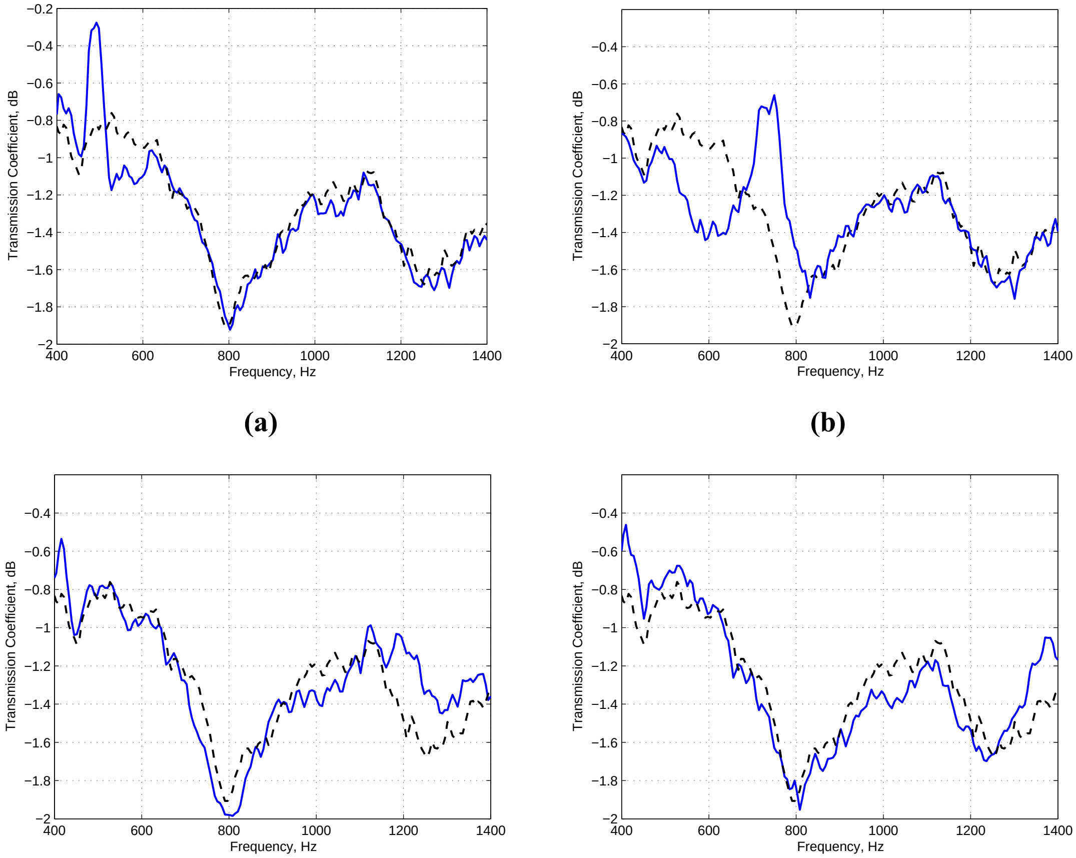

(a) **(b)**

(c) **(d)**

Figure 7.7: The measured transmission coefficient of an active Helmholtz resonator (blue) with an FIR feedback filter optimised to reduce transmission between (a) 500-600Hz, (b) 650-800Hz, (c) 850-1150Hz and (c) 1200-1300Hz, compared to the open loop response (dotted black)

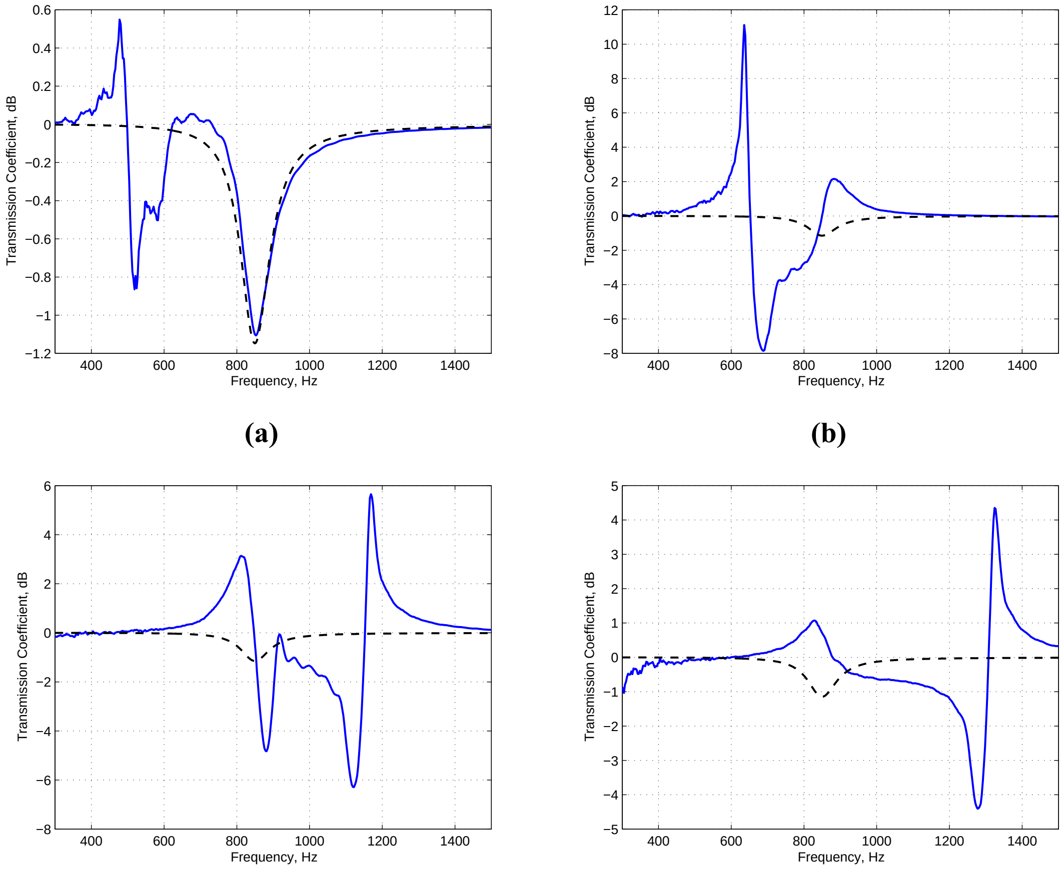

(a) **(b)**

(c) **(d)**

Figure 7.8: The predicted transmission coefficient of an active Helmholtz resonator (blue) with an FIR feedback filter optimised to reduce transmission between (a) 500-600Hz, (b) 650-800Hz, (c) 850-1150Hz and (d) 1200-1300Hz compared to the open loop response (black), using the model from Chapter 6, with G measured in the laboratory as an input.

FIR filters of 128 coefficients were designed to minimise transmission over four frequency ranges, chosen to examine the ability to enlarge the existing band gap or create new band gap regions. The frequencies targeted were 500-600Hz, 650-800Hz, 850-1150Hz and 1200-1300Hz and the feedback controllers were applied to the active resonator using the dSpace system. Once the filters were applied the transmission coefficient of the active resonator was measured. The measured results are shown in Figure 7.7. The values of attenuation being considered are very small, and evaluating the results is complicated by the presence of other mechanisms of environmental attenuation (losses in air etc) obscuring any behaviour below approximately 0.8dB. This is particularly notable by comparing the results presented here, performed on a very hot day, compared to those in the previous section, 7.4, when the laboratory was much cooler; the results in this section appear to have been shifted down in magnitude by approximately 0.5dB compared with Section 7.4, an effect that appears to increase with frequency. However, comparing all four results it is evident that the performance out of band (i.e. away from the influence of the controller) is consistent and the measurement is very repeatable; a useful quality when evaluating small quantities of attenuation.

Figure 7.7a shows the closed loop response when the filter was optimised to minimise transmission at 500-600Hz, and shows that a small amount of attenuation has been created in the target bandwidth. The magnitude of this attenuation is small, peaking at approximately 1.2 dB, with an enhancement occurring below 500Hz. The amount of attenuation predicted by the model is presented in Figure 7.8a, and this behaviour shows good agreement with the predictions. Optimising the filter over the range of 650-800Hz, Figure 7.7b produces a region of attenuation between 500Hz and 700Hz of approximately 1.4dB, with enhancement above 700Hz up to 850Hz. The magnitude of attenuation is much smaller than that predicted by the model, Figure 7.8a. The other two cases, Figures 7.7c from 850-1150Hz and 7.7d from 1200-1300Hz, attempt to create attenuation in ranges above the passive band gap and are less successful, failing to create the desired effect. Here there are no new regions of attenuation, disagreeing with that predicted by the model.

Discussion

Taking all the results presented in this section it appears the optimisation routine can create attenuation below the passive band gap but is not successful above the band gap frequencies. This is curious considering that below the band gap the plant response is lower than above it so one may expect control authority to be lowest here.

The active resonator model assumes the system behaves as a single degree of freedom, like a passive resonator, but with an additional volume velocity created by the loudspeaker. In reality the loudspeaker itself has a mass and stiffness and may contribute dynamics. The only inputs to the optimisation routine that contain measured quantities are the plant response $G(j\omega)$, and to a lesser extent $G_{ls}(s)$ which is a function of the measured plant response and the impedance model of the resonator. The predicted active resonator performance is then calculated purely using the model described in Chapter 6 with the transfer matrix approach from Chapter 5, which are approximations of reality. In addition the mapping between $G(j\omega)$ and $G_{ls}(s)$ uses a simple model that presumes the resonator is loaded with an infinite duct with a constant impedance z_d. The investigations in the next section, 7.6, demonstrate how reflections from the loudspeaker end of the duct mean this impedance assumption is not sufficient, as well as highlighting non-linearities in the response of the microphone used for the prototype that may further contribute to the discrepancies seen in the above results.

Taking all this into account, the model has been useful for initial investigations into the potential of active acoustic metamaterials and appears to predict some of the behaviour seen with the optimised filters and 2nd order controllers however it is clear that the design technique needs to be developed and refined before it can reliably produce controllers that produce attenuation using the active resonator. This is left as work for the future.

The following section uses an alternative analysis technique to examine the potential attenuation that may be achievable with the active resonator purely through the use of measurements of the resonator in-situ in the impedance tube.

7.6 Analysing the Resonator Using a Geometric Approach to Control Design

The approach used previously to determine the performance of the active acoustic metamaterial is based on examining the acoustic impedance of the resonator and the resulting transmission loss that occurs when incident with a plane wave. An alternative way of approaching the problem is to consider the system in a more traditional active control sense, where the resonator is acting as a radiator of 'anti-sound' to cancel out a disturbance at some error microphone. In the case of the active resonator laboratory set up the objective is to reduce the magnitude of the forward travelling wave as measured by the two microphones at the far end of the duct using a local control loop located at the resonator. This kind of remote control problem, where a local control loop is used to minimise the noise at a remote location, was studied by Daley and Wang [77] using a geometric approach.

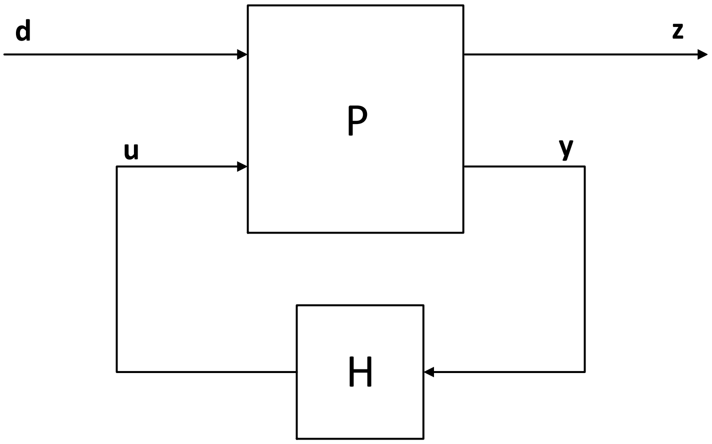

Figure 7.9: Linear Fractional Transformation representation of the system

The control problem is formulated in the linear fractional transform representation shown in Figure 7.9. Here $d(j\omega)$ and $u(j\omega)$ represent the disturbance and control signals respectively. $z(j\omega)$ and $y(j\omega)$ are the resulting noise signals at remote and local locations respectively: In the case of the resonator in a duct $z(j\omega)$ represents the forward travelling wave measured at in the duct and $y(j\omega)$ is the noise measured at the resonator neck. Now the vibrating system can be represented by a matrix of plant responses $G_{i,j}(j\omega)$

$$\begin{Bmatrix} y(j\omega) \\ z(j\omega) \end{Bmatrix} = \begin{bmatrix} G_{11}(j\omega) & G_{12}(j\omega) \\ G_{21}(j\omega) & G_{22}(j\omega) \end{bmatrix} \begin{Bmatrix} u(j\omega) \\ d(j\omega) \end{Bmatrix} \tag{7.3}$$

Daley and Wang demonstrate that it is possible to represent this system at a chosen frequency in a geometric fashion on a 'γ-plane' where each point on the plane represents a complex control gain. Full details of the method are available in the cited paper, but the upshot of the method results in two circles plotted on the γ-plane: the first a unit circle centred about (-1,0), and the second a circle with a centre point

$$-\frac{G_{11}(j\omega)G_{22}(j\omega)}{G_{12}(j\omega)G_{21}(j\omega)} \tag{7.4}$$

and a radius of

$$\left|\frac{G_{11}(j\omega)G_{22}(j\omega)}{G_{12}(j\omega)G_{21}(j\omega)}\right| \tag{7.5}$$

An example of such a plot is shown in Figure 7.10, for the active resonator measured response at 820Hz. Each point on this γ-plane represents a complex control gain through the relationship

$$H(j\omega) = \frac{-\gamma}{(1+\gamma)G_{11}(j\omega)} \tag{7.6}$$

The circles represent attenuation at the local and remote locations, such that choosing γ from within the unit circle leads to a reduction of noise at the local point, whilst a value of γ from within the remote circle (represented by the red circle in Figure 7.10) leads to reduction at the remote point. Values for γ which lie outside of the circles will lead to enhancement at the respective locations, and so where the circles overlap there exists a control gain that will create attenuation at both the local and remote positions. The centre of the circles represent the point at which optimal control at the respective locations would be achieved. Since in the case of the active resonator enhancement at the local point is of little consequence then, physical limits aside, the desired control gain to control the forward travelling wave is that set by the centre of the remote circle, i.e. Equation 7.4.

Whilst the centre of the remote circle can be used to determine the complex controller gain to annihilate the disturbance at the remote point, constraints on control effort may mean that such a controller is undesirable and the level of attenuation must be limited. Using this frame work Daley and Wang show that the noise at the remote point can be described using the following expression

$$z = \left[1 + \gamma\frac{G_{12}G_{21}}{G_{11}G_{22}}\right]G_{22}d \tag{7.7}$$

Note that the dependence on $j\omega$ of the terms in the above expression is implied, but for clarity is not included. Now it is possible to calculate a value for γ such that a desired level of reduction is achieved by setting the magnitude of the expression contained within the square brackets above to a constant value and solving for γ. For instance, by setting

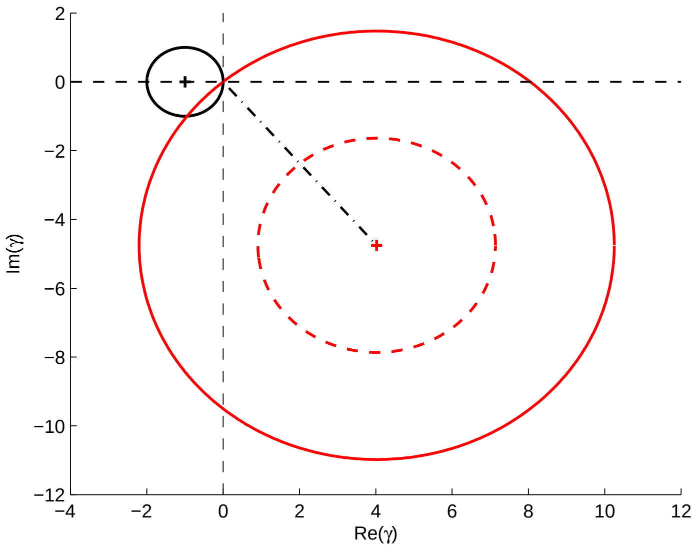

Figure 7.10: The complex γ-plane representation of the remote control problem of the active resonator at 820Hz. The remote circle is shown in red, with the 6dB remote circle dotted red.

this expression equal to 0.5, a controller can be attained that achieves 6dB of attenuation. The 6dB circle at 820Hz is shown in Figure 7.10 as the dotted red circle. In reality there are an infinite number of points lying upon the 6dB circle, however using the approach above picks the point that lies upon the straight line between the centre of the remote circle and the origin, shown in the Figure as a dot-dashed black line.

7.6.1 Applying Tonal Controllers to the Active Resonator

Using the above design method it is possible to determine, for a given frequency, the maximum level of control of the forward travelling wave that is feasible using the active resonator. This was applied in the laboratory and the results presented here. The controller was applied using the dSpace rapid prototyping system described previously in this thesis, which is also used to create a tonal disturbance and measure the forward travelling wave. The control is applied in the frequency domain, and therefore requires calculating an estimate of the gain and phase of the tonal signal using the microphone signals and a reference disturbance. This identification is carried out using the algorithm described by Daley and Zazas [78]. The complex frequency domain estimate of the resonator microphone signal is multiplied by the complex control gain, and then by a complex exponential harmonic reference to convert back to the time domain before it is fed to the resonator speaker.

Due to the anechoic termination the reflected wave from the end of the impedance tube should be small, however to account for any residual reflection the ongoing wave, $z(t)$, is determined in the time domain using the signal from the 2 downstream measurement microphones using the method described by Guicking and Karcher [107]. Assuming a speed of sound of 343.3m/s and a sampling frequency of 8000Hz, the 0.0428m separation between the two microphones corresponds to the distance a wave travels in 1 sample. The signal at the two microphones are a combination of both the incident and the reflected waves, and the incident wave can be isolated using a combination of the signal from one microphone combined with a delayed signal from the other.

$$z_i(t) = z_2(t - T_s) - z_1(t) \tag{7.8}$$

where the subscript i represents the incident wave, 1 and 2 represent the downstream microphone closer to the resonator and further from the resonator respectively, and T_s is the sampling constant.

Two control scenarios were tested in the laboratory, the optimum control gain and the control gain calculated to provide 6dB of attenuation. The control was applied to tonal disturbances in and around the passive band gap frequency at 10Hz intervals, covering a range of 700-1000Hz. The level of the onward travelling wave was measured with and without the control applied and a level of control in dB recorded. Figure 7.11 shows the resulting levels of control achieved. The form of the control achieved has a comb like structure, with frequency regions where maximum control is achieved and regions where little control is achieved. This comb structure mirrors the frequency response function G_{21}, plotted in Figure 7.12a which can be considered a measure of the control authority that the resonator has over the onward travelling wave; where the control authority is low, the amount of control achievable is very small. This comb structure is due to the measurement set up. When the resonator is active it acts as a radiating source, there are two propagation paths to the upstream microphones; a direct path from the resonator neck, and a delayed path reflected off of the disturbance loudspeaker. These two paths

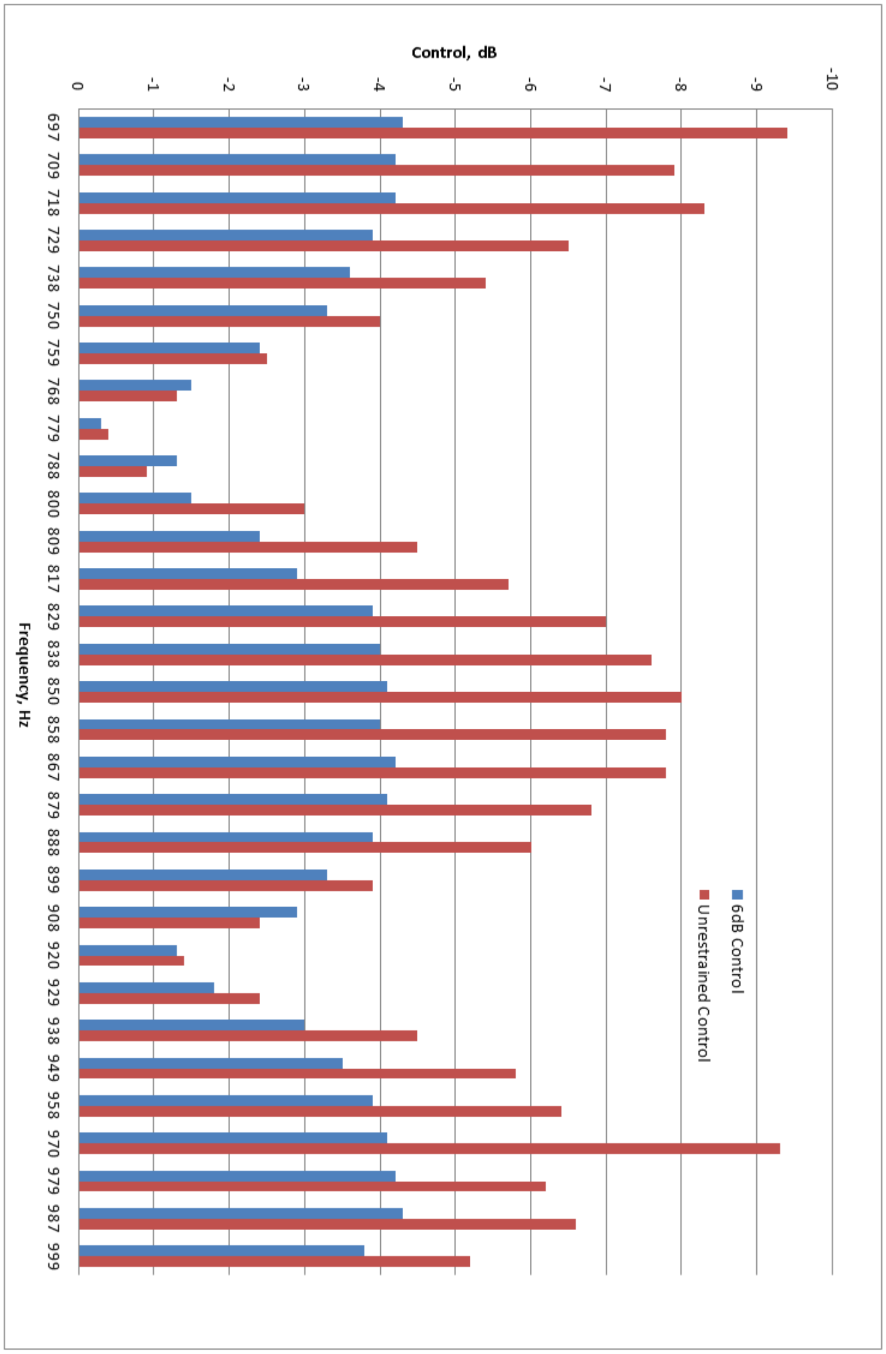

Figure 7.11: Magnitude of control achieved by applying the optimal control gain (red) and a gain calculated to achieve 6dB of attenuation (blue)

combine to create a comb filter effect, leading to the structure seen in G_{21}, and limiting the control achievable at the notch frequencies. This information about the influence of the active resonator on the far field is not available to the model used in the filter optimisations presented earlier in this chapter.

When the 6dB control coefficient is applied, the level of control achieved peaks at approximately 4dB; a useful level of control, however smaller than the predicted value. It was observed during the measurement stage that the instantaneous signal measured by the resonator microphone, $y(t)$ was often uneven, with the positive voltage values measured being larger than the negative values, even though the disturbance signal was symmetrical about 0V. This behaviour could be observed using both the disturbance loudspeaker or the resonator loudspeaker as a source, and after checking the microphone amplifier for linearity it was determined that this must be due to the microphone capsule. An example measured time history showing this behaviour is shown in Figure 7.12b. The non-linearity appears to be 'soft' saturation occurring as the amplitude is increased, limiting the value of the negative voltages measured. It is thought that it is the non-linear behaviour of the microphone that leads to the level of control being smaller than that predicted.

In spite of this non linearity, when applying the optimal control coefficient the level of control achieved reaches over 9dB at its peak, and remains above 5dB for much of the frequency span away from the notch frequencies. This is a useful level of control, but it is fair to assume that this could potentially be much larger if a linear microphone was used. This non-linearity will also contribute to the discrepancies between the predicted and achieved levels of control seen in sections 7.4 and 7.5 of this Chapter.

The tonal results here provide an indication of the maximum amount of control that could be achieved at each frequency. If a controller was designed such that it met the required gain and phase characteristics calculated above across the given frequency range, then this attenuation could be achieved over a wideband. An estimation of the transmission coefficient that could be achieved if a band limited controller (i.e. over the 700-1000Hz range) existed that produced the level of control achieved in the tonal cases is shown in Figure 7.13. This is calculated by applying the level of control achieved in Figure 7.11 to the passive resonator model, with the '6dB' controller shown by the blue line and the optimal controller by the red line. However, realising such a controller in the time domain is not trivial and would require additional constraints to ensure causality as

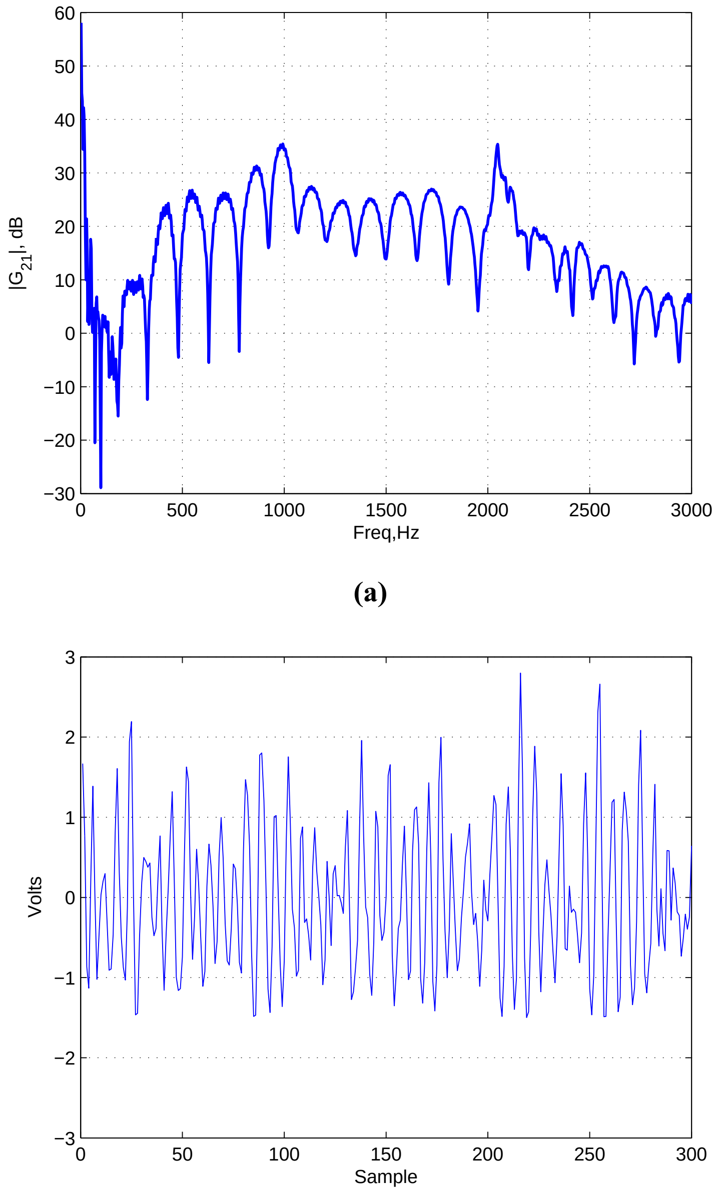

(a)

(b)

Figure 7.12: (a) The magnitude of G_{12} (b) A voltage trace recorded from the active Helmholtz resonator microphone when subject to random noise from the disturbance loudspeaker

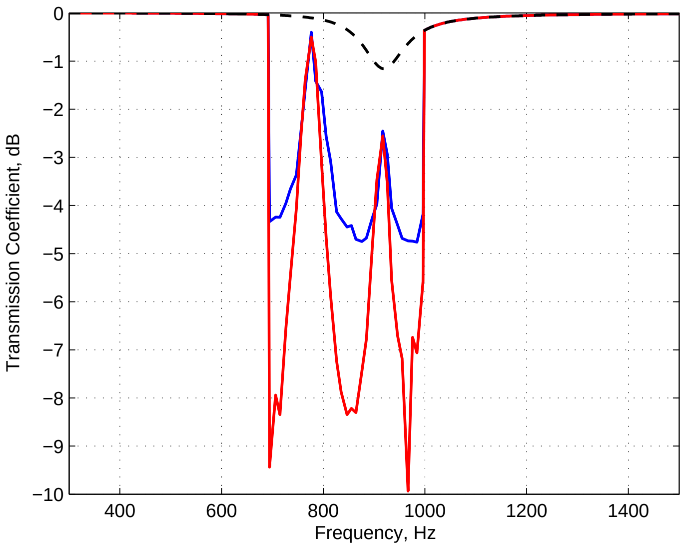

Figure 7.13: An estimation of the transmission coefficient of the active resonator with a theoretical controller based on the geometric control design results in Figure 7.11, the 6dB controller (blue) and the optimal controller (red) compared to the passive case (black, dashed)

well as taking into consideration power limits. A method for designing controllers to minimise remote signals across a given frequency band using this geometric approach has been developed and shown to be effective [108, 109] and could be a useful design method when creating acoustic isolators based on active resonators. However, this is out of the scope of this research and is left as a task for the future.

7.7 Conclusion

Based on the work described in Chapters 5 and 6 a prototype active resonator was produced to contribute to development towards an active acoustic metamaterial. The focus of the work was to investigate the potential of using active control to enhance the attenuation of the passive band gap. For expedience the active resonator was designed to be produced as much as possible from off the shelf components. The prototype was installed within the impedance tube set up described in Chapter 5 and its passive transmission loss measured, confirming the presence of a resonant band gap approximately 1.5dB deep. Whilst alone this amount of attenuation can be considered small it is intended to be used as a large array of resonators, and it is within the order of attenuation seen in Section 5.8 for a single resonator.

Based on the theoretical controllers designed in Section 6.4 2nd order feedback controllers and FIR feedback filters were designed and applied to the resonator. The 2nd order filters were designed manually to represent resonant analogue circuits, based on the results of the optimised 2nd order controllers from the previous Chapter. These controllers were shown to be effective at creating narrow, deep regions of attenuation, either enhancing the passive band gap or creating new regions of attenuation.

The optimised FIR filters were shown to create inconsistent results, with some regions of attenuation being successfully created at the targeted frequencies below the passive band gap as expected, but with less success achieved at frequencies above the band gap. The input to the optimisation routine relies heavily on the theoretical model of the system, with the plant response being the only measured quantity. Whilst it was shown in previous chapters that this model accurately predicts the performance of the passive metamaterial and appears to predict some of the behaviour seen with the optimised filters and 2nd order controllers it is clear that the in the future the design technique needs to be developed and refined before it can reliably produce controllers that truly reflect the potential performance of the active resonator.

Finally, to assess the potential levels of attenuation that may be achieved using a different control design method the system was reformulated as a remote control problem and optimal tonal controllers calculated using a geometric approach. The results of this highlighted that the placement of the resonator within the impedance tube created reflections from the disturbance loudspeaker leading to a comb structure in the frequency response from the ’local’ active resonator to the ’remote’ forward travelling. This comb structure meant that at the notch frequencies the control authority was very low and the amount of control achieved was limited. However, away from these regions the level of control achievable was good, peaking at over 9dB. Applying the tonal control highlighted the non-linear performance of the microphone capsule, which was thought to be limiting the control performance. If this microphone capsule was replaced with a more linear variant it would be expected that the level of control would increase even further.

Producing the active resonator prototype is the first step to create metamaterials with deep band gaps extended over a wide frequency region, and the results described above highlight the potential of the active metamaterial concept in achieving this using either simple resonant controllers or more complicated FIR filters. To further improve performance the model must be developed such that the constrained non-linear optimisation routine can reliably produce controllers that create wide bands of attenuation, or a different design method must be introduced. Combining many of these active resonators in an array structure could create powerful acoustic isolators achieving high levels of attenuation over large frequency bands, particularly when marrying the concept presented in this Chapter with ongoing research in areas such as 3D printed actuators [110] to increase the number and reduce the size of the resonators. In addition further research could include changing the goal of the controller design, for example to maximise absorption, or to control the effective material parameters.

Chapter 8
Conclusions and Further Work

8.1 Conclusions

The area of acoustic/viscoelastic metamaterials has attracted a great deal of research interest due to their dispersive material parameters which mean they have potential as elements of an acoustic cloak or an acoustic superlens. They also exhibit high levels of wave attenuation at resonance, known as band gaps, which mean they have potential for use as high performance low frequency isolators. However these interesting effects are due to resonant mechanisms and as such they occur over relatively narrow bandwidths. Previously in the literature it has been shown that adding active elements combined with shunt circuits can tune theses effects, however most (thought not all) of these active metamaterials remain theoretical and are yet to be realised. The work presented in this thesis describes the development of new metamaterials that incorporated fully active architecture designed to enhance the passive band gap behaviour over a wider frequency range. Prototypes of these active metamaterials were produced and their behaviour confirmed in the laboratory. The main focus of the work has been to increase the attenuation of the band gap region for isolation applications however in the future the concept could also be applied with respect to an acoustic superlens or cloak design, using active control to manipulate the material parameters and achieve negativity over a broad frequency range, therefore the effective material parameters of the materials are also considered. Two active metamaterials have been developed, a viscoelastic metamaterial that could be employed in the vibration domain and an acoustic metamaterial to be applied in the acoustic domain, these are described in the respective sections below.

8.1.1 Viscoelastic Metamaterial

For the initial part of the investigation an active viscoelastic metamaterial concept first described by Pope and Daley [12] was examined. This metamaterial was shown to have dispersive effective mass and a deep resonant band gap. By applying a distributed active control strategy to couple adjacent layers the effective stiffness could also be made to be dispersive. Using this initial model it was shown that due to the multilayer form of metamaterials the displacement of individual elements and hence the magnitude of individual control forces required is smaller. This provides an advantage over traditional active isolation methods. It was also shown that by adjusting the control gains as a function of the metamaterial layer that it is possible to ’smear’ the band gap over a wider frequency range.

This initial model is a useful tool to theoretical investigations but it has some practical shortcomings. The material requires the application of point forces to masses, normally achievable using inertial actuators. This introduces additional complexity and limitation into the design of the controller. In addition it requires the application of active control to achieve double negativity. To address these issues a new metamaterial was developed. This new metamaterial model still has a deep band gap in its transmissibility, but has additional viscoelastic connections that enable it to achieve double negativity passively, and the active forces now employed reactively between two resonator masses, meaning reactive actuators can be used. This simplifies the control design process, although at the expense of flexibility. A novel method for assessing the band gap profile was developed that consists of tuning 4 key frequencies, and it was shown that by tuning the band gap resonance to coincide with the natural frequency of the transmission units a wide, symmetrical passive band gap could be achieved. Next a concept design was developed based on this new metamaterial model that could be used as a vibration isolator, and a prototype active metamaterial produced from machined steel. The prototype was tested in the laboratory and the presence of a passive band gap confirmed.

Using active control to enhance the passive band gap was then investigated with both SISO feedforward FxLMS and SISO optimised feedback filters being implemented. It was shown that the application of active control was effective both in suppressing out of band resonances and increasing the bandwidth at which wave attenuation occurs when compared to the passive case. For both the SISO feedforward and feedback cases attenuation at frequencies below the band gap region was limited in part due to the small magnitude of plant response of the single actuator. It was then shown that greater performance could be achieved by implementing a MIMO controller consisting of optimised feedback filters. Three multi-channel controller structures were investigated. First a ’periodic’ controller was chosen to be true to the periodic structure of metamaterials, which was shown to improve the band width of the band gap significantly, although its performance is constrained by the need for each filter to be identical. When this constraint is relaxed to create a decentralised controller the performance increases, achieving nearly 10dB of attenuation across the target frequencies whilst retaining the peak passive band gap performance. The final multichannel controller structure was a fully centralised system consisting of 4 distinct filters, the least constrained of the three structures, and was expected to achieve the best results. However conditioning issues meant that it was difficult to achieve a solution to the optimisation problem in this case, and once a filter design was achieved the performance was less than expected.

The results demonstrate the ability to either suppress out of band resonances or enhance the bandwidth over which attenuation occurs either side of the band gap. When a wide range of frequencies were targeted the greatest levels of attenuation are achieved where the natural band gaps occur, demonstrating that a unified design process that matches the best features of both active and passive functionality can provide impressive levels of attenuation over wide bandwidths. This is a supporting argument for using, where appropriate, active periodic materials in vibration isolation applications over more traditional active isolation mounts.

8.1.2 Acoustic Metamaterial

The second half of this thesis focusses on a 1 dimensional acoustic metamaterial consisting of an array of Helmholtz resonators connected in parallel. The transmission behaviour of the metamaterial was modelled using the acoustic impedance of a Helmholtz resonator and a transfer matrix method, and by using a lumped parameter equivalent circuit model it was possible to derive the effective material parameters of the metamaterial. It was shown that such a metamaterial would exhibit a band gap at resonance, and have both a dispersive effective bulk modulus and density; most other studies on these types of metamaterials have focused on the bulk modulus only. Several samples of such a metamaterial were then produced, consisting of an array of seven split hollow spheres (SHS), manufactured using additive layer manufacturing. As metamaterial structures are developed into higher degrees of freedom and smaller dimensions 3D printing technology such as this is likely to be the most viable route to production, and the work here provides a validation of the design and manufacturing process of acoustic metamaterials in this way. The band gap and dispersive material parameters of the metamaterials were then confirmed in the laboratory, and it was shown that by mixing the natural frequencies of the resonators within the metamaterial multiple band gaps could be achieve. These multiple band gaps can also merge together to produce wider regions of attenuation, however to preserve a high level of attenuation many resonator elements are required.

One way to create a wide, deep band gap without resorting to impractical numbers of resonant inclusions is to create an active acoustic metamaterial. The first step towards that is to create an active Helmholtz resonator that could be used within a metamaterial, and this was the focus of the remainder of the thesis. Initially a model of an active resonator was developed and to investigate its potential performance the formal stability limits of a second order control loop are derived and the performance at these limits examined. Next optimised feedback controllers were designed to minimise sound transmission over a specified frequency range and the transmission coefficient and effective material parameters of the active resonator modelled. Two types of controller were designed, FIR filters and simple 2nd order pole-zero controllers. It was shown that using optimised FIR filters in this way can greatly increase the bandwidth over which attenuation is achieved, or create new regions of attenuation whilst retaining the passive band gap performance. The regions of attenuation coincide with the dispersive nature of the effective material parameters and negative bulk modulus can be achieved. The 2nd order controllers also achieve new regions of attenuation but due to the limit on the degrees of freedom of the system, the bandwidth of these new band gaps is narrower than that achieved with filters. When designing an active metamaterial like this there would be a trade-off between controller complexity and performance that would have to be decided based on the use case.

Finally, a prototype active resonator was produced and based on the work above feedback controllers were designed, applied to the resonator and tested in the laboratory. Manually designed 2nd order controllers were shown to create narrow regions of attenuation at resonance, as predicted. Optimising FIR feedback filters was shown to create inconsistent results, with regions of attenuation being successfully created in some cases, but with less success in others. The input to the optimisation routine relies heavily on the theoretical model of the system which, whilst shown to accurately predict the performance of the passive metamaterial and some active cases, contains approximations that appear to harm its accuracy in other cases. The design technique therefore needs to be developed and refined before it can reliably produce controllers that truly reflect the potential performance of the active resonator. To assess the potential levels of attenuation that may be achieved from the active resonator optimal tonal controllers were calculated using a geometric remote control approach and applied. The results of this demonstrated that the active resonator has the potential to achieve high levels of control and combining many of these active resonators in an array structure within a metamaterial could create powerful acoustic isolators achieving high levels of attenuation over large frequency bands.

8.2 Suggestions for Future Work

The work presented in this thesis has highlighted potential areas for future work to be carried out. The future work is split into two sections, governing the two respective metamaterial types investigated.

8.2.1 Practical Implementation of the Active Viscoelastic Metamaterial as an Isolator

The coupled viscoelastic metamaterial prototype demonstrated the potential of such a metamaterial to be applied as an active vibration isolator, and there are several areas in which this investigation could be extended further in the future. A useful case study would be to produce multiple instances of the metamaterial and install them on a piece of vibrating machinery, investigating its performance in a practical situation. Such a study would take the metamaterial one step closer to practical use, however there are many interesting problems that would have to be overcome. The vibration from a machine is unlikely to be purely vertical, requiring further development of the metamaterial configuration to consider additional degrees of freedom. In addition to the linear vibration, the machine will have 3 rotational modes which, with an active metamaterial unit at each of 4 corners for example, poses an interesting control problem. If such work was carried out it would allow a quantitative comparison between the active metamaterial, traditional active isolators and passive isolators.

8.2.2 Development of the Active Viscoelastic Metamaterial for Other Applications

The focus of the work carried out regarding the viscoelastic metamaterial has been on isolation applications, however the model has potential to be adapted and used as part of an acoustic cloak, lens or waveguide. Such work will require the model to be developed and expanded into multiple dimensions, for the metamaterial to be produced with more layers on a smaller scale and for a method to be employed that could directly measure the effective material parameters. Once such a metamaterial was developed it would be possible to examine the potential for using active control to manipulate waves as they travel through the material, focusing waves on a point, or bending them as desired. Such a material may have a lot of active elements, and the control design method may have to be adapted such that many simple, local control loops are used instead of a centrally administered controller.

8.2.3 Active Resonator Controller Design

The active resonator results presented in this thesis suggest that there is great potential for an active acoustic metamaterial consisting of active Helmholtz resonators to act as a high performance acoustic isolator. Feedback filters were designed that created regions of attenuation however it was also shown that the design technique needs to be developed further to reliably produce controllers that truly reflect the potential performance of the active resonator. One route towards this may be to develop an alternative control optimisation that contains more measured properties of the active resonators rather than relying so heavily on a theoretical model. There is also potential to create controllers that achieve alternative design objectives, such as creating an acoustic panel where the controllers are designed to maximise absorption, or manipulating the material parameters to create an acoustic lens or cloak.

The results presented feature a single resonator, so the next step towards a practical active acoustic metamaterial is to scale up to multiple resonators, and investigating the issues that this might create, such as modelling the coupling mechanism between, the resonators. In addition, if resonator numbers get larger it may be necessary to create simpler, decentralised controllers; perhaps even self-tuning controllers such as those proposed by Zilleti *et al* [111, 112]. Combining a strategy like this with work going on in other areas into additive layer manufacturing and 3D printed actuators etc, one could envisage producing such a high performance, active metamaterial containing many resonators on a micro scale.

Appendix A

Derivation of the Effective Material Parameters of the Viscoelastic Metamaterials

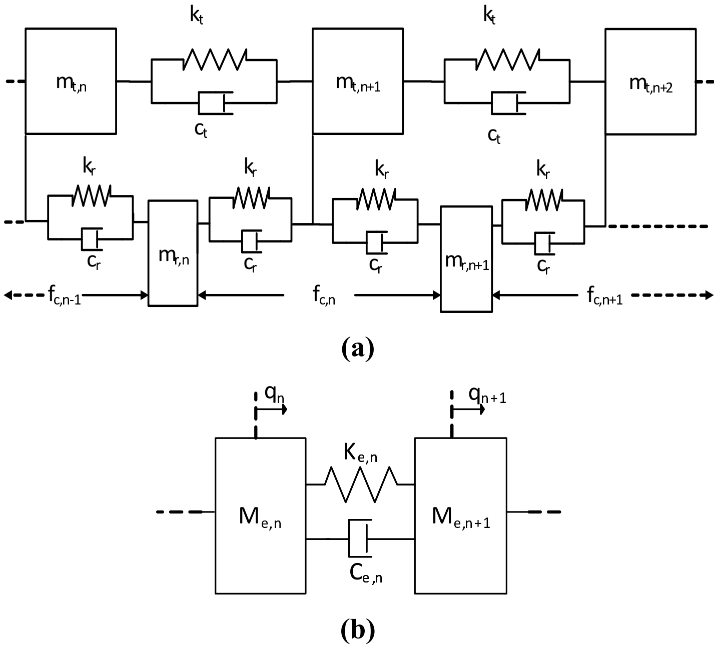

Figure A.1: (a) The coupled metamaterial structure. (b) A simple representation of the metamaterial chain using equivalent material parameter

Both the uncoupled viscoelastic metamaterial detailed in Chapter 2 and the coupled viscoelastic metamaterial presented in Chapter 3 have dispersive material parameters due to their resonant inclusions. The uncoupled variant has dispersive effective mass passively, but requires the use of a distributed active architecture to achieve dispersive effective stiffness also. The coupled metamaterial has dispersive effective mass and stiffness passively. The method used to derive the equations governing the material parameters are detailed here. The couple metamaterial is a novel development first presented in this thesis and is the focus of the calculations presented in this Appendix, the material parameters for the uncoupled metamaterial were first presented by Pope and Daley, however their derivation follows the same principle.

First consider a simple chain of effective mass elements connected by effective stiffness and damping elements, as shown in Figure A.1b. The equations of motion of this material can be constructed using either Newtonian mechanics or D'Alemberts principle [83] and are thus

$$-M_e q_n \omega^2 = (C_e i\omega + K_e)(q_{n-1} + q_{n+1} + 2q_n) \tag{A.1}$$

To derive an expression for the effective material parameters, the equations of motion of the metamaterial, shown in Figure A.1a, are built using the same principles, and then manipulated to give the same form as Equation A.1. The effective material parameters are then apparent through inspection. The equations of motion for the metamaterial are

$$-\omega^2 m_t q_{t,n} = (j\omega c_t + k_t)(q_{t,n-1} + q_{t,n+1} - 2q_{t,n}) + (j\omega c_r + k_r)(q_{r,n-1} + q_{r,n} - 2q_{t,n}) \tag{A.2}$$

$$-\omega^2 m_r q_{r,n} = (j\omega c_r + k_r)(q_{t,n} + q_{t,n+1} - 2q_{r,n}) \tag{A.3}$$

$$-\omega^2 m_r q_{r,n-1} = (j\omega c_r + k_r)(q_{t,n-1} + q_{t,n} - 2q_{r,n-1}) \tag{A.4}$$

Manipulating and combining A.3 and A.4 gives

$$q_{r,n} + q_{r,n-1} = \frac{j\omega c_r + k_r}{-\omega^2 m_r + 2(j\omega c_r + k_r)}(2q_{t,n} + q_{t,n+1} + q_{t,n-1}) \tag{A.5}$$

which can then be substituted into A.2

$$\begin{aligned} -\omega^2 m_t q_{t,n} = {} & (j\omega c_t + k_t)(q_{t,n-1} + q_{t,n+1} - 2q_{t,n}) - (j\omega c_r + k_r)2q_{t,n} \dots \\ & + \frac{(j\omega c_r + k_r)^2}{-\omega^2 m_r + 2(j\omega c_r + k_r)}(q_{t,n} + q_{t,n+1} - 2q_{t,n-1}) \end{aligned} \tag{A.6}$$

Now consider

$$
\begin{aligned}
&-(j\omega c_r + k_r)2q_{t,n} = -2q_{t,n}(j\omega c_r + k_r)\frac{-\omega^2 m_r + 2(j\omega c_r + k_r)}{-\omega^2 m_r + 2(j\omega c_r + k_r)} \\
&\therefore -(j\omega c_r + k_r)2q_{t,n} = -2q_{t,n}\frac{-\omega^2 m_r(j\omega c_r + k_r)}{-\omega^2 m_r + 2(j\omega c_r + k_r)} - 4q_{t,n}\frac{(j\omega c_r + k_r)^2}{-\omega^2 m_r + 2(j\omega c_r + k_r)}
\end{aligned}
\tag{A.7}
$$

Combining Equation A.6 with this expression A.7 and manipulating gives

$$
\begin{aligned}
&-\omega^2\left(m + \frac{2m_r(k_r + j\omega c_r)}{-\omega^2 m_r + 2(k_r + j\omega c_r)}\right)x_n \ldots \\
&\qquad + \left(k + j\omega c + \frac{(k_r + j\omega c_r)^2}{-\omega^2 m_r + 2(k_r + j\omega c_r)}\right)(2x_n - x_{n+1} - x_{n-1}) = 0
\end{aligned}
\tag{A.8}
$$

Comparing this expression to Equation A.1 it is evident that the effective mass, M_e and stiffness and damping $K_e+j\omega C_e$ are given by

$$M_e = m + \frac{2m_r(k_r + j\omega c_r)}{-\omega^2 m_r + 2(k_r + j\omega c_r)} \tag{A.9}$$

$$K_e + j\omega C_e = k + j\omega c + \frac{(k_r + j\omega c_r)^2}{-\omega^2 m_r + 2(k_r + j\omega c_r)} \tag{A.10}$$

Appendix B

Derivation of the Effective Material Parameters of the Acoustic Metamaterials

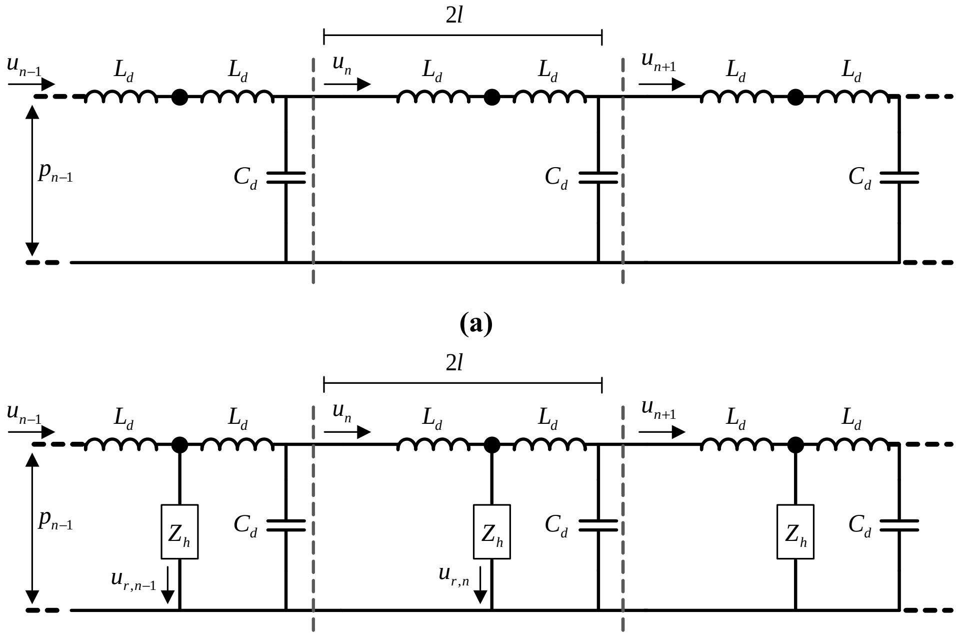

(a)

(b)

Figure B.1: (a) Equivalent lumped parameter circuit of 3 sections of empty duct, and (b) 3 layers of a metamaterial consisting of a duct containing a Helmholtz resonator

The derivation of the effective material parameters of the acoustic metamaterial follows the same philosophy to the viscoelastic metamaterial example given in Appendix A; the equations of motion are derived for the metamaterial are manipulated and compared to the equations of motion for a homogeneous material, the effective material parameters are then determined by inspection. The acoustic metamaterial however is a continuous system, and therefore before the equations of motion can be determined a lumped equivalent must be built. This lumped model will remain accurate as long as it is used within the long wavelength limit. An equivalent circuit model is used to represent the acoustic elements [95, pg. 50], where a the compliance of air is represented by capacitance C, inertia through inductive elements, L. Now the current flow represents the volume velocity, and the voltage represents acoustic pressure. The resonator elements themselves are kept as 'black box' impedances Z_h. The duct is assumed to have zero losses.

An empty acoustic duct is therefore represented as a chain of acoustic masses ($2L_d$) separated by acoustic compliance elements (C_d), Figure B.1a. To build the metamaterial model the resonators components are added between the 2 inductive elements in each layer, Figure B.1b. Using Kirchoff's voltage law the equation of motion for each loop can be determined. For the empty acoustic duct

$$-j\omega L_d u_n = \frac{1}{j\omega C_d}(u_{n-1} + u_{n+1} - 2u_n) \tag{B.1}$$

To determine the material parameters of the metamaterial, the equation of motion of 3 loops is considered; the loop immediately left of the nth layer, consisting of a Z_h, L_d and C_d element. And the two loops contained within the metamaterial layer.

$$-\frac{1}{j\omega C_d}(u_{n-1} - u_{r,n-1} - u_n) + j\omega L_d u_n + u_{r,n} Z_h = 0 \tag{B.2}$$

$$-u_{r,n} Z_h + j\omega L_d(u_n - u_{r,n}) + \frac{1}{j\omega C_d}(u_n - u_{r,n} - u_{n+1}) = 0 \tag{B.3}$$

$$-u_{r,n-1} Z_h + j\omega L_d(u_{n-1} - u_{r,n-1}) + \frac{1}{j\omega C_d}(u_{n-1} - u_{r,n-1} - u_n) = 0 \tag{B.4}$$

$$\tag{B.5}$$

Taking Equation B.3 solved for $u_{r,n}$ and Equation B.4 solved for $u_{r,n-1}$ and substituting into Equation B.2 gives

$$j\omega u_n + \frac{Z_h(j\omega u_n + \frac{1}{j\omega C_d}(u_n - u_{n+1})}{Z_h + j\omega L_d + \frac{1}{j\omega C_d}} = \frac{1}{j\omega C_d}(u_{n-1} - u_n)\cdots$$
$$- \frac{\frac{1}{j\omega C_d}(j\omega L_d u_{n-1} + \frac{1}{j\omega C_d}(u_{n-1} - u_n))}{Z_h + j\omega L_d + \frac{1}{j\omega C_d}} \tag{B.6}$$

Rearranging and collecting the current terms then gives

$$j\omega L_d\left(1 + \frac{Z_h + \frac{1}{j\omega C_d}}{Z_h + j\omega L_d + \frac{1}{j\omega C_d}}\right)u_2 = \cdots$$
$$\frac{Z_h}{j\omega C_d(Z_h + j\omega L_d + \frac{1}{j\omega C_d})}(u_{n-1} + u_{n+1} - 2u_n) \tag{B.7}$$

By comparing Equations B.1 and B.7 it is evident that the effective inertance and compliance given by the lumped parameter model of the acoustic metamaterial are given by

$$L_e = L_d\left(1 + \frac{Z_h + \frac{1}{sC_d}}{Z_h + sL_d + \frac{1}{sC_d}}\right) \tag{B.8}$$

$$C_e = \frac{C_d(Z_h + sL_d + \frac{1}{sC_d})}{Z_h} = C_d\left(1 + \frac{sL_d + \frac{1}{sC_d}}{Z_h}\right) \tag{B.9}$$

where $s = j\omega$. For an element of an acoustic medium length $2l$ and cross sectional area S_d, effective inertance and compliance are related to the effective density and bulk modulus respectively of the fluid, which can be calculated using Equations B.10 and B.11 [93].

$$\rho_e = \frac{L_e S_d}{2l} \tag{B.10}$$

$$B_e = \frac{2l S_d}{C_e} \tag{B.11}$$

Appendix C

Calculating 2 orthogonal rotational modes using 3 accelerometers placed at 120 degrees

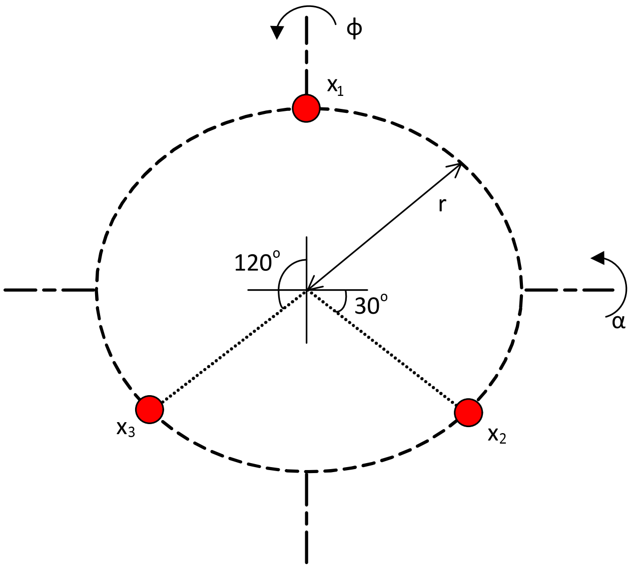

Figure C.1: The 3 accelerometers placed at 120 degree intervals around the centre axis

The motion of the coupled viscoelastic metamaterial is measured using 3 accelerometers on each mass, with the accelerometers placed at 120 degree intervals around the centre axis at a radius r, as shown in Figure C.1. The accelerometers can only measure vertical motion, denoted as x_n where n is the accelerometer index. The axial motion (z-mode) is calculated by adding the three accelerometer signals together such that the signal due to rotational modes cancels out, and dividing this by 3. The two rotational modes are calculated by considering the motion in the vertical axis, x, due to the rotation about each rotational axis, using simple trigonometry and the small angle theorem.

$$z = \frac{1}{3}(x_1 + x_2 + x_3) \tag{C.1}$$

$$\tag{C.2}$$

$$\alpha = \frac{1}{3}(\alpha_1 + \alpha_2 + \alpha_3) \tag{C.3}$$

$$\alpha_1 \approx \tan \alpha_1 = x_1/r \tag{C.4}$$

$$-\alpha_2 \approx \tan(-\alpha_2) = x_2/(r \sin 30) \tag{C.5}$$

$$-\alpha_3 \approx \tan(-\alpha_3) = x_3/(r \sin 30) \tag{C.6}$$

$$\phi = \frac{1}{3}(\phi_1 + \phi_2 + \phi_3) \tag{C.7}$$

$$\phi_1 = 0 \tag{C.8}$$

$$-\phi_2 \approx \tan(-\phi_2) = x_2/(r \sin 120) \tag{C.9}$$

$$\phi_3 \approx \tan \phi_3 = x_3/(r \sin 120) \tag{C.10}$$

Appendix D

LVCM-032-025-02 Actuator Datasheet

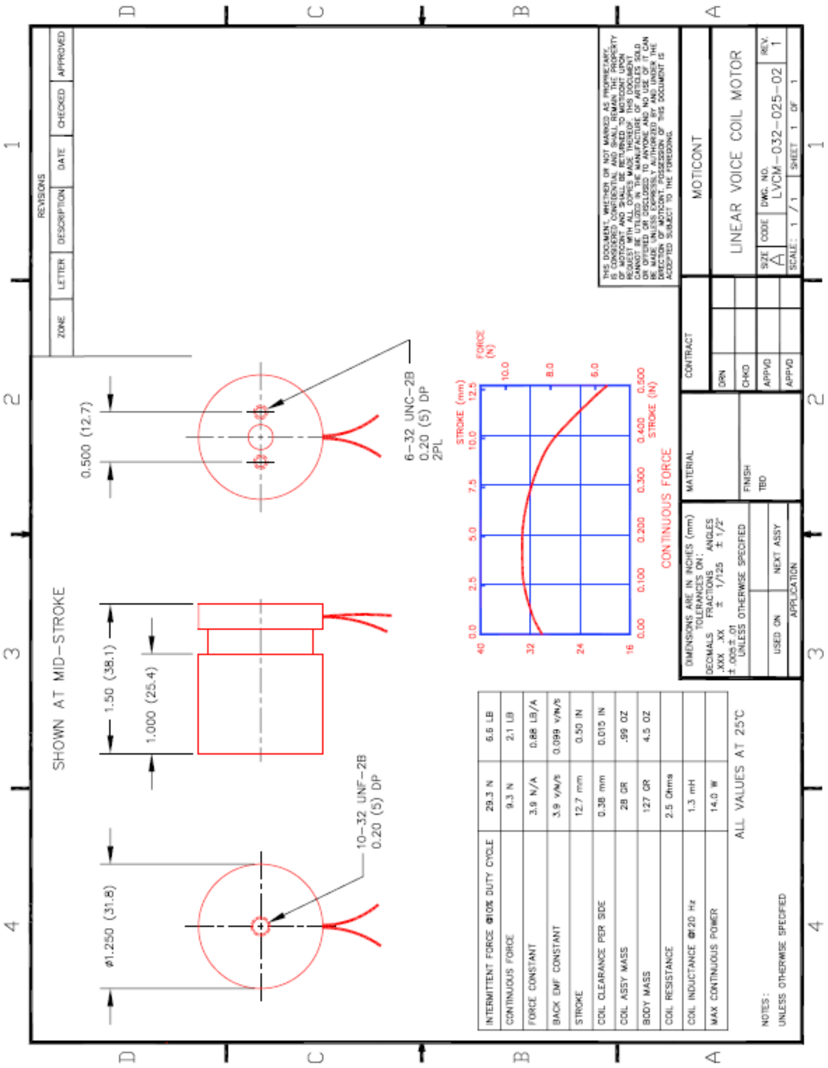

THIS DOCUMENT, WHETHER OR NOT MARKED AS PROPRIETARY, IS CONSIDERED CONFIDENTIAL AND SHALL REMAIN THE PROPERTY OF MOTICONT AND SHALL BE RETURNED TO MOTICONT UPON REQUEST WITH ALL COPIES MADE THEREOF. THIS DOCUMENT CANNOT BE UTILIZED IN THE MANUFACTURE OF ARTICLES SOLD OR OFFERED OR DISCLOSED TO ANYONE AND NO USE OF IT CAN BE MADE UNLESS EXPRESSLY AUTHORIZED BY AND UNDER THE DIRECTION OF MOTICONT. POSSESSION OF THIS DOCUMENT IS ACCEPTED SUBJECT TO THE FOREGOING.

INTERMITTENT FORCE @10% DUTY CYCLE	29.3 N	6.6 LB
CONTINUOUS FORCE	9.3 N	2.1 LB
FORCE CONSTANT	3.9 N/A	0.88 LB/A
BACK EMF CONSTANT	3.9 V/M/S	0.099 V/IN/S
STROKE	12.7 mm	0.50 IN
COIL CLEARANCE PER SIDE	0.38 mm	0.015 IN
COIL ASSY MASS	28 GR	.99 OZ
BODY MASS	127 GR	4.5 OZ
COIL RESISTANCE	2.5 Ohms	
COIL INDUCTANCE @120 Hz	1.3 mH	
MAX CONTINUOUS POWER	14.0 W	

ALL VALUES AT 25°C

Figure D.1: Datasheet for the LVCM-032-025-02 voice coil actuator [13]

Appendix E

AVA 124-20 Vibration Mount Datasheet

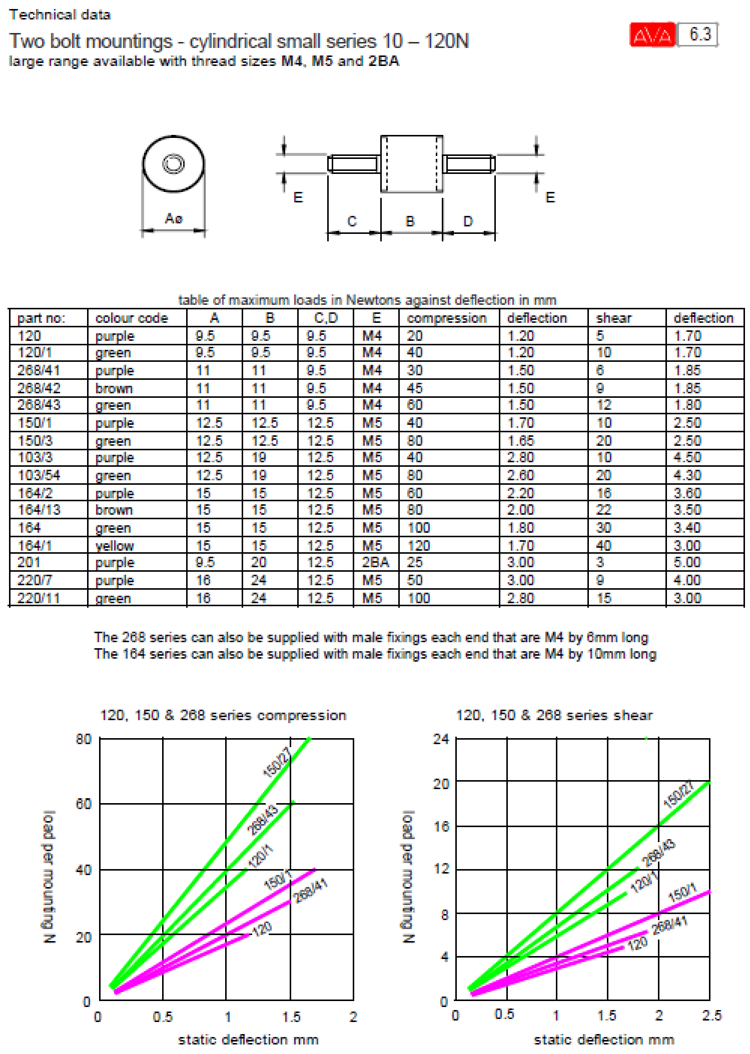

Technical data

Two bolt mountings - cylindrical small series 10 – 120N

large range available with thread sizes M4, M5 and 2BA

AVA 6.3

table of maximum loads in Newtons against deflection in mm

part no:	colour code	A	B	C,D	E	compression	deflection	shear	deflection
120	purple	9.5	9.5	9.5	M4	20	1.20	5	1.70
120/1	green	9.5	9.5	9.5	M4	40	1.20	10	1.70
268/41	purple	11	11	9.5	M4	30	1.50	6	1.85
268/42	brown	11	11	9.5	M4	45	1.50	9	1.85
268/43	green	11	11	9.5	M4	60	1.50	12	1.80
150/1	purple	12.5	12.5	12.5	M5	40	1.70	10	2.50
150/3	green	12.5	12.5	12.5	M5	80	1.65	20	2.50
103/3	purple	12.5	19	12.5	M5	40	2.80	10	4.50
103/54	green	12.5	19	12.5	M5	80	2.60	20	4.30
164/2	purple	15	15	12.5	M5	60	2.20	16	3.60
164/13	brown	15	15	12.5	M5	80	2.00	22	3.50
164	green	15	15	12.5	M5	100	1.80	30	3.40
164/1	yellow	15	15	12.5	M5	120	1.70	40	3.00
201	purple	9.5	20	12.5	2BA	25	3.00	3	5.00
220/7	purple	16	24	12.5	M5	50	3.00	9	4.00
220/11	green	16	24	12.5	M5	100	2.80	15	3.00

The 268 series can also be supplied with male fixings each end that are M4 by 6mm long

The 164 series can also be supplied with male fixings each end that are M4 by 10mm long

Figure E.1: Technical data for the AVA 06 Two Bolt Cylindrical Series of rubber bobbins, taken from [14]

Appendix F

Kingstate KDMG20008 Loudspeaker Datasheet

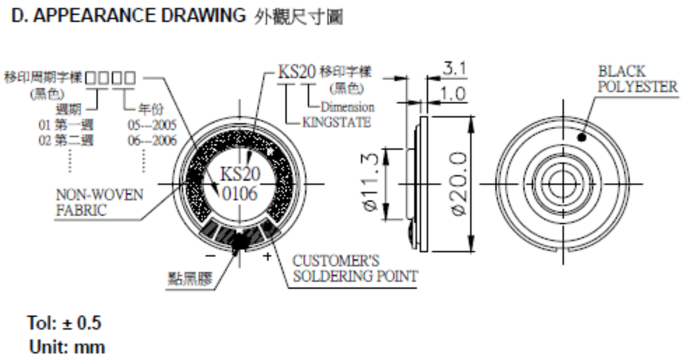

Figure F.1: The dimensions of the Kingstate KDMG20008 loudspeaker, taken from the datasheet [15]

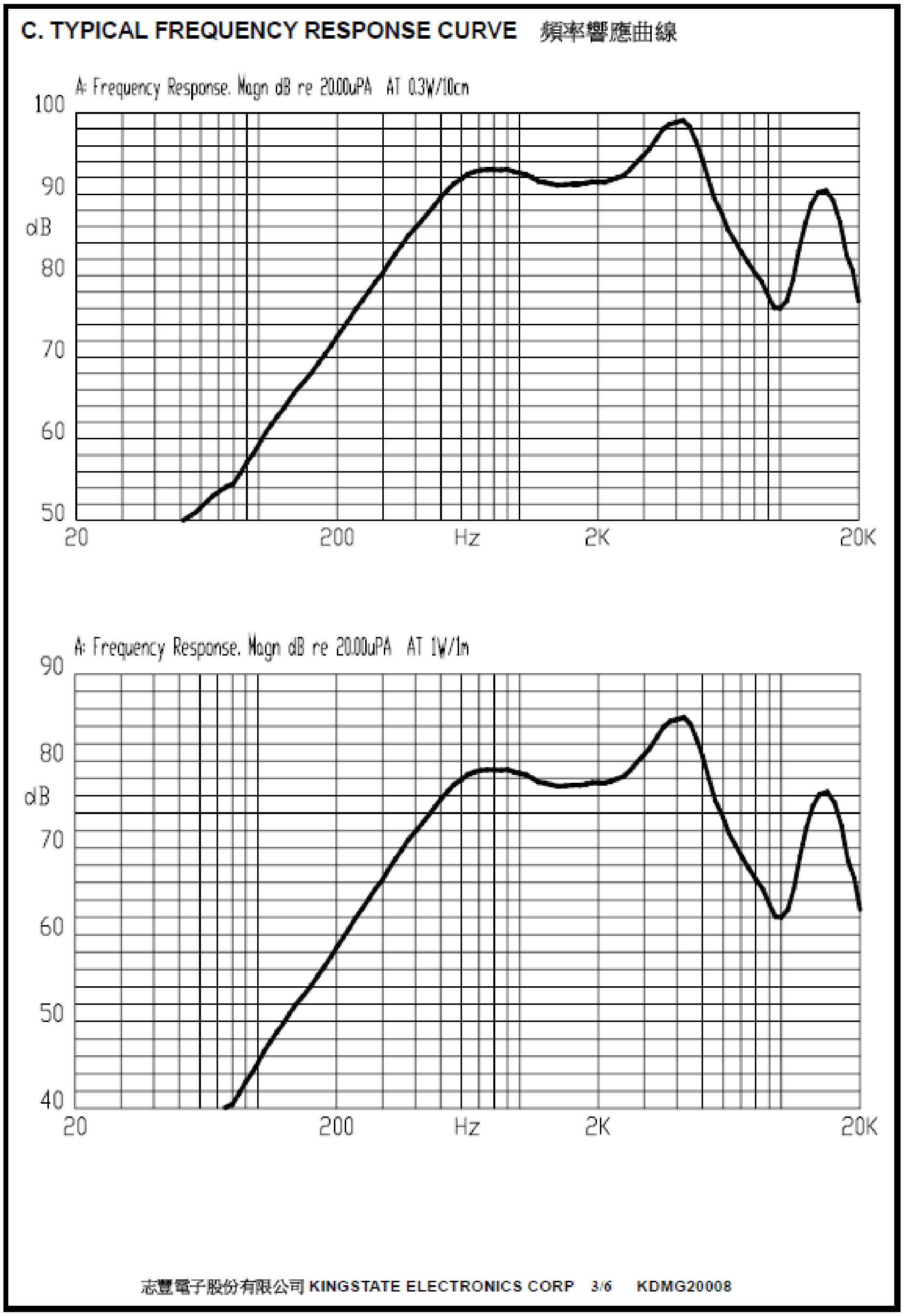

C. TYPICAL FREQUENCY RESPONSE CURVE 頻率響應曲線

志豐電子股份有限公司 KINGSTATE ELECTRONICS CORP 3/6 KDMG20008

Figure F.2: The frequency response of the Kingstate KDMG20008 loudspeaker, taken from the datasheet [15]

Appendix G

Knowles EA-21842-000 Datasheet

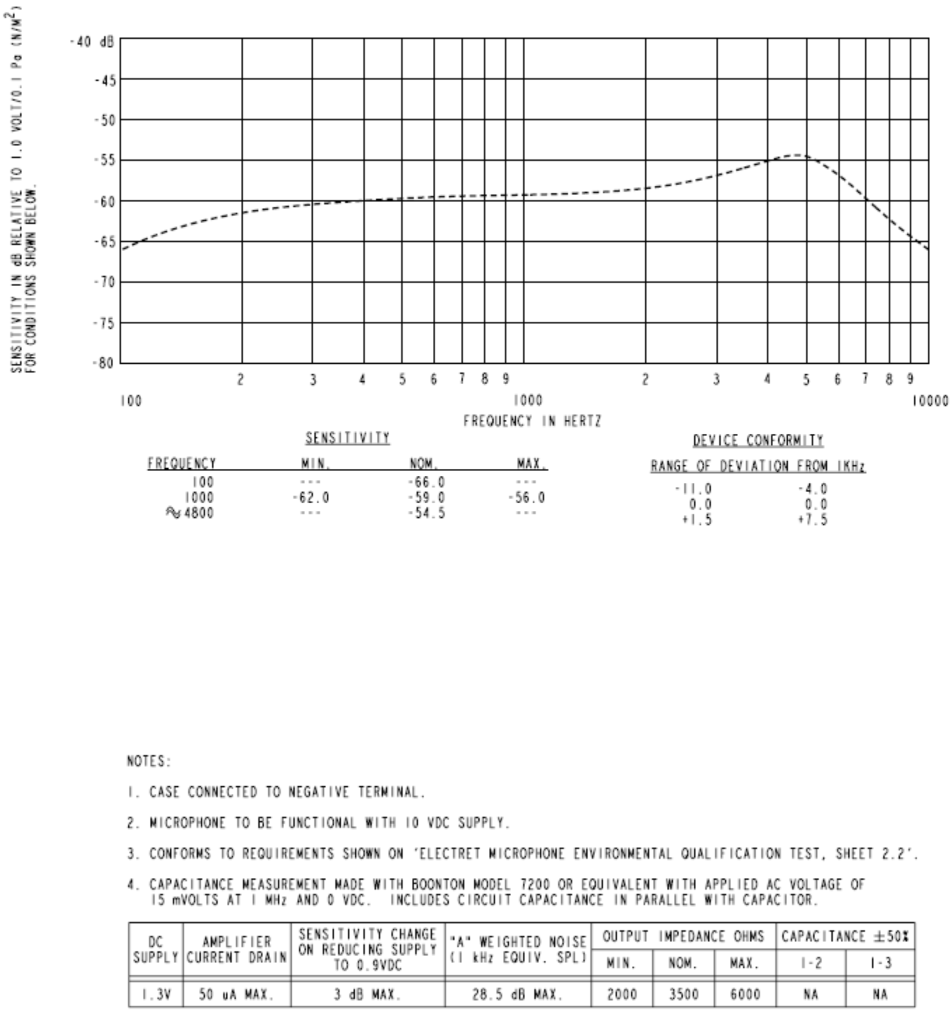

SENSITIVITY

FREQUENCY	MIN.	NOM.	MAX.
100	---	-66.0	---
1000	-62.0	-59.0	-56.0
≈ 4800	---	-54.5	---

DEVICE CONFORMITY

RANGE OF DEVIATION FROM 1KHz	
-11.0	-4.0
0.0	0.0
+1.5	+7.5

NOTES:

1. CASE CONNECTED TO NEGATIVE TERMINAL.
2. MICROPHONE TO BE FUNCTIONAL WITH 10 VDC SUPPLY.
3. CONFORMS TO REQUIREMENTS SHOWN ON 'ELECTRET MICROPHONE ENVIRONMENTAL QUALIFICATION TEST, SHEET 2.2'.
4. CAPACITANCE MEASUREMENT MADE WITH BOONTON MODEL 7200 OR EQUIVALENT WITH APPLIED AC VOLTAGE OF 15 mVOLTS AT 1 MHz AND 0 VDC. INCLUDES CIRCUIT CAPACITANCE IN PARALLEL WITH CAPACITOR.

DC SUPPLY	AMPLIFIER CURRENT DRAIN	SENSITIVITY CHANGE ON REDUCING SUPPLY TO 0.9VDC	"A" WEIGHTED NOISE (1 kHz EQUIV. SPL)	OUTPUT IMPEDANCE OHMS			CAPACITANCE ±50%	
				MIN.	NOM.	MAX.	1-2	1-3
1.3V	50 uA MAX.	3 dB MAX.	28.5 dB MAX.	2000	3500	6000	NA	NA

Figure G.1: The frequency response of the Knowles EA-21842-000 microphone capsule, taken from the datasheet [16]

References

[1] R. A. Shelby, D. R. Smith, and S. Schultz. Experimental verification of a negative index of refraction. *Science*, 292(5514):77–79, 2001.

[2] O. Sigmund and J. S. Jensen. Systematic design of phononic band-gap materials and structures by topology optimization. *Philosophical Transactions of the Royal Society of London Series a-Mathematical Physical and Engineering Sciences*, 361(1806):1001–1019, 2003.

[3] Z. Y. Liu, X. X. Zhang, Y. W. Mao, Y. Y. Zhu, Z. Y. Yang, C. T. Chan, and P. Sheng. Locally resonant sonic materials. *Science*, 289(5485):1734–1736, 2000.

[4] Y. Xiao, B. R. Mace, J. H. Wen, and X. S. Wen. Formation and coupling of band gaps in a locally resonant elastic system comprising a string with attached resonators. *Physics Letters A*, 375(12): 1485–1491, 2011.

[5] D. P. Elford, L. Chalmers, F. V. Kusmartsev, and G. M. Swallowe. Matryoshka locally resonant sonic crystal. *Journal of the Acoustical Society of America*, 130(5):2746–2755, 2011.

[6] C. L. Ding and X. P. Zhao. Multi-band and broadband acoustic metamaterial with resonant structures. *Journal of Physics D-Applied Physics*, 44(21), 2011.

[7] X. J. Liu, Y. Cheng, F. Yang, and J. Y. Xu. A multilayer structured acoustic cloak with homogeneous isotropic materials. *Applied Physics Letters*, 92(15), 2008.

[8] L. Zigoneanu, B. I. Popa, and S. A. Cummer. Three-dimensional broadband omnidirectional acoustic ground cloak. *Nature Materials*, 13(4):352–355, 2014.

[9] N. Fang, D. J. Xi, J. Y. Xu, M. Ambati, W. Srituravanich, C. Sun, and X. Zhang. Ultrasonic metamaterials with negative modulus. *Nature Materials*, 5(6):452–456, 2006.

[10] W. Akl and A. Baz. Stability analysis of active acoustic metamaterial with programmable bulk modulus. *Smart Materials and Structures*, 20(12), 2011.

[11] L. Airoldi and M. Ruzzene. Design of tunable acoustic metamaterials through periodic arrays of resonant shunted piezos. *New Journal of Physics*, 13, 2011.

[12] S. A. Pope and S. Daley. Viscoelastic locally resonant double negative metamaterials with controllable effective density and elasticity. *Physics Letters A*, 374(41):4250–4255, 2010.

[13] *Datasheet for the LVCM-032-025-02 Linear Voice Coil Actuator*. Moticont.

[14] *AVA 06 Two Bolt Cylindrical Series Technical Data*. AVA Ltd.

[15] *KDMG20008 Loudspeaker Datasheet*. Kingstate Electronics Corporation.

[16] *Knowles EA-21842-000 Microphone Datasheet*. Knowles Electronics.

[17] V. Veselago. The electrodynamics of substances with simultaneously negative values of permittivity and permeability. *Soviet Physics Uspekhi-Ussr*, 10(4):509–514, 1968.

[18] J. B. Pendry, A. J. Holden, D. J. Robbins, and W. J. Stewart. Magnetism from conductors and enhanced nonlinear phenomena. *Ieee Transactions on Microwave Theory and Techniques*, 47(11): 2075–2084, 1999.

[19] J. B. Pendry, A. J. Holden, W. J. Stewart, and I. Youngs. Extremely low frequency plasmons in metallic mesostructures. *Physical Review Letters*, 76(25):4773–4776, 1996.

[20] D. R. Smith and N. Kroll. Negative refractive index in left-handed materials. *Physical Review Letters*, 85(14):2933–2936, 2000.

[21] D. R. Smith, W. J. Padilla, D. C. Vier, S. C. Nemat-Nasser, and S. Schultz. Composite medium with simultaneously negative permeability and permittivity. *Physical Review Letters*, 84(18):4184–4187, 2000.

[22] D. R. Smith, J. B. Pendry, and M. C. K. Wiltshire. Metamaterials and negative refractive index. *Science*, 305(5685):788–792, 2004.

[23] J.D. Joannopoulos. *Photonic Crystals: Molding The Flow Of Light*. Princeton University Press, 2008.

[24] John William Strutt. *On the Remarkable Phenomenon of Crystalline Reflexion described by Prof. Stokes Scientific Papers*. Cambridge University Press, 2009.

[25] C. Goffaux and J. Sanchez-Dehesa. Two-dimensional phononic crystals studied using a variational method: Application to lattices of locally resonant materials. *Physical Review B*, 67(14), 2003.

[26] C. Goffaux, F. Maseri, J. O. Vasseur, B. Djafari-Rouhani, and P. Lambin. Measurements and calculations of the sound attenuation by a phononic band gap structure suitable for an insulating partition application. *Applied Physics Letters*, 83(2):281–283, 2003.

[27] Y. Q. Ding, Z. Y. Liu, C. Y. Qiu, and J. Shi. Metamaterial with simultaneously negative bulk modulus and mass density. *Physical Review Letters*, 99(9), 2007.

[28] M. Hirsekorn. Small-size sonic crystals with strong attenuation bands in the audible frequency range. *Applied Physics Letters*, 84(17):3364–3366, 2004.

[29] G. Wang, J. H. Wen, Y. Z. Liu, and X. S. Wen. Lumped-mass method for the study of band structure in two-dimensional phononic crystals. *Physical Review B*, 69(18), 2004.

[30] Z. Y. Liu, C. T. Chan, P. Sheng, A. L. Goertzen, and J. H. Page. Elastic wave scattering by periodic structures of spherical objects: Theory and experiment. *Physical Review B*, 62(4):2446–2457, 2000.

[31] P. D. C. King and T. J. Cox. Acoustic band gaps in periodically and quasiperiodically modulated waveguides. *Journal of Applied Physics*, 102(1), 2007.

[32] E. Pestel and F.A. Leckie. *Matrix methods in elastomechanics*. McGraw-Hill, 1963.

[33] J. Li and C. T. Chan. Double-negative acoustic metamaterial. *Physical Review E*, 70(5), 2004.

[34] C. T. Chan, Jensen Li, and K. H. Fung. On extending the concept of double negativity to acoustic waves. *Journal of Zhejiang University: Science*, 7(1):24–28, 2006.

[35] C. T. Sun, H. H. Huang, and G. L. Huang. On the negative effective mass density in acoustic metamaterials. *International Journal of Engineering Science*, 47(4):610–617, 2009.

[36] J. Mei, Z. Y. Liu, W. J. Wen, and P. Sheng. Effective mass density of fluid-solid composites. *Physical Review Letters*, 96(2), 2006.

[37] J. G. Berryman. Long-wavelength propagation in composite elastic media .1. spherical inclusions. *Journal of the Acoustical Society of America*, 68(6):1809–1819, 1980.

[38] Y. Cheng, J. Y. Xu, and X. J. Liu. Broad forbidden bands in parallel-coupled locally resonant ultrasonic metamaterials. *Applied Physics Letters*, 92(5), 2008.

[39] G. L. Huang and C. T. Sun. Band gaps in a multiresonator acoustic metamaterial. *Journal of Vibration and Acoustics-Transactions of the Asme*, 132(3), 2010.

[40] F. Farzbod. Analysis of bloch's method in structures with energy dissipation. *Journal of Vibration and Acoustics-Transactions of the Asme*, 133(5), 2011.

[41] F. Farzbod and M. J. Leamy. Analysis of bloch's method and the propagation technique in periodic structures. *Journal of Vibration and Acoustics-Transactions of the Asme*, 133(3), 2011.

[42] C. Goffaux, J. Sanchez-Dehesa, A. L. Yeyati, P. Lambin, A. Khelif, J. O. Vasseur, and B. Djafari-Rouhani. Evidence of fano-like interference phenomena in locally resonant materials. *Physical Review Letters*, 88(22), 2002.

[43] G. Wang, D. L. Yu, J. H. Wen, Y. Z. Liu, and X. S. Wen. One-dimensional phononic crystals with locally resonant structures. *Physics Letters A*, 327(5-6):512–521, 2004.

[44] G. Wang, X. S. Wen, J. H. Wen, L. H. Shao, and Y. Z. Liu. Two-dimensional locally resonant phononic crystals with binary structures. *Physical Review Letters*, 93(15), 2004.

[45] D. J. Mead. Wave-propagation and natural modes in periodic systems .1. mono-coupled systems. *Journal of Sound and Vibration*, 40(1):1–18, 1975.

[46] A. R. Diaz, A. G. Haddow, and L. Ma. Design of band-gap grid structures. *Structural and Multidisciplinary Optimization*, 29(6):418–431, 2005.

[47] Z Yang, HM Dai, NH Chan, GC Ma, and Ping Sheng. Acoustic metamaterial panels for sound attenuation in the 50–1000 hz regime. *Applied Physics Letters*, 96(4):041906–041906–3, 2010.

[48] K. T. Tan, H. H. Huang, and C. T. Sun. Optimizing the band gap of effective mass negativity in

acoustic metamaterials. *Applied Physics Letters*, 101(24), 2012.

[49] S. H. Lee, C. M. Park, Y. M. Seo, Z. G. Wang, and C. K. Kim. Acoustic metamaterial with negative density. *Physics Letters A*, 373(48):4464–4469, 2009.

[50] S. H. Lee, C. M. Park, Y. M. Seo, Z. G. Wang, and C. K. Kim. Acoustic metamaterial with negative modulus. *Journal of Physics-Condensed Matter*, 21(17), 2009.

[51] S. H. Lee, C. M. Park, Y. M. Seo, Z. G. Wang, and C. K. Kim. Composite acoustic medium with simultaneously negative density and modulus. *Physical Review Letters*, 104(5), 2010.

[52] H. H. Huang and C. T. Sun. Wave attenuation mechanism in an acoustic metamaterial with negative effective mass density. *New Journal of Physics*, 11, 2009.

[53] S. Zhang, L. L. Yin, and N. Fang. Focusing ultrasound with an acoustic metamaterial network. *Physical Review Letters*, 102(19), 2009.

[54] S. X. Yang, J. H. Page, Z. Y. Liu, M. L. Cowan, C. T. Chan, and P. Sheng. Focusing of sound in a 3d phononic crystal. *Physical Review Letters*, 93(2), 2004.

[55] J. B. Pendry, D. Schurig, and D. R. Smith. Controlling electromagnetic fields. *Science*, 312(5781): 1780–1782, 2006.

[56] D. Schurig, J. J. Mock, B. J. Justice, S. A. Cummer, J. B. Pendry, A. F. Starr, and D. R. Smith. Metamaterial electromagnetic cloak at microwave frequencies. *Science*, 314(5801):977–980, 2006.

[57] G. W. Milton, M. Briane, and J. R. Willis. On cloaking for elasticity and physical equations with a transformation invariant form. *New Journal of Physics*, 8, 2006.

[58] S. A. Cummer and D. Schurig. One path to acoustic cloaking. *New Journal of Physics*, 9, 2007.

[59] L. W. Cai and J. Sanchez-Dehesa. Analysis of cummer-schurig acoustic cloaking. *New Journal of Physics*, 9, 2007.

[60] A. N. Norris and W. J. Parnell. Hyperelastic cloaking theory: transformation elasticity with pre-stressed solids. *Proceedings of the Royal Society a-Mathematical Physical and Engineering Sciences*, 468(2146):2881–2903, 2012.

[61] B. Liu and J. P. Huang. Acoustically conceal an object with hearing. *European Physical Journal-Applied Physics*, 48(2), 2009.

[62] X. C. Huang, A. H. Jiang, Z. Y. Zhang, and H. X. Hua. Design and optimization of periodic structure mechanical filter in suppression of foundation resonances. *Journal of Sound and Vibration*, 330(20): 4689–4712, 2011.

[63] G. W. Milton and J. R. Willis. On modifications of newton's second law and linear continuum elastodynamics. *Proceedings of the Royal Society a-Mathematical Physical and Engineering Sciences*, 463(2079):855–880, 2007.

[64] S. S. Yao, X. M. Zhou, and G. K. Hu. Experimental study on negative effective mass in a 1d mass-spring system. *New Journal of Physics*, 10, 2008.

[65] Y. Gao, M. J. Brennan, and F. S. Sui. Control of flexural waves on a beam using distributed vibration neutralisers. *Journal of Sound and Vibration*, 330(12):2758–2771, 2011.

[66] Y. Cheng, J. Y. Xu, and X. J. Liu. One-dimensional structured ultrasonic metamaterials with simultaneously negative dynamic density and modulus. *Physical Review B*, 77(4), 2008.

[67] W. Akl and A. Baz. Configurations of active acoustic metamaterial with programmable bulk modulus. *Active and Passive Smart Structures and Integrated Systems 2010, Pts 1 and 2*, 7643, 2010.

[68] A. M. Baz. An active acoustic metamaterial with tunable effective density. *Journal of Vibration and Acoustics-Transactions of the Asme*, 132(4), 2010.

[69] W. Akl and A. Baz. Multi-cell active acoustic metamaterial with programmable bulk modulus. *Journal of Intelligent Material Systems and Structures*, 21(5):541–556, 2010.

[70] W. Akl, A. Elsabbagh, and A. Baz. Acoustic metamaterials with circular sector cavities and programmable densities. *Journal of the Acoustical Society of America*, 132(4):2857–2865, 2012.

[71] W. Akl and A. Baz. Experimental characterization of active acoustic metamaterial cell with

controllable dynamic density. *Journal of Applied Physics*, 112(8), 2012.

[72] M. Collet, P. David, and M. Berthillier. Active acoustical impedance using distributed electrodynamical transducers. *Journal of the Acoustical Society of America*, 125(2):882–894, 2009.

[73] S. A. Pope, M. Pelegrinis, and S. Daley. *A consideration of impedance matching issues with Metamaterials*. Proceeding of Internoise 2011. Osaka, Japan, 2011.

[74] S. A. Pope, H. Laalej, and S. Daley. *Active elastic metamaterials with applications in acoustics*. Proceedings of Acoustics 2012: 11th Congres Francais d'Acoustique and 2012 IOA annual meeting. Nantes, France, 2012.

[75] S. A. Pope, H. Laalej, S. Daley, and M. Reynolds. *Active elastic metamaterials with applications in vibration and acoustics*. Proceedings of Internoise 2012. New York, USA, 2012.

[76] H. Laalej, S. A. Pope, S. Daley, and M. Reynolds. Controllable broadband double negative active elastic structures. *Journal of Intelligent Material Systems and Structures (submitted)*, 2013.

[77] S. Daley and J. Wang. A geometric approach to the design of remotely located vibration control systems. *Journal of Sound and Vibration*, 318:702 – 714, 2008. ISSN 0022-460X.

[78] Steve Daley and Ilias Zazas. A recursive least squares based control algorithm for the suppression of tonal disturbances. *Journal of Sound and Vibration*, 331(6):1270 – 1290, 2012. ISSN 0022-460X.

[79] SA Pope, H Laalej, and S Daley. Performance and stability analysis of active elastic metamaterials with a tunable double negative response. *Smart Materials and Structures*, 21(12):125021, 2012.

[80] C.E. Brennen. *Hydrodynamics of pumps*. Concepts ETI, 1994.

[81] C. E. Bradley. Time harmonic acoustic bloch wave propagation in periodic waveguides. part i. theory. *The Journal of the Acoustical Society of America*, 96(3):1844–1853, 1994.

[82] S. Skogestad and I. Postlethwaite. *Multivariable feedback control: analysis and design*. John Wiley, 2005.

[83] W. Thomson. *Theory of Vibration With Applications*. Stanley Thornes, 1993.

[84] J.P. Den Hartog. *Mechanical Vibrations*. Mac Graw-Hill ; Dover, 1956.

[85] S. Elliott. *Signal Processing for Active Control*. Elsevier Science, 2000.

[86] J. C. Burgess. Active adaptive sound control in a duct - a computer-simulation. *Journal of the Acoustical Society of America*, 70(3):715–726, 1981.

[87] Speech IEEE Acoustics and Signal Processing Society. Digital Signal Processing Committee. *Programs for digital signal processing*. IEEE Press, 1979.

[88] J.R. Rowland. *Linear Control Systems: Modeling, Analysis, and Design*. Wiley, 1986. ISBN 9780471032762.

[89] P. Atkinson. *Feedback control theory for engineers*. Plenum Press, 1968.

[90] T. F. Coleman and Y. Y. Li. An interior trust region approach for nonlinear minimization subject to bounds. *Siam Journal on Optimization*, 6(2):418–445, 1996.

[91] R. H. Byrd, M. E. Hribar, and J. Nocedal. An interior point algorithm for large-scale nonlinear programming. *Siam Journal on Optimization*, 9(4):877–900, 1999.

[92] J.M. Maciejowski. *Multivariable feedback design*. Electronic systems engineering series. Addison-Wesley, 1989. ISBN 9780201182439.

[93] L.E. Kinsler. *Fundamentals of acoustics*. Wiley, 2000.

[94] U. Ingard. On the theory and design of acoustic resonators. *The Journal of the Acoustical Society of America*, 25(6):1037–1061, 1953.

[95] L.L. Beranek. *Acoustics*. American Institute of Physics, 1986.

[96] W.P. Patrick. *Sound Transmission Through Lined Ducts in Parallel*. Massachusetts Institute of Technology, Department of Aeronautics and Astronautics, 1979.

[97] B. H. Song and J. S. Bolton. A transfer-matrix approach for estimating the characteristic impedance and wave numbers of limp and rigid porous materials. *Journal of the Acoustical Society of America*, 107(3):1131–1152, 2000.

[98] British Standards Institution BSI. *BS EN 10534:2001 - Acoustics. Determindation of sound*

absorption coefficient and impedance in impedance tubes. Transfer-function method. BSI, 2001.

[99] F. P. Mechel. Notes on the radiation impedance, especially of piston-like radiators. *Journal of Sound and Vibration*, 123(3):537–572, 1988.

[100] T. A. Johansson and M. Kleiner. Theory and experiments on the coupling of two helmholtz resonators. *Journal of the Acoustical Society of America*, 110(3):1315–1328, 2001.

[101] K. J. B. Lee, M. K. Jung, and S. H. Lee. Highly tunable acoustic metamaterials based on a resonant tubular array. *Physical Review B*, 86(18), 2012.

[102] L. M. Hao, C. L. Ding, and X. P. Zhao. Tunable acoustic metamaterial with negative modulus. *Applied Physics a-Materials Science & Processing*, 106(4):807–811, 2012.

[103] J. Yuan. Active helmholtz resonator with positive real impedance. *Journal of Vibration and Acoustics-Transactions of the Asme*, 129(1):94–100, 2007.

[104] L.L. Beranek and T. Mellow. *Acoustics: Sound Fields and Transducers*. Elsevier Science, 2012. ISBN 9780123914866.

[105] W.J. Grantham and T.L. Vincent. *Modern control systems analysis and design*. J. Wiley, 1993. ISBN 9780471811930.

[106] J Cheer. Designing loudspeaker directivity for mobile devices. *Master's thesis, ISVR, University of Southampton*, 2009.

[107] D. Guicking and K. Karcher. Active impedance control for one-dimensional sound. *Journal of Vibration and Acoustics*, 106(3):393–396, 1984.

[108] X. Wang and C. M. Mak. Acoustic performance of a duct loaded with identical resonators. *Journal of the Acoustical Society of America*, 131(4):El316–El322, 2012.

[109] U. Ubaid, S. Daley, S. Pope, and I Zazas. Experimental validation of a geometric method for the design of stable and broadband vibration controllers using a propeller blade test rig. In *Control (CONTROL), 2012 UKACC International Conference on*, pages 369–374, Sept 2012.

[110] Y. Ishiguro and I. Poupyrev. 3d printed interactive speakers. *ACM Conference on Human Factors in Computing Systems (CHI),*, 2014.

[111] M. Zilletti, S. J. Elliott, and P. Gardonio. Self-tuning control systems of decentralised velocity feedback. *Journal of Sound and Vibration*, 329(14):2738–2750, 2010.

[112] M. Zilletti, S. J. Elliott, P. Gardonio, and E. Rustighi. Experimental implementation of a self-tuning control system for decentralised velocity feedback. *Journal of Sound and Vibration*, 331(1):1–14, 2012.